Ka Band
Propagation Experiments on the Australian Low Earth Orbit Microsatellite 'FedSat'

Thorsten Kostulski

Faculty of Engineering

University of Technology, Sydney

A Thesis Submitted for the Degree of

Doctor of Philosophy

2008

Certificate of Authorship/Originality

I certify that the work in this thesis has not previously been submitted for a degree nor has it been submitted as part of requirements for a degree except as fully acknowledged within the text.

I also certify that the thesis has been written by me. Any help that I have received in my research work and the preparation of the thesis itself has been acknowledged. In addition, I certify that all information sources and literature used are indicated in the thesis.

Sydney, September 2008

_____

Thorsten Kostulski

Für meine Eltern.

Acknowledgements

Contents

List of Figures

List of Tables

Nomenclature

Roman Symbols

A Attenuation

a_E Equatorial Earth Radius

c Speed of Light

C/N Carrier-to-Noise Ratio

D Antenna Reflector Diameter

d Distance

dB Decibel

dBm Decibels of Milliwatts

dBZ Decibels of Z

e_E Earth Eccentricity

El Elevation

f Frequency

G Gain

GHz Gigahertz

h Hour, Satellite height above Sea Level

H_0 Earth Station Height above Sea Level

H_E Rain Height above Sea Level

hPa Hectopascal

NOMENCLATURE

Hz Hertz

K Kelvin

k Regression coefficient, Boltzmann's Constant

kHz Kilohertz

km Kilometres

L Loss, Attenuation

Lat Latitude

Lon Longitude

M Link Margin

m Metres

MHz Megahertz

min Minutes

P Transmit Power

P_n Polynomial Coefficient

R Vector from the Centre of the Earth

$R_{0.01}$ Rainfall Rate for 0.01% Probability

s Seconds

SSP Sub-Satellite Point

V Volts

v Velocity

W Watts

X X-axis (pedestal)

Y Y-axis (pedestal)

Z Reflectivity Unit (in μm^3)

Greek Symbols

α	Elevation, General Angle
ϵ	Angular Error
γ_R	Specific Attenuation
λ	Wavelength
φ	Compensation Angle, Feed Offset Angle
ρ	Vector between Earth Station and Satellite, Water Vapour Density
θ	Tracking Pedestal Angle, Squint Angle

Subscripts

d	Downlink
ES	Earth Station
H	Horizon
Lat	Latitude
Lon	Longitude
M	Motor
P	Position
Rx	Receive
S	Satellite
tot	Total, Overall
Tx	Transmit
u	Uplink
Z	Zenith

Other Symbols

$^\circ$	Degrees

NOMENCLATURE

Acronyms

AC	Alternating Current
ACS	Attitude Control System
ACTS	Advanced Communication Technologies Satellite
ADAM	Advanced Data and Messaging
ADC	Analog-to-Digital Converter
ADEOS	Advanced Earth Observation Satellite
AEDST	Australian Eastern Daylight Savings Time
AEST	Australian Eastern Standard Time
AMSL	Above Mean Sea Level
AOS	Acquisition of Signal
AWGN	Additive White Gaussian Noise
AWM	Average-Worst-Month
BBP	Baseband Processor
BOM	Bureau of Meteorology (Australia)
bps	bits per second
BTU	British Thermal Units
C band	4-8 GHz frequency band
CDF	Cumulative Density Function
CDMA	Code Division Multiple Access
COTS	Component off-the-shelf
CP	Communications Payload
CRC	Cooperative Research Centre
CRCSS	Cooperative Research Centre for Satellite Systems

CSIRO	Commonwealth Scientific and Industrial Research Organisation
DAC	Digital-to-Analog Converter
DC	Direct Current
DDS	Direct Digital Synthesizer
DHS	Data Handling System
DL	Downlink
DPLL	Digital Phase Locked Loop
DSP	Digital Signal Processor
FedSat	Federation Satellite
FPGA	Field-Programmable Gate Array
GEO	Geostationary Earth Orbit
GPS	Global Positioning System
GSM	Global System for Mobile Communications
HF	Frequency band below 0.1 GHz
HPA	High Power Amplifier
HPCE	High Performance Computing Experiment
IF	Intermediate Frequency
IJK	Inertial Coordinate System
IST	Integrated Systems Test
ITR	Institute for Telecommunications Research, Adelaide
ITU	International Telecommunications Union
JAXA	Japan Aerospace Exploration Agency
JPL	Jet Propulsion Laboratory, USA
K band	18-24 GHz frequency band

NOMENCLATURE

Ka band	24-36 GHz frequency band
Ku band	12-18 GHz frequency band
L band	1-2 GHz frequency band
LCP	Left-Hand Circular Polarisation
LEO	Low-Earth Orbit
LNA	Low Noise Amplifier
LO	Local Oscillator
LOS	Loss of Signal
MEO	Medium-earth orbit
MMIC	Monolithic Microwave Integrated Circuit
MPA	Medium-Power Amplifier
N	Coaxial RF Connector (up to 11 GHz)
NASA	National Aeronautics and Space Administration
NASDA	National Space Development Agency
NCU	National Central University
NewMag	Name of the Magnetometer Experiment onboard FedSat
NTU	Nanyang Technological University
OSCAR	Orbital Satellite Carrying Amateur Radio
PCI	Peripheral Component Interconnect
PCS	Power Conditioning System
PDF	Probability Density Function
PID	Proportional-Integral-Derivative
PLL	Phase Locked Loop
PWM	Pulse-Width Modulation

Q band	36-46 GHz frequency band
QAM	Quadrature Amplitude Modulation
QPSK	Quadrature Phase Shift Keying
QUT	Queensland University of Technology
RCP	Right-Hand Circular Polarisation
RF	Radio Frequency
ROCSAT	Republic Of China Satellite
rpm	Revolutions per minute
S band	2-4 GHz frequency band
SEZ	Topocentric Horizon Coordinate System
SGP4	Simplified General Perturbations Satellite Orbit Model 4
SIL	Space Innovations Ltd.
SNR	Signal-to-Noise Ratio
STRAP	Satellite Transmission Rain Attenuation Project
TDM	Time-division Multiplex
TDMA	Time-division Multiple Access
TIP	Telecommunications and Industrial Physics
TLE	Two-Line Elements
TT&C	Telemetry, Tracking and Control
UHF	0.3-1 GHz frequency band
UL	Uplink
UTC	Universal Time Coordinated
V band	46-56 GHz frequency band
VHF	0.1-0.3 GHz frequency band

NOMENCLATURE

$WR28$ Waveguide Size (26.5-40 GHz)

$WR42$ Waveguide Size (18-26.5 GHz)

$WRESAT$ Weapons Research Establishment Satellite

$X\ band$ 8-12 GHz frequency band

Abstract

The emergence of the 20/30 GHz Ka band in satellite communications in recent decades has seen systems designers faced with the problem of severe signal attenuation though atmospheric effects, especially rain. Previous experimental missions, such as ACTS and OLYMPUS, have succeeded in collecting large amounts of propagation data, which has led to the development of various semi-empirical models for link design. However, all these experiments were carried out over geostationary satellites, and with a recent tendency towards constellations of low-earth orbit satellites for true global coverage and increased system capacity for real-time services, these models are in need of adaptation for variable elevation angles and the effects of rapid satellite movement.

The work contained in this largely experimental thesis presents the Australian 'FedSat' LEO microsatellite, carrying a Ka band beacon and a bent-pipe mode transponder, as an ideal research platform for such investigations. The in-house design, deployment and operation of a very low-cost, fast-tracking earth station is examined in-depth, and particular attention is paid to systems design aspects involving numerous hardware and software technologies, which interact with each other in a highly complex manner, for example Doppler frequency tracking, pointing accuracy control and precise signal power measurements. Prior to and during the operational phase, several crucial design improvements are discussed, implemented and verified. Successful and reliable tracking by using pointing coordinates derived from two-line elements, as opposed to GPS data, is experimentally proven.

The design of the earth station prototype is validated by the collection of Ka band propagation data in both beacon and bent pipe modes. After post-processing of the data, attenuation results for various weather conditions and down to elevation angles well below 10° are illustrated and interpreted in conjunction with the prevailing weather conditions. While a comparison with the measurements from geostationary satellites widely confirms the validity of the

results, other interesting phenomena are unveiled that require further investigation. In particular, the extent of low-angle scintillation appears to be wider band than previously reported in published literature, which is a potentially important finding.

Finally, the experience gathered during the late-stage design and the operation of the earth station gives rise to several recommendations for further design improvements and operational strategies, which may be helpful for future research groups in this field wishing to conduct similar LEO Ka band propagation experiments on a low budget.

Chapter 1

Introduction

Several decades after the launch of the first man-made satellite "Sputnik" in 1957 and the first active repeater communication satellite "Courier 1B" in 1960 [1], modern life without today's sophisticated satellite communication systems is almost unimaginable. The political stability of governments, the success of military operations and entire economies all depend to a large extend on the flexible, immediate and global availability of information, which is principally provided via satellite systems. Although easily taken for granted by corporate, government and military clients, the further improvement of satellite communication services still poses numerous challenges for scientists and engineers. Selected aspects of those open questions will be further investigated in this research thesis.

1.1   Research Context and Motivation

The design of contemporary communication systems is largely based on models developed through both established theoretical knowledge and empirical analysis of previous experiments. The extensive validation of proposed models through practical trials is often both difficult and expensive, hence even limited results gained from actual experiments can be quite valuable. Space research is regarded as particularly demanding and costly, and initial projects are often been heavily funded by governments to support the establishment of an aerospace industry in their country. With the very limited resources available for university-based space research in Australia, it can be regarded as both a challenge and a privilege to make a contribution to this field in the form of a research thesis.

In a chiefly experimental context, this dissertation aims at the design validation of a very low-cost, largely in-house developed, fast-tracking Ka band earth station (transmit and receive), with an additional goal of 20 GHz propagation data collection and analysis.

1. INTRODUCTION

Due to the complexity of the interrelated design aspects in a very wide variety of engineering fields, it shall also be regarded as proof of the author's knowledge on the systems engineering level, which is a prerequisite for the operational success. The following sections will justify the significance of the earth station operation presented in this work for particular aspects of satellite communications.

1.1.1 Review of Frequency Bands used in Satellite Communications

While the first satellite communication experiments took place in the HF and VHF bands, most commercial and military services were quickly moved to microwave frequencies due to the increased bandwidth availability. Today, only selected emergency, weather and amateur satellite services still remain active in the lower bands, while most communication and direct broadcast services have moved to the higher frequency bands as outlined in Table 1.1, as defined in [2] [3] [4].

Band Designation	Frequency Range (GHz)	Predominant Satellite Services
HF	<0.1	Early experiments, not used today
VHF	0.1 - 0.3	Weather, navigation, emergency
UHF	0.3 - 1.0	Emergency
L	1.0 - 2.0	Mobile, navigation
S	2.0 - 4.0	Mobile
C	4.0 - 8.0	Fixed, mobile
X	8.0 - 12.0	Fixed
Ku	12.0 - 18.0	Direct broadcast, fixed
K	18.0 - 24.0	Fixed, mobile
Ka	24.0 - 36.0	Fixed, mobile
Q	36.0 - 46.0	Research, Future Applications
V	46.0 - 56.0	Research, Future Applications

Table 1.1: Frequency band designations and primary use in satellite communications

While navigation, emergency and weather satellites only require a relatively small share of the available spectrum, the traditional frequency bands used by fixed and mobile communication and data services (C, X and Ku) have increased steeply in demand over the last two decades, resulting in an overcrowding of those bands [5] (p. 398). Since most of these services are currently provided via closely-spaced geostationary earth orbit (GEO) satellites, mutual interference has also become a problem, resulting in the strict regulation of power, pointing accuracy and sidelobe suppression on the uplink [6].

1.1.2 Emergence and Challenges of the Ka Band in Satellite Communications

As the looming congestion in the classical satellite bands was first realised in the late 1970's, researchers looked into the viability of a new commercial frequency band - Ka band - in anticipation of the emergence of high-data rate applications, such as real-time multimedia services, and therefore high bandwidth demands [7]. With several GHz of bandwidth available in the commercial Ka band, large evaluation projects were launched in the late 80's and early 90's to establish the commercial viability of high data rate communications via geostationary satellites carrying Ka band transponders (see Chapter 2). The purpose of the experimental satellites was the assessment of performance in this new frequency band, compared to the classical C and Ku satellite bands. Compared to the C and Ku bands, the advantages and disadvantages of Ka band satellite communications can be briefly summarised as follows:

Key Advantage of Ka Band

- Exhaustive bandwidth resources (Gigabit capacity [8])

- Higher antenna gain $G \propto f^2$, for a given reflector diameter)

Disadvantages of Ka Band

- Propagation is severely affected by atmospheric attenuation effects, such as rain, limiting the availability of services *(key factor)*

- Higher cost of components

- Higher free-space path loss, $FSL \propto f^2$

Although the free-space path loss is greater on Ka band, there still is a significant overall advantage, due to the fact that the gain on *both* the transmit and the receive antennas increases with frequency squared:

$$\frac{G_{Tx}G_{Rx}}{FSL} \propto f^2$$

With few other options, the demand for more bandwidth has since driven the desire to overcome those challenges and to make the Ka band commercially viable. While higher cost and increased free-space path loss can be taken into account as deterministic figures, an in-depth understanding of the largely stochastic nature of tropospheric effects is crucially required on Ka band frequencies (and higher).

1.1.3 Demand for Ka Band Propagation Research

An important figure in satellite communication systems is availability [3], which is particularly crucial for real-time multimedia applications, where system outages must be minimised as much as possible. However, especially on Ka band, outages are directly related to the prevailing *rain rate* along the propagation path, which causes signal attenuation easily reaching "...levels in excess of 20 dB in many areas of the world" [9]. Since the complete mitigation of this degradation leads to significantly higher spacecraft cost as one alternative, or decreased system capacity on the other, it is more economic to design the system for an acceptable percentage of outage only (usually in the order of 99.9%, [10]). In this approach, long-term rain rate statistics are collected from a wide range of locations in order to develop a suitable model for predicting the degradation. These models rely to a great extent on the *long-term* measurement of beacon signals transmitted from test satellites, for which GEO satellites are most suitable due to the relative ease of continuous observation. The models that have been developed for GEO satellites over the past 20 years can be regarded as very extensive and accurate (see Chapter 2).

1.1.4 Ka Band on Low Earth Orbit Satellites

In recent years, low-earth orbit (LEO) satellites and satellite constellations carrying Ka band payloads have increasingly emerged [11]. Compared to GEO satellites (36,000 km altitude), the use of Ka band on a LEO satellite (160-2000 km altitude) has the following advantages:

- Significantly lower path loss

- Lower signal latency (<15 ms vs. 250 ms return)

- Lower launch cost

- Smaller earth station terminals, suitable for rapid transport & deployment

- Coverage of high latitudes (for LEO satellites in near-polar orbit)

- Less interference and higher capacity due to possible frequency re-use in constellations

- Military applications

Conversely, the disadvantages are:

- Limited area of visibility, therefore shorter pass duration (10-20 minutes)

- Large constellations required for simultaneous global coverage

- Earth station requires a fast-tracking antenna system

- The high satellite velocity introduces large Doppler frequency shifts on Ka band

Naturally, Ka band communication via LEO satellites also suffers from the same propagation degradations as with GEO satellites, however the rapidly varying elevation angle during a satellite pass, anywhere from near-horizon to zenith, introduces additional effects, which have not been well covered in the existing literature. With the exception of [12], all LEO satellites carrying Ka band payloads to date have been for military use or have kept the results of their propagation experiments commercial-in-confidence. Although there are adaptations of the well-understood GEO propagation models for Ka band, they are yet to be validated through actual experiments.

1.1.5   Role of the UTS Ka Band Propagation Experiments

The demand for accurate Ka band propagation models and the verification of these models for the LEO case justifies the hardware implementation of a research platform. With the opportunity of designing and launching its own satellite, the Australian Cooperative Research Centre decided to include a Ka band payload for communication and propagation research purposes, which constitutes the very *first* Ka band research payload on a LEO microsatellite. Due to the spacecraft's limitations, the design challenges for a suitable Ka band earth station have been rigorous. Additional, financial constraints have given rise to doubts whether it would be possible to develop and operate a fully functional fast-tracking Ka band earth station over 7 years within a budget of less than US\$ 1 million [13], including all material and salaries. The work contained in this dissertation will accurately explain the circumstances and design challenges under which this goal has been achieved.

1.2   Thesis Structure

Following this introductory chapter, the thesis is divided into two parts. **Part I** provides a brief literature review of the underlying theory with previous experiments and presents the space segment of the experimental research platform. **Part II** focusses on the experiments and results obtained, followed by a critical project review. The organisation of the individual chapters is illustrated in Fig. 1.1.
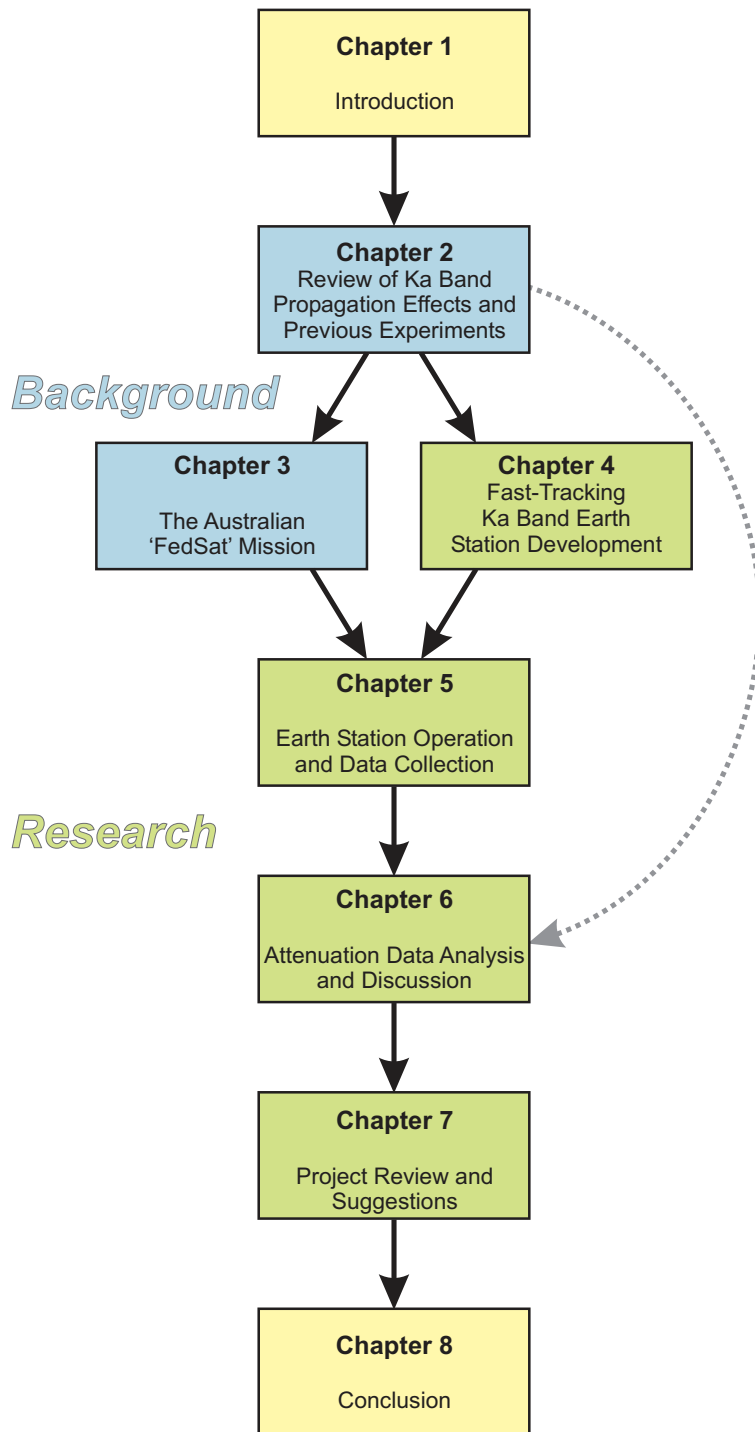
Figure 1.1: Thesis Structure

Chapter 2 concisely reviews the predominant propagation effects on Ka band satellite links, as published in current literature. A summary of previous Ka band propagation experiments over geostationary and low earth orbit satellites, as well as comparable research microsatellite and earth station developments is also provided.

Chapter 3 introduces the recent Australian microsatellite mission "FedSat". After a brief summary of the project structure, the key design aspects and properties of the spacecraft are presented, with particular focus on the low-earth orbit implications and the complexity of the payloads. As the space platform for the propagation experiment, the designs of the Ka band and communication payloads are discussed in greater detail, together with operational considerations.

Chapter 4 constitutes the first focus of this work. It presents the significant challenges faced in the design of a fast-tracking Ka band receive and transmit earth station on a small budget. From a systems point of view, all aspects of the earth station development within the scope of this project are thoroughly examined, which includes a very wide variety of engineering fields. Particular attention is paid to the post-deployment assessment and noteworthy improvement of spatial pointing accuracy through mechanical and software design improvements, along with the implementation of further design advancements.

Chapter 5, as the second key focus, illustrates the circumstances under which the earth station has operated and how the data was collected and pre-processed. It begins with a critical analysis of the number of satellite passes that are available for experiments, and establishes proof that tracking coordinates derived from two-line elements are reliable enough for the high-accuracy spatial tracking requirements in this project. Necessary systematic model corrections of the power measurements are suggested and implemented, before the observation of weather conditions and the course of a typical experiment is described. Secondary objectives, such as calibration procedures and Doppler tracking performance, conclude this chapter.

Chapter 6 is dedicated to the presentation of measurement data that has been collected with the earth station. Through numerous examples of passes in beacon and bent pipe modes, the measured path attenuation is related to the observed weather conditions and interpreted accordingly. Interesting observations are highlighted, and the validity of these measurements is assessed by comparing them to similar results from experiments over geostationary Ka band satellites.

Chapter 7 focusses on a critical review of technical and organisational aspects of the project, especially on the large number of difficulties encountered in conducting the operations successfully. It concludes with several suggestions for design improvement for future low-cost Ka band earth station designs for LEO satellite tracking.

1.2.1 Thesis Objectives

This **experimental thesis** aims to achieve the following objectives:

Primary

- Creation of a highly complex, low-cost, fast-tracking *operational* Ka band earth station.

- Prototype verification of the earth station's system design and implementing significant design improvements.

- Development of an earth station with the purpose of enabling the collection of LEO satellite Ka band propagation data and presentation of preliminary attenuation results.

Secondary

- Demonstration of the author's knowledge and practical skills in experimental research, especially in the fields of high-accuracy LEO satellite tracking operations and Ka band propagation data collection.

As substantiated further in Section 5.6, it is *not* an objective within the scope of this thesis to establish any quantitative comparison with existing propagation models, or to propose any modifications of such models. Consequently, the extensive field of propagation *modelling* is not explicitly included in the literature review; however the author is well aware of those theories and their implications.

It must also be noted that, from 2003 onwards, the author has been the *only* researcher working on this experiment (with sporadic support by a software engineer until 2004). Within this project, he was solely responsible for:

- The regular operation of the earth station,

- Practical hardware and software modification of the earth station for enhancing its performance,

- Pass scheduling and preparations,

- Fault investigation and correction,

- Technical maintenance, and

- Data processing, evaluation and visualisation.

1.2.2 Nomenclature

The nomenclature in this thesis attempts to follow the definition of symbols and terms as presented in [2] and [3] as primary literature sources. It should also be noted that, since spatial angles are traditionally expressed in degrees in the wider literature, they will consistently be stated in degrees ($°$) in this work. However, numerical calculations and coordinate transformations conducted in Matlab™ code include a conversion to radians and vice versa.

1.3 Key Contributions

At this point, the author would like to acknowledge the substantial research and initial designs that have been provided by the early members of the Cooperative Research Centre for Satellite Systems at UTS under the leadership of A/Prof Sam Reisenfeld. Their dedicated efforts were the basis for the ultimate success of the project. The author himself claims several key contributions in the areas of original investigation, design and design improvements.

With respect to Chapter 4:

- Critical design review of the fast-tracking UTS Ka band earth station and identification of design weaknesses.

- Development of final-stage design improvements in the areas of vibration reduction, pointing accuracy enhancement and digital signal processing.

- Practical implementation and verification of the devised design improvements.

With respect to Chapter 5:

- Operation of the earth station and data collection over three years (2003-2005).

- Investigation of the suitability of satellite passes for Ka band experiments via FedSat under the time, elevation and operational constraints of the UTS Ka band earth station.

- Experimental investigation of the reliability of using two-line elements for accurate tracking of FedSat, in comparison with GPS coordinates and actual observations (proof of concept).

- Investigation of the earth station's pointing accuracy uncertainty and translation to possible power measurement errors.

- Experimental verification of a novel frequency tracking algorithm by Reisenfeld [14] in the working earth station.

With respect to Chapter 6:

- Software design and implementation for the processing and visualisation of the collected propagation data.

- Presentation of initial results of Ka band attenuation measurements collected from a low-power LEO microsatellite, which is non-existent in current literature.

- Interpretation of initial attenuation results and qualitative comparison with existing attenuation data from GEO satellites.

With respect to Chapter 7:

- Suggestions of further design improvements for future low-cost, fast-tracking Ka band earth stations.

1.4   Related Publications

The work conducted in this research project has resulted in two fully peer-reviewed papers [15], [16], and several other publications. Some aspects contained in the second paper exceed the work covered in this thesis.

1. T. Kostulski and S. Reisenfeld, "Ka band Propagation Experiments on the Australian Low-Earth Orbit Microsatellite 'FedSat' ", Proceedings of the 6th Australian Communication Theory Workshop, pp. 95-99, Brisbane, Qld, 2-4 Feb 2005

2. T. Kostulski and S. Reisenfeld, "Variable Slant-Path Ka-Band Propagation Measurements on the Australian LEO Microsatellite 'FedSat' ", Proceedings of the 11th Ka and Broadband Communications Conference, pp. 365-372, Rome, 25-28 September 2005

Part I

Background

Chapter 2

Review of Ka band Propagation Effects and Previous Experiments

2.1 Introduction

This chapter contains a brief review of the propagation impairments affecting Ka band satellite communications (Fig. 2.1). Over decades, radio science projects have aimed at the accurate quantification and modelling of these factors, and to advise on possible mitigation techniques. In preparation for the interpretation of attenuation measurements via the experimental Ka band satellite 'FedSat' in this project, the identification of the significant individual effects is reviewed in the first sections.

Subsequently, a summary of previous Ka band propagation experiments between 1969 and 2005 is provided, which have yielded a significant understanding of the challenges faced by satellite communications in this commercially emerging band. While the review of all experiments conducted and the conclusions drawn is well beyond the scope of this work, significant findings for later chapters will be identified.

2.2 Ionospheric Scintillation

Energy radiation from the sun affects the uppermost layer of the earth's atmosphere, the ionosphere, by increasing and decreasing the total number of electrons by several orders of magnitude [3]. This effect varies from day to night, and especially the transition causes rapid fluctuations (scintillations) of radio signals passing through the ionosphere. As shown in Fig. 2.2, some low-earth orbits lie within the upper reaches of the ionosphere. FedSat is located in the lower magnetosphere, which means that all signals have to pass through the ionosphere.
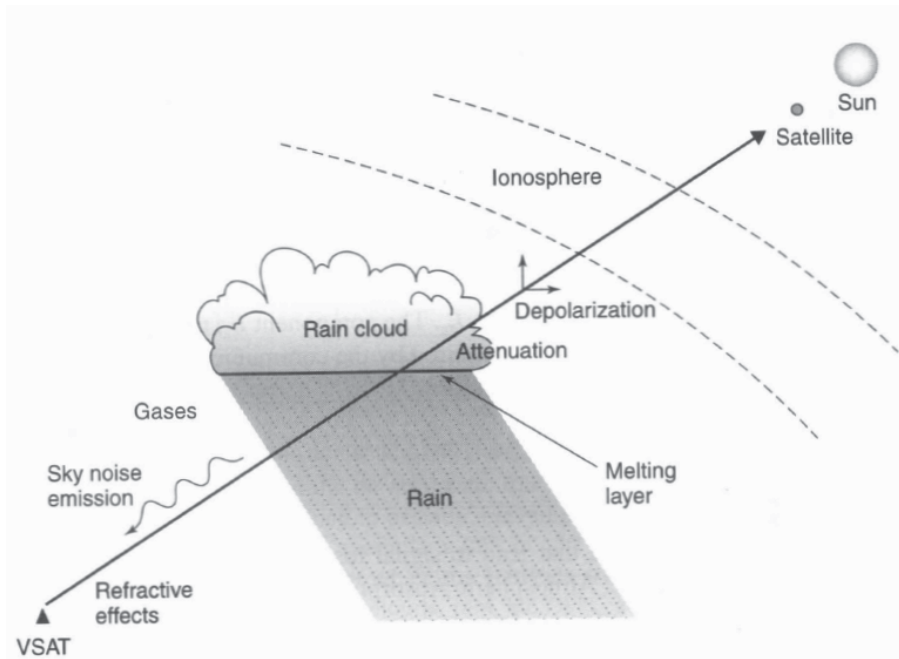
Figure 2.1: Illustration of the various contributors to path attenuation on satellite links
(not to scale) [3]

However, it has already been established in 1977 [18] through the extensive modelling
of geophysical processes that the significance of ionospheric scintillation is decreasing for
frequencies above 10 GHz [2]. Consequently, this effect is irrelevant on Ka band frequen-
cies.

For completeness, it should be mentioned that the magnetosphere (as indicated in
Fig. 2.2), in which FedSat's orbit lies, can be subject to very violent geomagnetic storms
caused by solar flares, which can lead to complete and permanent satellite loss. For
example, in 2003 a very large earth observation satellite, ADEOS-II, lost all communication
after a solar flare and had to be declared inoperative. Since ADEOS-II was launched
together with FedSat, they both occupied similar orbits. Surprisingly, FedSat was very
fortunate to survive without any damage [19].

2.3   Significant Tropospheric Effects

Conversely, effects in the earth's troposphere have much more adverse effects on microwave
propagation, resulting in attenuation and depolarisation. Although significant for satellite
systems operating with linear polarisation, the investigation of the latter effect is not
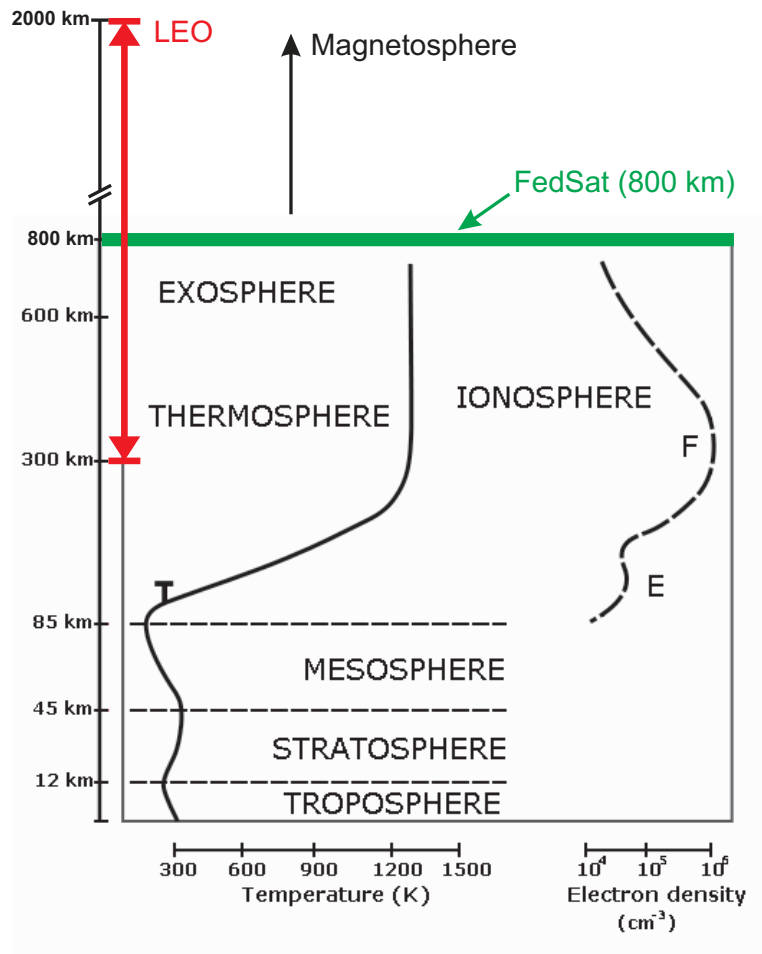
Figure 2.2: Location of the earth's ionosphere and magnetosphere in relation to a low-earth orbit (modified from [17]). The altitude ranges indicated are not precise limits, but transitional

the subject of this thesis. Attenuation effects of various kinds, such as absorption and tropospheric scintillation, are very significant in Ka band communications and deserve a review.

2.3.1 Atmospheric Absorption

Due to the interaction of radio waves with molecules in the earth's atmosphere, some of the energy is absorbed, causing signal attenuation. The actual absorption frequency depends on the structure of the molecule, with the most dominant contributors being oxygen and water vapour, as indicated in Fig. 2.3. It is customary to separate attenuation effects into dry atmosphere and standard atmosphere models, where a *dry* atmosphere includes all gases present in the earth's atmosphere (principally nitrogen, oxygen and carbon dioxide) at 15°C and at a nominal pressure of 1013 hPa, but *excludes* water vapour. A *standard* atmosphere additionally incorporates water vapour at a density of $\rho = 7.5 g/m^3$ [20].

The abscissa reveals that even around the Ka band absorption peak, the standard atmosphere *zenith* attenuation amounts to less than 0.2 dB/km. While this figure should be taken into account when calibrating the received signal strength, the (fairly predictable) order of magnitude of standard atmosphere attenuation is unlikely to have any impact on systems operating at higher elevation angles and with large link margins.

2.3.2 Cloud Attenuation

Clouds concentrate large amounts of water vapour and droplets of various sizes and have therefore the potential to contribute to attenuation at Ka band frequencies and higher. Due to the variable geometries of the droplets and the distribution, depending on the type of cloud, frequencies are affected to different extents [21]. Since clouds are rarely of a uniform nature, their precise attenuation can only be stochastically described. The climatic region of the earth station also needs to be considered [3]. In order to estimate certain bounds, extensive studies have been conducted, resulting in statistical data (Fig. 2.4). More recent models, such as in [22], are based on GEO satellite Ka band beacon experiments and radiometer data.

2.3.3 Tropospheric Scintillation

Contrary to ionospheric scintillation, tropospheric scintillation takes place in the lower atmosphere close to the earth's surface, the boundary layer. It is caused by convective turbulence in this layer, which rapidly changes the refractive index in different sections
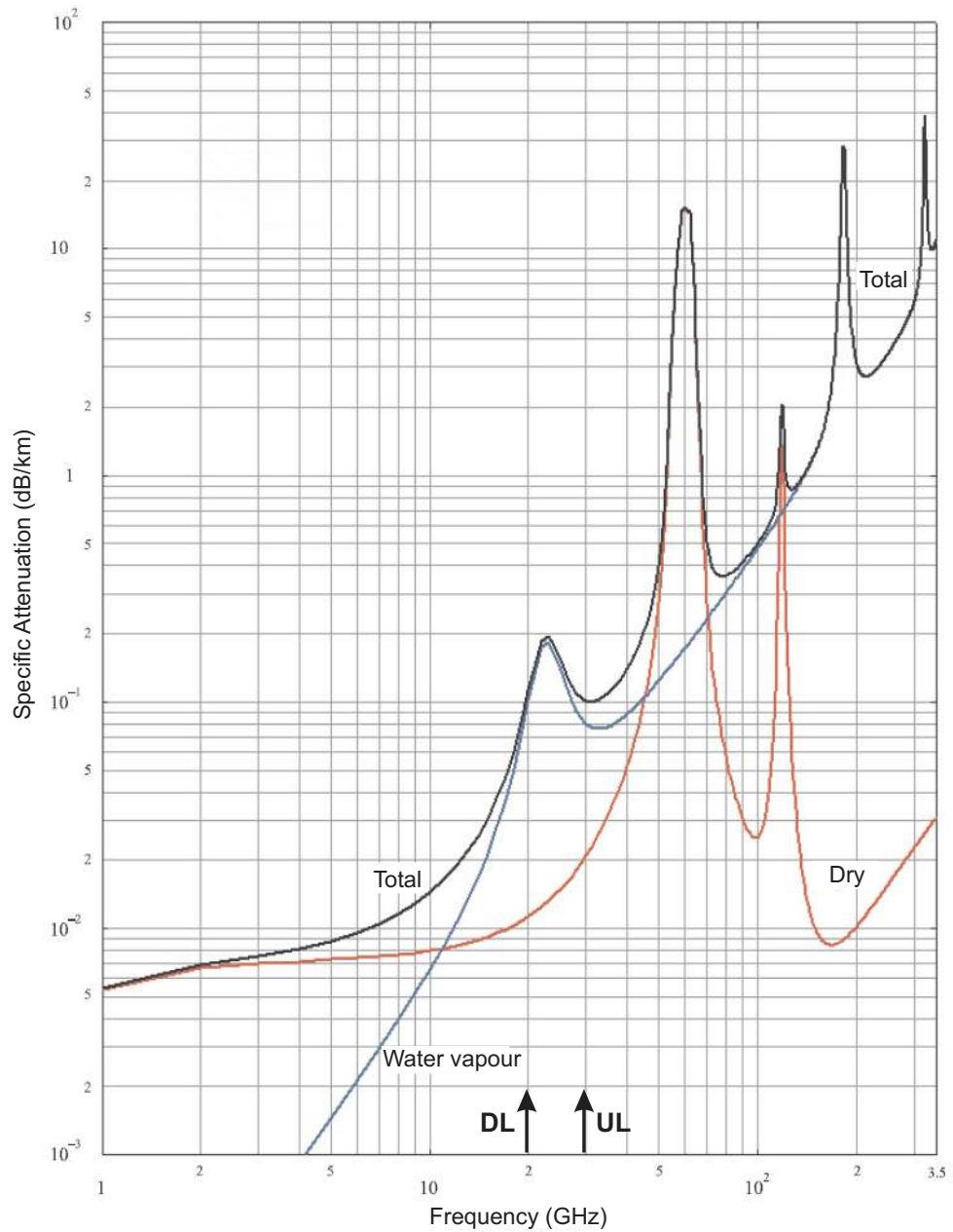
Figure 2.3: Specific attenuation for water vapour, dry atmosphere and standard atmosphere. The absorption regions can be clearly identified, especially in the Ka band (around 22.2 GHz) due to water vapour. The Ka band uplink (UL) and downlink (DL) frequencies are also indicated (modified from [20]).
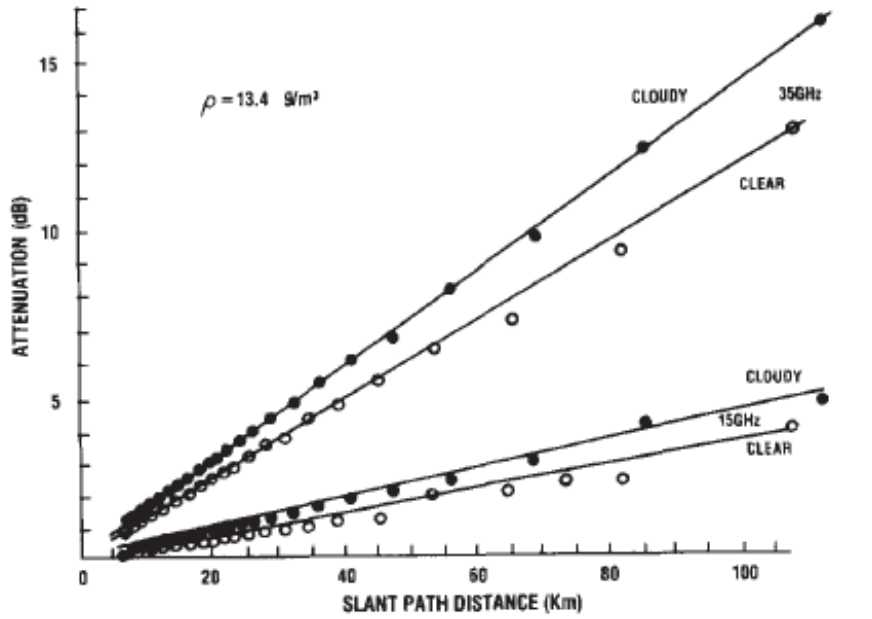
Figure 2.4: Cloud attenuation vs. slant path length for 15/35 GHz and clear sky and cloudy conditions [21]

and therefore causes disturbances in the propagation properties of this medium [3]. The extent of scintillation effects depends on the following factors:

- Frequency,

- Antenna aperture,

- Climate (temperature, humidity), and

- Slant path length.

Scintillations are highest under warm and humid conditions, and the effects also intensifies at lower elevations as the slant path length increases. As it can be seen in Fig. 2.5, the effect is very variable, and the magnitude cannot always be inferred from the visually observed weather conditions (clear sky, cloud, rain).

At elevation angles below approximately 10°, the effect of low-angle fading occurs, resulting in very severe signal fluctuations of 10 dB and more on Ka band. Low-angle fading is essentially a multipathing effect similar to reflection in terrestrial communication, but caused by refraction in the boundary layer. Due to the rapidly varying fluctuations with high magnitude, Ka band satellite communications at low elevation angles may be limited.
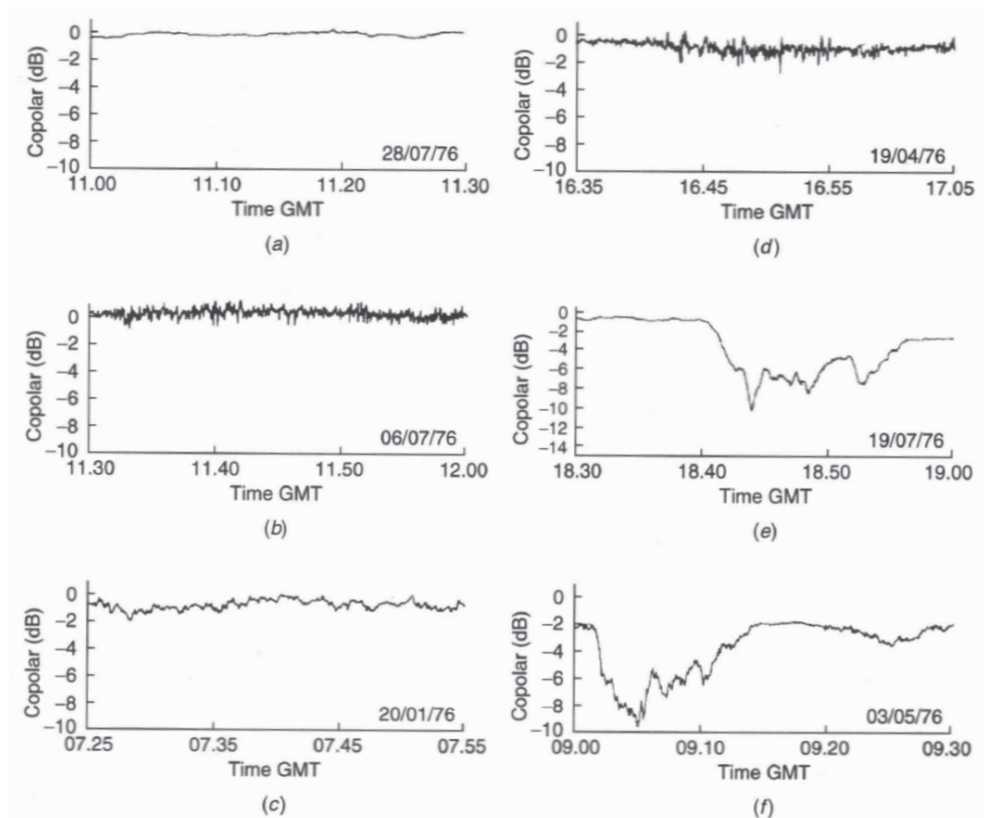
Figure 2.5: Scintillation observed on a 30 GHz beacon signal under clear sky conditions (a,b), cloud (c,d) and rain (e,f) [3]

In [23], Section 2.4, both tropospheric scintillation in general and low-angle fading in particular have been extensively modelled, resulting in comprehensive attenuation estimates for GEO satellites. The suggested adaptation for the LEO case in the mentioned work is kept relatively brief.

2.4 Rain and Ice Attenuation

At Ka band frequencies, attenuation due to hydrometeors (rain drops) is the most dominant impairment. Below 30 GHz, ice crystals are predominantly responsible for depolarisation effects only, however polarisation effects are not the subject of investigation in this thesis. Rain attenuation is starting to emerge as a significant factor at frequencies above 10 GHz and is the dominating factor in determining link availability on Ka band frequencies, hence predictions of the relation between the occurrence of rain and the resulting attenuation are needed.

2.4.1 Rain Attenuation

Depending on the climate, rain attenuation has the potential to introduce attenuation anywhere between 20 and 40 dB for short periods of time, often causing system outage. Similar to the difficulties with accurately describing the structure of clouds in the previous section, it is also very complex to gain precise knowledge of physical aspects of rain, such as raindrop size, raindrop distribution, raindrop temperature and rain intensity at any point along the satellite path [10]. Since the depth and duration of signal fades is directly related to the type of rain, for example originating from stratiform or from convective clouds, the accurate assessment of the related rain *rates* has been the foremost goal of many studies around the world. There have been several significant approaches to model the occurring attenuation of a physical level, for example by Crane [24], but empirical studies concentrating on the statistical description of the *probability of exceedance* have paved the way for more unified and practical approaches. Since a comprehensive review of all noteworthy models, such as the Crane-Global, Crane-Two Component, Dissanayake/Allnutt/Haidara (DAH) and the ITU-R models, is not possible nor within the experimental scope of this thesis, only some common, conceptual aspects of rain attenuation theory and the semi-empirical approach of modelling shall be discussed here.

2.4.2 Rain Climate and Contour Maps

Since representative, long-term averaged rain rate data is rarely available on a global scale, attempts have been made to group similar climatic conditions of locations into cli-

mate zones (15 in the ITU model [25] and further subdivisions in the Crane models). Each zone is then numerically characterised by the rainfall rate values that exceed certain percentage-of-time thresholds (for example 0.001%, 0.01%, 0.1%), therefore linking them to attenuation and to the likelihood of outage. Although the boundaries are arbitrary and errors of $\pm 10\%$ are possible [3], these maps provided a first unified approach. It is important to note that unlike meteorological maps, the rain climatic zones only characterise rain *rates*, but do not provide any information about rain accumulation. An example of a combined ITU and Crane model maps for rain climatic zones is shown in Section 2.5.3.

More recently, ITU rain climatic maps have been replaced by the direct use of "Rainfall rate exceedance contour maps" [26], resulting in more accurate coefficients for the model. These worldwide and regional maps contain averaged contour lines of rainfall rates for the exceedance of certain percentages, most commonly 0.01%. This allows the direct extraction of the rainfall rates required for the ITU model, which is described in the following section.

As more accurate data becomes available form meteorological services, especially with respect to observations intervals (1 minute vs. formerly 6 minutes), the contour maps are frequently re-drawn. An example of the changes between the most recent ITU recommendation [26] (2007) and the previous version [27] (2003) for the Australian region is illustrated in Fig. 2.6. Significant changes have been made in the Australian region, and the steep gradient in the vicinity of Sydney is an indication for a rapid change of rain characteristics within a small geographic area. This topic will be further explored in Section 4.7.2.2. According to the latest map version, a good estimate for Sydney would be $R_{0.01} = 48 \ mm/h$. However, the use of reliable, long-term averaged, local rainfall rate data, where available, is still preferred over the use of the contour maps.

It must be mentioned that, due to the severity of rain events, Ka band propagation study is still very much an ongoing research topic especially in tropical climates. Current studies, for example, include the work by NTU in Singapore [28] and by NASA in Puerto Rico [29].

2.4.3 Rain Attenuation Modelling

In this section, the propagation model proposed by the International Telecommunications Union (ITU) for GEO satellites is considered. In order to statistically model the effect of rain, several terms need to be explained first. The lower altitude limit of clouds is often very clearly defined and can even be visually observed on stratiform cloud types.
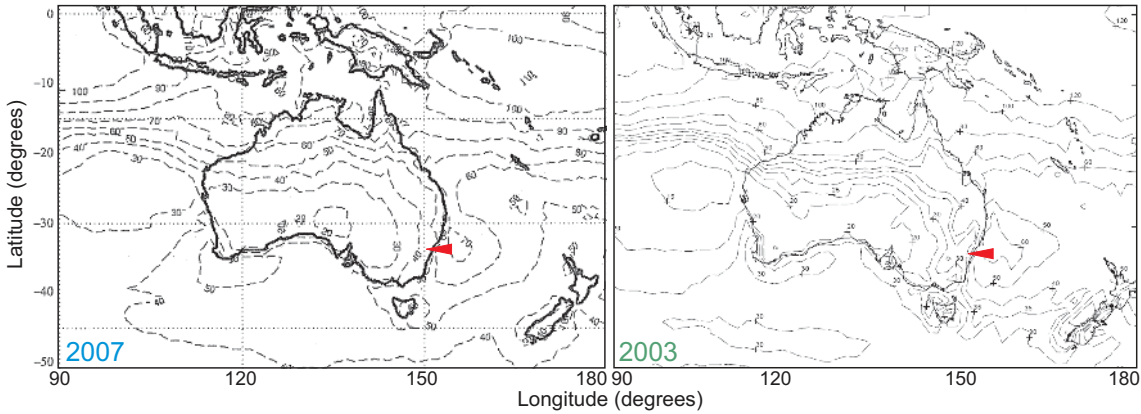
Figure 2.6: Australian rainfall rate contour map for 0.01% exceedance (in mm/h) for the average year, issued in 2007 and 2003 (modified from [27] and [26]). Significant corrections have been made for the Sydney region (red marker).

This 'melting layer' separates ice particles, mostly present in the higher parts of the cloud and in the upper troposphere, and the raindrops below. Except for tropical regions, it is considered identical to the 0° isotherm [30]. The height of the melting layer above sea level, H_E, is defined as the rain height, and as a model, rain attenuation is deemed to occur from the ground up to this altitude. The path length L describes that particular part of the slant path at a fixed elevation El between the satellite and earth station at height H_0 that lies below the melting layer and is therefore affected by rain attenuation. Fig. 2.7, adapted from [3], illustrates these definitions.
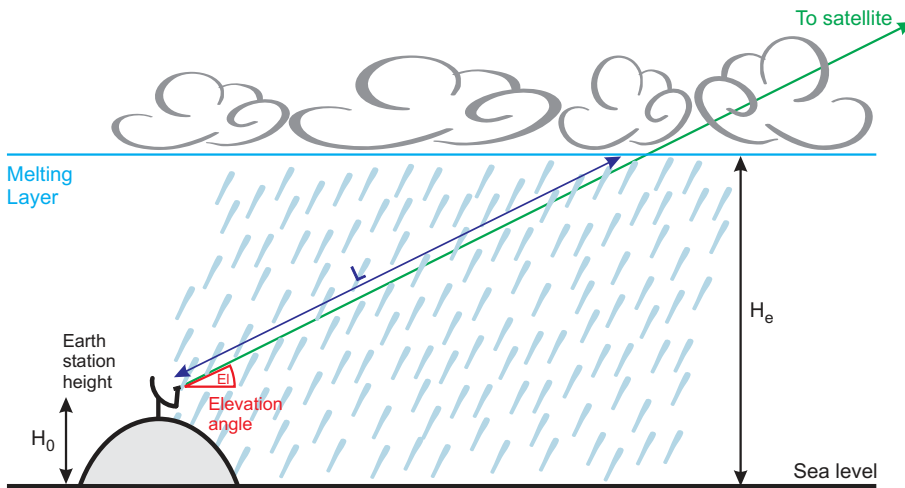
Figure 2.7: Illustration of the geometry for a satellite signal passing through rain

Theoretically, the path attenuation A can now be calculated by

$$A = \gamma_R \, L \tag{2.1}$$

with

$$\gamma_R = k \, (R_{0.01})^\alpha \, \text{dB/km} \tag{2.2}$$

where γ_R is the specific attenuation coefficient, $R_{0.01}$ is the rainfall rate measured for 0.01% of the average year at that location, and k and α are frequency and polarisation dependent coefficients from a table published in [31]. The problem is that the rainfall rate along the path L is rarely uniform, hence γ_R will vary over the path length L. In order to account for this fact, an *effective* path length L_{eff} is introduced, which takes the statistical height of the melting layer H_E, the height of the earth station H_0 and the elevation angle El into account. There is little value in reproducing the well-established and widely known derivations of L_{eff} and A from [32], [26] and [31] in this context, and the interested reader is referred to [3] for a comprehensive example. However, it should be mentioned that [23] does propose an adaptation of the GEO calculations for non-GEO orbits.

Within the scope of this thesis, availability and long-term attenuation models derived from this procedure are of interest for comparison purposes only, since signal observations are of 10-15 minutes duration only; hence the *prevailing*, rather than long-term, weather conditions dominate the propagation. For reasons stated in Section 4.5.2, the observation of depolarisation effects by ice particles and other propagation phenomena are not part of this study.

2.5 Ka band Propagation Experiments on Geostationary Satellites

The above mentioned models have largely been developed on the basis of empirical data. A number of geostationary research satellites with Ka band beacons, bent pipe mode transponders and even onboard processing capabilities have been launched between 1974 and 1993. [33] provides a very good overview of previous Ka band propagation studies on GEO satellites as a basis for Table 2.1. Subsequently, an increasing number of commercial Ka band satellites were launched, some of which also carry experimental Ka band beacons (for example ANIK-F2, Optus B), which are no longer listed here.

System	Country	Launch Date	Frequency (GHz)
NASA ATS-5	USA	1969	15.4
NASA ATS-6	USA	1974	20/30
CTS	Canada/USA	1976	11.7
COMSTAR Series	USA	1976-1981	19/28
SIRIO	Europe	1977	20/30
ETS I-VIII	Japan	1975-2006	20/30/40
OLYMPUS	Europe	1989	12.5/20/30
ITALSAT	Italy	1991	20/40/50
ACTS	USA	1993	20/27.5
COMETS	Japan	1998	21/31, 44/47
WINDS	Japan	2008	18.9

Table 2.1: History of space-to-earth propagation studies on GEO satellites

In the following sections, a brief overview of the research objectives and experiments conducted over the most successful platforms will be provided, limited to relevance to the scope of this thesis.

2.5.1 Olympus

The European Space Agency's OLYMPUS F1 project aimed at at 5 year mission and was launched in 1989. The 2,600 kg satellite was positioned in a GEO at 19° W with coverage of Europe and the eastern parts of North America. In addition to its Ku and Ka band communication transponders, it also carried three beacons at 12, 20 and 30 GHz for propagation research. The beacons were linearly polarised, and the 20 GHz beacon could be switched at 1 kHz for differential measurements. The great advantage of OLYMPUS was that all three beacons could be observed at the same time in the same orbital slot, hence it was possible to correlate the influence of propagation impairments on each band. Many universities and organisations in Europe, Canada and the US participated in the study, and apart from a multitude of locations in Europe, especially at Surrey, UK, and Darmstadt, Germany, important low-angle observations (14°) were contributed from Blacksburg, VA, and Ottawa, Canada. This has resulted the collection of cumulative attenuation statistics in numerous, significant publications in this field, for example [34]. In the US, propagation experiments with OLYMPUS were widely seen as an ideal preparation for the upcoming ACTS experiments. First cumulative attenuation statistics from the OLYMPUS beacons are shown in Fig. 2.8.
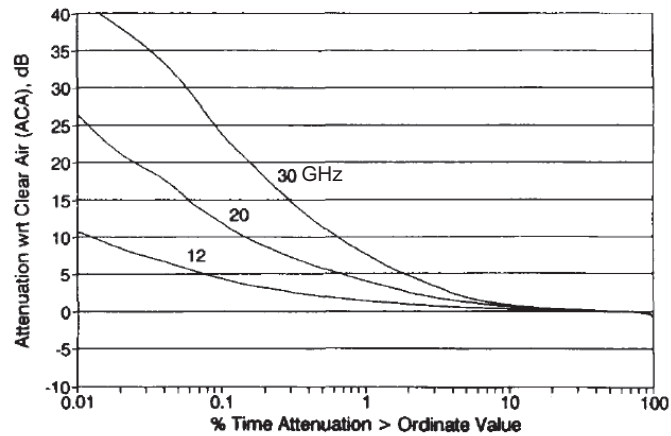
Figure 2.8: Cumulative attenuation results from OLYMPUS for Ku and Ka band, 1991-92 [34]

2.5.2 ITALSAT

Placed at 13.2° E and launched in 1991, ITALSAT-1 (1,850 kg) was a predominantly commercial satellite that also carried propagation experiments on the Ka, Q and even V bands, which is particularly noteworthy with respect to propagation research. Unlike OLYMPUS, unfortunately its beacon coverage area was focussed on Italy and central Europe only (Fig. 2.9), therefore limiting access to European research groups. Experiments contributed significantly to the further understanding of Ka band propagation, especially in urban and suburban environments [35].
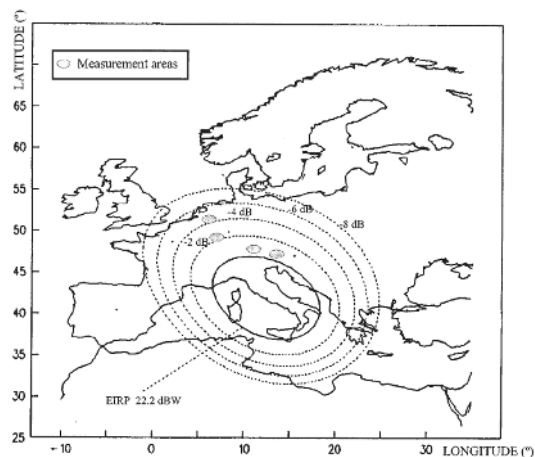
Figure 2.9: Coverage area of the ITALSAT 18.7 GHz beacon [35]

2.5.3   ACTS

The "Advanced Communication Technologies Satellite" (ACTS) must be regarded as one of the most ambitious projects dedicated to demonstration and research purposes of its time. Launched in 1993, weighing 2,240 kg and stationed at 100° W, it was the first all-digital, high-speed regenerative communication satellite with Gigabit capacity, and it was equipped with multiple, high-gain hopping-beam antennas for Ka band use. It operated virtually flawlessly until mid-2000 [36].

The Ka band beacon coverage allowed the reception in a wide variety of latitudes and therefore climatic regions [37], and the elevation angles of the seven designated experiment site locations, predominantly universities, ranged from 8.1° in Fairbanks, AK, to 52° in Tampa, FL. A map of the receiver sites, also indicating the previously discussed ITU/Crane rain climate zones, is shown in Fig.2.10 [38]. Comparative, cumulative measurement results for the 20 GHz beacon are presented in Fig. 2.11.
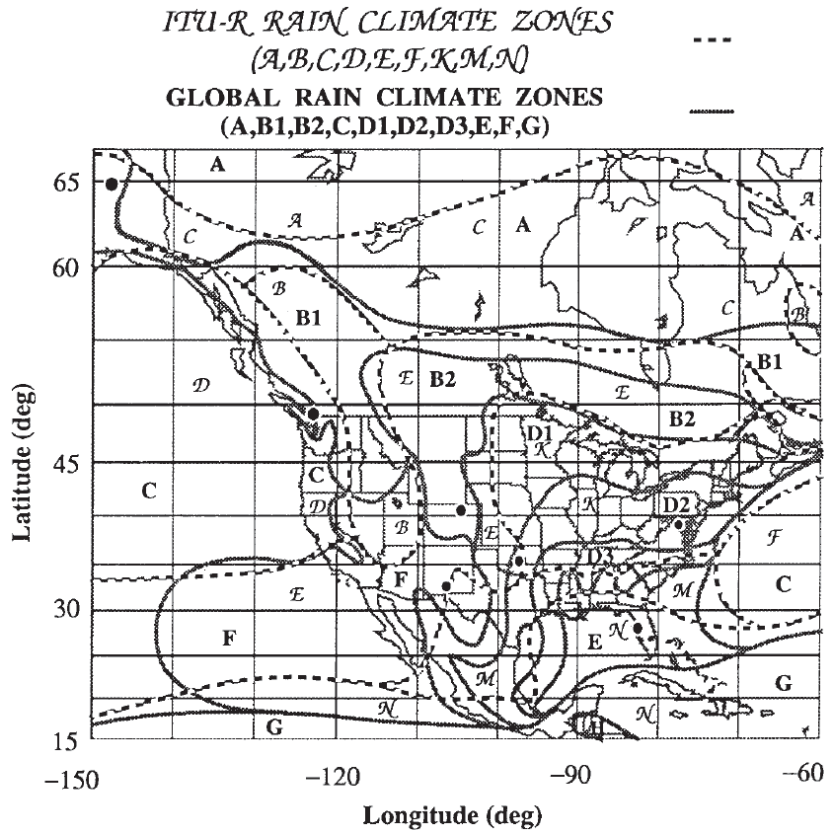
Figure 2.10: ACTS experimental beacon observation sites with Crane and ITU rain climate zones [38]
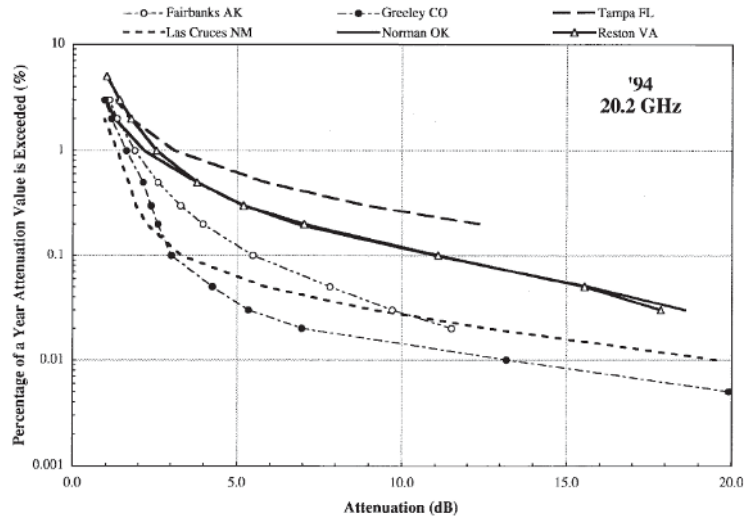
Figure 2.11: Cumulative 20 GHz propagation results collected from six of the ACTS observation sites [39]

The objectives of the ACTS propagation experiment are comprehensively explained in [40], which also provides a short review of the NASA involvement in the OLYMPUS campaign and the knowledge that has been gained for the ACTS mission. The extent of topics covered by publications originating from the ACTS beacon experiments alone (attenuation, polarisation, scintillation, systems design) is too extensive to cover in all aspects within this scope. Major contributing authors to propagation research via ACTS include (but is not limited to) Crane, Ippolito, Rogers, Dissanayake, Davarian, Chakraborty, Bauer, Helmken and Henning. From the specialist field of propagation research, several interesting publications in the field of systems design have also emerged from the ACTS experiments, for example [39] and [41].

2.6 Ka band Propagation Experiments on Low-Earth Orbit Satellites

Despite the advantages of operating Ka band transponders on LEO satellites outlined in the introductory chapter, the investment in commercial systems has resulted in the discontinuation of a planned constellation after a prototype test in one case, and a considerable financial loss in another. However, it is not the purpose of this work to examine the technical and/or business-related causes for these outcomes, and the following review shall simply demonstrate the need for further research in the area of LEO satellites carrying Ka band payloads.

2.6.1 Teledesic T1

The T1 satellite was the demonstration satellite of a large-scale LEO project by the company Teledesic in order to provide global, real-time voice and high-speed internet services via satellite, with Ka band links directly to customer terminals [42]. The initial constellation consisted of 840 active satellites in 700 km inclined orbits, which was later revised to only 288 satellites in 1350 km orbits, as illustrated in Fig. **2.12**. Extensive, laser-based inter-satellite Gigabit links were also planned [43]. Launched in 1998 into a polar orbit of only 565 km, the goal of this single demonstration satellite was to evaluate the system performance in the 28.6-29.1 GHz range for the planned services, including propagation measurements. It is interesting to note that the initial design included an elevation mask of 40° to account for the expected rain fade on Ka band, and clearly one of the goals of T1 was to evaluate the link margin figure through propagation experiments. In 2003, Teledesic announced that the constellation would not be realised, and all gathered Ka band LEO propagation data remained commercial-in-confidence.
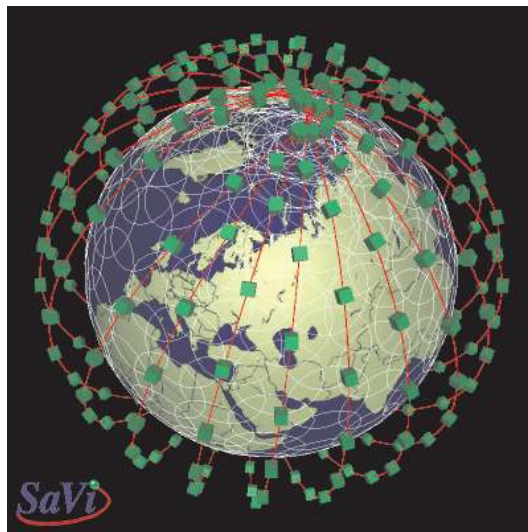
Figure 2.12: Visualisation of the revised Teledesic Ka band LEO constellation with 288 satellites [44]

2.6.2 Iridium

Similar to Teledesic, the Iridium system has aimed at providing global high-speed, real-time voice and data services through a LEO constellation, using L band frequencies and spot-beams for direct links to subscriber handsets. The original constellation included 77 satellites in 86.4° inclined orbits, which was later revised to 66 satellites. In 1997/98 (initial

constellation) and again in 2002 (replacements), over 90 satellites were launched, weighing in at almost 700 kg each. Besides using 23 GHz for satellite interlinks, the pioneering Iridium network employs Ka band frequencies for their three gateways (30/20 GHz), therefore requiring propagation measurements and models adapted for low-earth orbits for successful operation. Again, information about the link design and the underlying assessment of propagation effects on Ka band have been kept commercial-in-confidence.

For completeness, it should be mentioned that the Iridium system, despite its remarkable, technical achievements and the exorbitant cost of over US$5 billion, had initially been a business failure and was scheduled for de-orbiting in 1999 [45]. It saw a resurrection in 2001 when the US Department of Defense and an international investor consortium took over under a new business plan. The system is currently actively used and maintained.

2.6.3 ROCSAT-1

The LEO series ROCSAT (also known as FORMOSAT) is operated by the National Space Organization (NSPO) of the Republic of Chinsa (Taiwan) and started in 1999 with the launch of ROCSAT-1. Its main goals were space science, Ka band communication (TV broadcast, data, frequency-hopping) and especially imaging experiments, hence its 600 km, 35° inclination orbit, which provides coverage only for low to medium latitudes [46]. At a lifetime of 4 years and although weighing over 400 kg (and therefore almost 7 times as much as FedSat, see Chapter 3), it is probably the closest comparison, because of the inclusion of a 19.5 GHz beacon aimed at extensive propagation measurements from a fixed and a transportable, receive-only ground station (Fig. 2.13). However, the link margin for measurements and the technical facilities at the ground station differ greatly from the challenges faced by the FedSat project.

Figure 2.13: Photos of the remote and the transportable terminals for ROCSAT [47]

2. REVIEW OF KA BAND PROPAGATION EFFECTS AND PREVIOUS EXPERIMENTS

It is apparent that the tracking ground terminals employed for ROCSAT are full commercial units and must have come at a great cost, similar to the power and capabilities of the spacecraft itself. The Ka band propagation experiment itself, conducted by the Institute of Space Science at the National Central University (NCU) in Chung-Li, Taiwan, is also very well supported by ancillary instruments and facilities. A VHF weather radar is located very close to the earth station site, and extensive weather monitoring equipment (radiometer, optical rain gauge, disdrometer) are installed [46]. There have been very thorough preparations for the correlation of weather events and the sky noise in this tropical climate with the ROCSAT-1 beacon measurements, predominantly published by Chu, Shih and Liu in the local "Terrestrial, Atmospheric and Oceanic Sciences" journal, for example [48], and only to a limited degree international publications, [49] for instance.

[50] provides proof that a large number of passes have been successfully conducted and the beacon signal received, with low-resolution, raw graphs provided. Given the enormous cost and technical capabilities of this project, both in space and on the ground, therefore it seems quite surprising that the results of this research have not been made available to a wider audience. Most of the publications about the ROCSAT Ka band propagation measurements are pre-launch (1998 and earlier), or were collected during the first few months of operation. The only significant post-launch publication, presenting a very basic analysis of measurements, is [12]. A Masters Thesis [51] has also been submitted in relation to the campaign (in Chinese language), which is included in the bibliography as a potential source of further information. It is very regrettable that the publicly available data from this project is extremely limited, and the author has made, unfortunately unsuccessful, attempts to contact the main NCU researchers involved in the campaign. Subsequent ROCSAT missions did not carry any further Ka band payloads.

Summary: It has been shown that both commercial and research spacecraft carrying Ka band payloads have successfully operated, or are still operating, in a low-earth orbit with the potential to contribute to Ka band propagation research. However, the data is either kept commercial-in-confidence or remains largely unreleased for unknown reasons. The 'FedSat' mission presented in this thesis can therefore be regarded as a rare source of *experimental* LEO Ka band propagation research, which has already been acknowledged by international researchers [52] [53].

2.7 Rain Attenuation Measurements in the Australian Region

Historically, Australia has always had a great interest in recording accurate rainfall data due to the large variations in its climatic regions. Extensive studies in the late 1970's and early 1980's have resulted in several reports by Flavin [54] [55], characterising significant sites in Australia through ITU-compliant rainfall rate statistics and by making specific recommendations for the Australian region for the Ku and Ka bands, predominantly for GEO satellites. An example of the early measurements, in the average-worst-month (AWM) notation, is shown in Fig. 2.14, which has resulted in early rainfall rate contour maps for Australia [55].

In 2001, Flavin recommended certain amendments for the Australian models to the ITU for the inclusion in the official recommendation (ITU-R P.841-2), including algorithms for conversion of statistics and a significant simplification of a modification factor, relying on rain*fall*, not rainfall *rate*, statistics only [56]. For comparison with the historic chart above, a recent chart is shown in Fig. 2.15. An immediate observation is that the likelihood of higher rainfall rates is now estimated higher than in 1980 due to the inclusion of more recent data.

The Australian Bureau of Meteorology is the original source of rainfall rate statistics, which have been collected in 6-minute intervals so far and are currently converted 1-minute intervals [57]. The data provided can easily be interpolated and converted to the form required in the ITU model. With the availability of precise, location-based rainfall rate data, the use of contour maps for $R_{0.01}$ for the Sydney region is not required. For comparison purposes, [56] quotes 50 mm/h for $R_{0.01}$, compared to the estimated 48 mm/h from the contour map in Section 2.4.2.

There has also been a notable propagation study in the tropical regions of Australia near Townsville (Queensland), conducted by Kikkert from James Cook University [58]. While the main focus has been on the development of digital beacon receivers for L, C, Ku and Ka band, the team has also been involved in the 'Satellite Transmission Rain Attenuation Project' (STRAP) since 1983 to aid in the collection of rain attenuation data in tropical regions [59]. There is also a strong cooperation with the Nanyang Technological University (NTU) in Singapore, who is operating a STRAP beacon receiver at the Bukit Timah earth station, and the CRC in Ottawa. Current activities include the development of a dedicated Ka band beacon receiver [60].
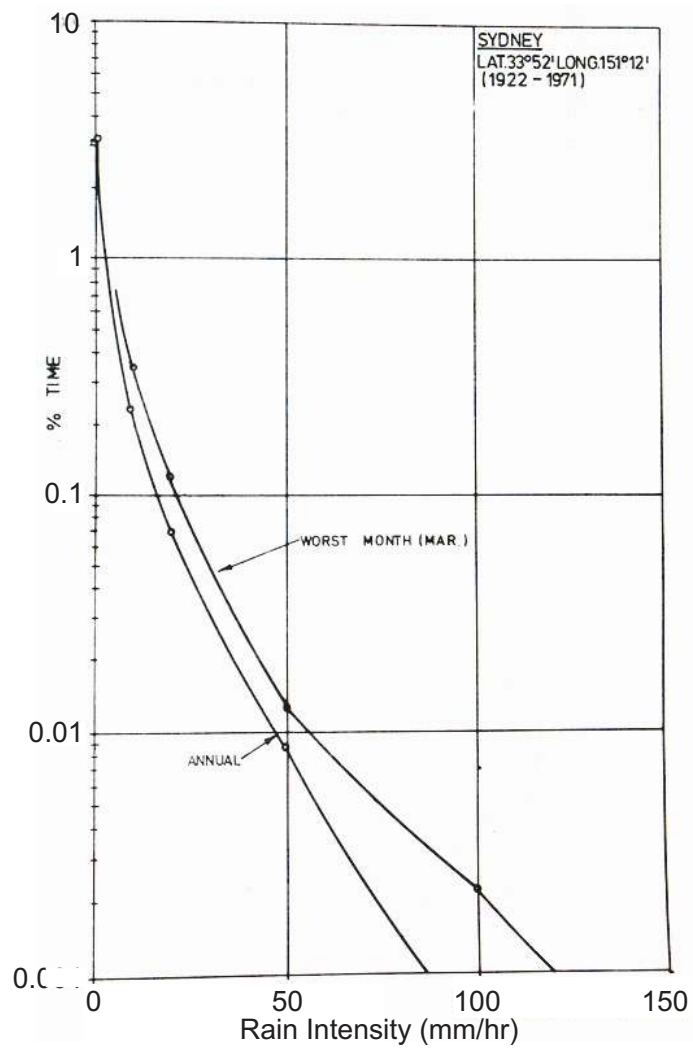
Figure 2.14: Cumulative distribution functions of the average rainfall rates (6 minute intervals) recorded in Sydney 1922-1971 (49 years) [54]
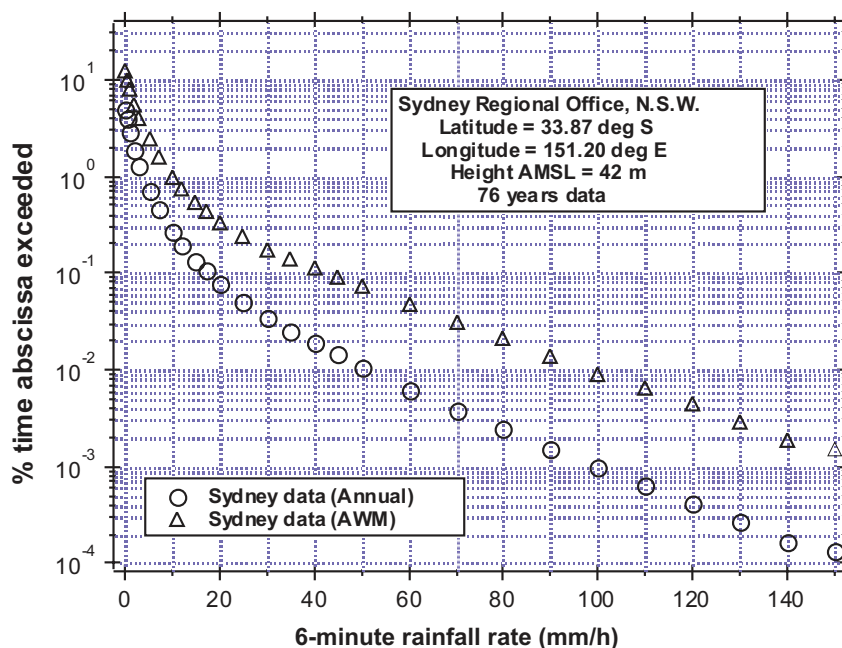
Figure 2.15: Cumulative distribution functions of the average rainfall rates (6 minute intervals) recorded in Sydney 1922-1998 (76 years) [56]

This literature review chapter has demonstrated that Ka band propagation research is a very active topic, and that amendments to the developed models are frequently made. While models for GEO systems appear to be fairly well established, there has been little to no usable experimental data available for the verification of theoretical models [52] for low-earth orbit satellites, which enter the commercial sector. Although of great interest, it should be noted that the military sector has been excluded from this review due to the classification of most technical information and propagation data.

Chapter 3

The Australian 'FedSat' Mission

Australia has previously been involved in the development of satellite technology, first through the co-construction and the launch of WRESAT (Weapons Research Establishment Satellite) from Woomera, South Australia, in 1967 [1]. Following the USSR, USA and France, Australia was the fourth nation to achieve a successful satellite launch from its own territory. The 45 kg spacecraft was operational for only 5 days and re-entered after 42 days. 1970 saw the successful launch of the 15.8 kg Australian amateur radio satellite "OSCAR-5" from Vandenburg Air Force Base (USA), carrying HF and VHF transponders. It remained partially operational for no longer than 46 days [61].

It was not before 1996 that the Government decided to revive Australian spacecraft design and construction capabilities by funding a demonstration program in the form of the "Cooperative Research Centre for Satellite Systems" (CRCSS). The main goal was to develop expert skills in satellite and payload design and manufacture, to verify intellectual property developed in Australia, and to provide a space research platform for Australian universities and organisations [19]. The satellite was named "Federation Satellite", or FedSat, after the Australian centenary of federation in the year 2001, for which the launch was initially planned.

Unlike WRESAT, FedSat was to be launched from the Japanese Space Centre in Tanegashima by an H-IIA rocket, together with three Japanese satellites. This made FedSat the first foreign spacecraft to be launched from Japan, and the launch itself and all associated expenses were donated by the Japanese Government to the people of Australia in celebration the centenary of federation. In exchange, the CRCSS provides selected data gathered by the satellite to Japanese researchers.

This chapter first introduces the CRCSS as an organisational framework under which the research for this dissertation was conducted. A brief history of key events is also

provided. Since FedSat's orbital dynamics were of great importance for the Ka band propagation experiment, the launch parameters and resulting orbital properties are illustrated and analysed in the next section.

Subsequently, FedSat is introduced as a complex research platform from a technical point of view. Since it is important to understand how the Ka band propagation experiment ties in with the other payloads and the housekeeping, all subsystems are briefly discussed [62]. Since the communication payload is most significant for the propagation experiment, it is explained in much greater detail. In conjunction with the orbital properties, operational considerations and restrictions and their impact on the propagation experiment are finally reviewed.

3.1 The "Cooperative Research Centre for Satellite Systems"

The Australian Government supports scientific and engineering innovation through a series of "Cooperative Research Centres" (CRCs) with the aim to develop new products, services and technologies for Australia's future. It focuses heavily on the collaboration between universities, the industry and Government organisations to generate intellectual property and educate highly-skilled professionals [63]. Funding from the Government is limited to a certain period (normally 7 years) and needs to be matched by cash and in-kind contributions by the participating members.

With the high-profile aim of a successful satellite launch and operation in the year of Australian federation, the FedSat bid won the Government's support and officially commenced on 1 January 1998 as a joint venture between all participants (Table 3.1). In 2004, after a further 1-year extension beyond the usual CRC duration, the Australian Government decided to discontinue funding for the CRCSS, which essentially forced the centre into formal closure at the end of 2005 while active research was still ongoing.

3.1.1 Organisational Structure of the CRCSS

Fig. 3.1 illustrates the internal Organisation of the CRCSS. All core participants from Table 3.1) are represented on the board, which sets the financial and operational boundaries for the executive. The executive supervises progress in the R&D programs and ancillary divisions. The Ka band earth station development and the Ka band propagation experiment are both part of the communications program, which is led by the University of South Australia.

Core Participants
University of South Australia University of Technology, Sydney Queensland University of Technology University of Newcastle CSIRO Vipac Engineers & Scientists Ltd Auspace Ltd
Supporting Participants
Defence Science and Technology Organisation Dspace Ltd Codan Ltd La Trobe University Curtin University of Technology

Table 3.1: CRCSS Participants (as of 2003)
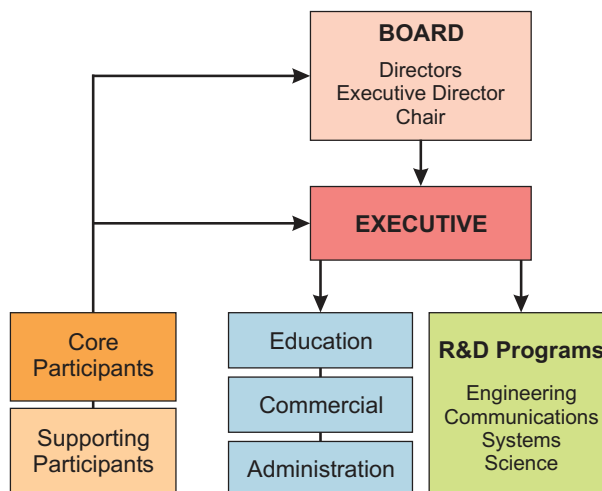
Figure 3.1: Organisational structure of the CRCSS

Within this administrative and technical framework, funding has frequently been re-allocated to adapt to changing conditions on this low-cost space mission. These board decisions have often propagated down to the individual experiments, where loss of funding has caused limitations in staffing and equipment. Under those circumstances, some original experimental objectives had to be re-defined over the course of the experiment.

3.1.2   Key Events of the FedSat Project

After the formal establishment of the CRCSS, the planning phase began for each of the individual programs listed in 3.1.1. Since a satellite manufacturing industry did not exist in Australia, the assembly of the structure and the payloads was contracted out to the UK company Space Innovations Ltd (SIL). A suitable and proven microsatellite platform was selected, which needed to support all housekeeping functions and multiple experimental payloads. Besides, it had to meet the launch requirements set by the Japanese Aerospace Exploration Agency, JAXA (formerly NASDA).

After the original participant SIL had ceased operating, the largely unfinished satellite was brought to Australia. Auspace Ltd. in Canberra integrated all payloads, completed the software and prepared the spacecraft for launch. The resulting funding and time limitations dictated that - unlike for larger satellite missions - only one satellite was built, which was the actual flight model. Despite the relatively low total cost of an estimated US$ 11 million [64], FedSat is believed to be "...one of the most complex spacecraft of its size ever built" [65]. The design aimed at a 3-year mission.

Prior to launch, the model underwent extensive vibration, vacuum and thermal testing. Unfortunately, this caused damage to one of the space-hardened FPGAs, which had to be replaced by a standard type in order to avoid further delays. Some payload software updates were also postponed until after launch as in-orbit maintenance.

The launch also experienced several delays due to continuing issues with the launch vehicle. Eventually, the H-IIA F4 mission lifted off successfully from Tanegashima on 14 December 2002 at 01:31 UTC. After separation from the launcher according to plan and several stabilisation orbits, FedSat made contact with the telemetry, tracking and control (TT&C) earth station in Adelaide shortly after. The operation of payloads commenced in January 2003 and continued as planned in most cases, so that FedSat achieved all of its milestones during the mission period [19]. After the CRCSS closure, the Australian Department of Defence officially took ownership of FedSat on 1 January 2006 and conducted several of their own experiments, but allowed most other ongoing research activity to continue as before [66].

FedSat first developed minor power supply problems in April 2007 before being declared permanently inoperative in September 2007. Still, after 4 years and three months of service and nearly 20,000 orbits, it has exceeded its lifetime expectation by no less than 40%. FedSat is Australia's most successful space project to date.

3.2 Orbital Dynamics of FedSat

FedSat's orbital parameters are principal attributes for the on-board and especially for the communication experiments, since they dictate the local pass time, pass duration and the spatial pointing coordinates for the earth stations. This section provides a brief overview of the specific features of FedSat's orbit, including the implications for the Ka band propagation experiment.

3.2.1 Launch

After several postponements of the launch date, the launch of the H-IIA F4 mission finally transferred four satellites into a low-earth orbit: the 3,680 kg Advanced Earth Observation Satellite ADEOS-II (US$ 570 million) as the primary payload, Micro-Labsat, a technology demonstration satellite, WEOS, a whale ecology observation and tracking satellite and FedSat. All three 'piggyback' microsatellites are of similar weight and size, with FedSat being the most complex of them and the longest design lifetime. A photo of the three microsatellites mounted on the separation structure can be seen in Fig. 3.2.

The launch from Tanegashima took place under perfect conditions, and FedSat was the first of the microsatellites to be separated in an altitude of approximately 800 km (Fig. 3.3). A camera onboard the launch vehicle recorded the manoeuvre and verified that FedSat moved away from the payload compartment with only a gentle tumble, since any faster spins may have been been very difficult to correct (see Section 3.6.2).

3.2.2 Orbital Properties

Since FedSat carries no propulsion system, its orbit is completely determined by the time and the parameters of the launch, i.e. location and velocity at tip-off. The very slow and minor variation of these figures has no significant effect on the experiments of interest. An example of mid-mission parameters is given in Table 3.2; a good explanation of the terms is given in [2].

These parameters can be visualised by special satellite tracking software, which is either commercially or freely available. Out of many on offer, the UTS CRCSS research group selected the program package "Nova" [67] for reasons that will be further discussed
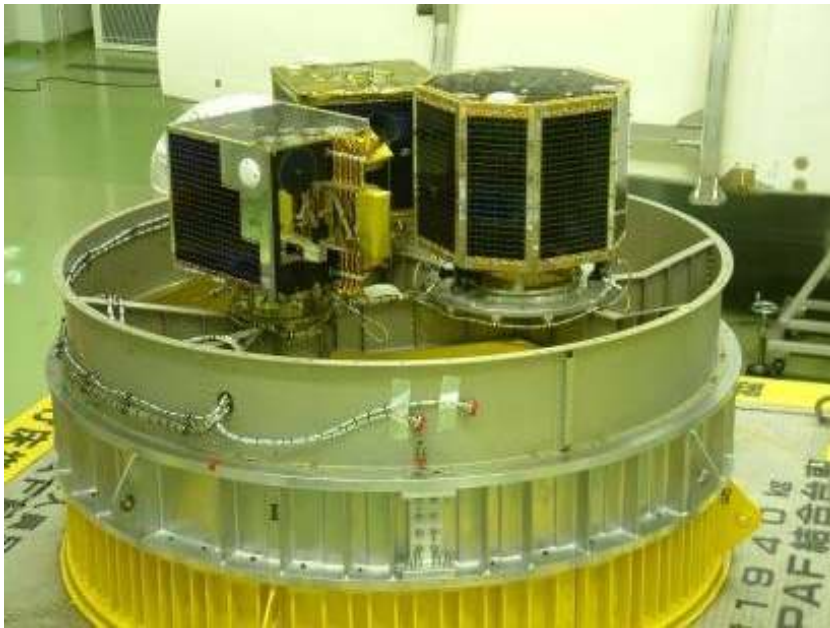
Figure 3.2: FedSat, WEOS and Micro-Labsat mounted on the launcher's payload separation structure (Photo: JAXA)

Figure 3.3: FedSat several seconds after separation, as recorded by the onboard camera (Photo: JAXA)

Inclination	98.61°
Eccentricity	0.00084480
Apogee Height	804.54 km
Perigee Height	792.85 km
Revolutions per Day	14.278
Orbital Period	100 min 51 sec
Orbital Velocity	7.45 km/s

Table 3.2: Selected mid-mission orbital parameters of FedSat (7 Jun 2004)

in Section 5.2. Fig. 3.4 illustrates the low, circular, near-polar characteristic of the orbit (white) very well. As the earth rotates, the angle between the orbital plane and the sun is fixed, which implies that the spacecraft's orbit is sun-synchronous.
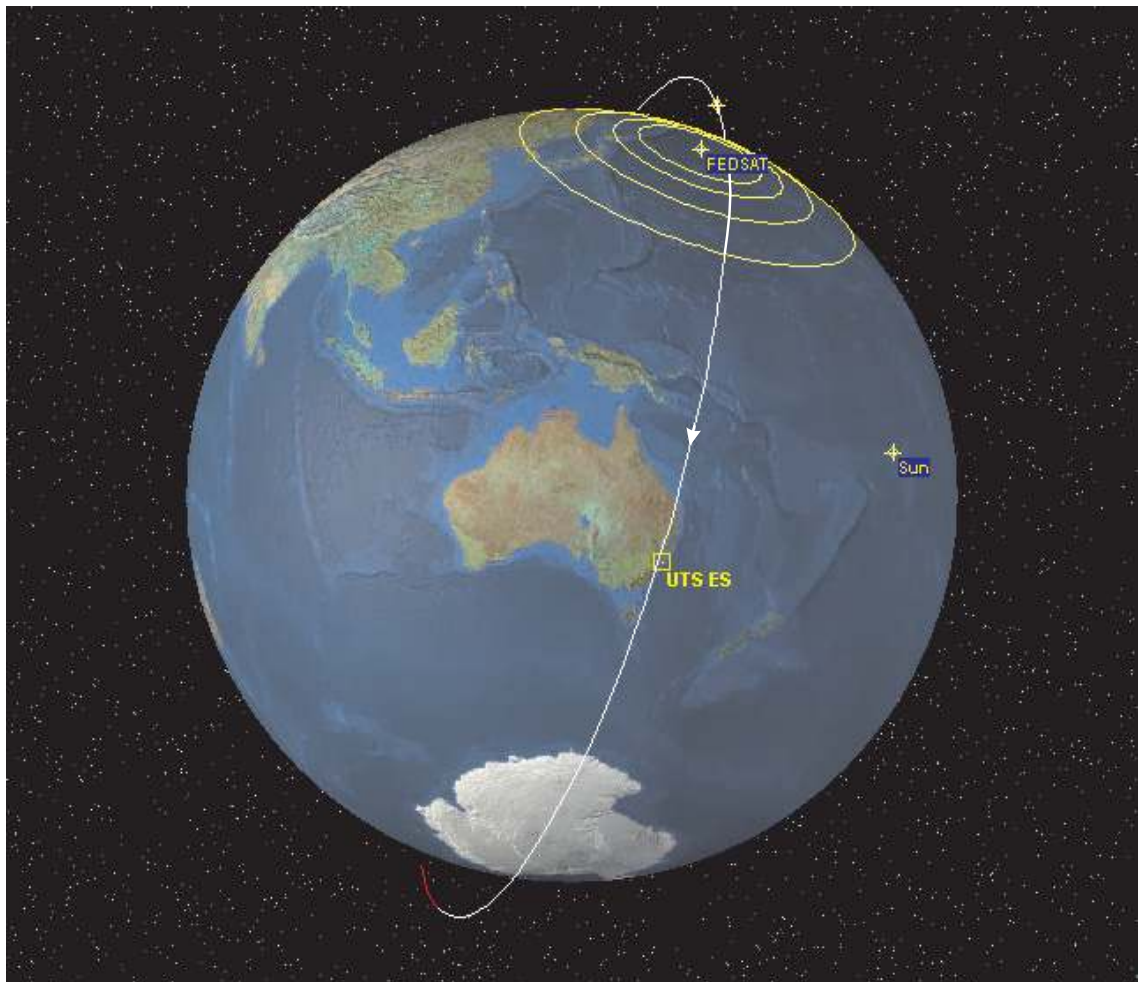
Figure 3.4: Illustration of FedSat's low-earth orbit (white) and the corresponding visibility footprint, with elevation contours from 0° to 30° (yellow).

Due to the small eccentricity, the orbit can be classified as circular for all practical purposes. The inclination of 98.6° indicates a retrograde, near-polar orbit with daily coverage of the entire earth, most frequently near the poles.

3.2.3 Implications for the Ka Band Propagation Experiment

The orbital parameters have a major impact on the experiments conducted with FedSat's payloads, particulary the sun-synchronous orbit. In this special type of orbit, the spacecraft passes the same point on the earth's surface at the same time of the day. While this is a highly desired feature for the magnetometer experiment (see Section 3.3.3.1), it is disadvantageous for the propagation experiment. Referring to Fig. 3.5, the following observations can be made for tracking FedSat from the UTS earth station location (indicated):
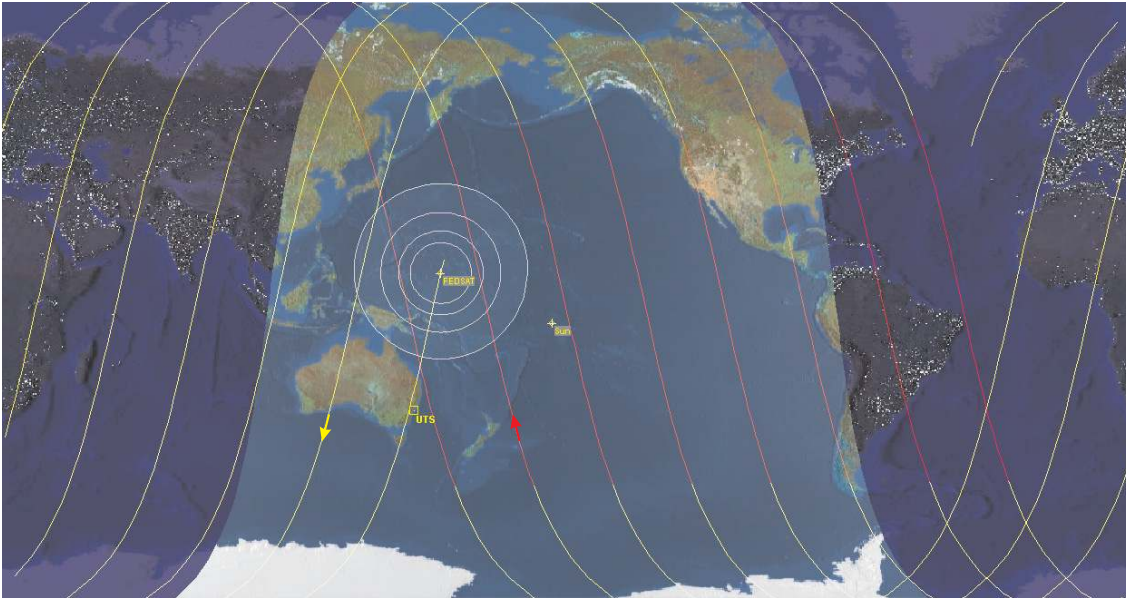
Figure 3.5: Orthographic map view of FedSat's ground tracks over a period of 8 orbits. Descending paths are always exposed to the sun (yellow), ascending paths mostly in eclipse (red).

- The maximum theoretical pass duration is 15'15" (915") from horizon to horizon.

- *All* ascending passes occur approximately between 09:30 and 14:00 UTC, which is night time local time. The spacecraft is in eclipse.

- *All* descending passes occur between 20:50 and 01:22 UTC, which is mid-morning local time. The spacecraft is exposed to the sun.

- Practically *usable* passes (i.e. during daytime with a sufficiently high elevation and pass duration) are descending and only occur approximately between 23:00 and 00:30, which is between 9:00am and 10:30am local standard time.

- Passes that meet the usability requirements (see Section 5.1.3) only occur about 2-3 times per week on average.

- Since the local pass time does not change significantly over the duration of the mission, only the weather conditions at the same time of the day can be investigated, i.e. mid-morning local time.

The significance of these limitations will become clearer in the discussion of the experimental results (Chapter 6) and in the suggestions for improvements (Section 7.2). However, it must be acknowledged that FedSat is meant to be a compromise in many design and operational aspects amongst the participating parties.

3.3   FedSat Housekeeping Functions and Payload Overview

3.3.1   Satellite Structure

The basic satellite bus structure is based on a standard cube-shaped design with a side length of 50cm and a nominal mass of 58kg [68]. Four of the six cube faces are covered by solar cells, the remaining two are occupied by the launch vehicle separation ring and by external devices, such as various antennas, the magnetometer boom and the star camera. Internally, the available space is divided into housekeeping systems (bottom) and payloads (top), as shown in Figs. 3.6 and 3.7.

Fig. 3.8 shows FedSat after closure and mounted on the launch vehicle separation ring. Arrows indicate several external components and sensors as part of the payloads or housekeeping systems.

3.3.2   Housekeeping Systems

"Housekeeping system", is a collective term for all *essential* components of a satellite, as opposed to payloads. Their function is to provide power to the payloads, process and store data, maintain a desired spacecraft attitude and communicate with the TT&C ground station. The housekeeping system and the satellite structure together are often referred to as the satellite "bus", which is based on the MicroSIL™ design for FedSat.
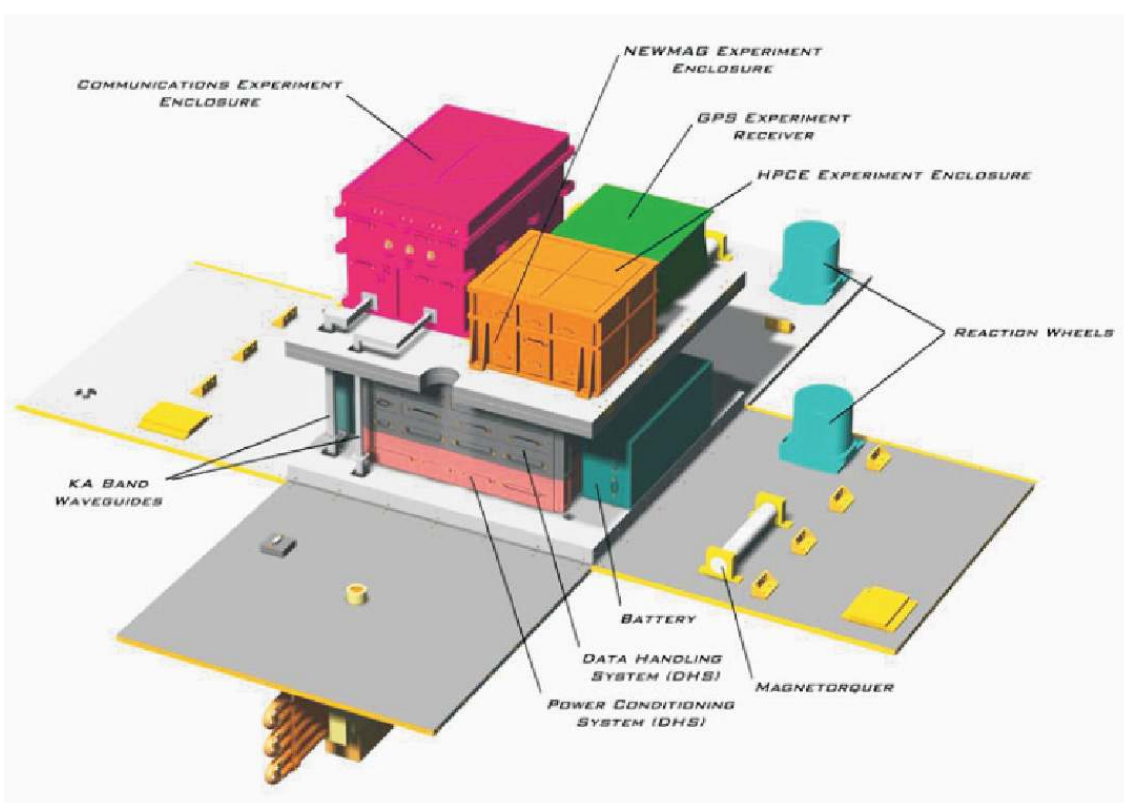
Figure 3.6: Locations of housekeeping systems and payloads within the satellite structure
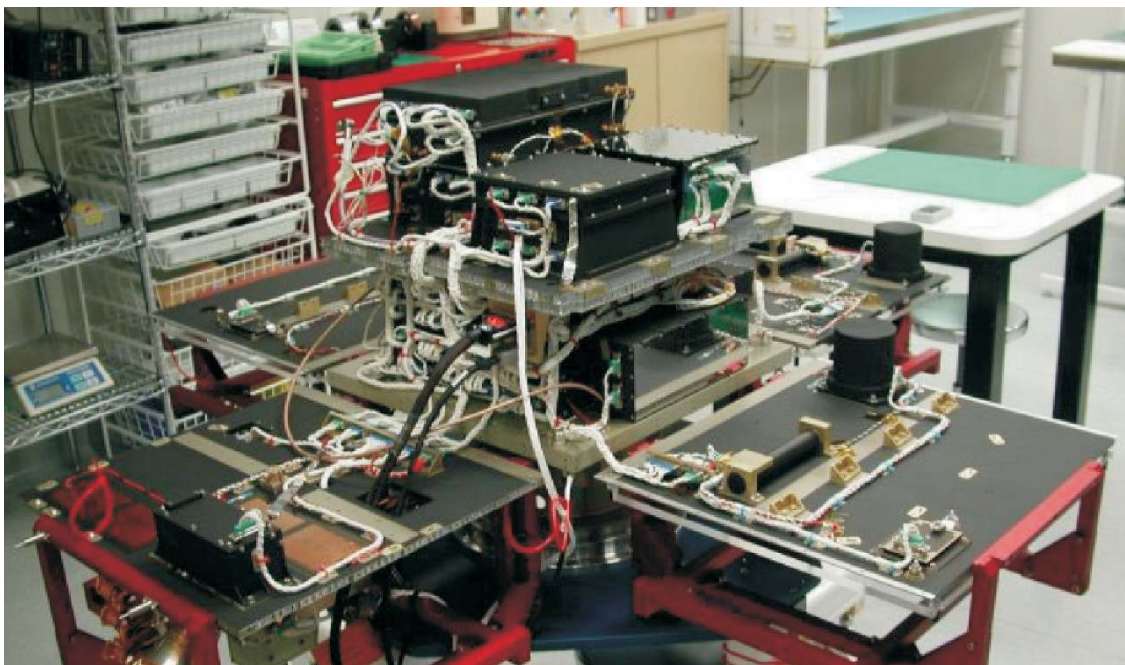
Figure 3.7: FedSat before closure
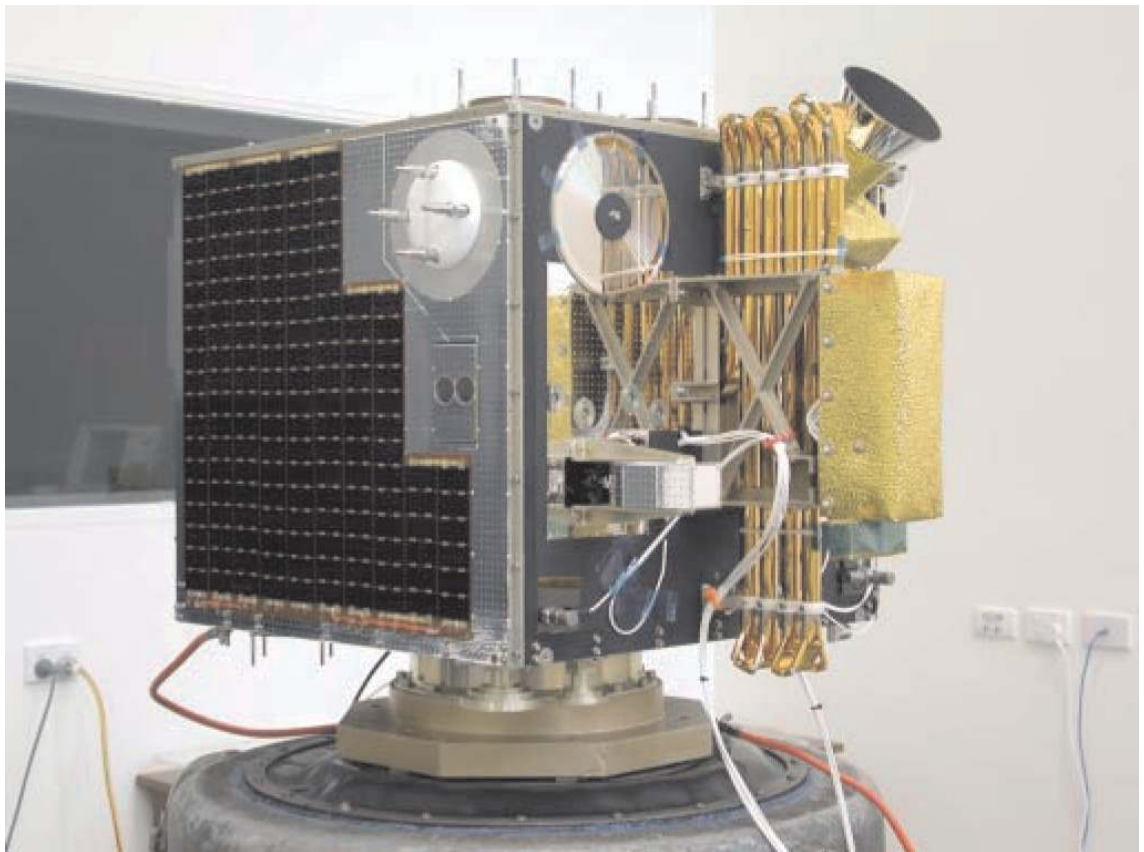
Figure 3.8: FedSat (closed) with some external payload and housekeeping components

3.3.2.1 Power Supply System

The power supply consists of three components: the power source, the power conditioning system (PCS) and batteries.

Four Gallium-Arsenide solar panels provide an power of 35W (averaged over one orbit) to the spacecraft. At least one of the panels is always exposed to the sun (unless eclipsed). Solar cells are very sensitive to physical damage, for example by space debris, and their efficiency and output decay over time.

An array of Nickel-Cadmium batteries forms a 20V, 4Ah secondary power supply and stores the energy for short-term high power demands or during eclipse. Only some of the capacity is available to power payloads though, since discharges deeper than 25% can permanently damage the cells. Due to the constant charge-discharge cycle in each orbit, both the capacity and the maximum voltage will decrease over time until it is no longer sufficient to power the housekeeping system. This scenario is a very common cause for satellite failure.

The PCS controls both the charging and discharging of the batteries. In particular, it restricts power consumption by the payloads to protect the most vital functions, such as attitude control and TT&C communications. After a critical discharge, it may take several orbits to fully recharge the batteries and allow payload operation. The typical power conversion efficiency lies around 46%. It is important to note that the power budget does *not* allow all payloads to be switched on at the same time for extended periods. Only selected payloads are designed to run continuously, see Section 3.3.3.

3.3.2.2 Data Handling System

The data handling system (DHS) can be described as the "brain" of the satellite. Its task is payload monitoring and control, data interfacing between the housekeeping system components, receiving and executing time-tagged or immediate telecommands from the TT&C ground station, data storage and telemetry/payload data transmission. The payload data is received and processed by a separate data acquisition unit and stored in a radiation-resistant mass memory.

The DHS also interfaces with some payloads to support its operation, such as the magnetometer, star camera and GPS unit described below, especially for attitude control. An internal clock provides a basis for time-stamping.

With respect to the propagation experiment, it is important to note that the DHS can be programmed hours or even days in advance to perform actions, such as turning certain payloads on and off and switching signals. However, if a critical event occurs in

the meantime, for example a low power or attitude warning, the DHS may reset and lose *all* stored commands and payload data. This occurrence can usually not be diagnosed until the telemetry is evaluated by the TT&C ground station.

3.3.2.3   Attitude Control System

The term attitude describes the satellite's orientation in space, usually in relation to earth or in terms of its velocity vector. Since FedSat is not equipped with a propulsion system, it has no capability changing its orbit or performing other displacement manoeuvres, defined by its orbit. Consequently, it only possesses three *rotational* degrees of freedom: yaw, pitch and roll, see Fig. 3.9 [69], [70]. It should be noted that the FedSat definition of the X, Y and Z axes may be different from other spacecraft.
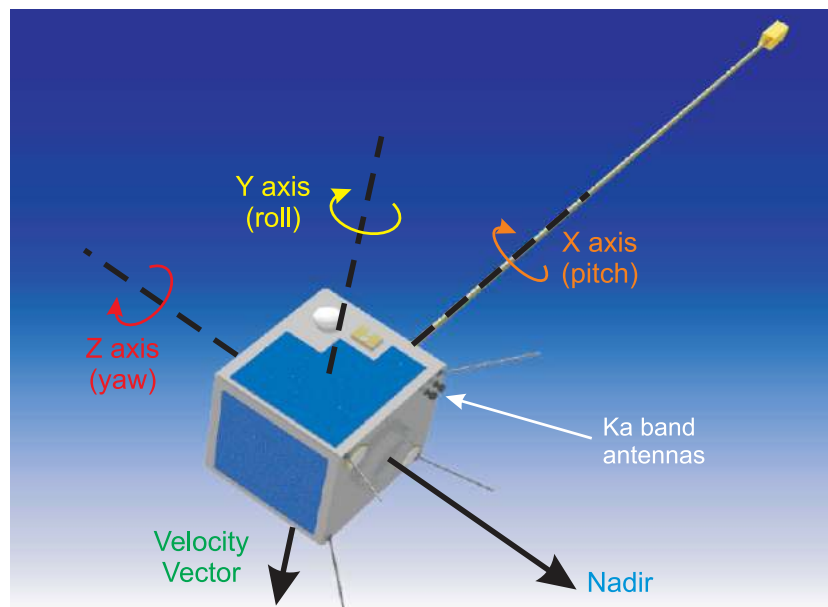
Figure 3.9: Definition of yaw, pitch, roll and nadir axes in relation to FedSat's velocity vector

The attitude control system (ACS) has the function of ensuring optimum orientation of the spacecraft with reference to the topocentric horizon coordinate system (SEZ frame, see [2]). In "pointing mode", all external sensors are in the correct position for their function and all antennas are pointing towards nadir. In conjunction with the DHS, the ACS will process the sensor data and execute actions to achieve and maintain optimum attitude on all three axes. It may only be activated periodically in order to save power.

To a large extent, attitude disturbances originate from asymmetries in the satellite mass distribution and the associated gravitational forces. For FedSat, the long, outlying

magnetometer boom (see Section 3.3.3.1) can easily been identified as a source. However, the drifting is very slow and gradual, and it can usually be automatically corrected by the ACS under normal operational circumstances.

The ACS can determine the spacecraft attitude by evaluating data from several sensors. The primary source is the set of three 2-axis digital sun sensors; secondary sources are the GPS, magnetometer and star camera payloads, which have the potential to greatly improve accuracy.

It will be shown in Chapter 6 that accurate attitude control within tenths of degrees is vital for precise Ka band signal power measurements, since the Ka band antennas are relatively directive. Any significant deviation from nadir can result in inaccurate data, hence the ACS performance during a satellite pass needs to be monitored by telemetry.

Since FedSat does not have any propulsion system (thrusters or jets), other techniques for attitude correction need to be employed. Reaction wheels and magnetic torque coils (magnetorquers), which can be automatically activated by the ACS, are a very power-efficient way to achieve the desired effect. Each of them consist of sets of three, which are mounted orthogonally to each other along the roll, yaw and pitch axes of the spacecraft. Attitude corrections are primarily performed by electric motor driven reaction wheels, whose inertia causes a change of the satellite's angular momentum. By combining all three axes, optimum pointing can be restored. Magnetic torque coils interact with the earth's magnetic field and are mainly used for cancelling undesired side effects of the reaction wheels. While deviations of a few degrees are usually corrected autonomously, the correction of major attitude problems with FedSat requires the intervention of the TT&C ground station.

A very undesirable scenario is the uncontrolled "tumbling" of the spacecraft at high angular velocity in more than one axis, often requiring real-time interaction with the TT&C ground station. This is only possible with a stable TT&C radio link, which may not exist due to the tumbling or due to the limited visibility time window. Typically, the satellite will recover in several orbits up to several days.

3.3.2.4 Telemetry, Tracking and Control Communication System

The TT&C communication system forms the satellite's interface to the commanding ground station, and it closely interacts with the DHS. It is composed of digital transceivers for the uplink and downlink, as well as associated RF hardware and patch antennas. The spacecraft is equipped with two sets of transmit/receive antennas, one pair on the nadir face and a second, redundant one on the zenith face in case of attitude problems.

FedSat has a dedicated 2 W, 1 Mbps S band downlink (2.205 GHz), which is used to download stored telemetry and payload data (store & forward). The 4kbps S-band uplink (2.030 GHz) is used to upload command sequences and optional software updates. In interactive mode, command sequences can also be sent for immediate execution, for example for the activation/deactivation of payloads or for attitude control manoeuvres. FedSat typically communicates with the TT&C ground station twice or more per day, depending on the ephemeris.

3.3.3 Experimental Payloads

For a microsatellite like FedSat, the number of scientific and engineering payloads is unusually high. The main reason for a successful co-existence that the payloads have quite diverse properties in terms of their weight, duty cycle, data accumulation and power requirements. Each payload represents the research field of one or more participating CRCSS member, who were responsible for the payload hardware before launch, as well as for the evaluation of the telemetry and data during the operational phase.

3.3.3.1 Magnetometer

The "NewMag" magnetometer is a highly sensitive device to accurately measure properties and disturbances of the earth's magnetosphere, especially around the polar regions. In conjunction with similar experiments on other LEO satellites and on the ground, it contributes to the understanding of physical principles in the ionosphere and significant events in the geomagnetic field.

It consists of triaxial fluxgate sensors, which take samples every 10 Hz, and the ancillary electronics. Due to interference caused by on-board components, the sensors have to be physically separated from the structure by an extendable 2.5 m boom, supplied by Stellenbosch University in South Africa. Fig. 3.8 above shows the boom folded up in its storage position for transport and launch. A spring-loaded mechanism, commanded by telemetry, triggers the in-orbit extension of the boom once the satellite is stabilised.

The magnetometer is one of the payloads that needs to be repeatedly operated for long periods at at time in order to collect meaningful data. It also has the potential in aiding the ACS in maintaining correct attitude.

3.3.3.2 Global Positioning System Receiver

FedSat carries a NASA/JPL-designed BlackJack GPS receiver. The aim of the GPS experiment is the precise orbit determination through short bursts of signal reception

from a subset of the currently 31 GPS MEO satellites. GPS signal propagation through the earth's ionosphere and atmosphere is also studied, from which deductions about space weather and terrestrial weather can be made.

The raw GPS receiver data is accumulated by the DHS, sent to the TT&C ground station and forwarded to the GPS experiment group for further processing. It should be noted that the evaluation of the GPS data does *not* take place in real time on the spacecraft. The result is a high-precision orbital model, which is typically of much higher accuracy than that derived from two-line elements (TLEs, see Section 5.2). Since this is a crucial point for the Ka band earth station design, orbit determination and extrapolation based on GPS and two-line element data is further discussed in Chapter 5.

In addition to spatial data, the GPS receiver also supplies a highly accurate timing signal, which is used for timestamping both payload data and telemetry. This has proven very useful when comparing spacecraft events with observations at the Ka band earth station.

3.3.3.3 Star Camera

The star camera was the latest addition to FedSat's payloads. It can greatly improve the pointing accuracy of the spacecraft, which is particularly important for the magnetometer and the Ka band communication experiments. By comparing the photos taken by the camera in regular intervals to a star map in the camera's memory, it can precisely determine any deviation up to 20 arc seconds [71]. This information is provided to the DHS and the ACS for corrective measures. Unfortunately, the star camera gave inconclusive results some time into the project and was deemed unreliable for the remaining satellite lifetime.

3.3.3.4 High-Performance Computing Experiment

The HPCE hardware is supplied by John Hopkins University (USA), and as a mostly stand-alone payload, it aims at demonstrating reorganising algorithms in field-programmable gate arrays (FPGAs) in a space radiation environment. When exposed to space radiation, random parts of the highly integrated circuits are destroyed, either limiting or disabling the functionality of that device. In this experiment, the FPGA repeatedly runs internal algorithms and verifies the output. It automatically detects the occurrence of radiation damage and relocates the algorithm to an undamaged area of the chip. The results are reported to the DHS.

3.4 Communications Payload

FedSat's communications payload provides the space segment for the Ka band propagation research. The following sections will highlight the most important functionality of and interactions between the separate communication payloads, since power and weight constraints dictate the shared use of resources. The Ka band payload will be studied in greater detail.

3.4.1 Overview

The communications payload (CP) consists of three main units: the baseband processor (BBP), the Ka band payload and the UHF payload [72]. The block diagram in Fig. 3.10 illustrates that both the BBP and the Ka band experiments share most of the UHF electronics on the intermediate frequencies of 314 MHz, 21.4 MHz and 400 MHz, which will be further explained in Section 3.4.2. Not shown are the power supplies to the different modules, which can be enabled and disabled separately via telecommand. Hence it is possible to operate the UHF/BBP path only without turning the Ka band modules on, saving battery power. Similar to the other payloads, the CP is equipped with several dozen analogue and digital telemetry points, for example for voltage, temperature and switchline status readouts, in order to provide remote information about the spacecraft's condition. This is especially vital during fault-finding procedures.

3.4.2 Operation Modes

In order to conduct a variety of communication experiments, the payload can be switched into different modes. Due to the shared signal paths in the UHF module, concurrent Ka band and BBP experiments are mutually exclusive.

BBP experiments on UHF frequencies are conducted from ITR in Adelaide. Main research activities include on-board processing and store & forward tests at low power and flexible data rates, designed for the use with simple mobile terminals. An optional in-orbit software upgrade is intended to extend the on-board processing capability to Ka band data transmissions.

3.4.3 UHF Payload

Fig. 3.11 shows a detailed block diagram of the UHF payload, including nominal signal power levels (in dBm) and important telemetry points. The coloured boxes indicate the different IFs in use, and the connection points between the block diagram sections can be recognised in Fig. 3.12 (modified from [73]) as shielded compartments inside the module.
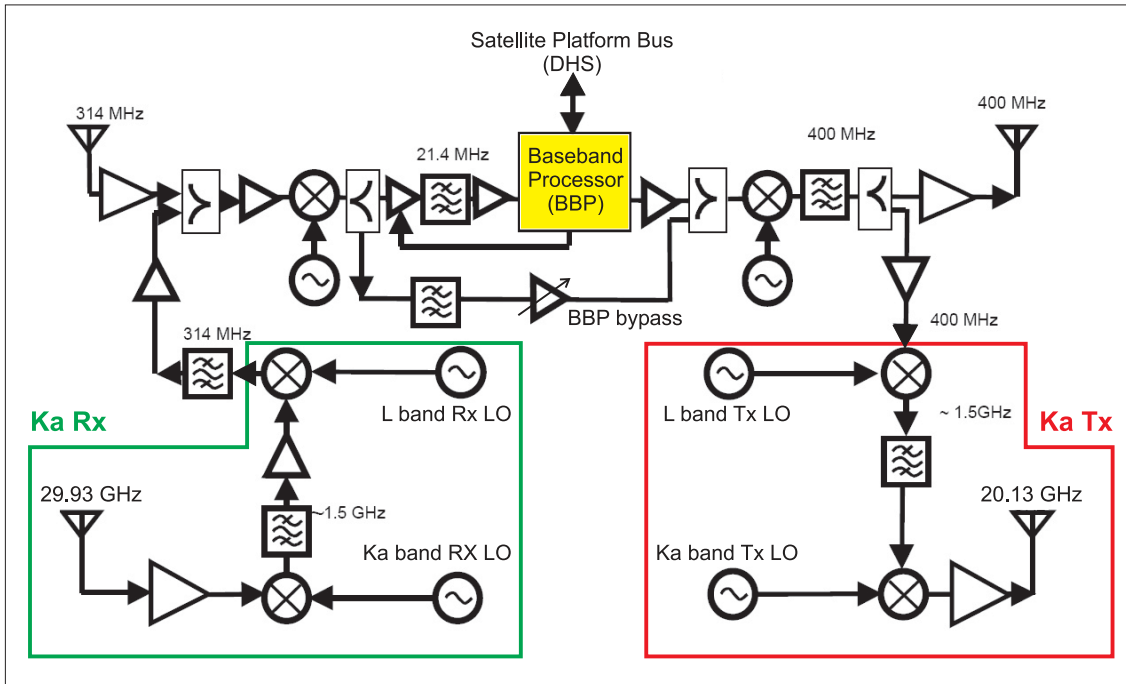
Figure 3.10: The communications payload with Ka band and UHF signal paths

The payload essentially follows standard transponder design with several conversion stages, amplifiers and narrow bandpass filters for image signal rejection. The received signal from the Ka band payload (see Section 3.5) enters the UHF module on a 1.5 GHz IF, is further downconverted to a 314 MHz 2nd IF and combined with the signal from the UHF experiment path. The 3rd IF, 21.4 MHz, forms the RF interface with the BBP and provides flexibility in its usage for both UHF and potential Ka band experiments. An RF switch can be activated to select a narrow 1 MHz bandpass filter only for Ka band bent pipe mode, while the wide-band BBP signal remains unfiltered at this stage. The BBP bypass, which also contains a switchable 2-level attenuator, is essential for bent pipe mode experiments without the involvement of the BBP. The output signals of both paths are combined and upconverted to a 400 MHz IF, which is also the transmit frequency of the UHF experiment. For Ka band operation, a further stage (1.5 GHz) follows before the signal is fed into the Ka band HPA module. The UHF front end and HPA (not pictured in Fig. 3.11) use two monopole antennas for transmit and receive, which are located at two corners of the spacecraft. Due to the fact that some local oscillators are physically located within the BBP payload, both the UHF module and the BBP need to be powered up for Ka band operation. The implication of this design, in conjunction with the use of combiners instead of RF switches, will be shown in Section 7.1.
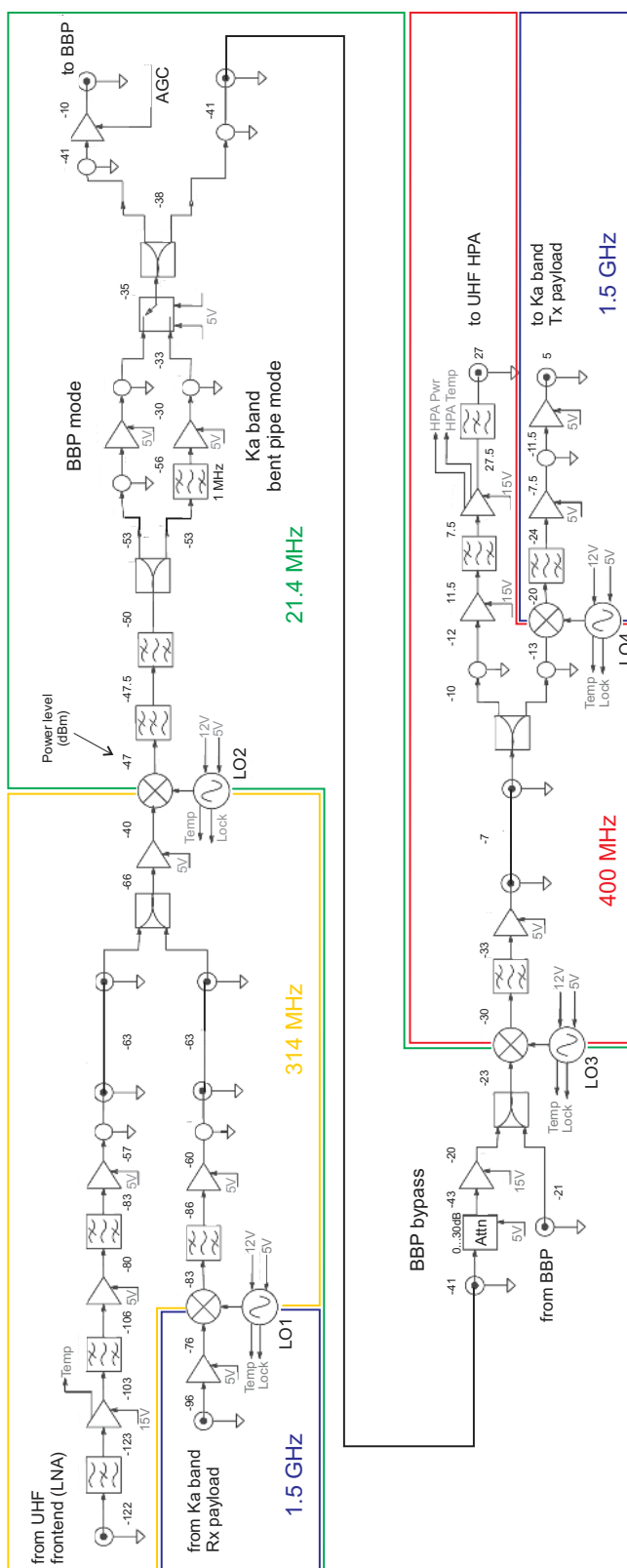
Figure 3.11: Detailed block diagram of the UHF payload

Figure 3.12: The UHF payload module (Photo: ITR)

3.4.4 BBP/ADAM Payload

Developed by ITR and DSpace Pty Ltd, the Baseband Processor is an advanced packet modem with on-board processing capabilities. It has been designed specifically for small satellite missions, and FedSat serves as a test bed for various communications modes and internal functions. The BBP's main purpose is to support small, mobile ground terminals at data rates up to 128 kbps, and an additional messaging service for remote data collection ("Advanced Data and Messaging", ADAM), for example ocean buoys, at up to 4 kbps. The BBP employs TDMA on the uplink and TDM on the downlink. The BBP telemetry and data is interfaced with the DHS and transmitted via the S band TT&C link.

Proposed UHF experiments include store & forward, code upload, beacon and bent pipe mode operation. With the transponder in Ka band operation, beacon and carrier bent pipe mode support are implemented, while Ka switching at up to 256 kbps and TT&C backup modes require an in-orbit BBP firmware update. Due to the proprietary BBP message structure, a BBP is also required on the ground station side for data communication. A basic block diagram of the BBP architecture is provided in Fig. 3.13 [73]. More details about the BBP and the ADAM experiments can be found in [74].

3.5 Ka Band Transponder

FedSat is the first satellite of its size to carry a Ka band transponder [75], which is the key payload for the propagation experiment and will therefore be explained in greater detail. It consists of the Ka band receiver module, the Ka band transmitter module and two horn
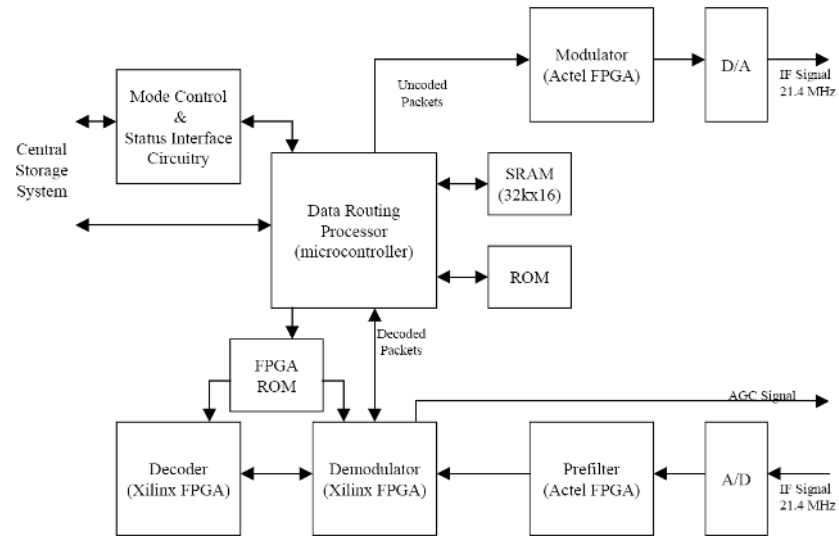
Figure 3.13: BBP Architecture

antennas. As illustrated in Fig. 3.10 above, the Ka band modules directly interface with the UHF module. Fig. 3.14 shows the Ka band payload in mounted in its flight housing.

Figure 3.14: The Ka band transponder module with receive/transmit circuits and local oscillators

3.5.1 Ka Band Modules

The responsibility for the design of the Ka band receiver and transmitter modules, as well as the antennas, lay with the Telecommunications and Industrial Physics (TIP) group of the CSIRO. Since the UHF module uses an IF of 1.5 GHz both for the uplink and the downlink, the Ka band modules were constructed separately to avoid any spurious effects and to allow individual testing. Due to stringent requirements with respect to noise figure, reliability in space and cost, TIP developed the circuits as Gallium-Arsenide MMICs, which were later fabricated by TRW in the United States [76].

Figs. 3.15 and 3.16 display block diagrams of the onboard Ka receiver and transmitter modules, respectively [72]. Nominal RF power levels and important telemetry points are also indicated.
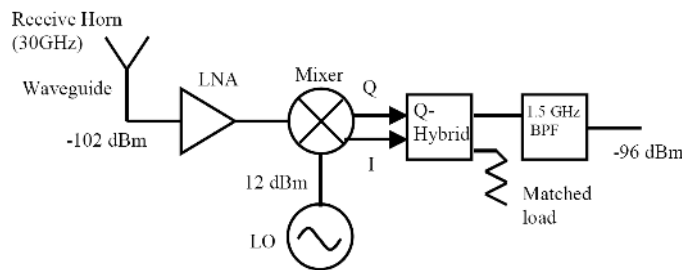
Figure 3.15: Ka band receiver block diagram
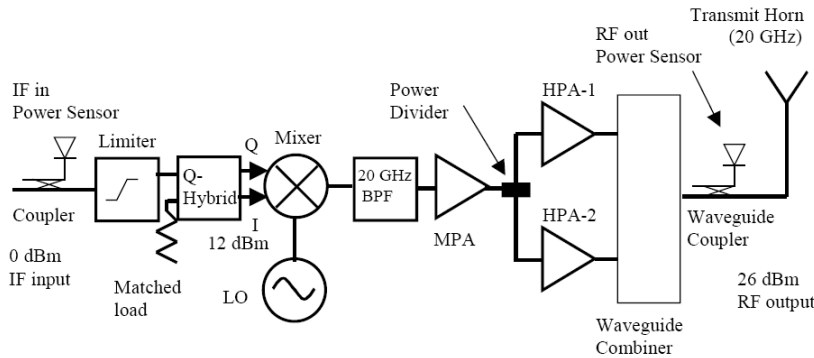
Figure 3.16: Ka band transmitter block diagram

The receiver module is designed for an uplink frequency of 29.93 GHz and for a 1st IF of 1.5 GHz. The 3.0 dB noise figure front end yields 18 dB gain before the signal is mixed with the external LO. Fig. 3.17 shows the miniature MMIC and ancillary circuits mounted onto the substrate and enclosed in the housing.
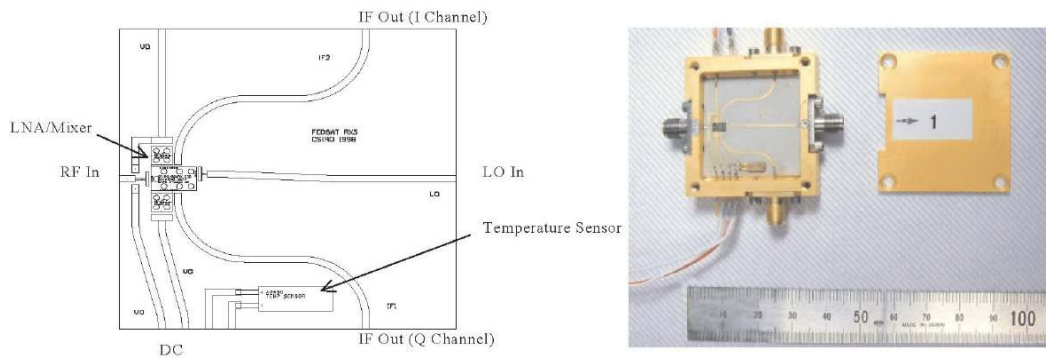
Figure 3.17: Ka band downconverter MMIC mounted on substrate and with external connectors (CSIRO prototype)

To a large extent, the transmitter module is also an in-house design of TIP, comprising an upconverter-mixer, a medium-power amplifier (MPA) and two parallel high-power amplifiers (HPA), plus peripheral circuits (Fig. 3.18). In order to protect the MMIC against excessive input power levels at 1.5 GHz, a limiter is placed in front of the internal up-conversion circuit. The subsequent MPA with 18 dB gain is an in-house design by TIP specifically for this project, while the two parallel HPA devices are supplied by TRW. The transmitter module was initially designed to yield an output power of 26 dBm (400 mW) at 20.13 GHz, later corrected to 24 dBm (250 mW), which can be monitored by telemetry through a waveguide coupler.
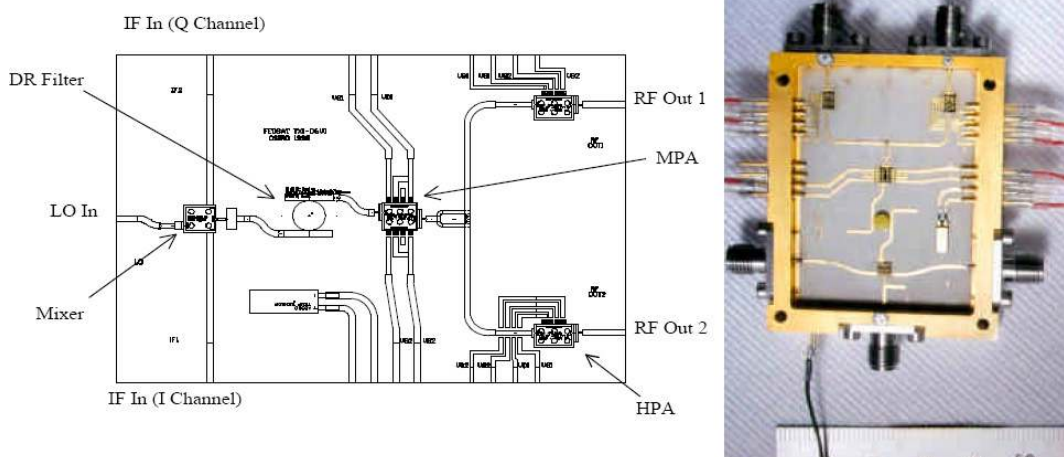
Figure 3.18: Ka band transmitter package (CSIRO prototype)

3.5.2 Ka band Antennas

The design and fabrication of two Ka band antennas, which was also performed at the TIP facility of the CSIRO, aimed at meeting the specific requirements of LEO experiments, i.e. maximising the illuminated area of the theoretical satellite footprint and maximising the antenna gain within this area. Obviously, these two goals have to be balanced, along with other design aspects, such as polarisation, bandwidth and physical size.

Commonly, satellite communication systems use circular polarisation to avoid the effects of Faraday rotation [2]. Monitoring the cross-polarisation discrimination (XPD) between the co- and cross-polar components of *linear* polarisation does have merits in the field the propagation research, but for FedSat, the design for data communication dominated the choice of polarisation and also simplified the tracking by one degree of freedom (yaw axis). For FedSat, the polarisers and compact multi-mode horn antennas are designed to use right-hand circular polarisation (RCP) for the 29.93 GHz uplink and left-hand circular polarisation (LCP) for the 20.13 GHz downlink. Both Ka band antennas, depicted in Fig. 3.19, are essentially of the same fundamental design, but for different frequencies.

Figure 3.19: 20 GHz compact multi-mode horn antenna for FedSat (Photo: CSIRO)

CSIRO ran very extensive antenna measurements on a replica of FedSat, a hollow, galvanised iron cube ("TinSat"), simulating the antenna operating environment as closely as possible in an anechoic chamber and on an outdoor range. The radiation patterns of each of the spacecraft antennas, i.e. the UHF monopoles, the S band patch and the Ka band horn antennas, were experimentally obtained and incorporated in the respective link budgets. Using the test setup illustrated in Fig. 3.20 [70], the radiation pattern

was measured in 4 planes, i.e. the antenna was rotated around its own axis in steps of $\Delta\phi = 45°$.
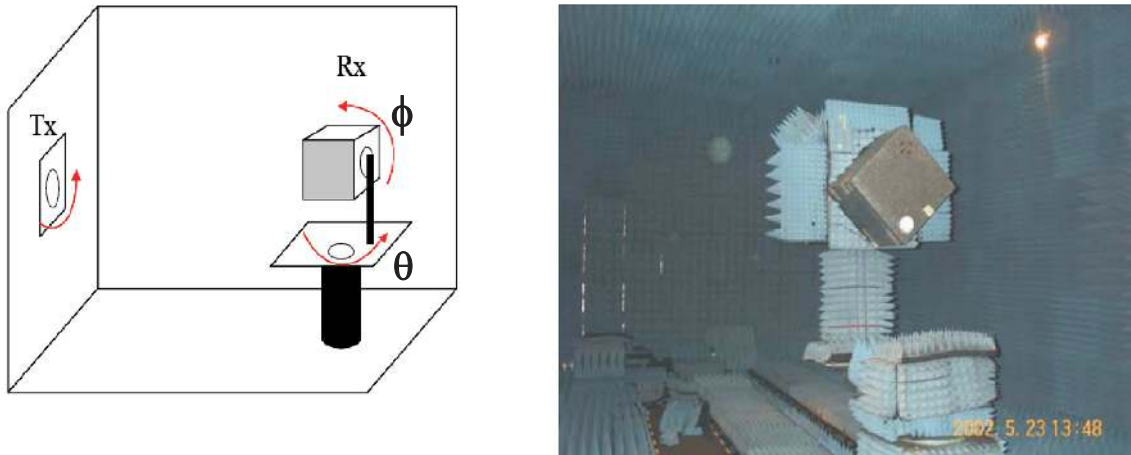
Figure 3.20: Antenna measurement arrangement (left) and TinSat in the anechoic chamber (right)

The resulting report [77] contains very comprehensive radiation pattern measurements of the UHF, S and Ka band antennas. The Ka band receive antenna (23.93 GHz uplink) achieves a gain of 6.15 ± 0.25 dBi in its pointing direction, while the transmit antenna (20.13 GHz downlink) was measured to have a 5.50 ± 0.25 dBi gain. From the exemplary downlink radiation pattern depicted in Fig. 3.21 [77], it can be seen that the maximum gain does not occur in the pointing direction of the antenna ($\theta = 0$), but approximately at $\theta = \pm45°$ off-axis angles.

This pattern was specifically designed to partially compensate for the increased path loss as the angle between the spacecraft nadir and earth station's zenith increases (squint angle). It therefore roughly approximates an isoflux radiation pattern, allowing a longer link time. The gain decreases rapidly at off-axis angles greater than about $\pm60°$. All measurements taken at different angles Φ indicate that the antenna is not significantly influenced by scattering from the spacecraft and can therefore be regarded as rotationally symmetric for all practical purposes. This is an important simplification which will be taken advantage of in Section 5.3.3.

3.5.3 Experimental Objectives

FedSat's five payloads pursue different mission objectives. For the already space flight-proven magnetometer and GPS receiver, data collection is the most important goal. For
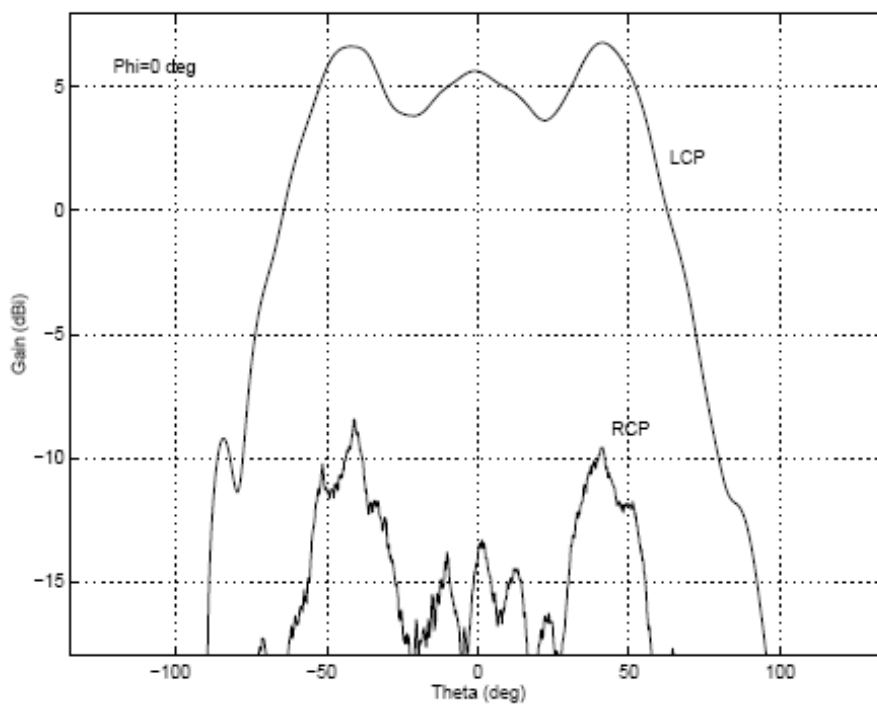
Figure 3.21: Measured RCP and LCP gain patterns of the Ka band transmit antenna at 20.13 GHz, rotation $\phi = 0°$

the more design-driven payloads, such as the communications payload, the HPCE and the star camera, proof of concept, space qualification and the provisioning of an experimental platform in a low-earth orbit are the milestones to be achieved during the mission lifetime.

With respect to the Ka band payload, all design aspects undertaken by CSIRO aim at meeting military specifications, and successful space qualification is a major objective of this project. This would enable the design expertise for FedSat to flow on into commercial projects for other spacecraft in future. Under optimal operational circumstances (battery status and satellite stability), the Ka band payload is turned on for certain periods of time, even without tracking of any earth station, and the power output is monitored via telemetry to provide long-term performance statistics (see Section 5.3.1).

The Ka band communication and propagation experiments crucially rely on the success of the Ka band hardware, as well as the supporting UHF and housekeeping systems.

3.6 Operational Considerations and Restrictions

The broad overview of the housekeeping system and the payloads onboard FedSat in this chapter now allow a critical assessment of operational restrictions that limit the experimental objectives of the Ka band propagation experiment.

3.6.1 On-board Power Requirements

As previously mentioned in Section 3.3.2.1, FedSat's platform is not designed to support the housekeeping functions and all payloads simultaneously. The available average power of 35W per orbit is easily exhausted, and considering that FedSat is in eclipse from sunlight for almost half of its orbit, it may sometimes take several orbits to fully recharge the batteries. Hence it is required that payloads are scheduled in time slots. This is especially important for the larger loads, such as the communication payload, and the Ka band modules in particular.

Consequences of the battery voltage dropping below a certain safety threshold are the immediate shutdown of all payloads, and in severe situations even some of the non-essential housekeeping systems. This usually results in a loss of research data for the payloads with long-term operation requirements, for example the magnetometer. However, the maximum visibility window from the Ka band earth station is 15'19", therefore the transponder is not required to operate for longer than 20-25 minutes.

Considering all available and all suitable passes for Ka band communication experiments (see Section 5.1), it was agreed with the mission manager that an average number of 1-2 passes per week would be scheduled under normal conditions.

3.6.2 Satellite Attitude

A correct satellite attitude is essential for successful Ka band experiments. Due to the rotational symmetry of the onboard antennas, rotation on the yaw axis *alone* (see 3.9) can be neglected, however any significant deviation on the pitch and roll axes will result in wrong power measurements.

Two scenarios are likely to occur:

- The rotation on all three axes is mostly within the operational requirements ($\leq 1°$, 20 arc sec with the star camera) and experiences little disturbance. Corrections can easily be made by the ACS through occasional manoeuvres with the reaction wheels and the torque rods.

- Major disturbances have cause the spacecraft to be significantly out of pointing mode, and the ACS is unable correct the deviation automatically. An intervention of the TT&C ground station is required to manually correct the spacecraft's attitude into a margin that can be handled by the ACS.

The impact of the second point on the ability to run successful Ka band experiments will be shown in Section 5.6.

A potentially terminal, but rare scenario is spacecraft "tumbling" where the angular displacement on one or more axes is not constant, but rapidly fluctuating. This can occur if small deviations start to oscillate and increase if the error remains uncorrected over long periods of time. Under these circumstances, it is even possible to lose TT&C communication with the satellite, since the antennas are spinning to fast to receive the signals properly.

3.6.3 Satellite Platform Stability and Intervention

This section deals with the overall reliability of the satellite platform, and with the challenge to time the payload activation to coincide with FedSat's visibility from Sydney.

Normally, a Ka band beacon or bent pipe mode experiment would be time-tagged by uploading the necessary commands via the TT&C link on prior passes. All required payloads would then turn on automatically at the pre-defined time, and would deactivate later. Due to the previously mentioned impact of low power warnings, DHS resets and attitude problems, these commands may not execute as planned, so all preparations on the ground are futile. In more serious circumstances, the satellite may not be available for several days before attitude or power problems are resolved.

If the spacecraft is visible from both the Ka band ground station *and* the TT&C earth station, human intervention is possible and direct telecommands may be sent to the satellite to turn the desired payloads on [78]. However, if successful at all, this only takes place several minutes into the pass so that a lot of measurements are lost. If the spacecraft malfunction has occurred due to a ACS problem, even that partial data may be useless, but that can only be determined from the attitude telemetry at a later time.

3.6.4 Interference between Payloads

Since the Ka band propagation experiment does not require any data (apart from some payload telemetry) to be stored onboard FedSat, the Ka band payload is only interfaced with the UHF module for signal exchange. Although all payloads have been tested in a system integration test prior to launch, there is a small chance that in-orbit software changes in the BBP can lead to undesired interference with the UHF and Ka band modules. This topic is further explored in Section 7.1.2.

3.7 Summary - FedSat and Ka band Payload Specifications

Chapter 3 has introduced the CRCSS a collaborative organisation for Australia's ambitious FedSat mission, as well as the FedSat satellite as a research platform for a wide variety of experiments. Spacecraft and Ka band payload specifications are summarised in Tables 3.3 and 3.4.

Catalog No.	28598, FEDSAT
International designator	2002-056B
Structure	50 cm cube, 58 kg
Launch Date	14 Dec 2002
Launch Vehicle	H-IIA (F4)
Launch Site	Tanegashima, Japan
Orbit	793 km × 806 km, sun-synchronous
Inclination	98.5°
Mean altitude	800 km
Orbits per day	14.28
Orbital period	100' 51"
Stabilisation	3-axis
Average power per orbit	35 W
TT&C link	1 Mbps, S band
Payloads	Magnetometer, GPS receiver, star camera, FPGA experiment, UHF and Ka band communications

Table 3.3: Summary of FedSat specifications

Uplink frequency	29.93 GHz (RCP)
Downlink frequency	20.13 GHz (LCP)
Transponder bandwidth	1 MHz
Receiver front end	Custom-design MMIC
Noise figure	3 dB
Intermediate frequencies	1.5 GHz, 300 MHz, 21.4 MHz, 413 MHz, 1.5 GHz
Transmitter	1 MPA and 2 parallel HPAs
Transmit power	24 dBm
Antenna type	Multi-mode horn
Antenna gain (boresight)	6.15 dB @29.93 GHz, 5.50 dB @20.13 GHz
Antenna gain (max.)	7.25 dB @29.93 GHz, 6.70 dB @20.13 GHz
Antenna beamwidth	120° (isoflux approximation design)
Operation modes	Beacon mode, bent pipe mode

Table 3.4: Summary of Ka band payload specifications

Part II

Research

Chapter 4

Fast-Tracking Ka Band Earth Station Development

After the introduction of the space segment for the CRCSS propagation experiment in the previous chapter, the design and construction of the Ka band earth station will be explained and illustrated in detail in this part. It will be shown that the number of considerable design constraints had to be carefully balanced against each other, and especially against financial limitations. The fundamental earth station design was created by the early members of the UTS CRCSS, and the author would like to acknowledge especially those people named in [79] for their substantial input and dedication. However, many adaptations and design improvements still had to be implemented during the final development stage, the deployment and three years of operation, to which the author made important contributions (from 2002 onwards).

4.1 Earth Station Design Overview

Unlike the general-purpose S band TT&C earth station at ITR in Adelaide, the UTS Ka band earth station was purposely designed to meet the challenges posed by the communications payload specification outlined in Chapter 3. Since some of the payload modules were developed on an experimental basis, some crucial figures were unknown until well into the project, for example the spacecraft EIRP. This prompted a review of the link budget and the earth station design, and resulted in several changes. The figures presented in this section represent the latest version of these revisions.

4. FAST-TRACKING KA BAND EARTH STATION DEVELOPMENT

4.1.1 Critical Design Issues

In order to establish successful communication between FedSat and the Ka band earth station, either in beacon, carrier bent pipe or data bent pipe modes, several key issues had to be addressed.

4.1.1.1 Spatial Tracking and Keyhole Problem

Once properly adjusted, most communication systems for GEO satellites only require minor spatial tracking at the ground station, since the spacecraft's motion is very small. For LEO satellites, the situation is vastly different. Considering the orbital parameters from Table 3.2, it is evident that only a mechanical tracking pedestal system would be able follow the spacecraft's *rapidly* changing trajectory during a pass. Two degrees of freedom are required for full hemispherical coverage, which is commonly realised by an elevation-over-azimuth (tilt/pan) tracking pedestal, such as in Fig. 4.1.

Figure 4.1: Commercial elevation-over-azimuth satellite tracking pedestal [80]

At an average altitude of $h = 800\ km$ and an orbital velocity of $v = 7.45\ km/s$, the maximum *angular* tracking velocity on the elevation axis can be sufficiently approximated by $\omega_{El} \approx \arctan \frac{v}{h} = 0.534°/s$ during an overhead (zenith) pass, because the spacecraft moves predominantly in a north-south direction (descending path) or south-north direction (ascending path). This statement is true only for LEO satellites with a highly inclined (near-polar) orbit, like FedSat.

Referring to the high-elevation pass shown in Fig. 3.4, this typical example immediately illustrates the emerging problem when a standard elevation-over-azimuth tracking pedestal is employed for tracking LEO satellites. The graphs in Fig. 4.2 show the look angles and angular velocity for this particular example.
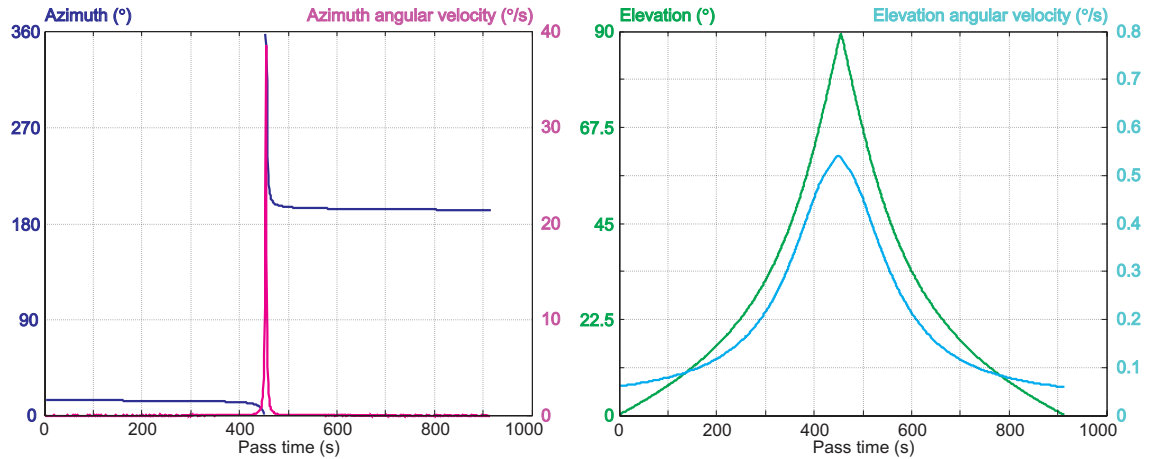
Figure 4.2: Calculated azimuth and elevation angles for an overhead pass with related angular velocities

The blue curve represents the azimuth look angle from the earth station to the satellite, which appears on the horizon just east of north (14° azimuth), decreasing very slowly. When the spacecraft approaches zenith, the azimuth angle has to rapidly swing around by 180° to about 194° within a few seconds, which results in a required angular velocity of $\omega_{Az} \approx 39°/s$ (pink curve), making it very likely that the signal is lost during the manoeuvre. Although less severe at lower maximum elevations, this effect poses significant design issues for the tracking pedestal dynamics and is commonly known as the "Keyhole Problem", illustrated in Fig. 4.3. By comparison, the elevation axis only experiences a maximum angular velocity $\omega_{El} = 0.53°/s$ (cyan curve), which confirms the approximation from above.

A solution to this problem is discussed in Section 4.4.1.

4.1.1.2   Link Budget vs. Tracking Accuracy Requirements

In order to close the link between the spacecraft and the earth station (and vice versa), the received power must be high enough to be detectable in the noise floor. In the case of the 20.13 GHz ($\lambda = 1.5$ cm) downlink, the spacecraft EIRP ($EIRP_S$) is defined by the output of the Ka band HPA and the horn antenna gain for boresight [2]:

$$[EIRP_S] = [P_S] + [G_S] = -6 \; dBW + 5.50 \; dBi = -0.5 \; dBW \qquad (4.1)$$

Calculating the free-space path losses for the horizon case ($d_H = 3320$ km) and zenith ($d_Z = 800$ km),
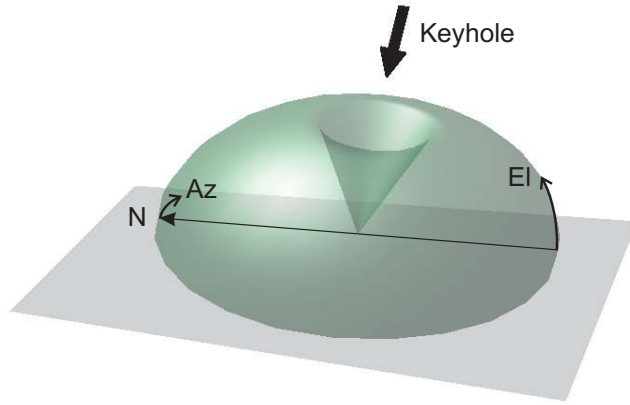
Figure 4.3: Limitations of hemispherical coverage by an Az/El tracking system due to the keyhole problem (modified from [81])

$$[FSL] = 10 \cdot \log_{10} \left(\frac{4\pi d}{\lambda} \right)^2 \text{ dB} \tag{4.2}$$

$$\therefore \quad [FSL_H] = 188.9 \text{ dB} \quad \text{and} \quad [FSL_Z] = 176.5 \text{ dB} \tag{4.3}$$

For an isotropic receive antenna and not including any other losses at this time, such as antenna misalignment or atmospheric losses, this would result in a received power level $[P_R] = [EIRP_S] - [FSL]$. Converted from dBW to dBm, $[P_R]$ lies between -147 dBm and -159.4 dBm and therefore well below any desired signal-to-noise ratio for a given Ka band front end, thus requiring a high-gain receive antenna. The selection of a suitable antenna system is a trade-off of several key factors:

- **Size** - the reflector needs to be physically small and light enough to be driven by the electromechanical system due to torque limitations, and to minimise wind load and manufacturing cost.

- **Gain** - the antenna gain needs to be large enough to amplify the received signal, providing sufficient power levels to the receiver front end (LNA). The gain is directly related to the physical size (aperture) and the signal wavelength ([2], p. 143):

$$G = \eta \left(\frac{4\pi}{\lambda^2} \right) \left(\frac{\pi D^2}{4} \right) = \eta \left(\frac{\pi D}{\lambda} \right)^2 \tag{4.4}$$

where η denotes the efficiency, and D is the diameter of the antenna reflector.

- **Beamwidth** - the half-power beamwidth (HPBW) needs to be large enough to allow for small spatial tracking errors, which can be caused by TLE inaccuracies or tracking system tolerances. For a parabolic dish reflector of diameter D, the HPBW in degrees can be approximated by ([2], p. 143)

$$HPBW \cong 70\frac{\lambda}{D} \qquad (4.5)$$

  but it is more accurate to physically measure its radiation pattern. Therefore, a higher antenna gain leads to more stringent spatial tracking requirements and vice versa.

The last point is particularly difficult to quantify at the design stage, since mechanical and systematic uncertainties, such as orbital element errors and the effect of mechanical tolerances (for example gearbox backlash) are still largely unknown, see Section 5. A theoretical approach, however, is provided in [82]. With a given required carrier-to-noise ratio C/N_0 or link margin M (depending on the operation mode), the solution of this parametric optimisation problem is of iterative nature, since a narrower beamwidth causes a larger pointing loss, which then needs to be considered in turn. The resulting properties of the antenna subsystem are discussed in more detail in Section 4.3.

4.1.1.3   Doppler Frequency Tracking

When tracking a LEO satellite signal from a particular earth station location, the range r between the two objects changes dynamically with the trajectory. This leads to a variation in the observed signal frequency at the receiver, depending on whether the satellite is moving towards or away from the earth station. Known as the Doppler Effect, the frequency difference (or "Doppler shift") Δf can be quantified as:

$$\Delta f = v_S\frac{f_S}{c} = \frac{v_S}{\lambda} \qquad (4.6)$$

where $v_S = \dot{r}$ is the relative spacecraft velocity component towards the earth station, f_S is the spacecraft transmit frequency, c is the speed of light and λ is the transmit signal wavelength [3]. Fig. 4.4 demonstrates the range of Doppler shift encountered on the downlink during an overhead pass (black curve). Maximum and minimum are encountered at the horizon ($\pm 450\ kHz$), and Δf is zero when the satellite passes through zenith. However, the first derivative of Δf, the Doppler rate, is maximised at this point with $3.9 kHz/s$. For marginal passes further away from zenith, these values are gradually getting

smaller. For the uplink, the Doppler shift and Doppler rate observed at the *spacecraft* would be $\pm 670\ kHz$ and $5.8\ kHz/s$, respectively.
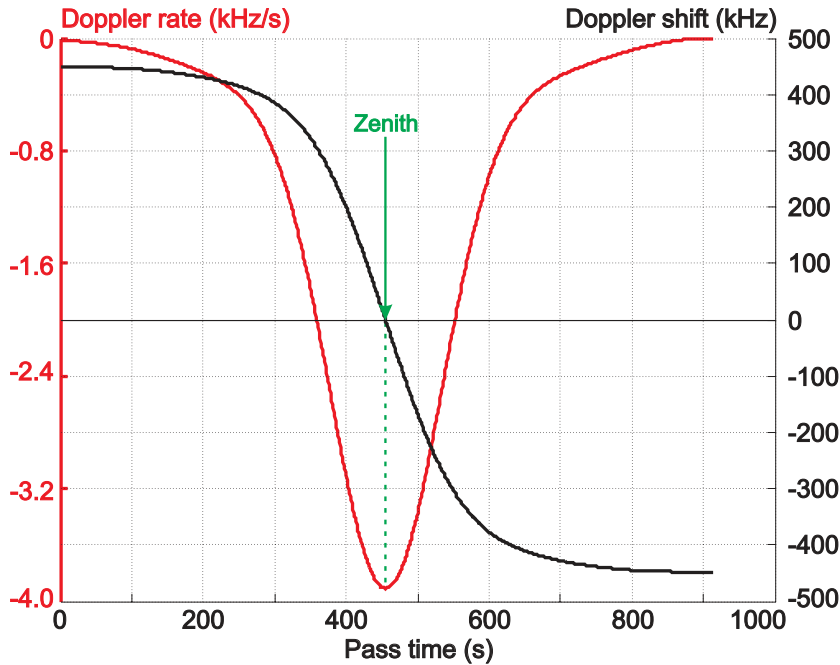
Figure 4.4: Calculated downlink Doppler shift and Doppler rate for an overhead pass

The combination of high LEO spacecraft velocity and the use of Ka band frequencies poses the following challenges:

- Doppler shift detection and rate estimation,

- Doppler shift tracking, and

- Doppler shift compensation.

The solution of these issues at the earth station is paramount not only for the precise power measurement of the satellite beacon signal for the propagation experiment, but also for data communication. Standard VSAT modems require a stable carrier frequency, or they only allow for the tracking of very small frequency offsets (several kHz), as they are occasionally encountered on GEO satellites. Hence these modems cannot be directly employed for Ka band LEO systems, and other solutions must be devised (see Section 4.5.4).

4.1.1.4   Project Completion Time

With only five years development time from the foundation of the CRCSS to the eventual launch of FedSat, time and manpower proved to be an issue for the earth station development. In conjunction with limited funding, capable staff had to be rapidly appointed or quickly trained in the required specialist knowledge. Significant design changes at the space segment also prompted re-designs at the earth station, with some design specifications induced by other CRCSS projects and teams, for example the Ka band earth station interfacing with the BBP and the processing of spacecraft GPS data.

The parallel design of earth station RF hardware, control software and the electro-mechanical system demanded a highly developed systems design approach with great attention to detail. However, with the restrictions of funding and time, several design compromises had to be made, the majority of which later proved to be very reasonable. Some design issues had to be corrected during the deployment and operational phases, which is discussed in detail in Chapter 7.

4.1.1.5   Flexibility

The Ka band earth station's fundamental design aims at maximum flexibility in terms of deployment location, satellite trajectory, IF interfacing and types of experiments. This flexible design can potentially be very helpful for future research teams wishing to develop similar earth stations with only minor modifications to this proven design. Aspects of flexibility include:

- **Deployment:** The earth station has to be designed for mobile deployment, i.e. the indoor and outdoor units need to be easily transportable. The software must support a rapid adaptation to a new location and adjust the look angles accordingly.

- **Satellite trajectory:** The electro-mechanical tracking system must be suitable for all types of satellites and orbits. Since tracking a low-power LEO satellite like FedSat poses the greatest challenge in terms of required tracking velocity and accuracy, it automatically meets the conditions for MEO and GEO spacecraft.

- **IF interfacing:** The modular structure of the RF module must allow for easy interfacing with both commercial and in-house RF hardware and modems, while still providing specialist functions, such as Doppler tracking and compensation. Industry-standard IFs should be chosen in order to facilitate the requisitioning of parts.

- **Support of experiments:** The design must support a variety of maintenance functions and experiments in hardware and software, such as tracking calibration, drive tuning, beacon mode, bent pipe mode, data transmission and bit error analysis; see Section 4.1.2.

These flexibility aspects will be frequently referred to in the remaining sections of this chapter.

4.1.1.6   Commercial vs. In-House Design

As previously mentioned, the considerable financial restrictions for virtually all programs within the CRCSS led to the necessity to develop several components in-house. After great difficulties in simply locating a commercial Ka band earth station capable of LEO tracking, an initial inquiry with one potential supplier revealed a cost of well over US$ 1 million [83], with many customisations still required. Also for the purpose of training and research, it was therefore decided to design the earth station from the beginning, using as many commercially available components-off-the-shelf (COTS). Analogous to the flexibility considerations, this approach involved a lot of systems level engineering, tied in with the procurement of suitable and available parts. In some cases, this required extensive in-house fabrication, costly custom orders from manufacturers, and in the case of the earth station signal processing software, a full development from Assembly code to user interface.

The result of this combination of in-house design and COTS is a state-of-the-art, fast-tracking Ka band earth station prototype for a material value of approximately US$ 250,000 [83].

4.1.2   Spatial Tracking and Operation Modes

Initial plans included several other experiments to be conducted with the Ka band earth station, aside from the propagation experiment. Due to operational and funding changes, eventually only the propagation experiment was carried out. Further illustrated in Chapter 5, the earth station tracking unit, RF circuits and software have the capability for the following maintenance, calibration and experimental modes:

4.1.2.1   Maintenance and Calibration

- *Manual move mode* allows full manual handling and positioning of the pedestal while the brakes are disengaged. This is used for mounting/dismounting parts of the dish structure or for crash recovery.

- *Automatic move mode* allows the pedestal to be directed to a given coordinate by use of the motors. Angular velocities are variable within certain limits. This mode is also used for the precision calibration (levelling) of the spatial tracking system.

- *Simulation mode* allows the testing of the earth station under simulated satellite pass conditions, but without activating the servo motors. This is mainly used for testing of the RF circuits and improvements to software algorithms which do not require spatial tracking.

4.1.2.2   Experimental Operation

For experimental operation, the antenna must first be driven to the "Acquisition of Signal" (AOS) coordinate, from which spatial tracking follows the satellite's trajectory. From this point, the RF circuits and signal processing are active and record the experimental data. After the end of the pass, ("Loss of Signal", LOS), the antenna will return to the stowage position.

- *Positioning move* is used to drive the tracking system to the first coordinate, and after the tracking part back to the stowage position. It is similar to the *automatic move* above, but integrated with and time-coordinated to the tracking moves below.

- *Time-coordinated positional move* allows the tracking system to point at pre-defined coordinates along the satellite trajectory. This mode is used only for a comparison of NASA and GPS timing (see Section 5.2.3).

- *Beacon mode* switches the earth station to receive-only, Doppler shift tracking and power measurement operation. This is the mode predominantly used for the propagation experiment.

- *Carrier bent pipe mode* enables the transmission of a Doppler pre-compensated carrier signal on 29.93 GHz, in addition to the Doppler shift tracking and power measurement functionality of the beacon mode.

- *Data bent pipe mode* engages either the VSAT modem or the BBP for data transmission of a Doppler pre-compensated, QPSK modulated signal on 29.93 GHz. On the downlink, a pre-calculated Doppler shift is used to feed the compensated receive signal back into the VSAT modem or the BBP. This mode is intended for bit error rate measurements via FedSat's bent pipe mode or on-board processing capabilities.

4.2   System Integration

A broad overview of the earth station's realisation shall be provided at this point to facilitate the understanding of the entire system. Each of the modules and components is described in greater detail in the following sections of this chapter. In order to optimise its operation and serviceability, the earth station has been subdivided into two separate units (Fig. 4.5).
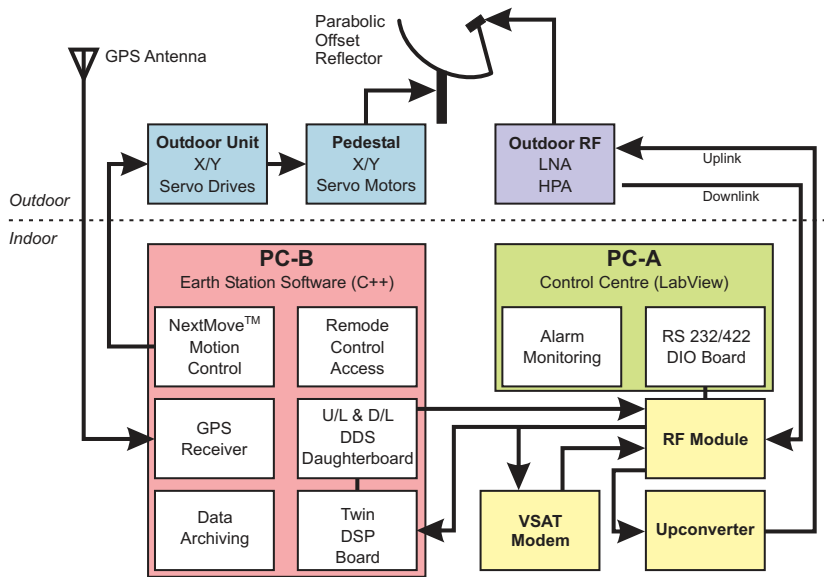
Figure 4.5: Functional block diagram of the UTS earth station

4.2.1   Indoor Unit

While some components are required to be located near the antenna to minimise signal loss or cable length, most of the RF equipment and control electronics are located in the indoor unit for better environmental protection and for security purposes. The indoor unit consists of a compact 19" rack on wheels and contains the following modules (from top to bottom, see Fig. 4.6):

- The *Direct Digital Synthesizer (DDS) & Power Supply Module* houses various power supplies for the RF electronics and circuits contained in the indoor unit, as well as two autonomous DDS boards used in the original earth station design. (The latter were later replaced by two DDS daughter boards, see Section 4.6.3.)
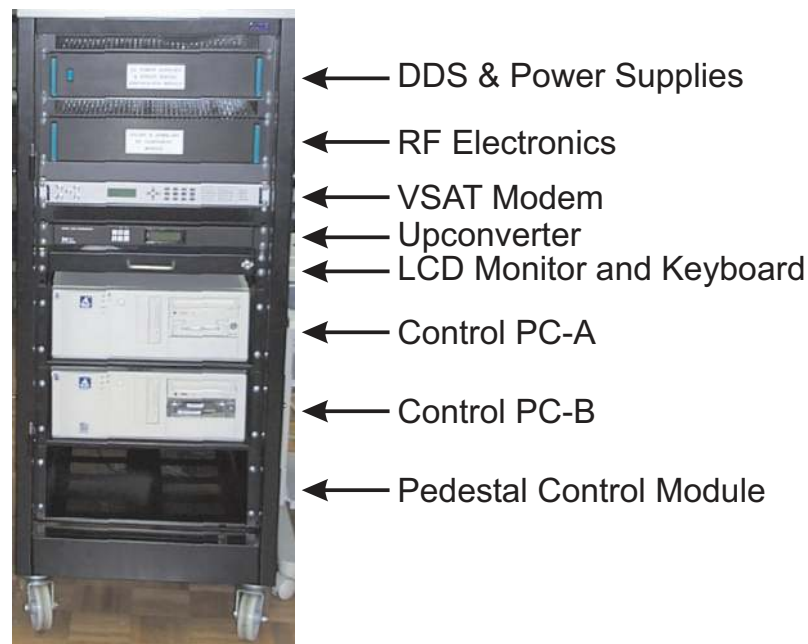
Figure 4.6: The indoor unit of the Ka band earth station

- The *RF Module* contains the IF conversion circuits with mixers, amplifiers and filters, as well as the reference oscillators, programmable attenuators and RF switches, Fig. 4.7. Since each individual functional component is sufficiently shielded (with the exception of the case mentioned in Section 5.3.7), uplink and downlink circuits can be accommodated together in the same rack. All controls, inputs and outputs are interfaced to the other modules via connectors on the rack's back plane, and the use of SMA connectors for internal connectivity makes maintenance, measurements and fault-finding more convenient.

- The *VSAT Modem*, originally intended for the proposed data communication experiments with FedSat, generates the beacon signal for carrier bent pipe mode. It can be completely remotely controlled and monitored from the software on PC-A.

- The *Upconverter* is employed to convert the uplink IF signal to L band. It features low phase noise and a flexible input frequency range, which is required for the 60 MHz (instead of 70 MHz) signal. It is remotely controlled from the software on PC-A.

- *LCD Monitor and Keyboard* are incorporated into the rack design so that no external devices are required for the earth station operation. The keyboard and screen can be switched between the two control PCs.
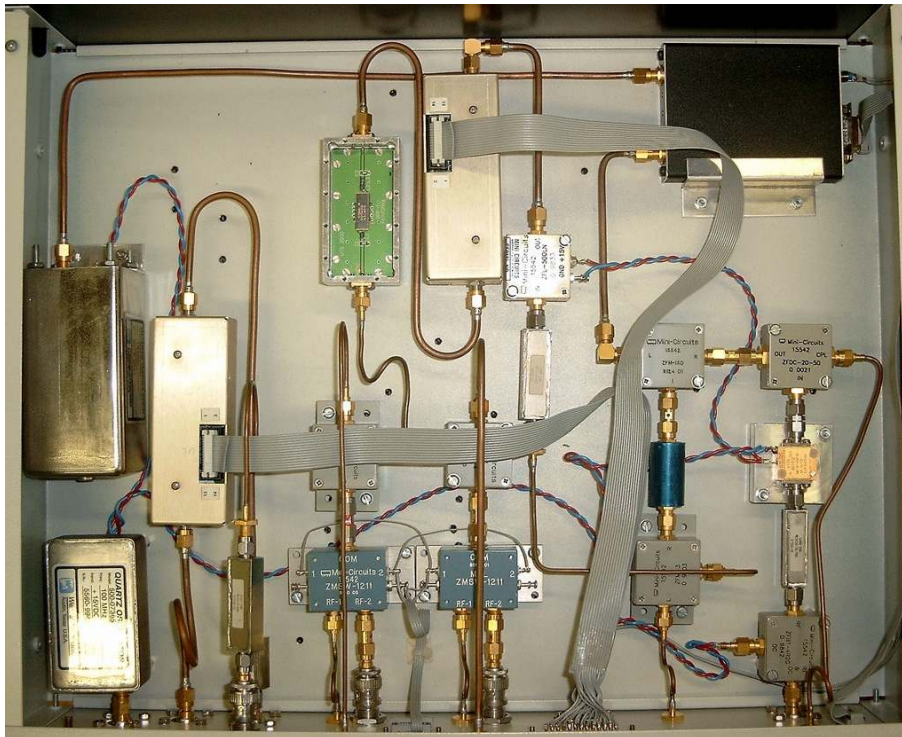
Figure 4.7: Photo of the RF Module

- *Control PC-A* is dedicated to remotely controlling the settings on the VSAT modem, upconverter, RF switches and attenuators via serial interfaces and digital I/O lines. It also monitors faults on various components, including the outdoor unit and the pedestal. The software on PC-A is programmed in LabView™.

- *Control PC-B* form the centre of the earth station and accommodates the spatial control and the digital signal processing (DSP) functions. The motion controller, GPS and DSP/DDS cards are connected via PCI slots and controlled by the earth station software, written in C++ and Assembly code.

- The *Pedestal Control Module* provides connectivity from the motion controller card in PC-B to the outdoor unit and pedestal. It carries various breakout boards for the signals between them, for example analog servo drive voltages, resolver and position encoder signals and digital switchlines. It also supplies power to some of the components in the outdoor unit.

The indoor unit requires a considerable amount of connections to the outdoor unit, both RF, analog and digital. High-quality RF cable and connectors are used to reduce cable losses over the distance of approximately 25 metres, which carry the L band uplink

and downlink signals, a 100 MHz reference oscillator signal to the LNB and connect to the GPS antenna. Over 60 other digital and analog sensor, fault and control signals are also exchanged via shielded multi-core cables and high-density connectors.

4.2.2 Outdoor Unit

The outdoor unit can be subdivided into the servo drive enclosure and the tracking pedestal. The enclosure contains the two servo drives, several breakout boards for the cables interfacing it with the indoor unit and the HPA power supply. It is located near the tracking pedestal for minimum power cable length between the drives and the motors. The tracking pedestal comprises the mounting base, the motor housing, the support structure for the reflector and the feed assembly and the external RF electronics (LNB, HPA and OMT). In Fig. 4.8, the drive enclosure can be seen mounted on a wall near the pedestal base.

Each of the indoor and outdoor unit components will now be explained in greater detail in order to demonstrate the issues arising out of the design requirements.

4.3 Antenna and Reflector

After solving the parametric, iterative optimisation problem from above [84], the final downlink budget (C/N_0) can be devised (Table 4.1). It now incorporates a specific antenna gain, as well as all other losses that need to be considered. Due to the very low spacecraft transmit power, this is an example of a downlink-limited earth-space-earth communication system, hence the receive antenna gain is the most important one to consider. The following result has been attained for the UTS earth station case as a compromise of physical reflector size, gain and required tracking accuracy, with cost as an additional factor.

4.3.1 Reflector Type

After the required gain has been determined, the antenna type must be selected. Due to the very high gain figure of almost 45 dBi, the only viable solution is a classical parabolic reflector with a feed horn in its focal point[1]. A patch antenna solution with similar gain is not considered here due to open issues with cross-coupling between elements in a very large array, as it would be required for this application.

---

[1]The term ''antenna" is commonly used to represent an assembly of reflector, feed and associated waveguides, and shall collectively refer to those components in this work.

Figure 4.8: Outdoor unit with drive enclosure and pedestal

Quantity	dB
Spacecraft transmit power	−6.0
Spacecraft antenna gain (average)	5.5
Free-space loss (zenith)	−176.5
Pointing loss	−2.0
Antenna moisture loss	−0.5
Atmospheric loss	−2.4
Receive system temperature	−25.2
Receive antenna gain	44.9
Boltzmann's constant $-[k]$	228.6
$[C/N_0]$ (dB Hz)	66.4

Table 4.1: Downlink Carrier-to-noise ratio calculation

The feed horn in the focal point of the reflector needs to be mechanically supported by rigid structures, for example tubular metallic stays. At Ka band, the dimensions of these structures cause not only undesired blockage, but also multipathing effects, which lead to losses and depolarisation. Therefore an elliptical derivative of the full, circular parabolic reflector is preferred so that neither the feed horn nor the support structure are in the path of incident waves from the spacecraft. The geometric derivation of the offset parabolic reflector is depicted in Fig. 4.9 [85].
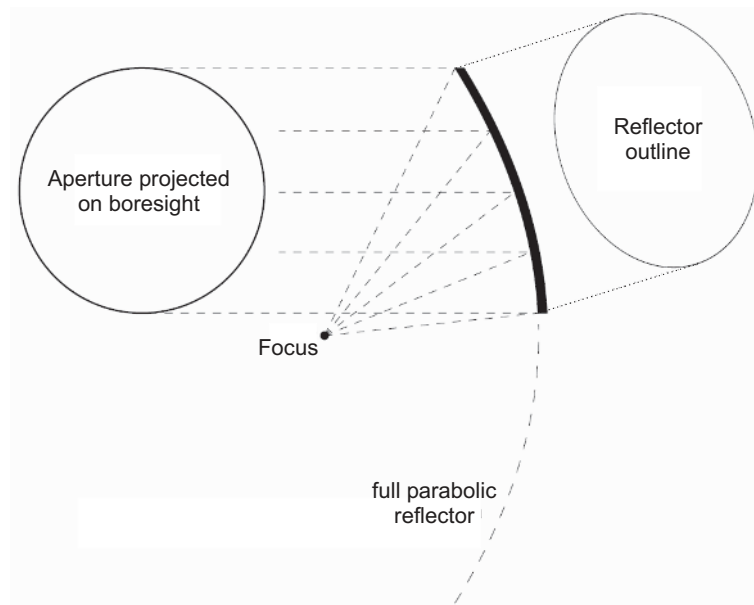
Figure 4.9: Boresight aperture and physical outline of a parabolic offset reflector

Fig. 4.10 illustrates an important quantity, the offset angle φ. Relative to the full parabolic reflector, *all* incident waves on the offset reflector are tilted by the angle φ in the vertical plane. This leads to the experimentally important conclusion that when the rim of an offset reflector is mechanically horizontal, its electrical boresight direction is actually tilted by the angle φ. The significance of this fact will be shown in Section 5.2.

At Ka band wavelengths (1 cm transmit, 1.5 cm receive), the coherence of all incident waves can only be achieved with great precision. The surface accuracy of the entire reflector with a 1.2 m diameter needs to be less than one mm [86]in order to attain a good efficiency, minimise side lobes and reduce cross-polarisation. Any mechanical flexing on the reflector structure due to gravity or wind should also be prevented, especially when in operation. The position of the feed horn in the focal point is also precisely determined by the design. These considerations demonstrate that the calculation, practical design and manufacture of a large reflector at Ka band is very challenging and not possible in-house.
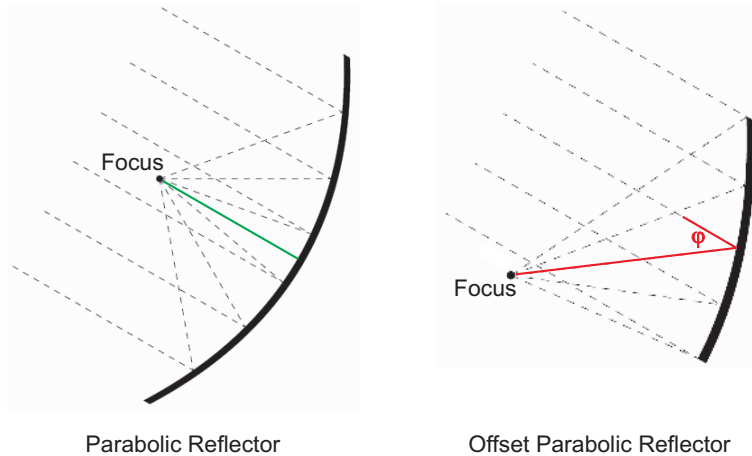
Figure 4.10: Illustration of the offset angle φ

Initially, a commercial antenna system as required had been unavailable, so that the design and manufacture of an antenna according to UTS specifications was contracted out to the Prodelin Corporation (now General Dynamics). Today, this 1.2 m reflector with Ka band specifications is incorporated in their standard product line as "Series 3120" [87], and further antenna specifications can also be obtained from this source.

However, the Prodelin dish design is not specifically manufactured for use on a tracking pedestal, although the very rigid SMC fiberglass mould with a reflective layer on the surface is very lightweight, and is therefore certainly suitable for this purpose. Unfortunately, the standard feed horn support structure is built with a GEO VSAT system in mind and therefore very heavy. This topic is dealt with in Section 4.9.1. Fig. 4.11 shows the reflector from underneath on a laboratory test structure, and the LNA and the HPA mounted on the original, heavy support arm.

The manufacturer-supplied radiation patterns, measured at the intended frequencies of operation, are reproduced and complemented in Fig. 4.12. The transmit gain is shown in two orthogonal planes, but shows no significant differences in the pattern. The uplink HPBW of 0.58° and the strong side lobe suppression meet ITU standards for GEO VSAT operation, however for LEO use, this is only of bureaucratic interest for ITU licensing issues. A 22.6° feed offset angle φ is quoted by the manufacturer.

4.3.2 Environmental Issues

Besides technical specifications, there is a considerable number of environmental considerations that need to be taken into account:

Figure 4.11: 1.2 m Ka band antenna system under laboratory test

- **Wind load:** The physical size of the dish raises the issue of wind load which could potentially pose a problem, given the exposed location of the tracking pedestal. On a fixed mount, the reflector's operational and survival ratings are satisfactory, but the transfer of the wind force to the electro-mechanical system is a concern, especially when unsupervised. On an experimental basis, it has later been considered the most practical solution to stow the dish in a load-balanced, slightly tilted position.

- **Surface wetting, rain:** Reflector surface wetting can be the cause of several dB of signal degradation on Ka band, which has been the – occasionally controversial – topic of several publications [88–90]. While antenna wetting cannot be completely avoided, the active surface is coated with a highly hydrophobic paint so that droplets immediately run off the tilted dish without leaving significant amounts of moisture behind. Only when the reflector is positioned close to horizontal, it is possible that rainwater can briefly collect inside the concave shape. But since the antenna moves fairly quickly at near-overhead passes, any possible effect on the measurements is most likely short-lived and negligible under the then probably heavy rain storm conditions prevailing at that time. The feed horn is the only vulnerable part, and although it is sealed by a clear, RF-transparent plastic cover, it is possible for droplets to accumulate on the surface.

- **UV exposure, pollutants:** Most hydrophobic coatings are known to degrade

Transmit (uplink)

Normalised Gain (dB) @ 30 GHz

49.5 dBi

vertical

49.5 dBi

HPBW = 0.58°

vertical

Azimuth (deg)

Elevation (deg)
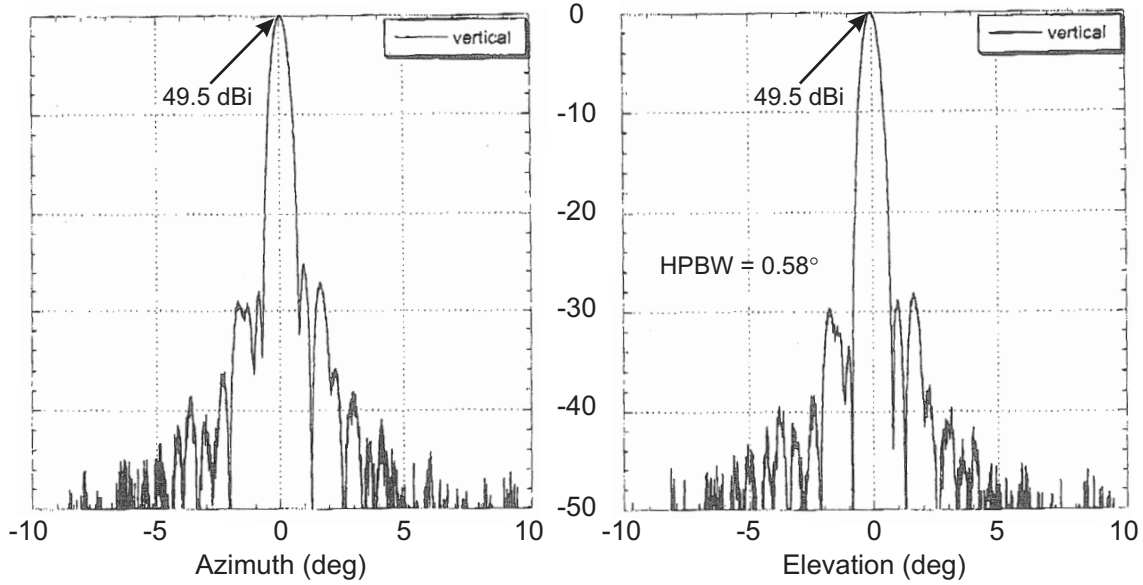
Receive (downlink)

Gain (dBi)

44.88 dBi

HPBW
=0.92°

Azimuth (deg)
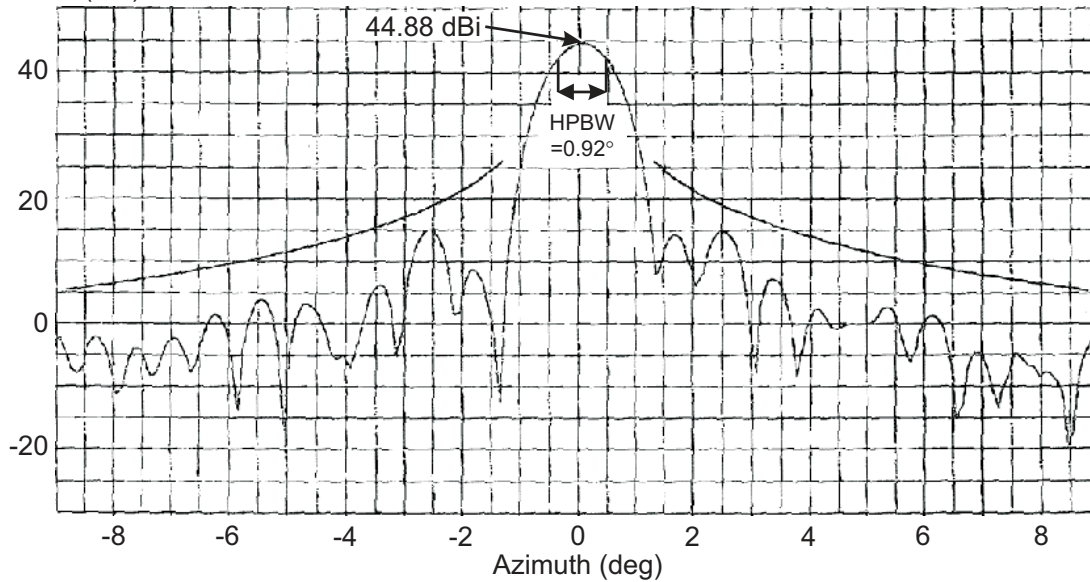
Figure 4.12: Transmit and receive radiation patterns of the 1.2 m Ka band earth station antenna system (Prodelin)

slowly over time [86]; a process which is accelerated through extreme exposure to ultraviolet (sun) light and through airborne pollutants. However, neither of these factors is believed to be significant at the selected location, and irradiation energy calculations conducted for the given latitude are well below the specified limits. No chemical pollutants are known to be present in the area, however it will be shown later in Section 7.1.7 that bird excrements can have a very drastic effect on the surface.

Other ancillary RF components attached to the feed horn are incorporated in Section 4.5.2.

4.4 Mechanical Subsystem

Together with the antenna and the Ka band components, the mechanical subsystem is one of the most expensive components of the earth station. As previously mentioned, tracking stations with similar capabilities are commercially sold at multiples of the development budget, hence posing great challenges in the design and manufacture.

4.4.1 Development of a Tracking Pedestal

Following the conclusions from the keyhole problem explained above, other axis arrangements were investigated. The research into the advantages and disadvantages of certain tracking pedestal systems for the UTS CRCSS is covered in [82] in great detail, and only the final result shall be presented here. In principle, instead of the azimuth and the elevation arrangement, the two axes are orthogonally mounted on top of each other, forming an "elevation-over-elevation" cross. In reference to a Cartesian coordinate system, it is termed X-over-Y or X/Y, with the top (X) axis pointing in the east-west direction and the bottom (Y) axis pointing in the north-south direction as in Fig. 4.13. Contrary to the Az/El definitions, there is no clear convention for positive or negative values in the X/Y coordinate system. The directions indicated here are arbitrarily chosen and consistently applied throughout the design process. The origin is defined as both axes being in a horizontal position (zenith-pointing).

An X/Y pedestal is more suitable for LEO tracking because through coordinate transformation [82], the keyhole is moved to two opposite locations on the horizon where the satellite moves at its lowest velocity, relative to the earth station. While it is not possible to fully eliminate the keyhole problem for full hemispherical coverage, the X/Y arrangement moves it to more manageable locations. In addition, when high dynamics are required
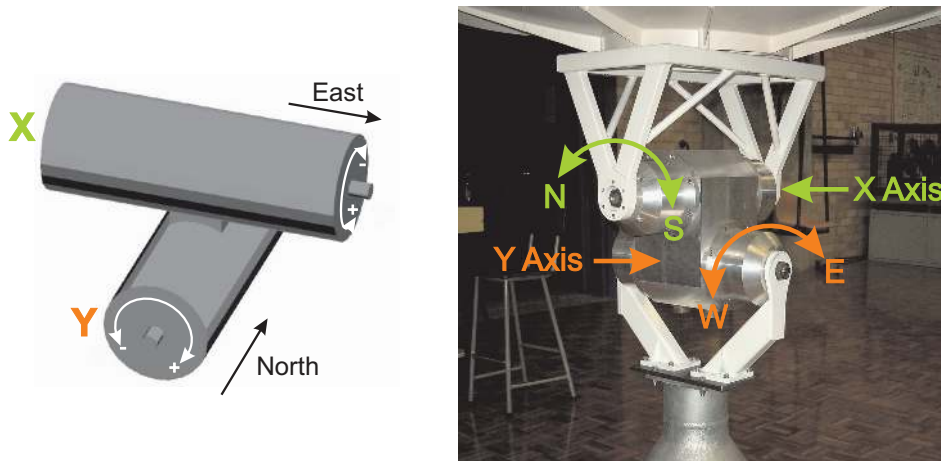
Figure 4.13: Graphic of the X/Y mount, also indicating the coordinate system definitions (left); the finished tracking system in a laboratory test setup (right)

(i.e. at near-overhead passes), the pedestal actually operates at its optimum, mid-range point. Particularly for FedSat's orbit and experimental objectives, the tracking velocities required on each axis are well within achievable limits.

It should be pointed out that the pedestal underwent several iterations and design improvements in the aspects of machining, ease of assembly/disassembly, waterproofing, weight, stiffness, external connections and accommodation of motors before the final in-house pedestal prototype was ready for deployment, as illustrated in Fig. 4.14. It was entirely designed and manufactured at UTS, and completed in 2002 [91]. The bottom (Y) axis is attached to two brackets, which are bolted to the pedestal base. When activated, the Y axis rotates inside these brackets, covering approximately $-87.5° \ldots + 87.5°$ from west to east and also moving the entire top (X) axis with it. A rigid frame is attached to the ends of the X axis shafts, covering approximately $-89° \ldots + 89°$ from south to north and clearing the structure underneath when activated. The antenna assembly is mounted on top of the frame and further secured with the four rigid stays to minimise flexing (not shown in the drawing).

It is apparent that the torque on the Y axis in generally higher, since it also has to bear the turning moment of the X axis *and* the moment of the antenna assembly. The X and Y alignments along the E-W and N-S directions is purposely chosen, since most of the movement occurs on the less critical north-south axis due to FedSat's near-polar orbit. Contrary to the Az/El pedestal, in X/Y coordinates, no tracking velocity ever exceeds the maximum value of $0.534°/s$ for practical FedSat passes (from Section 4.1.1.1). Diligent calculations have been made to determine the maximum torque requirements for
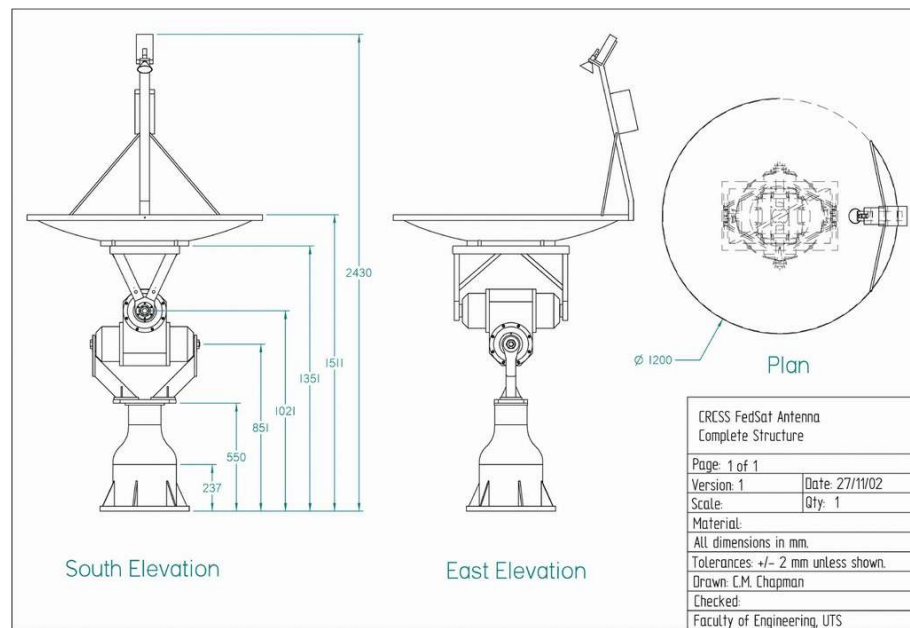
Figure 4.14: Basic technical drawing of the final X/Y pedestal design

worst-case situations and optimised for the most likely pass scenarios.

4.4.2 Electro-Mechanical Components and Servo Drives

Both axes are driven by identical, brushless AC servo motors mounted inside the X/Y housing, therefore eliminating the need for costly pivot joints. A search for readily available, commercial solutions ended with the selection of the high-end Baldor BSM product range, which also provides a wide range of complementing accessories, such as gearboxes, encoders, servo drives and PC control systems. The chosen motor type, model BSM90B-275AA provides 4.3 Nm continuing torque at 6000 rpm and 12.3 Nm peak torque [92]. The motor housing also includes a resolver for position information and a mechanical brake on the output shaft.

Due to the tight pointing accuracy requirements and the restricted space inside the housing, a very low backlash gear box with a small form factor had to be selected to convert the revolutions of the motor shaft into the required angular velocities, which lie in the order of only several degrees per minute. In order to achieve this low velocity at high torque, a 2-stage, a planetary gearbox with a total ratio of 100:1 (two cascaded stages of 10:1) was employed. Compared to standard gearboxes of various types, these planetary gearboxes provide a low backlash (7 arc min) even at this high conversion ratio, however the torque transmitted through the 100:1 gearbox is quite considerable at several

hundred Nm (at 85% efficiency). It will be shown later that the unavoidable compromise in weight, tolerances, cost, high conversion ratio and robustness can potentially lead to a catastrophic failure of gearbox elements under some conditions. The Baldor motor and gearbox are shown in Fig. 4.15.

AC Servo Motor   Planetary Gearbox
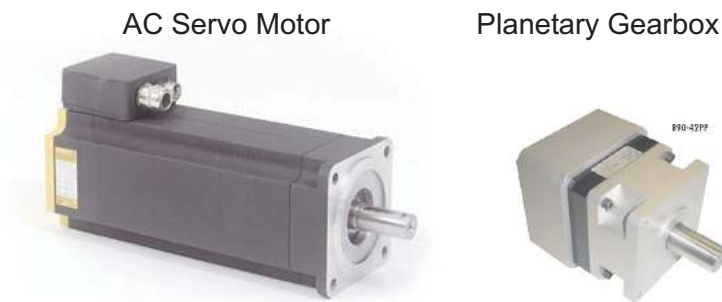
Figure 4.15: Baldor AC Servo Motor and Planetary Gearbox [92]

The output shaft of the gearbox protrudes through the housing. In case of the X axis, the reflector frame is securely mounted on it by means of a keyless bushing (Trantorque™). For the Y axis, the driven shaft is attached to one of the fixed brackets that connects to the pedestal base. On the other side on the housing on the same axis, a free-spinning (non-driven) shaft provides support in both cases and has a shaft encoder attached on the inside for positional feedback. A schematic diagram of the drive train is shown in Fig. 4.16, also including incoming and outgoing signal connections. This setup is identical for both axes.

Two programmable servo drives (Baldor FlexDrive™ FD2A05TB) supply the electrical power to the motors. The modules contain the one-to-three phase AC conversion power electronics, encoder/resolver inputs and the control circuits. The drive is initially configured to match the attached motor through a built-in RS-232 interface, but it must subsequently also undergo precise load tuning to set the parameters of the motor-resolver control loop correctly (see Section 4.6.2.1). The software provided by the manufacturer for this purpose proved to be more suitable for constant-load, high rpm applications, hence other tuning strategies had to be pursued.

Each drive is also connected to the control terminal of the earth station, which provides the position and velocity commands to the drives through voltage level signals. All resolver and feedback encoder signals are not only utilised by the drives, but also by the control terminal for dynamic pointing accuracy improvements.
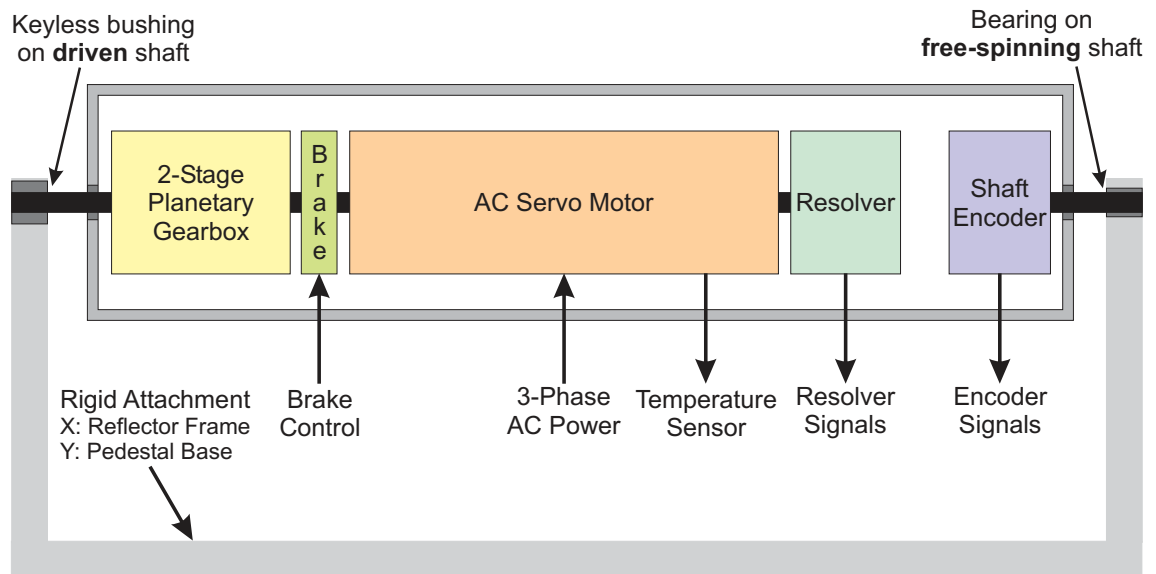
Figure 4.16: Schematic diagram of the power train, brake, resolver and encoder in the housing

4.4.3   Feedback Encoders

As indicated in Fig. 4.16, the tracking unit relies on high-resolution, 5000-line quadrature feedback encoders, effectively reducing the positional uncertainty of the tracking system to less than 0.02° after calibration. Although the motors themselves contain built-in, 1000-line quadruple motor encoders (also termed "resolvers"), which are attached directly to the motor shaft, their accuracy and location on the *input* side of the gearbox was deemed insufficient for the required precision. Since there is a stiff connection between the driven and the free-spinning shafts on each axis, the position information provided by the feedback encoder rather than the resolver is considered to be the *true* position. This is an important realisation that has allowed the author to improve the pointing accuracy significantly over the initial design, see Section 4.9.2.

The initial earth station design included the use of *relative* encoders that can be electronically reset. In conjunction with the problems outlined in Section 4.4.4, this later proved to be an unfortunate choice over the use of absolute encoders, which will be further considered in Section 7.2.4.

4.4.4   Antenna Position Calibration

Previous sections have demonstrated the great diligence that has been taken in keeping mechanical tolerances and positional uncertainties as low as possible. Link budget require-

ments dictate a *required* tracking accuracy of less than 0.3° (cross/long), and a *desired* accuracy of 0.1°; the latter therefore constitutes the official design specification. Any positional errors have to be within these while the antenna is in motion, or the signal may be lost. Without the facilities to confirm the manufacturer's specifications for the reflector beamwidth and feed offset angle, the exact supplied values were taken into account in the calculations.

As previously demonstrated, the tracking pedestal has been designed for the reflector to lie perfectly horizontal ("level") on a zenith-pointing mounting frame. For an east-west aligned X axis and the feed assembly mounted on the northern reflector end, this would mean that all *X axis angles* only would be offset by -22.6°. This is a very important realisation that needs to be taken into account in all tracking coordinate calculations (see Section 4.6.5). As a further consequence, the acquisition elevation angle for satellites rising directly from the north was shifted to 22.6° due to mechanical constraints.

In order to achieve the desired tracking accuracy, the reflector position must be calibrated to a known reference. While the site-specific orientation of the pedestal (azimuth declination) is dealt with in Section 4.8.2, the procedure employed to attain a horizontal level as precisely as possible is discussed here.

Initially, the mounting frame was equipped with an electronic inclinometer (EZ-Compass-3, [93]), providing tilt angle information (roll/pitch) via a serial interface to the earth station control software. After an initial calibration by means of surveying, a fully automatic reflector levelling procedure was implemented in the software, allowing the pedestal to return to its calibrated position after a pass and after maintenance manoeuvres. While the tilt accuracy of ±0.02° and the short-term repeatability were fully sufficient for the intended purpose, the long-term variability over days was in the order of several tenth of degrees and therefore unacceptable. Attempts have been made to improve the long-term repeatability, but eventually, the use of the inclinometer for precise automatic levelling was abandoned. Due to the use of relative instead of absolute position encoders, the calibrated level position is lost once the power is turned off, hence a reliable value could not be obtained from here either.

It should be mentioned that there are commercially available precision levelling systems with excellent accuracy and repeatability, for example transducer-based sensors, however the cost of these systems was prohibitive. Since the earth station had already been deployed at this stage, the use of a simple gravity-based spirit level as a temporary replacement was contemplated. Surprisingly, the high-quality Stabila spirit level at hand was specified with a tolerance of only 0.029°, equivalent to 0.6 mm imbalance from one

side of the rim to the other [94]. This figure is in the required order and is very accurately repeatable. Trials have shown that deviations from the horizontal plane of $0.01°$ are easily detectable in the vial by the human eye. In addition, no initial, survey-based calibration is required, hence this time-consuming procedure is also obsolete. A clear disadvantage is the fact that the use of a spirit level would require human intervention. A fully automatic mode, as intended, would not be possible. Balancing these points, the decision was made to proceed with the spirit level in order to keep the earth station operational, despite the disadvantage of a limitation to supervised operation. Also, this practice would require two people - one to take the measurements directly at the reflector, the other manually executing the corrective measures at the earth station terminal.

4.5 RF Electronics Subsystem

While standard upconverters, downconverters and modems are commercially available for Ka band frequencies, their inability to deal with FedSat's Doppler shift tracking requirements and the focus on the beacon measurements led to the decision to develop a customary RF electronics subsystem for the earth station [79]. While some commercial devices are still used in the earth station, such as the VSAT modem and the upconverter, most IF-stage modules were designed from single-function components like mixers, amplifiers and filters. For flexibility and serviceability purposes, modular components equipped with SMA connectors were employed wherever possible. This section provides an overview of the RF hardware on Ka band and on the intermediate frequencies, as well as the concept of rapid acquisition, open-loop Doppler shift tracking aided by a novel algorithm.

4.5.1 Overview

The description of the earth station's RF subsystem can be subdivided into three major areas: the Ka band hardware, the frequency conversion circuits for uplink and downlink, and the devices and software required for open-loop Doppler shift tracking and compensation. These some of these components are directly computer-controlled, which is further described in Section 4.6.4. A commercial Vitacom M4000 variable rate VSAT satellite modem serves as both the source of the QPSK modulated transmit signal and of a pure carrier (beacon). It was also originally intended to receive and demodulate its own bent pipe mode signal from the spacecraft for bit error rate testing. Since the ITR-developed BBP uses a proprietary protocol and synchronisation, communication with the BBP on-board FedSat would have also required a BBP in the earth station, in addition to the

VSAT modem. Provisions for its inclusion have been made in the UTS design, but this direction of the project was not further pursued by the CRCSS.

4.5.2 Ka Band Hardware

In addition to the previously described Antenna subsystem, the Ka band hardware consists of the LNA with built-in downconverter to L band (LNB), the block upconverter (an HPA including an upconverter from L band to Ka band), the diplexer with polarising circulator (orthomode transducer, OMT), the feed horn and connecting waveguides (Fig. 4.17). In order to avoid losses, LNB and HPA are mounted directly on the antenna structure. Unlike for linear polarisation used in other propagation experiments, separating co- and cross-polar components in circular polarisation requires significantly more hardware and complicates the system further, hence this option was not implemented and only the co-polar component is considered.
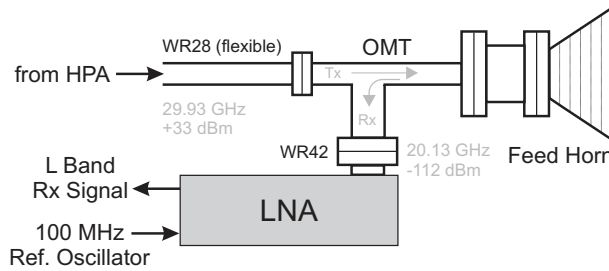
Figure 4.17: Earth station Ka band hardware assembly

The aperture of the corrugated feed horn is specifically designed by the manufacturer for operation with the dimensions of the supplied reflector, and placed at a certain focal length in the phase centre of the reflector. It attaches to the circular polarising port of the OMT, or polarisation diplexer, that *orthogonally* separates LCP receive and RCP transmit signals into a WR42 waveguide (20.13 GHz downlink) and a (WR28 waveguide (29.93 GHz uplink) at an isolation of >30 dB [87]. The WR42 LNB input flange is directly connected to the OMT for minimum signal attenuation, while the other port extends to the HPA via WR28 waveguide. Flexible waveguide was initially chosen to allow for optimum placement of the HPA on the feed assembly arm close to the OMT, however the location of the HPA had to be revised later (see Section 4.9.1). All flanges and connectors have been carefully waterproofed to avoid internal corrosion of the waveguides or the components.

Both the LNB and the HPA are supplied by NewTec Cy [95] [96]. The LNB requires an 100 MHz reference signal in order to achieve very low phase noise with its internal

local oscillator, which is supplied externally. Important specifications are summarised in Tables 4.2 and 4.3.

Quantity	Value
RF input range	19.7-20.2 GHz (WR42)
IF output range	950-1700 MHz (N)
Equiv. noise temperature	150K @ 23°C
Noise figure	1.8 dB
Gain	50 to 65 dB
External reference oscillator	100 MHz
Weight	0.7 kg

Table 4.2: Selected Low Noise Block (LNB) specifications

Quantity	Value
IF input range	1000-1500 MHz (N)
RF output range	29.5-30.0 GHz (WR28)
Gain at saturation	73 dB
Saturated output power	+33dBm
Internal LO frequency	28.5 GHz
Weight	2.0 kg

Table 4.3: Selected solid-state High Power Amplifier (HPA) specifications

4.5.3 RF Circuit Implementation

The selection of specific intermediate frequencies for uplink and downlink paths was dominated by the frequency range of the other COTS equipment, such as LNB, HPA, upconverter and VSAT modem. In addition, the Doppler frequency compensation circuits were incorporated according to suitable frequency range specifications of the DSP board and the DDS daughter boards. The final IF of 70 MHZ is jointly used for both the Ka band propagation and the data communication experiments to avoid a further downconversion. A simplified downlink block diagram illustrating the significance of various IFs and the principle of Doppler shift compensation is shown in Fig. 4.18. A detailed block diagram, including reference power levels and manufacturer part numbers (predominantly procured from [97] and [98]), can be found in Appendix A.

The internal 18.6 GHz LNB LO is slaved to an external 100 MHz reference oscillator with a very low phase noise. Following amplification and downconversion to the 1st IF,
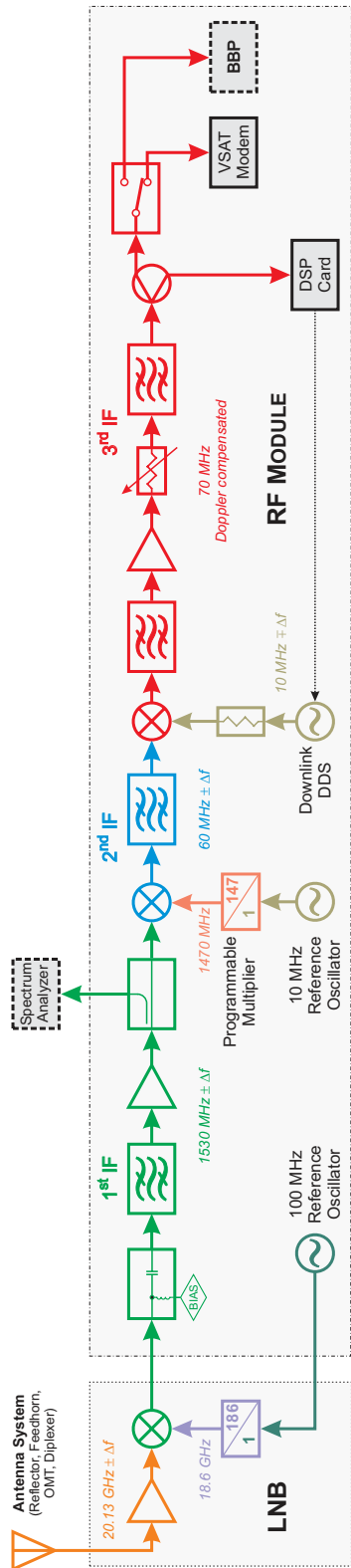
Figure 4.18: Simplified downlink RF block diagram of the Ka band earth station; the coloured sections represent different intermediate frequencies.

the L band signal is filtered and amplified. A 20 dB coupler provides a signal observation point at 1630 MHz for an optional external spectrum analyser, which is very useful for the immediate verification of the presence of a Doppler-shifted signal during a satellite pass. Considering the VSAT modem's standard input IF and the DDS's resolution relative its centre frequency, the 2nd IF was chosen at 60 MHz. A 1470 MHz signal is derived from a low phase noise 10 MHz local oscillator so that mixing results in the desired 2nd IF of 60 MHz. Followed by filtering, the variable 10 Mhz DDS compensation signal is USB mixed with the still Doppler-shifted input, arriving at the 3rd IF of 70 MHZ. A wide bandpass filter is followed by a remotely programmable attenuator, which allows the adjustment of the IF power levels to suit the dynamic range of the modem. A narrow 1 MHz SAW filter provides the input signal to the VSAT modem and the DSP card. The procedure by which this *stable*, fully Doppler-compensated signal is achieved through a DSP algorithm implementation and the DDS is described in Section 4.5.4.

For data or beacon bent pipe mode only, the uplink path is used. Here, the source signal essentially follows the reverse method (see block diagram in Fig. 4.19): The 70 MHz pure carrier or QPSK modulated data signal is mixed with a separate, DDS-generated compensation signal. The DDS' *inverse* Doppler offset frequency is precisely pre-calculated so that the uplink signal is fully compensated for the Doppler shift perceived at the spacecraft, hence resulting in a frequency-*stable* input to the spacecraft Ka band payload.
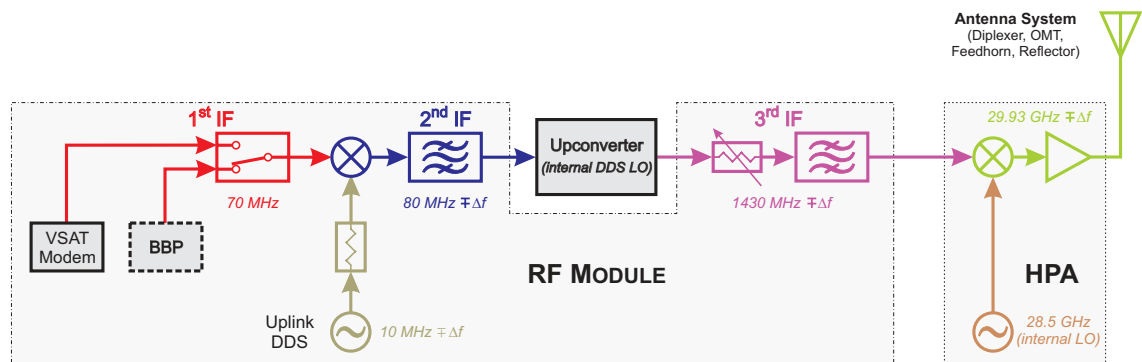
Figure 4.19: Simplified uplink RF block diagram of the Ka band earth station

Referring back to the UHF payload block diagram in Fig. 3.11 and particularly to the path labelled "Ka band bent pipe mode", it is the narrow 1 MHz bandpass filter that requires these pre-compensation measures because the Doppler-affected uplink signal must stay within its bandwidth. A commercial Satellite Systems Corporation programmable upconverter (Model 5420) brings the 80 MHz (2nd IF) transmit signal to the 3rd IF of 1430 MHz. Again, a programmable attenuator provides the opportunity to match the IF

power level optimally to the required HPA input level. Mixed with the internal LO of the block upconverter, the signal finally arrives at the desired Ka band transmit frequency of 29.93 GHz, plus/minus the inverse of the calculated uplink Doppler shift.

Some of the RF components mentioned in this section are dynamically configurable and therefore controlled by software, for example the attenuators, the multiplier for the 2nd Rx IF LO and the two DDS. While the attenuators and the multiplier only require calibration once after deployment, the DDS are very frequently updated, which is further explained in the following section.

4.5.4 Doppler Shift Tracking and Compensation

As outlined in the requirements, the detection of and compensation for uplink and downlink Doppler shifts is one of the key objectives of the earth station development. With today's availability of powerful DSPs, it is reasonable to dedicate this task to specialised hardware, which in turn drives DDS and other RF components. As shown in the previous section, this concept has been realised in the design of both the uplink and the downlink RF paths.

However, accounting for the Doppler shift is not the only uncertainty that must be considered. When using the spacecraft's Ka band transponder system, up to four Ka band oscillators are active: one in the transmitting earth station, and two onboard the spacecraft, and one in the receiving earth station. Each of these oscillators is independently subject to ageing or frequency drifts caused by a change of the ambient temperature. Since FedSat is subject to cyclic heating and cooling on each orbit, this effect is rapid and not negligible. For the earth station's relatively temperature-stable environment, an oscillator tolerance of $\pm 10^{-6}$ is a reasonable assumption [96]. The two spacecraft Ka band oscillators are specified with $\pm 5 \cdot 10^{-6}$ over a temperature range of $-20 \ldots +65°C$, meeting military specifications [99]. In comparison to the up to four Ka band LOs, depending on the operation mode, all other earth station or spacecraft LO drifts are negligible. Table 4.4 summarises the possible LO drifts to demonstrate the order of frequency uncertainty.

Thus, even if the Doppler shift is known a-priori and compensated for, there still is a frequency uncertainty range up to approximately ± 3 MHz. Additionally, this offset may also slowly vary with time, hence a simple frequency acquisition strategy with subsequent pre-calculated compensation would not be precise enough. For this reason, an open-loop or "blind" tracking approach was sought, which locks onto a present signal within a defined acquisition range and tracks it without the knowledge of the Doppler shift.

Local Oscillator	Nominal frequency	Tolerance	max. Drift
Earth station transmitter	28.50 GHz	10^{-6}	± 285.0 kHz
Spacecraft receiver	28.43 GHz	$5 \cdot 10^{-6}$	± 1421.5 kHz
Spacecraft transmitter	18.63 GHz	$5 \cdot 10^{-6}$	± 931.5 kHz
Earth station receiver	18.60 GHz	10^{-6}	± 186.0 kHz
Sum of the absolute offsets	(worst case)		± 2824.0 kHz

Table 4.4: Frequency uncertainty range resulting from Ka band oscillator drifts

This challenge has led to the development of a very efficient acquisition and tracking algorithm for single-tone frequencies at the UTS CRCSS, which is capable of blind tracking with high accuracy. The performance is particularly notable at low signal-to-noise ratios at a margin of 0.0625 dB above the theoretical limit, the Cramer-Rao lower bound [14] [100]. It makes use of an error frequency discriminant in a frequency-locked loop to track even rapid frequency changes, and has been implemented on a DSP board (see Section 4.6.3). Within a 6 MHz uncertainty range, the acquisition algorithm cyclicly searches for a signal in 6 sequential blocks of 1 MHz. The lock indicator exploits certain spectral characteristics over time and is very reliable.

The DSP implementation of this novel algorithm was initially verified in laboratory experiments, and it has since performed virtually flawlessly with FedSat during the entire operational period with minor parameter adjustments. Experimentally confirmed figures are a typical signal acquisition time of less than 500 ms (C/N<10 dB) and a maximum Doppler tracking capability of 50 kHz/s, which is more than one order higher than required for FedSat.

The *negative* value of the detected frequency offset is then sent to the receive DDS with a 10 MHz centre frequency which, when mixed with the 60 MHz IF, results in a perfectly stable 70 MHz signal. It should me mentioned that there is a small processing delay of approximately 5 milliseconds between the DSP input and the DDS output, however the resulting tracking offset (<20 Hz) is negligible for all practical purposes even at the maximum Doppler rate.

The accurate tracking of the downlink Doppler shift is crucial to the propagation experiment, since only the peak power of the estimated "centre" frequency is recorded at a high sampling rate. Any false locks or drop-outs inevitably lead to wrong results. Some examples of Doppler tracking performance are shown in Section 5.5.

4.6 Earth Station PC Hardware and Software Design

The close interaction between the earth station control software, the RF circuits and the electromechanical system in real time requires a very diligent design approach. It has previously been shown that virtually all software aspects, for example tracking and signal processing, are very challenging in terms of the required accuracy and timing. It has therefore been decided to split the design of timing-critical processes and ancillary support software into two physical systems, PC-A and PC-B (Fig. 4.20). Particularly the software running on PC-B, controlling spatial tracking, frequency tracking and data archiving, runs on the very limit of its hardware capability. Interacting with a multitude of add-on boards, the software had to be developed from the very beginning. It reflects continuing adaptations of the initial prototype design from 1999 to the actual operational demands from 2003 onwards. As with many aspects in this experimental work, commercial products for fast-tracking earth stations are available, but do not meet the financial constraints. Also, due to the use of a wide variety of COTS and in-house components, most of the software had to be custom designed for the system integration.

At this point, the highly valued contributions of the CRCSS software engineer (2002-2004), Y.S. Kim, shall be much acknowledged. Based on earlier CRCSS work, a considerable share of the operational earth station software was implemented by him, and many of the signal processing improvements presented in this chapter are founded on the very successful teamwork between him and the author.

The following sections portray the PC hardware used in the earth station, specialised daughterboards, software design issues and the user interface for various functions.

After an overview of the PC hardware, the functionality performed by each software implementation will be discussed, with a particular focus on spatial tracking and signal processing.

4.6.1 PC Hardware

Since the basic design of the earth station was conducted between 1998 and 2002, the selection of the PC hardware and the operating system reflects the availability of processor power, third-party hardware, required drivers and development software during *that* period. For example, Intel Pentium III™ processors were state-of-the-art, and most drivers for the required boards (DSP, motion controller, GPS) were only available for Windows NT™ or Windows 95™. The implementation of the software in Linux was briefly considered, but a lack of drivers eventually led to the selection of Windows NT™ as the preferred operating system. Due to several years of development time, the hardware
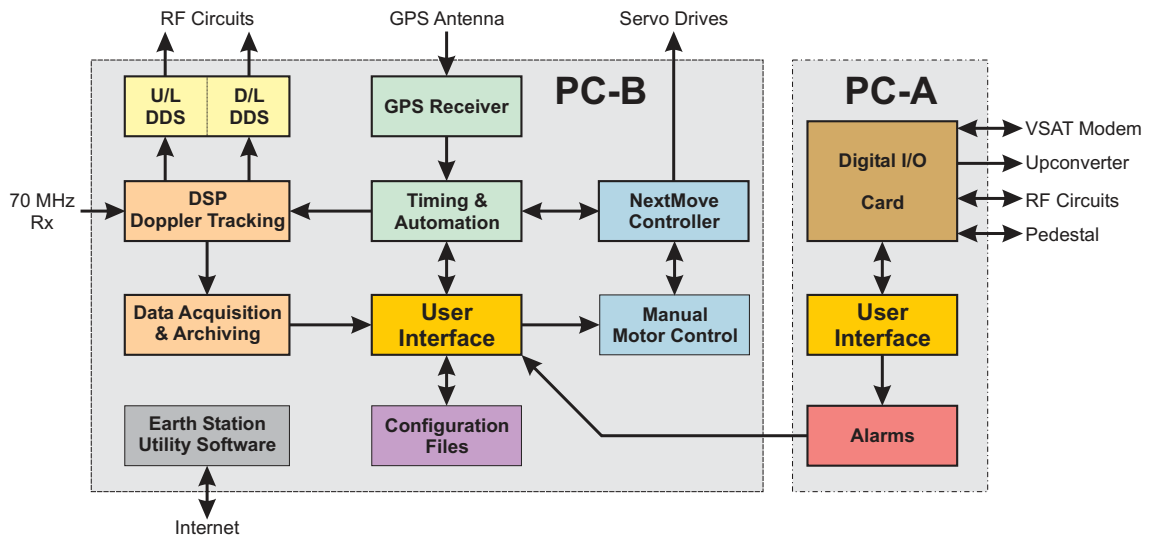
Figure 4.20: Interaction between software modules and add-on boards. The bold frame indicates that those modules are required to operate in real-time.

and operating system platform could already be considered outdated at the time it was deployed.

Referring back to Fig. 4.5 and Section 4.2.1, the earth station requires two PCs (A and B) to control the RF hardware, spatial tracking and signal processing. The hardware and software configuration of each PC is briefly summarised in Table 4.5.

PC-A	**PC-B**
(RF Control, Alarm Monitoring)	(Motion Control, Signal Processing)
Pentium III, 600 MHz	Pentium III, 600 MHz
Windows NT™ 4.0, LabView™	Windows NT™ 4.0, Visual C++
National Instruments DIO Card	BlueWave DSP Board
Quadruple RS232/422 Card	NextMove™ Controller
	SATPAK GPS Card

Table 4.5: Hardware and software configuration of the earth station PCs

PC-B performs the most complex and timing-critical tasks within the earth station and shall therefore be discussed in greater detail (for an overview of PC-A and its software, see Section 4.6.4). The key design objectives fulfilled by the earth station control software on PC-B are as follows:

- *Motion Control* - to provide manual and automatic real-time control over the servo

drives through the NextMove™board, including tuning, error handling and logging of motion data.

- *Timing* - to synchronise all actions required before, during and after a satellite pass with the timing signal supplied by the GPS add-on board, and to provide an accurate source for time-stamping.

- *Signal Processing* - to provide signal acquisition and Doppler shift tracking capabilities in real-time through the BlueWave™ dual DSP board, including spectrum and peak power measurements.

- *DDS Signal Generation* - to provide variable, DDS-generated local oscillator signals for uplink and downlink for Doppler pre-and post-compensation (real time).

- *Data Archiving* - to provide basic data processing, formatting and archiving capabilities of the power measurements and motion log files for external software (MatLab™).

- *User Interface* - to integrate all of those functions into a single application with a functionally well-designed user interface, including graphical displays of motion and signal data. Maintenance functions, such as tuning and RF circuit testing, should also be included.

Due to the wide variety of design aspects and especially the real-time demands, the programming language of choice has been Visual C++, with the core of the frequency tracking algorithm programmed in Assembly code. An image of the graphical user interface (in idle mode) is depicted in Fig. 4.21

4.6.2 Spatial Tracking and Automation

The initial design objective for the earth station was a completely automatic operation and data collection without the need of human intervention. In order to run passes automatically, future satellite passes would be scheduled by remotely placing script files, containing timing parameters, configuration commands and tracking coordinates, in a particular directory on the control PC, which is constantly being monitored. Detected pass files would be checked for validity and placed in a queue. Around the scheduled pass time, the earth station software would activate the servo motors and the RF components accordingly, track the satellite and record all received data locally, which could be remotely retrieved over the internet. This procedure is described in more detail in Chapter 5. Due to the reasons outlined in Section 4.9.3, only supervised operation was eventually possible,
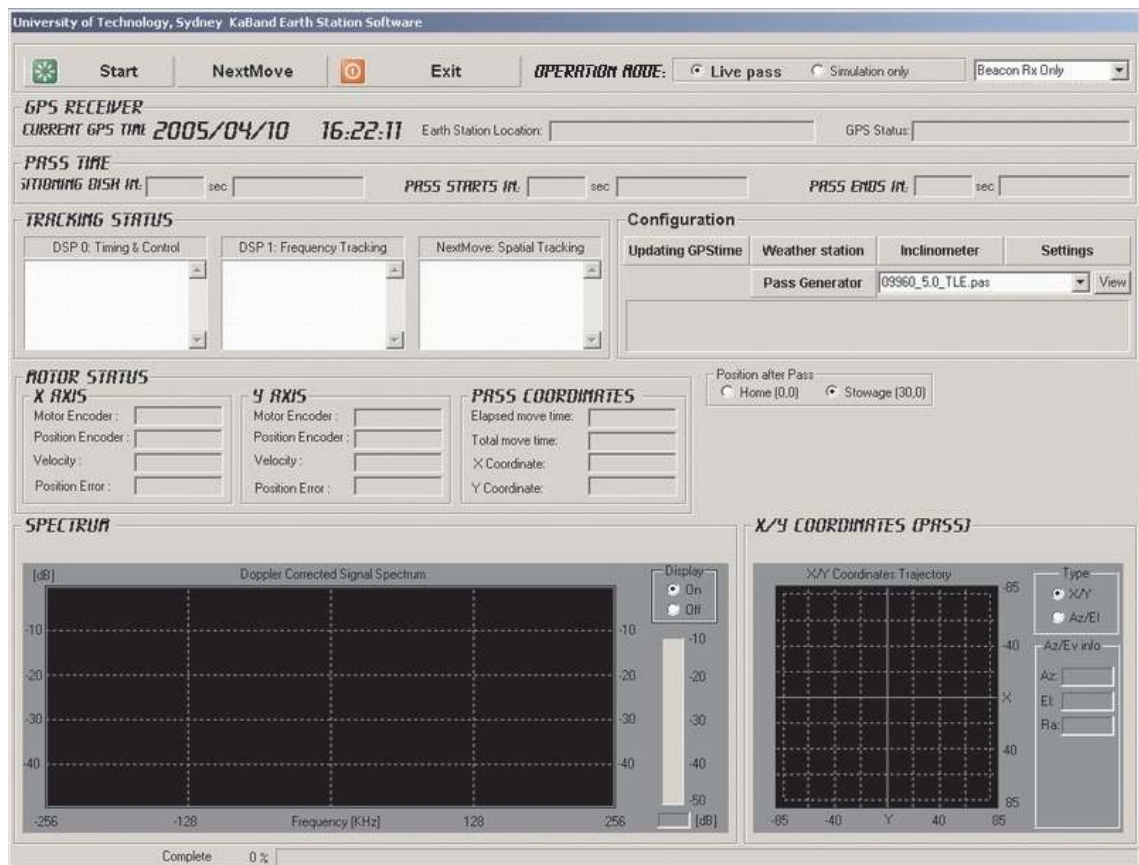
Figure 4.21: Image of the tracking and signal processing control software user interface (idle)

however the earth station control software itself is capable of supporting fully automated operation.

4.6.2.1 Motion Control

The hardware components of the electro-mechanical tracking subsystem have already been introduced in Section 4.4.2. While the two X/Y servo drives contain control circuits themselves, they still require extensive external programming for the complex positioning and tracking tasks to be performed (Fig. 4.22). The earth station control software provides the positioning information and tracking coordinates to the external MINT software package (see Section 4.6.2.3), incorporates them into a custom-designed array of positional commands, velocities, acceleration/deceleration parameters, fault handling and precision timing synchronisation. The code generated by MINT is downloaded onto the NextMove™ PCI board, which contains intelligent motion controllers for the processing of the four resolver/encoder signals and for creating the DC velocity signal for the X/Y drives. It also provides a number of digital inputs and outputs (not shown in Fig. 4.22), which are used for fault detection (for example limit switches) and for digital controls (brakes, HPA enable etc). The NextMove™ card also provides a software interface to access the motion data (positions, velocities, voltages) of the last MINT routine and for graphical display, which is very helpful for control loop calibration and optimisation.
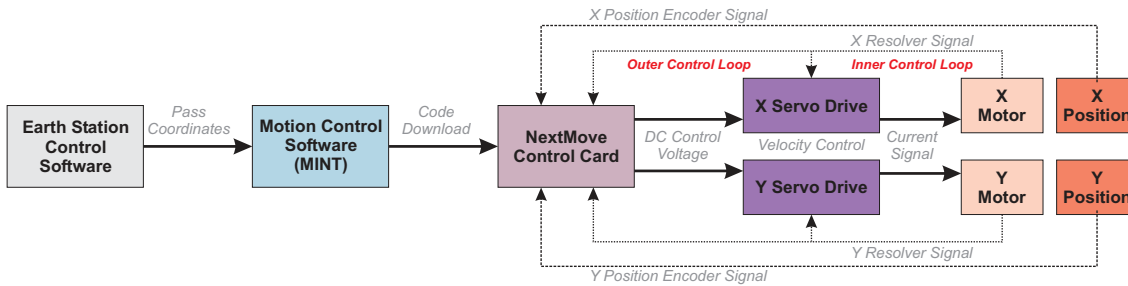
Figure 4.22: Signal flow diagram of the motion control system (fault signals not shown)

It is important to note that the motion control ensemble of motor, motor/position encoders, servo drive and NextMove™ board channel contains *two* concatenated control loops, as indicated in Fig. 4.22:

- the *inner* loop with motor, motor encoder (resolver) and servo drive, and

- the *outer* loop with position encoder, servo drive and NextMove™ board.

However, due to the errors introduced by the gearbox between the motor and the load (reflector frame), the position indicated by the resolver may not be the true position of the frame. For this reason, the position encoder on the free-spinning shaft provides accurate feedback to the NextMove™ card. This information is not only used for the correction of any offsets at the end of a move, but also to dynamically adjust any offsets *during* the move (see Section 4.9.2).

The inner loop provides for a very basic parameter match between the servo drive and the motor only, while the outer loop, which can be dynamically software-controlled at runtime, offers full access to extended control modes and parameters. The communication between the sensors on one side and the servo drive and PCI card inputs on the other side is done via analog signal lines. The control signal from the NextMove™ card is an analogue, continuous-time DC voltage ($-10\ V \ldots + 10\ V$), which is applied to an input port on the servo drive. This signal is then translated by the power electronics into a pulse-width modulated (PWM) velocity command signal with *quantised* magnitudes and eventually into a 3-phase AC current for the motors. In "velocity control mode", the motor velocity is proportional to the DC voltage.

4.6.2.2 Servo Drive Tuning

The servo drive tuning procedure can be separated into two subsequent steps. Firstly, the inner control loop must be calibrated for each axis, which is basically a matching of the motor model to the servo drive model. This tuning not only needs to be conducted without any load attached (free spinning *driven* shafts), but this must also be done with great diligence before the outer loop can be calibrated. The user-accessible inner loop control parameters are those of a simple proportional-integral-differential (PID) controller, which adjusts the drive currents according to its parameters in velocity control mode. The programming is done from the indoor unit via an RS-232 connection to the servo drives. The manufacturer provides empirical starting values, which need to be modified in order to minimise both the rise time and the overshoot of the system's step response. Typically, only the proportional and the integral values need to be adjusted, while the derivative part is set to zero. The graphs of the input step and the motor's response can be observed using the FlexDrive RS-232 tuning software, which allows both automatic (self-) and iterative manual tuning. Both methods have been explored during the tuning process, and the built-in automatic method has been found to be very efficient and was therefore used. In addition, the tuning software allows to specify a DC offset, so that the shaft is completely steady at nominal zero volts input.

Having completed the inner loop (load-free) tuning, the load (reflector frame, reflector and feed assembly on the X axis, base bracket on the Y axis) is attached to the driven shafts. Due to the nature of the application, load conditions are non-linear during the course of a typical pass movement, hence the optimisation of the PID tuning parameters using established empirical procedures is a compromise, resulting in degraded controller performance in the outer control loop [101].

The manufacturer provides guidelines and empirical formulae for the selection of initial PID controller parameters for the outer loop, including velocity feedforward and feedback gain values. However, the optimisation of those values has proven extremely challenging when following standard tuning theory and methods, such as in [102]. An additional factor of difficulty is also suspected in the very low rotation speeds combined with high, very variable torque requirements, which appears to be a borderline use for this particular system. Eventually, satisfactory results under various load conditions were achieved after a great number of iterative attempts and empirical approaches, founded on the basic understanding of control and tuning theory. It is assumed that the tuning of this multi-dimensional system could possibly be further optimised by devoting a considerable amount of time to the profound understanding of non-linear control theory and tuning. However, primarily due to the demand for immediate earth station operability and that this topic would have been outside the scope of the project and this thesis, the obtained parameters were believed to be sufficient. After a large number of successful passes, this assumption was later proven reasonable. The main objectives of the optimisation were:

- *Steady-state error* - minimum dynamic error during the move

- *Position accuracy* - minimum deviation from the final commanded position,

- *Vibration* - minimisation of vibrations at *any* inclination of the structure and therefore at any torque demands,

- *Torque* - the ability to support the weight of the structure, especially at low elevation angles, and

- *Velocity* - minimisation of the time required for positioning the pedestal at the pass start coordinates.

The reduction of vibrations is not only important for improved pointing accuracy, but also in order to reduce wear on the gearbox. It has been proven very difficult to reduce the steady-state error *and* minimise the vibrations at the same time, which is normally achieved by the adjusting the integral component. Also, the control loop was exceptionally

sensitive even to very small changes in the integral value. It is suspected that the main problem lies in these two points of the initial design:

- Even when considering the 100:1 gearbox, the highest required velocity (used only for positioning the frame at $2°$/s) lies in such a low range of the motor's capabilities ($\frac{33.3\ rpm}{6000\ rpm} = 0.56\%$) that the PWM constantly alternates between zero current and the first current quantisation level. The effectiveness of the control loop in this velocity range must be questioned, although limits were not clearly specified by the manufacturer.

- The torque demand varies greatly over the duration of a pass, especially on a marginal one (low east or west elevations), and therefore requires a wider range of angles on the Y axis. When the Y axis, which carries a much greater load than the X axis, is fully tilted over east or west, the required torque is close to the maximum allowable. However, when the Y axis passes through the zero point (mechanical balance), the load is nearly zero. Configuring the control loop for both extremes, with high accuracy *and* with minimum vibrations, has proven very challenging.

It must be pointed out that the proper configuration of the drive parameters by the author, although eventually successful, has been the most time-consuming task of the entire earth station deployment and operation. Due to its significance for the precision tracking requirements, it has given rise to several design improvements and suggestions (see Section 4.9.1). It should be noted that the specific, numerical PID controller *values* obtained during the tuning procedure for each axis are highly dependent on the configuration of the antenna assembly (for example mass distribution) and on the electro-mechanical Baldor parts. It was also recognised that, after each re-assembly of the pedestal, load changes or the replacement of a servo drive, all control loop calibration procedures had to be completely repeated.

4.6.2.3 MINT Software

The BASIC-like programming language "MINT"™ was developed by Baldor specifically for motion control applications. It has a specialised set of commands that make it very simple, for instance, to spin a motor for a certain time at a set speed, or to drive an axis from position A to position B at a given angular velocity. It is also capable to process faults through limit sensors (via digital inputs) or to enable/disable brakes. MINT™ functions by downloading code and data to the NextMove™ motion controller board, on which this code can run autonomously. MINT™ can accept input data from calling programs, such

as the earth station control application, before downloading the data and code to the NextMove™ board, and small amounts of data can be exchanged while the program is running through special communication registers, accessible by both the MINT™ program running on the NextMove™ board and by the PC application. However, this exchange is fairly slow and therefore not suitable for real-time use.

With the exception of tuning, which is done directly through a RS-232 connection between the servo drive and a PC running the Baldor tuning application, all motion control is implemented with MINT™. From a separate "NextMove Control Panel" (see Fig. 4.23), the drives can be moved very precisely to certain positions, the parameters of the external control loop (i.e. NextMove™ - motors) can be adjusted and the results of the last move are graphically displayed for error and vibration analysis. Some of the maintenance functions implemented are basic control (brakes on/off, field on/off), positional move, simulated pass (from file), and time-referenced positional move. The "normal" live pass mode is accessible from the main window, because it also includes RF circuit activation. Some of these functions will later be referred to.

Each motion control function requires a separate MINT™ program to be downloaded. For instance, for a live pass the control software loads the X/Y coordinates from a text file that also contains the starting time of the pass, and selects the correct MINT program. With sufficient time to spare before the start of the pass, it downloads both the MINT™ code and the data points into the NextMove™ board memory. Shortly before the pass, NextMove™ receives a command to position the antenna at the first set of coordinates (AOS). Precisely timed at the start of the pass, another routine is triggered that subsequently reads the X/Y coordinate pairs (in 1 second intervals due to memory limitations) from the memory and generates the drive signals accordingly. It should be noted that these coordinates are internally interpolated in intervals of only several milliseconds, hence there are no discontinuities in the movement. This is an important feature that must be kept in mind for a design improvement discussed below. Current coordinate and the motor and position encoder values are exchanged with the user interface via the communication register, so that the trajectory can be graphically displayed. The data flow between MINT™, NextMove™and the application is visualised in Fig. 4.24.

In addition to the *inner* control loop between the motor, motor encoder and servo drive only, the NextMove™ board has knowledge of all four encoders. The *outer* control loop, incorporating the position encoder, can be dynamically influenced by the program running on the card. Several extended PID controller templates exist, which can be manually optimised. Due to the unusual application in this case, a very customary design improvement using this capability is discussed in Section 4.9.2.
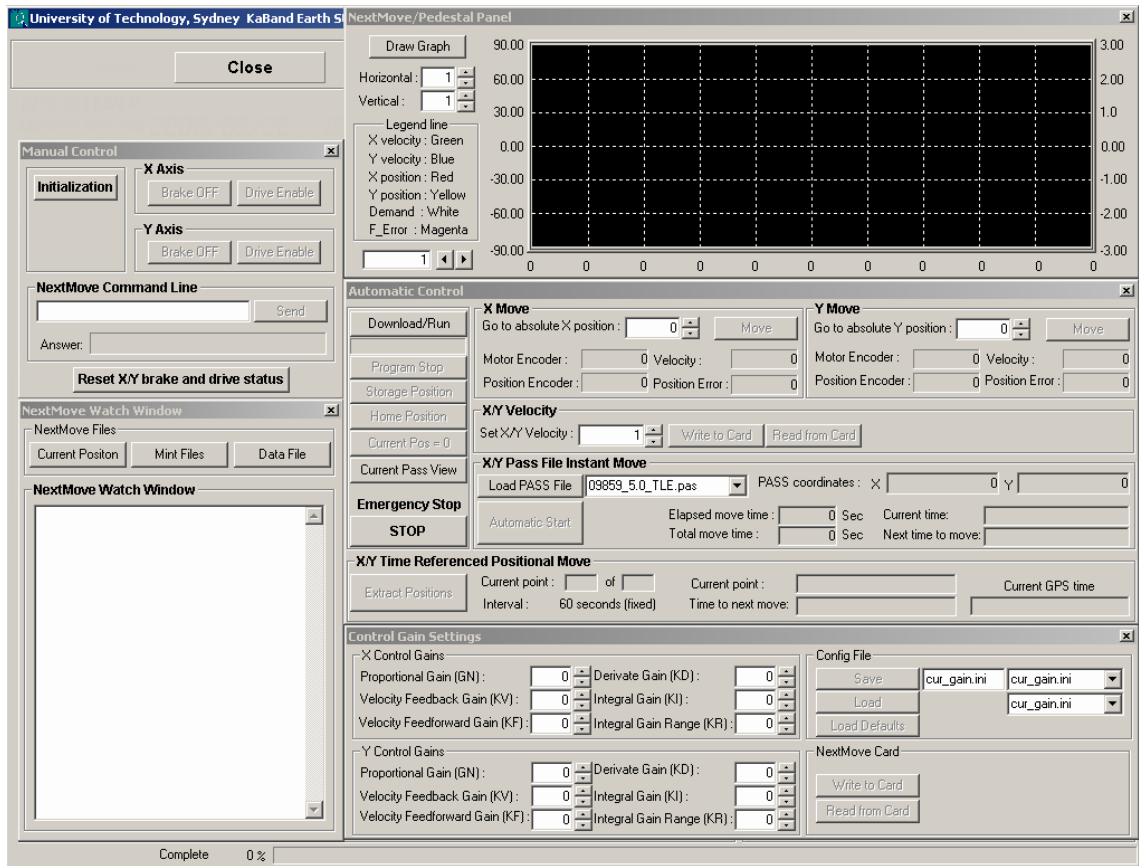
Figure 4.23: Screenshot of the manual NextMove™ motion control panels for testing and configuration)
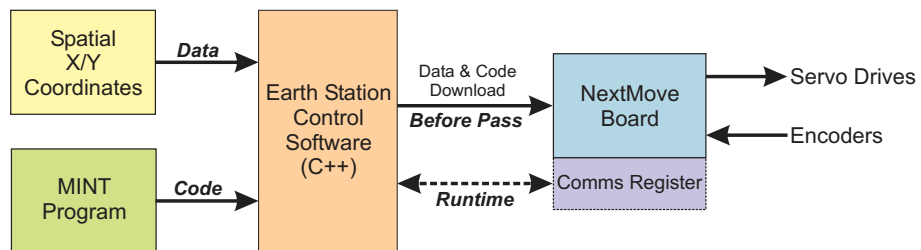
Figure 4.24: Data flow between MINT™, the control software and NextMove™ *before* and *during* a tracking event)

4.6.2.4 Timing Automation

PC-B contains a GPS receiver PCI card (SATPAK-PCI with a Trimble™ ACE-III chipset, [103]), which is interfaced to the main control software by a virtual COM port. Besides location information, it provides a highly accurate timing signal to the earth station control software. Date, hour, minute and second of the earth station's internal system time are frequently synchronised with the GPS clock, and the rising edge of a 10 μs pulse with a one second period signal is precisely aligned with the beginning of a GPS second epoch (with a 100 ns tolerance) [104], therefore exceeding the stringent timing accuracy requirements.

Since the spacecraft's telemetry time stamp is based on GPS time (derived from the onboard GPS receiver), it was decided to choose the same system time for the earth station for an easier match of time stamps, especially for the planned use of onboard GPS data for spatial tracking. It should be noted that the worldwide standard for timing is usually not GPS time, but Universal Time Coordinated (UTC), and all orbital elements and associated software products usually assume UTC (or local time) for their calculations. UTC and GPS time are corrected for relativistic effects. They only differ by the number of leap seconds which have been introduced on earth (but not in space) in order to compensate for the fact that the earth's rotation is progressively slowing down at a small rate. Since 1980, 14 leap seconds have been introduced, and during FedSat's experimental phase (2003-2005), the difference was a constant 13 seconds [105].

The precise timing signal from the GPS satellites is decoded to UTC by the GPS receiver. In order to calculate the desired GPS time, it is convenient to use the offset information already contained in the GPS data frames (subframe 4, page 18 [106]) by adding the given number of leap seconds to UTC time, and by subsequently correcting any other time and date-related parameters affected. The leap second difference has consistently been taken into account for timing synchronisation, time-stamping and comparison with external data. All times referred to in this work are in GPS time, unless otherwise stated.

Based on this GPS timer, all preparations for a scheduled satellite pass are made automatically, allowing enough time to energise the servo motors and to position the antenna at the AOS coordinates. Great care has been taken to consider changes of date, month and even leap year during or just before the start of a pass when calculating the required preparation time.

4.6.3 Digital Signal Processing

The Doppler tracking and power level measurement are performed by the digital signal processing subsystem, which consists of three functional units:

- BlueWave Systems™ PCI DSP board with dual Texas Instruments TMS320C6711 DSPs (DSP Starter Kit, DSK) [107]

- BlueWave Systems™ SB3410 analog interface daughterboard [108]

- Two Analog Devices™ AD9835 Direct Digital Synthesizer (DDS) daughterboards [109]

Only the DSP board interfaces directly with the host PC. The DDS and analog daughterboards are accessed through expansion interfaces located on the DSP card. This has the advantage that the DSP card can communicate with the expansion cards directly when required. Conceptually, the DDS creates a variable-frequency, analog output from a single, fixed-frequency clock source, where the frequency offset is proportional to a *digital* input, the tuning word. A DDS' main components are a numerically controlled oscillator with phase accumulator, cosine lookup table and digital-to-analog converter (DAC), plus a low-pass filter (Fig. 4.25). For the Doppler tracking application, it is imperative that the DDS output is *phase-continuous* upon any commanded frequency change.
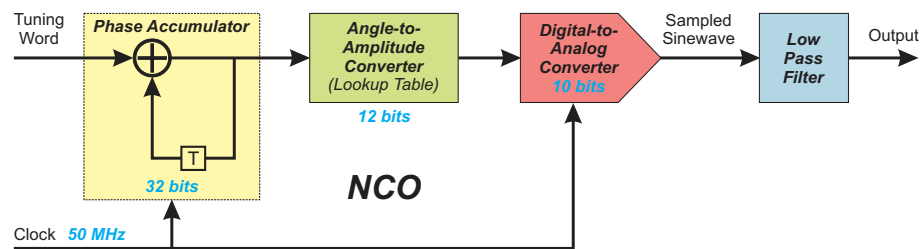
Figure 4.25: Basic functional diagram of a direct digital synthesizer with selected AD9835 specifications (blue), (modified from [110])

A brief summary of the DSP, DDS and analog interface card specifications is provided in Table 4.6.

The DSP software has been designed over a number of years by several members of the UTS CRCSS team, with particular credit to A. Thoms [111]. A detailed description of the the multitude of functions performed by the DSP board, in conjunction with the control software, the analog interface card and the two DDS, is beyond the scope of this work, and an in-depth description can be found in [112], which has been developed under the guidance of the author. Hence, only specifications and functionality relevant to the experiment shall be mentioned in this section. For further reading on DDS theory and the programming of the AD9835, the manufacturer's manual, [109], an in-depth DDS tutorial [110] and, for a practical implementation, [113] are recommended.

TMS320C6711D DSK	200 MHz clock
	1200 MFLOPS
	64MB on-board memory
	Two buffered serial ports (DDS/SB4310 interface)
SB3410 Card	Full Duplex Transceiver
	70 MHz IF input/output
	40 dB dynamic range
	12/10 MHz receiver/transmitter bandwidth
	12 bit, 65 Msps A/D converter
	14 bit, 100 Msps D/A converter
AD9835 DDS	50 MHz clock
	32 bit programmable divider
	10 bit D/A converter
	RS-232 interface

Table 4.6: Selected specifications of the DSP board, analog interface board and DDS

Once initiated, the spatial tracking functions are almost autonomously performed by the motion controller (see section 4.6.2.3), freeing up resources on the host PC and the DSP board. Very timing-critical DSP code, such as the frequency tracking algorithm, is written in Assembly code. One DSP is dedicated to performing the spectral analysis, acquisition and Doppler tracking of the receive signal, which has been downconverted and sampled by the analog interface card. The first DSP also updates one or both DDS, depending on the mode of operation, at least every 4 ms with the correction frequency at a resolution of better than 0.012 Hz. The second DSP time-stamps and records the spectrum around the detected centre frequency ($\pm$500 kHz) in intervals of 100 ms, and the power level at the centre frequency in intervals of 4 ms. The very short sampling interval of the receive power level is essential for the Ka band propagation experiment, since it enables the detection of rapid attenuation fluctuations (scintillations). Instead of fully time-stamping every single sample, each data entry contains incremental timing information, which can be precisely referenced to the start of the pass. This procedure was adopted to avoid exchanging time-stamping information between host PC and DSP board during the pass. The outlined data acquisition strategy is a significant improvement to the initial earth station design, therefore it is described in Section 4.9.4 in greater detail.

After the end of the pass, each data sample of the spectral and power measurement is properly time-stamped in GPS time and saved in several files on the host PC's hard disk, together with other relevant pass information. This process is further dealt with in section 5.4.4.

4.6.3.1 RF Power and Spectrum Measurement

In the initial design, the DSP sampled and recorded the entire spectrum within the selected 1 MHz section, with the detected signal in its centre bin. While this approach allows to plot a spectrogram for interference analysis and remote fault finding, it proved to be very resource inefficient and slow, hence some changes were made (see Section 4.9.4) that allowed a much faster sampling of the *peak power* only, reducing the sampling interval to an average of 4 ms. It must be stressed again that this fast sampling is crucially required for the propagation measurement due to the rapid *movement* of the satellite across the sky, in addition to recording the atmospheric and tropospheric variability that is the goal of this research.

After the deployment of the earth station, the input power level to the analog interface card needs to be adjusted by means of a software-controlled attenuator in order to match the dynamic range (approx. -60 to -20 dBm), which means that the receiver's signal-to-noise ratio is large enough to record fades of up to 40 dB without distortion. The attenuator value then remains unchanged to allow fully reproducible measurements. However, since the input level is not calibrated to a specific received signal strength, an absolute quantification of the actual power level has to be achieved by other means, which is discussed in Section 5.3. The sampled spectrum and peak power values are then stored in the DSP board's internal memory for performance reasons, and transferred to the host PC after the end of the pass when no more processing is required. The results of the power measurements are extensively discussed in Chapter 6.

4.6.4 RF Control and Alarm Monitoring Software

Certain components in the RF up and downconversion chain require external configuration and adjustment. For this purpose, an extensive, separate software package has been developed under LabView™. Referring to the RF block diagrams in Section 4.5.3, most RF components only require an initial calibration. The programmable multiplier, providing the LO signal for the 2nd IF, is set to a fixed multiplying factor of 1:147 and does not need any further ongoing adjustments. The variable attenuators in the downlink path adjusts the power level to suit the dynamic range of the DSP card (downlink) and the uplink attenuator compensates for the cable loss at the HPA input. Both attenuators can be interactively controlled from the user interface of PC-A, however they have not been modified after the initial calibration to ensure consistent power measurements. Although never incorporated in the earth station, the baseband processor is included in the design through software-controlled RF switches and software/hardware interfaces for mode

commands. The upconverter parameters (frequency, gain) and the entire configuration of the VSAT modem (modulation, data rate, transmit frequency, coding) are also controllable through the software on PC-A, and the entire communication protocol for these devices was implemented in LabView for easy operation from one terminal. A Image of the LabView control software is shown in Fig. 4.26.
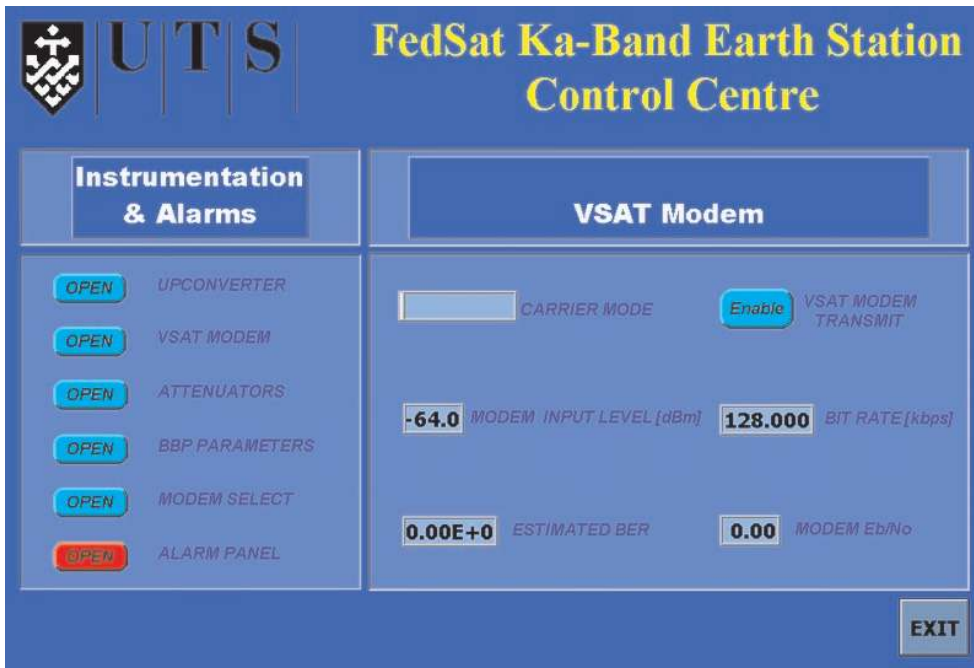
Figure 4.26: User interface of the LabView "Control Centre Software" on PC-A

The in-house developed signal processing software on PC-B interacts with the RF hardware only in terms of the DSP card and the two DDS daughterboards, which is described in 4.6.3, and by enabling and disabling the HPA through a digital switchline.

4.6.5 Support Utilities and Third-Party Software

For the preparations of a LEO satellite pass, some external software is required to generate the look angle coordinates and to perform required coordinate transformations.

Firstly, for reasons explained in Section 5.2.3, software for the calculation of the ephemeris and the pass coordinates was considered. Due to the wealth of existing software (either free, shareware of commercial) capable of converting NASA two-line elements into look angle with reliable timing, an in-house implementation was not contemplated. Due to the stringent pointing accuracy and timing requirements, the following key criteria were established:

- *Resolution* - the number of significant digits produced for azimuth and elevation angle

- *Time Interval* - minimum time interval between Az/El coordinates

- *Simplicity* - ease of use, suitable range of functionality and good user interface

A large number of free, shareware and semi-commercial products was examined; most of the professional software on offer was more targeted towards corporate and military use [114]. All these sources use the "Simplified General Perturbations Satellite Orbit Model 4" (SGP4) algorithm, which is recommended for the use with TLEs of LEO/MEO satellites. After a thorough assessment, it was revealed that many programs did not provide the required angular resolution of at least 0.01°, or did not generate an output every second. Eventually, the software "NOVA for Windows" [67] was selected predominantly due to the 0.01° resolution output of the look angles at 1 second intervals. It also allows easy text-based export of the data and provides an attractive visualisation of the satellite path, footprint and ephemeris. All TLE-based pass files for this research have been generated by Nova.

The second software required is for the conversion of Az/El look angles to X/Y coordinates. In addition, other factors like feed offset, imperfect pedestal alignment (see Section 4.8.2) and pass restrictions (minimum elevation and duration) have to be taken into account. Based on the work already done for the CRCSS in [82], Section 6.8, a utility software was in-house developed [115] that allowed a very flexible input of either Nova-generated ASCII data or the extrapolated FedSat GPS data supplied by the CRCSS GPS research group at QUT. In addition, it included any declination from north, feed offset, minimum elevation or minimum pass duration in the calculations for a given earth station location. A normalised Doppler shift value is also generated for each data set, usually computed in 1 second intervals. The earth station control software is adapted to the use of the data structure produced by the utility software. A screen shot can be seen in Fig. 4.27.

4.7 Earth Station Siting

The choice of a suitable earth station location is much dependent on the purpose and the type of satellite. For example, for a GEO VSAT application with its fixed look angles, it is theoretically sufficient if only a small area of sky is visible around the direct path to the satellite. For the continuous tracking of a single LEO satellite in a variety of trajectories, optimally the entire hemisphere must be free of obstructions down to
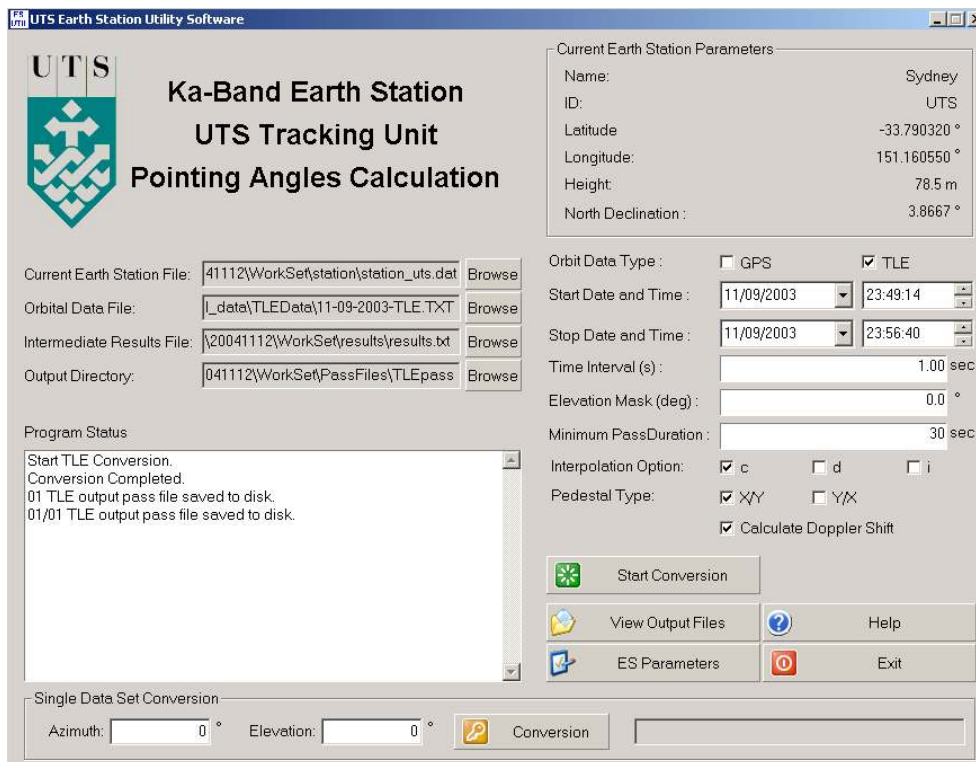
Figure 4.27: Screenshot of the UTS Earth Station Utility Software for coordinate conversion [115]

the horizon. Considering practical aspects, such as the link budget and the spacecraft's illumination footprint, these requirements can be somewhat relaxed. In FedSat's case, it was established that data communication would require a minimum elevation angle of 30°, and a beacon signal would be trackable down to a minimum of between 5° and 10°. Here, the term "site" refers to the outdoor location of the tracking pedestal, but a convenient location of the indoor unit also needs to be taken into account.

4.7.1 Location Selection Criteria

Apart from operational and environmental aspects, the site selection considerations for this project were also constrained by other factors, in a likely order of priority:

1. The site must be provided free-of-charge and at minimum restrictions regarding the installation.

2. The site should preferably be located on UTS grounds.

3. The site should have maximum visibility of the sky, especially in north-south direction.

4. The site must have a suitable and secure space for the indoor unit with a cable run to the outdoor unit as short as possible.

5. The site must have restricted access from the public.

6. The site should have a low risk of radio interference (especially on IFs) from neighbouring transmitters.

7. The site should not be located too far away from the usual UTS CRCSS research staff offices.

8. The installation and operation of the earth station should not affect the surrounding residences in any way.

Especially considering priorities, several compromises had to be made when the site was eventually selected in 2002. Unfortunately, it later turned out that one of the points initially awarded a low priority, No. 7, turned out to have a significant impact on the number of experiments that could be conducted, as a result of the manual levelling requirement and the fragility of the gearbox (Section 7.1). Other important limitations are discussed below.

4.7.2 Limitations of the Chosen Site

Due to the large number of high-rise buildings in the vicinity of Sydney's central business district (CBD), which would have been obstructing major parts of the sky, installing the earth station near the UTS CRCSS laboratory at the City Campus was not possible. Hence, another site at the university's Kuring-gai Campus in the Sydney suburb of Lindfield was considered, about 15km (40 min) north of the CBD. While the site in Lindfield is generally free of surrounding high-rise buildings, the actual number of suitable locations on UTS grounds was limited, especially due to the fact that exposed building were already occupied by commercial telecommunications equipment. An overview of the restrictions and limitations experienced at the selected site are summarised in the following sections.

4.7.2.1 Obstructions

The drawing in Fig. 4.28 illustrates the built environment in which the tracking pedestal was installed (red dot). Although it may seem from the drawing that a supposedly more suitable site could have been selected, this was the only one that had been officially approved. Unfortunately, a number of structures impacted on the clear view of the sky:

1. Large tower with metallic extensions and numerous mobile phone panel antennas and terrestrial point-to-point links (distance=31m, azimuth=270...283°, elevation=20°)

2. Chimney with metallic extensions and mobile phone panels (distance=10m, azimuth=311...322°, elevation=37°)

3. Single, metallic pole (20cm diameter) with a single panel antenna (distance=2m, azimuth=28...32°, elevation=60°)

The polar horizon chart in Fig. 4.29 visualises these obstructions in a more practical way. It is apparent that the most important north-south path is largely unobstructed, however some degradation could be expected on low elevation westerly passes and especially on most easterly passes. Structures 1 and 2 later proved not to impact on the operation at all, while the effect of the metal pole relatively close to the antenna caused some interesting, but undesired effects (see Section 5.3.6). On the positive side, the higher metallic structures provide some protection from direct lightning strikes, but not from electrostatic effects. In retrospect, especially the pole should have received more consideration during the site selection process.
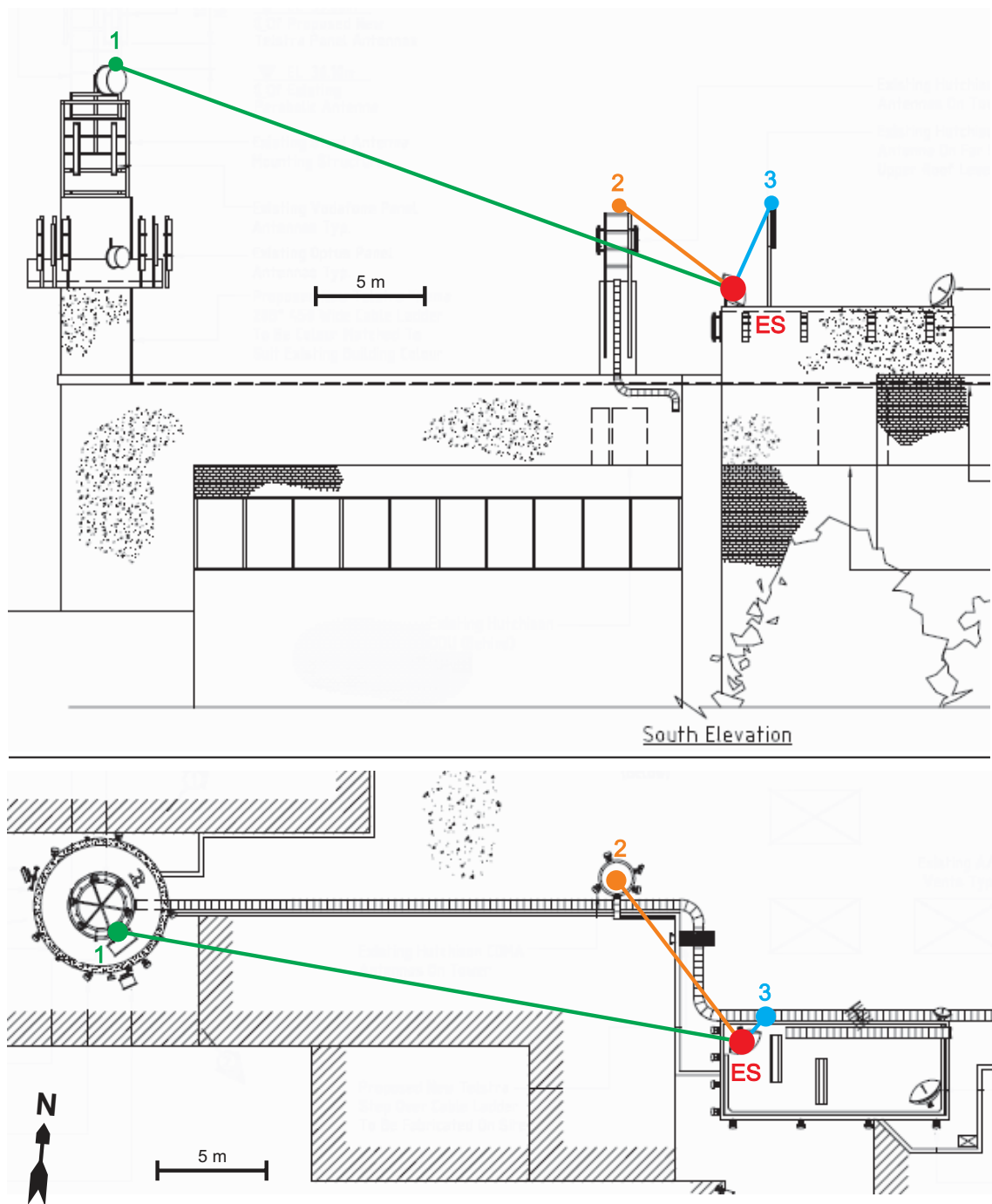
Figure 4.28: Drawing of the earth station site in elevation view and top view. Items 1-3 denote significant horizon obstructions.
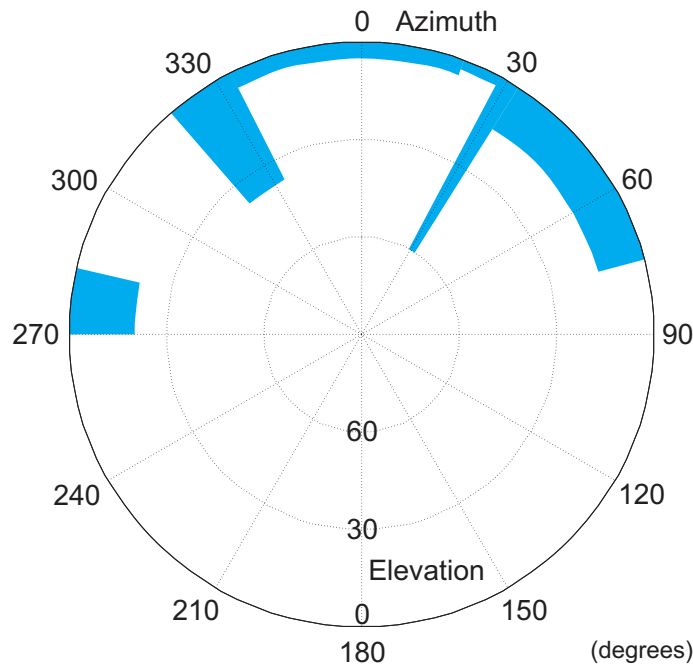
Figure 4.29: Horizon chart of the obstructions surrounding the tracking antenna site

4.7.2.2 Environment

The UTS Kuring-gai campus is located in a residential area on top of a ridge and overlooking forested valleys to the east, south and west (Fig. 4.30). Due to the site's 12km proximity to the shore line, it can clearly be classified as being located in a coastal/maritime environment in terms of weather patterns (for example sea breezes, thunderstorms), however the Great Dividing Range (elevation up to 1100m) ascends only about 45km west from there. This narrow strip between the mountains and the sea creates a local climate which can be very difficult to predict, especially for the development of convective cloud formations. Even more locally, it is established that there are no artificial sources of pollutants or large amounts of humidity (for example cooling towers) in the vicinity. The site is fairly exposed in all directions, which raises the question of protection against high winds and storm gusts.

4.7.2.3 RF Interference

As previously mentioned, the site is shared with a large number of telecommunication operators. Numerous GSM, 3G and CDMA base stations are installed in the vicinity, and point-to-point microwave links also exist. Since the highest risk of RF interference with the earth station exists through feed-through on the IFs, the presence of strong signals
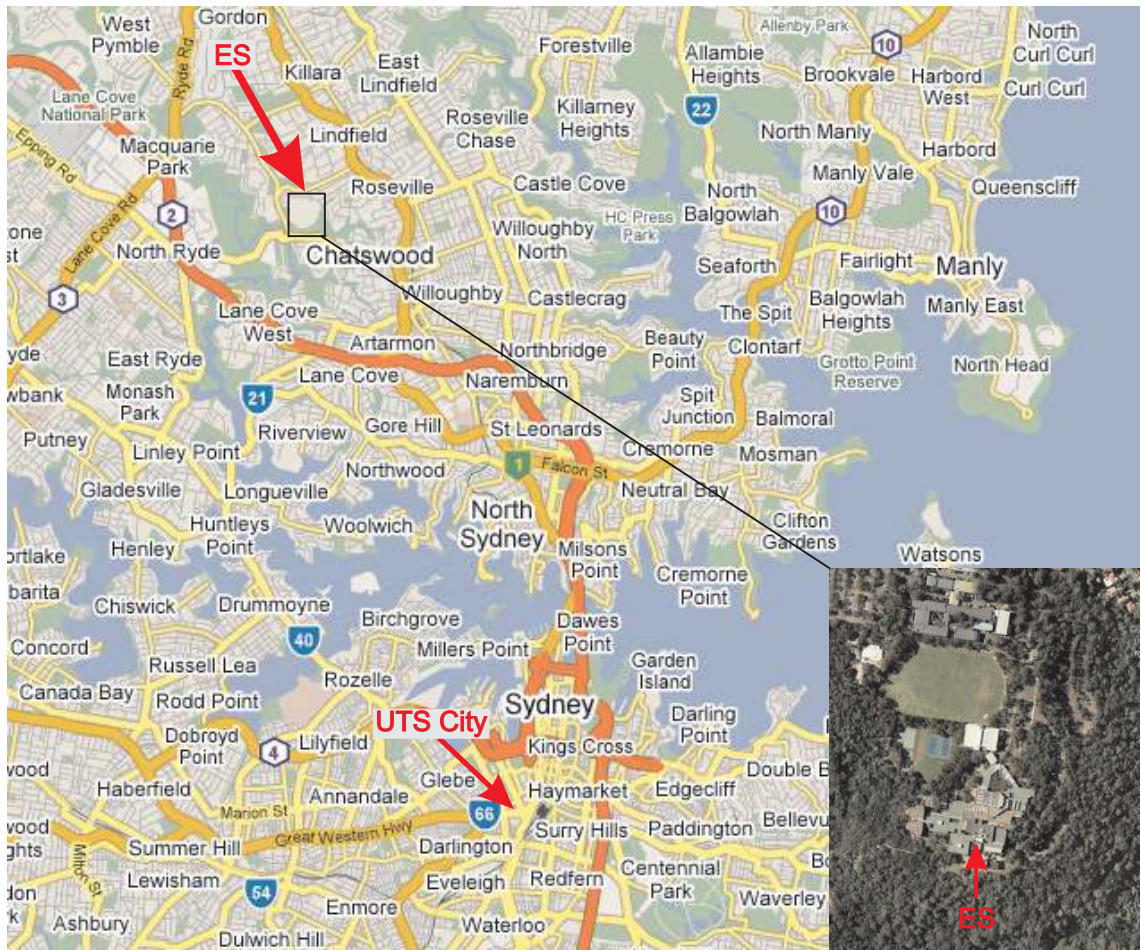
Figure 4.30: Map indicating the UTS City Campus, the earth station location and the surrounding environment (inset)

of the various earth station IFs was tested with a spectrum analyser. The high-powered mobile phone transmitters all operate in significantly different frequency ranges, and no other source of concern was found. During operation itself, the spectral analysis of the received signal did not reveal any external interference patterns either.

4.7.2.4 Safety

Both during installation and operation, personal safety on the site had to be observed. The location of the pedestal and the servo drive enclosure atop a lift motor room can only be reached by means of ladders, and the pedestal is also located close to a 15m vertical drop. In critical situations, safety harnesses had to be worn. Since the area is not open to public access, it is not equipped with any lighting and does not have any other safety support for access after dark. Consequently, roof access at night was strictly prohibited by the university's health and safety regulations. Since manual levelling of the reflector required access to the antenna, it was impossible to conduct any ascending satellite passes, which *always* happen at night (local time) in FedSat's sun-synchronous orbit.

4.8   Earth Station Deployment

Before the earth station was installed on location and well before the launch of FedSat, the Ka band communication system of earth station had been tested extensively in Ka band loopback bit error rate tests, and more importantly in an integrated system test with the payload. Later, the various components of the earth station's indoor and outdoor units were installed and taken into operation over a period of approximately two months between December 2002 and February 2003, which involved most of the four UTS CRCSS staff at that time. After the physical installation, a period of function testing, calibration and further development followed, together with ongoing design improvements and advances especially in the software development. The successful first-time reception of the satellite's Ka band beacon signal marked the start of the operational phase.

4.8.1   Integrated System Test with FedSat Communications Payload

After the completion of the communication and Ka band modules by ITR and CSIRO, the payloads were shipped to Auspace Ltd in Canberra for the integration into the Fed-Sat structure. Since no other engineering model existed, a final integrated system test (IST) between the actual payload and the RF circuits of the Ka band earth station was conducted, which also required the transport of the indoor unit to Canberra.

With all components connected exactly as they would be in operation, the free space link between them was simulated through an equivalent attenuating cable and a programmable attenuator on Ka band for both uplink and downlink. The full functionality of beacon mode and data bent pipe mode was confirmed, and all design specifications and link budgets were well within the expected and calculated margins. A photo of an earlier Ka band RF loopback test setup and the resulting bit error rate performance (including coding gain) in data bent pipe mode can be seen in Fig. 4.31 [116].
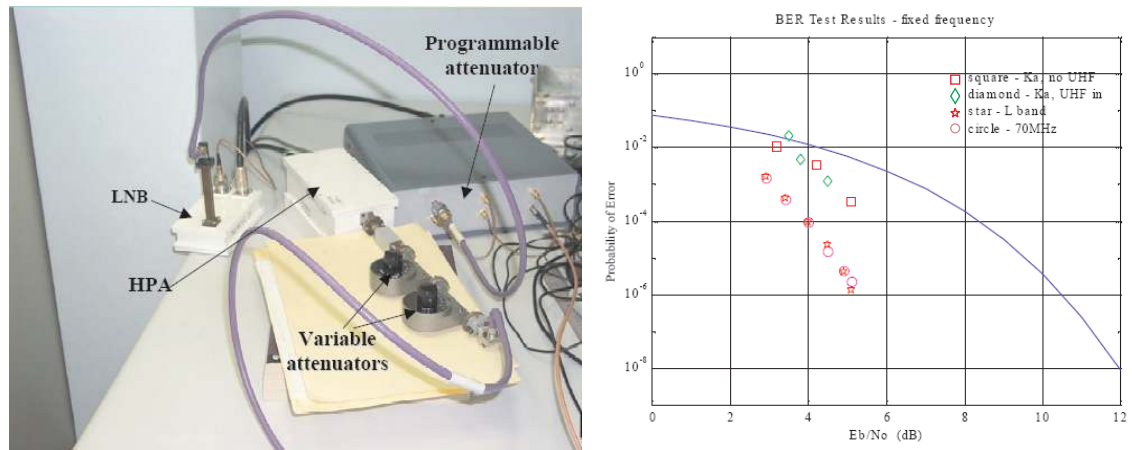
Figure 4.31: Ka band RF loopback test setup (left) and resulting bit error rate measurements for various tests (right)

4.8.2 Surveying

As emphasized in previous sections, great care has been taken in the earth station design to minimise mechanical tolerances and other sources of error that could compromise the accuracy of the pointing angles. All this effort would have been in vain if there were significant errors or uncertainties about the azimuth orientation of the antenna on site, since this is the only site-specific parameter that cannot be self-determined through GPS receiver or the reflector levelling procedure. Consequently, the pedestal had to be precisely surveyed. For rapid earth station deployment considerations not requiring precision surveying, see [82].

Instead of attempting to align the pedestal base precisely in north-south direction, it was decided to install it to the best manual accuracy in that direction and to take any declination into account later in the calculation of the pointing angles. After the installation, an experienced civil engineer from the UTS Faculty of Engineering surveyed the pedestal mount in relation to known trigonometric points in the surrounding area

(Fig. 4.32). A reference 'level' position for the reflector was also established. In addition, the exact earth station coordinates and height were determined at a higher precision than possible with GPS alone. The results of the surveying are summarised in Table 4.7 [117].

Figure 4.32: Photos of the precision surveying campaign: overview of the location (left) and equipment (right). Some of the obstructing towers and masts can also be seen here.

Latitude	151.160550° East
Longitude	33.790320° South
Height above Mean Sea Level	78.5m
North Declination of Pedestal	3.8667° to the West

Table 4.7: Earth station survey results

The most critical result is the declination, which was measured using a 1" theodolite. Due to the small dimensions of the gearbox housing, the surveyor only felt comfortable to confirm an accuracy of ±0.04 degrees, however this tolerance could later be improved by adding attachments to the pedestal, if required. Since the given figure was significantly better than the required accuracy, it was decided to repeat the measurements only if spatial tracking of FedSat was unsuccessful. In preparing the pointing coordinates, all theoretically calculated azimuth values had to be corrected by the declination value to achieve correct pointing. Due to the immediately successful first tracking attempts, it was eventually confirmed that the surveyed figures must have been extremely close to the true values.

4.8.3   Connectivity and Ancillary Devices

The physical 25m-separation of the indoor and the outdoor unit necessitated the use of multi-core cables for the drive signals, encoder signals and other sensors and controls. Due to the sensitivity of the encoder signals to noise and interference, they were separated from high-power signals (such as the AC servo power), and double-shielded cables were additionally used. The four RF signals (L band uplink/downlink IF, reference oscillator and GPS antenna) were connected by high-quality coaxial cable to minimise losses, all of which were installed in cable conduits. The GPS antenna was mounted several metres away from the pedestal structure to maximise its signal reception. For propagation measurements, the rainfall data from official Australian Bureau of Meteorology weather stations [118] and from Sydney Water pluviometers [119] located very close to the site have been used. Due to financial constraints, there has been no opportunity to install a costly tracking radiometer or even a rain radar, which would have allowed to monitor the propagation conditions between the satellite and the earth stations quite accurately.

4.8.4   Functional On-Site Testing

It should only briefly be mentioned that the weeks following the installation and deployment of the earth station hardware were dedicated to very extensive on-site tests of the electro-mechanical system (including tuning and confirmation of specifications), RF system (receive and transmit tests) and the earth station software. Some of these functional tests, which were conducted under the direction of the author by some of the CRCSS staff, revealed the necessity of design improvements, which are outlined in Section 4.9.

Although the test phase was quite considerable in time and has provided more insight into the complexity of the earth station operation, only one of the many test should be mentioned here as an example; other relevant calibration procedures are included in 5. While the CRCSS laboratory owns RF instruments up to 50 GHz, only equipment up to 22 GHz was transportable enough to be used at the antenna site. As a result, a method had to be devised to qualitatively prove successful transmission *on-site* at 29.93 GHz. In order to use the available instruments (HP 8350A signal generator and HP 8592A spectrum analyser), an external microwave circuit was devised which converts the Ka band transmit signal to lower frequencies (Fig. 4.33).

While this uncalibrated test setup does not allow for quantitative output power measurements, it does *qualitatively* confirm transmission, including spectral characteristics and the proper functioning of the uplink Doppler pre-compensation. Since all components
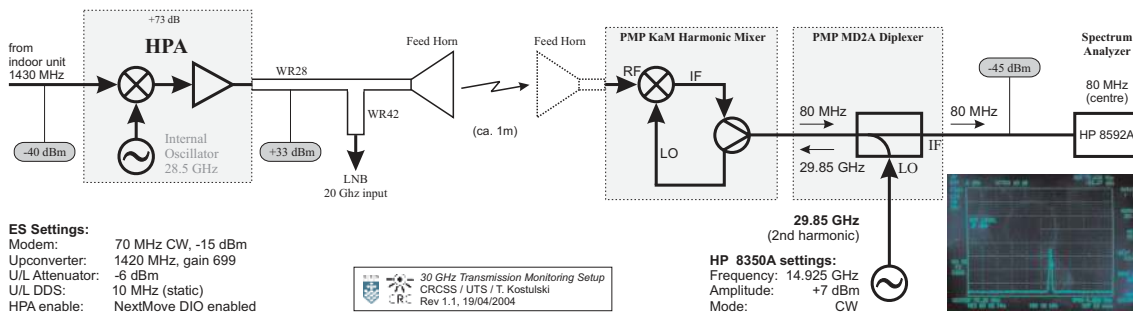
Figure 4.33: 30 GHz transmit monitoring setup using a harmonic mixer and diplexer as a conversion circuit

had been thoroughly tested before deployment, this seemed to be a sufficient functional test with the existing equipment. A spectrum analyser image of the 29.93 GHz transmit signal is included in the lower right corner of Fig. 4.33.

4.9 Post-Deployment Design Modifications

The previous sections have already highlighted several points of compromise in the earth station design. Some issues identified by the author during the deployment and the functional testing stages have led to important modifications, most in terms of the improvement of the initial specifications and of the operational reliability, but some also as necessary measures to prevent damage to the hardware.

4.9.1 Improvement of the Control Loop Dynamics through Mechanical Changes

During servo drive tuning, it was discovered that position-dependent vibration occurred predominantly during positional movement of the dish, but also during tracking (magenta line in Fig. 4.34). It should be noted that the following error scale (-0.05...0.05) is magnified by a factor of 10, compared to the velocity scale (-0.5...0.5). The key improvement to achieve a both smooth and accurate movement, especially on the Y axis, has been the reduction of load. Since changes to the heavy reflector support structure would have meant a major reconstruction, the attention was drawn to reducing the mass of smaller objects at a great distance to the axis, therefore reducing the turning moment at the axis. Clearly visible in Fig. 4.11 above, the following items were identified and modified:

- **Feed assembly support arm** - Originally intended by the manufacturer for a GEO VSAT application, the arm was constructed from folded sheet metal and weighted in
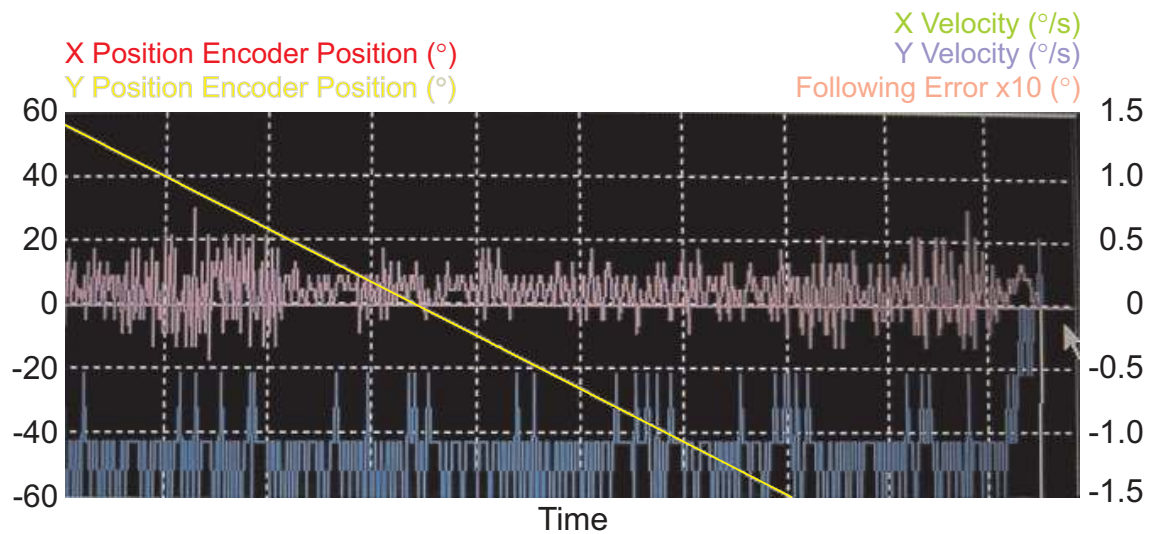
Figure 4.34: X/Y position encoder, velocity and following error during a 58° to -87° test move. The vibrations in the order of ±0.05° at certain tilt angles are clearly visible, as are the velocity quantisation levels and the associated PWM control by the servo drive.

at around 5 kg. Maintaining precisely the same dimensions and angles, a replica was machined and welded from aluminium in-house at a mass of less than 1.5 kg. This was further reduced to 1 kg by perforating the new arm with large holes, without compromise of its structural integrity. The new arm was precisely positioned to match the manfacturer's feed horn location specifications within 1 mm ($\cong 0.07°$).

- **HPA relocation** - Since the bent pipe mode link budget is clearly downlink limited, it was decided that a few tenths of dB could be sacrificed by relocating the HPA away from the diplexer and closer to the rim of the reflector. A rigid WR28 waveguide was mounted on the arm across the gap and connected to the existing flexible waveguide at the top of the diplexer.

These two design improvements were modelled in the computer-aided design software to assess the effect on the required torque and then realised (Fig. 4.35, left). As expected, they had such a profound effect on the dynamics of the structure that a compromise in the calibration parameters of the inner control loop was eventually found. While even the X axis is running noticeably smoother than before, very small vibrations on the Y axis are now barely noticeable only around zenith, when the backlash tolerance briefly comes into play. A photo of the new design is provided in Fig. 4.35, and related NextMove™ results are presented in the next section.
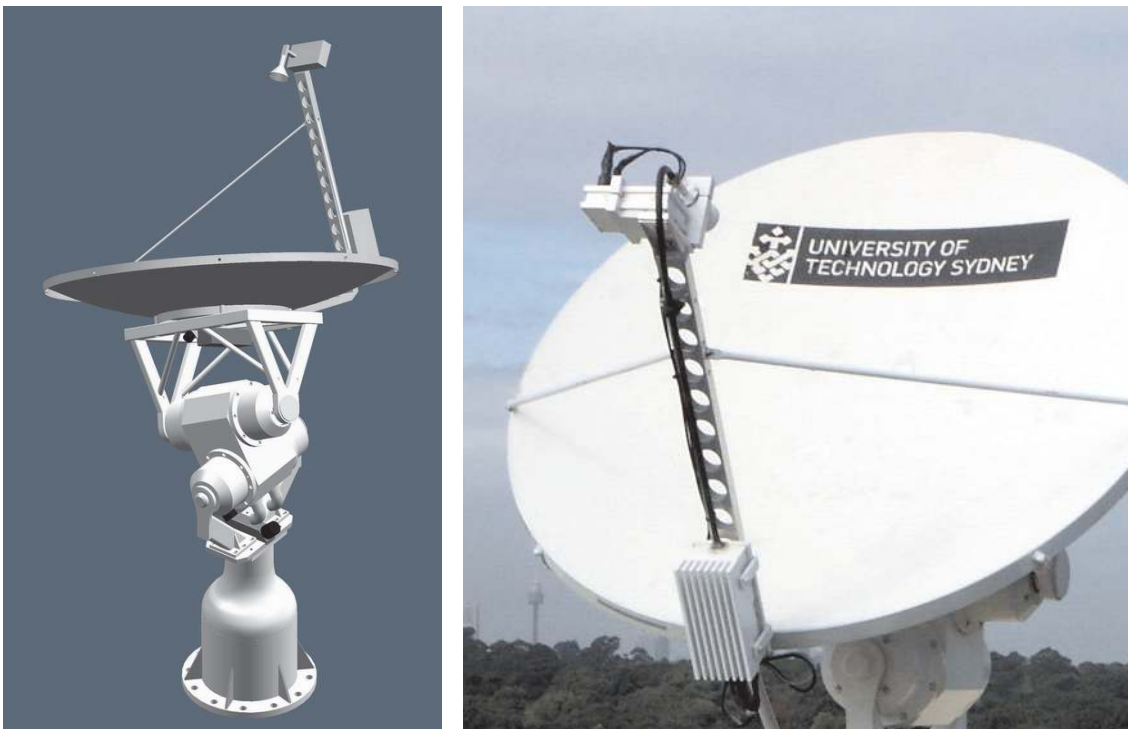
Figure 4.35: 3D model (left) and realisation of the modified feed assembly design, reducing the torque demand on both axes

4.9.2 Dynamic Improvement of the Pointing Accuracy

Functional tests have shown that the high-ratio gearbox and the unusual application of the servo drives cause some discrepancy between the indicated position of the motor and the position encoder. Especially for very long positioning moves, for example from the home position $(X = 0°, Y = 0°)$ to $\pm 85°$, the error tends to accumulate and results in a wrong final position up to about $0.5°$ on long moves. The effect can be clearly observed in Fig. 4.34 above, where the magenta following error has a non-zero average value. Normally, an increased integral coefficient in the PID control loop would take care of a steady-state error, but as previously mentioned, the adjustment of the control loop parameters is very sensitive and can easily cause vibrations in other load situations. It was therefore decided to pursue another strategy. Since a highly accurate position is only required at the *end* of, but not *during* positional moves, the accumulated error was simply post-compensated through a small, additional manoeuvre. However, this is not possible during tracking, hence an addition to the MINT code was devised by the author in cooperation with the CRCSS software engineer.

Instead of letting any following error accumulate, a loop periodically measures the position and the motor (following) errors, and produces a corrective angle value, which is then used to *update* the motor encoder value with the correct position, eliminating any build-up and propagation of errors. While apparently quite simple, the algorithm only uses variables that are measured or otherwise available to NextMove™, making it very efficient in the use of resources. The concept is visualised in Fig. 4.36.
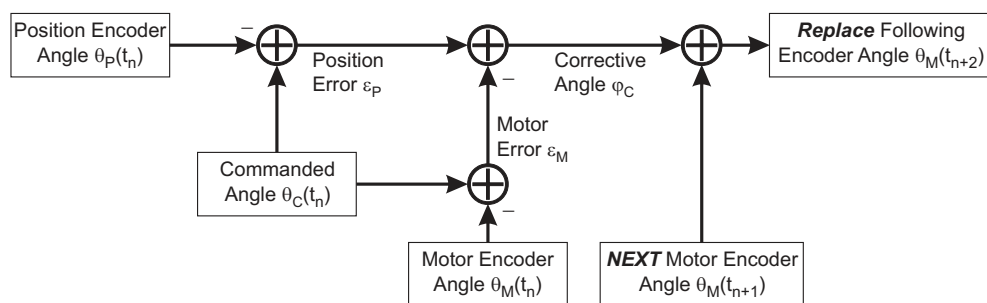
Figure 4.36: Concept of following error elimination through frequent updates of the motor encoder value

While the commanded angle is only provided in 1 second intervals, it must be remembered that NextMove™ automatically interpolates these values to suit the internal encoder update interval (several ms). For each instance, the position error ϵ_P, i.e. the *true*

discrepancy between the commanded angle θ_C and the actual angle θ_P, is calculated and compared with the motor (following) error ϵ_M, which the servo drive control loop *regards* as the true error. Subtracting those errors gives a compensation value φ_C, which is added to the motor encoder angle θ_M in the next step, resulting in a new motor encoder value very, very close to the true position, since the time increment and the angular velocity are both quite small. This value then *overwrites* the motor encoder value in the next step, eliminating the error and providing a better input to the inner control loop. The read-and-update procedure is illustrated in Fig. 4.37
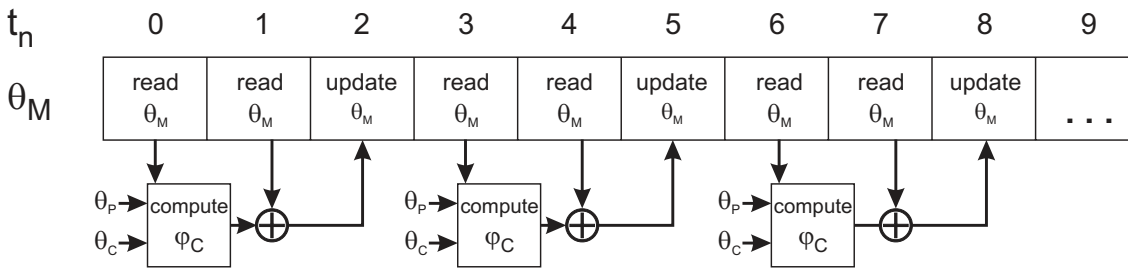
Figure 4.37: Illustration of the periodical read-and-update procedure to instantly eliminate the following error

The processing delay in this case is up to two intervals (one for the motor encoder value and two for the corrective angle), but tests have shown that this does not degrade the effectiveness of the algorithm, as proven by Fig. 4.38. Again, it should be noted that the compensation is active *only* during the tracking phase, and correction limits have been implemented to ensure unconditional stability of the loop. The graph shows the motion records of an actual satellite pass, including positioning moves (slightly truncated at the start and end), tracking phase and return to home position. The data was recoded *after* the feed assembly arm modification described the previous section.

The first (left) section shows how the two axes simultaneously drive to their respective AOS positions (red/yellow), which the Y axis reaches earlier and therefore keeps the motor energised until the start of tracking. The X axis following error is well visible during the positioning phase, as are (minor) vibrations. After the precisely time-coordinated start of tracking, the following error is immediately reduced close to zero, with about $\pm 0.01°$ deviations from time to time, which is in the order of the position encoder resolution and is therefore unlikely to originate from physical vibrations. After the end of tracking, the antenna is driven back to the home (0,0) position, which causes a temporary rise of the following error during the move only.
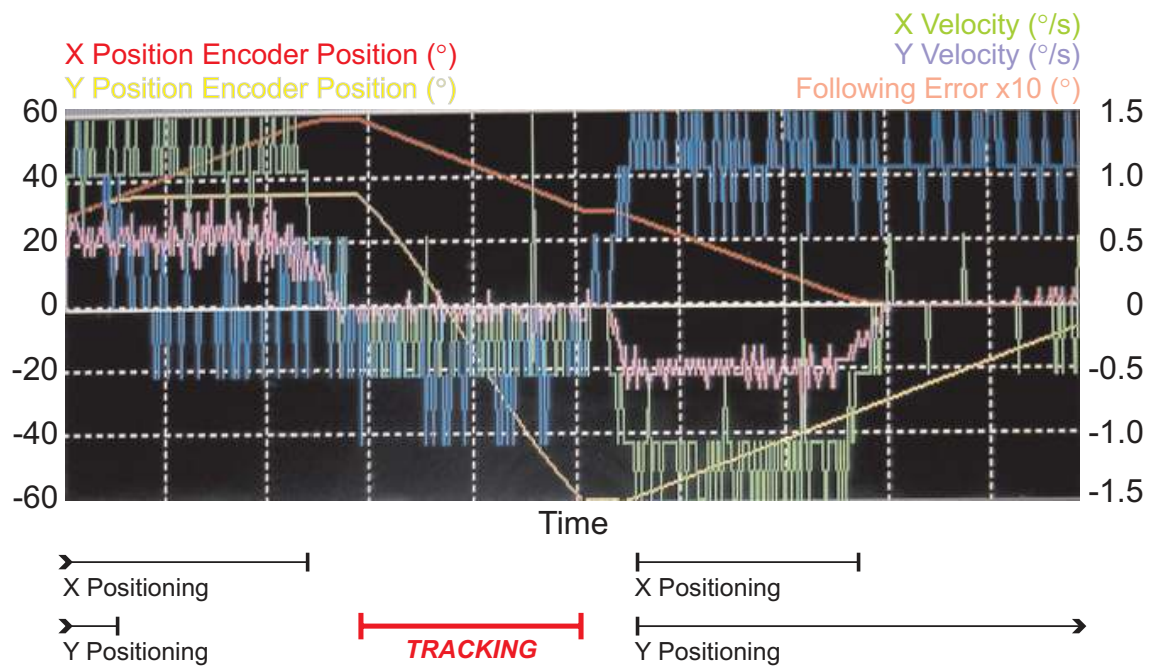
Figure 4.38: Satellite pass recorded by NextMove™, showing the X/Y axis position, velocities and following error. The difference in error between positioning moves and tracking is evident, as is the reduction of vibrations.

The performance has even been tested under very adverse weather conditions during a pass, with wind gusts exceeding 60 km/h on one occasion. Recorded motion data confirms that the tracking accuracy is virtually unaffected by the gusts due to the rapid position update.

Conclusion: The compensation algorithm has been proven an effective measure to eliminate the effect of the following error on position accuracy. The positional error is reduced below encoder resolution during tracking and is therefore not expected significantly contribute to the overall earth station pointing error.

4.9.3 Limitation to Supervised Operation

It has already been outlined Section 4.4.4 that the automatic levelling had to be abandoned due to the unexpectedly large long-term drift of the inclinometer and due to the use of relative position encoders instead of absolute ones. Another reason why the author eventually preferred supervised operation over remote/automatic passes, although associated with a considerable logistic effort for every single pass, was the vulnerability of the gearbox to sudden jolts or unexpected faults, which are more likely to occur when

unsupervised. In the deployment phase and at a later stage, there have been two very unfortunate incidents of gearbox damage (see Section 7.1) as a result of software and/or hardware malfunction. Both incidents rendered the earth station inoperative for up to two months while spare parts were on back-order. Since the severity of the damage is a direct result of the initial pedestal design, which could *not* be changed during the operational phase, the causes of these incidents and possible remedies are further discussed in Section 7.2. The limitation in supervised operation resulted in a reduction of the initially anticipated number of passes that could be run, mainly due to the limited availability of *two* staff to come to the site for several hours for every pass.

4.9.4 Improvement of Sampling Interval

The initial design of the DSP software mainly aimed at the compensation of the Doppler shift and the recording of the received spectrum for modulation analysis purposes. When the propagation measurements were included in the Ka band experiments, the original sampling intervals of 70...100 ms was not considered sufficiently small any more. Since the DSP board already operated at maximum capacity, the author and the CRCSS software engineer sought ways to improve the efficiency of the DSP routines to allow a sampling rate of 5 ms or less. An investigation revealed that the bottleneck did not lie within the code running on the DSP board itself, but in the frequent transfer of data between the DSP board and the host PC. A change in the data transfer strategy resulted in a decrease of the peak power sampling interval to an average of only 4 ms. The design improvement is illustrated in Fig. 4.39.

It was identified that the DSP memory was a largely unused resource. Instead of transferring the sampled spectrum (1024 bins, I/Q channel, double precision) to the host PC immediately, it is now efficiently transferred to the DSP board's on-board memory and entirely stored there. The freed processing power was used for a vast increase in the peak power sampling rate (1 bin, double precision) every 4 ms, which is also stored in the DSP board's memory. The memory available for user data storage on the board is conveniently just big enough to hold the spectrum and the samples for expected tracking durations. At the end of the pass, when no more DSP processing is required, the entire memory content is transferred to the host PC and stored in separate hard disk files.

It should be mentioned that this method has worked very well and reliably during all live passes. However, a possible issue was identified during a test run, when an error occurred during the pass and the DSP board had to be reset. In a fault case like this, the entire data recorded in the DSP memory to that point would be lost. In that respect, the original method can be considered "fail safe", but much slower.
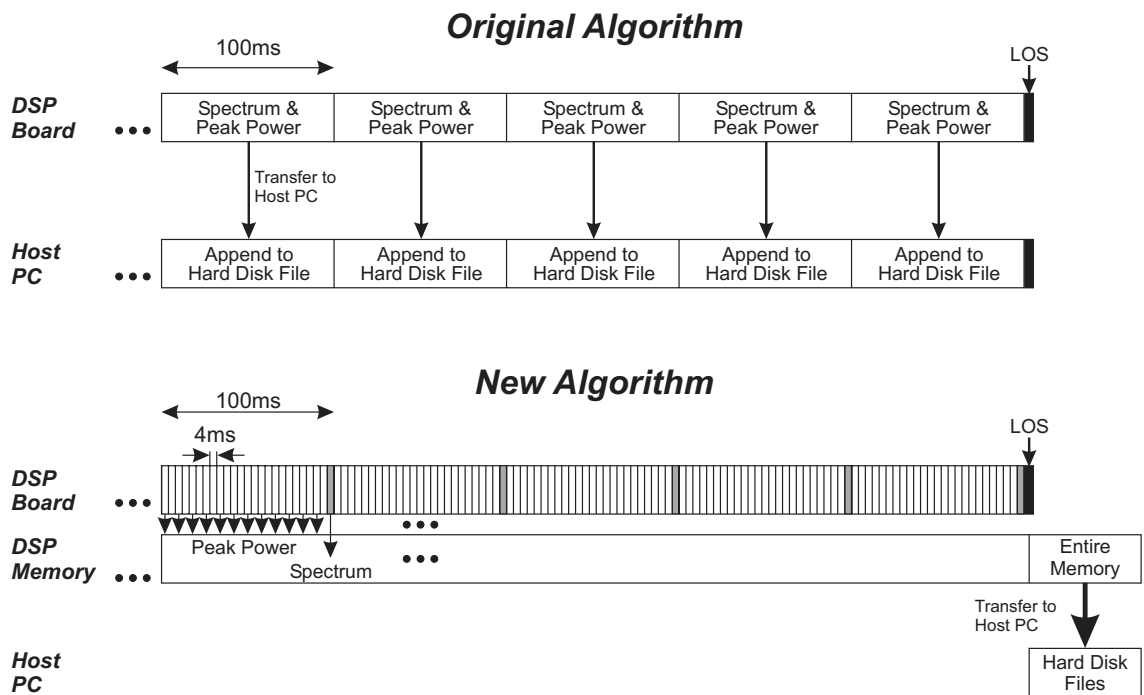
Figure 4.39: Algorithm improvement strategy for a shorter power sampling interval

4.10 Summary - Earth Station Specifications

The following Table 4.8 summarises the most important features of the UTS fast-tracking Ka band earth station in one place for later reference.

General	
Location	Sydney, Australia (UTS Kuring-gai)
	33.79° S, 151.16° E, 78.5m ASL
Deployment	February 2003 (fully operational: May 2003)

Tracking System	
Pedestal	X/Y configuration, custom design prototype
Electromechanics	Baldor AC servo motors with 100:1 low-backlash
	planetary gearboxes, FlexDrive servo drives and
	5000-line quadrature position encoders on each axis
Motion Controller	NextMove™ controller board using MINT™
	motion control software
Tracking accuracy	better than 0.02° (long/cross)

RF System	
Operating frequencies	Uplink 29.93GHz (RCP), downlink 20.13GHz (LCP)
Reflector	1.2m parabolic offset (Prodelin, custom-made)
Antenna gain	44.9dBi receive @20GHz, 49.5dBi @30GHz
3dB beamwidth	0.92° @20GHz, 0.58° @30GHz
LNB	NewTec, 1.8dB noise figure, 50-65dB gain
HPA	NewTec, 33dBm output power, 73dB gain (sat.)
System noise temperature	25.22dBK
Modem	Vitacom VSAT M4000, 128kbps
Operation modes	Beacon receive, beacon bent pipe, data bent pipe

Doppler Tracking	
Strategy	Blind acquisition and high-precision open-loop tracking
Signal Processing System	Blue Wave dual TMS320C6711 DSP board with
	analog 70MHz IF interface card
Sampling interval	4ms
Doppler compensation	Downlink: real-time DDS 10MHz LO signal
	Uplink: pre-calculated DDS 10MHz LO signal
Acquisition range	$\pm$3MHz
Acquisition time	<500ms (typ.)
max. Doppler rate	50kHz/s

Software Design	
Platform	2 PCs (P-III 600MHz), Windows NT™
Control software	Visual C++ (in-house development)
DSP Software	Assembly code (in-house development)
RF component control	LabView™ (in-house development)

Table 4.8: Summary of selected earth station specifications

Chapter 5

Earth Station Operation and Data Collection

In the previous chapters, the space segment (FedSat) and the ground segment (UTS earth station) have been introduced as experimental platforms for the propagation experiment. This chapter examines the outcomes that could realistically be expected under the given experimental circumstances of FedSat and the earth station, and some interesting findings that have had a significant impact on the day-to-day operation of the earth station. Furthermore, a description of the procedures conducted for a typical satellite pass leads to an overview of the collected data. It will also be shown that substantial corrective post-processing is required to maintain a reasonable integrity of the measured attenuation values. The chapter concludes with some examples of the successful Doppler tracking algorithm, which has been the key to accurate power measurements.

5.1 FedSat Pass Characteristics

The general orbital properties resulting from FedSat's launch parameters have already been discussed in Section 3.2, highlighting advantageous and disadvantageous consequences for the propagation experiment. Now that the capabilities and limitations of the earth station can also be taken into account, it is possible to make a realistic assessment of what amount of data could be collected by a single LEO tracking station under ideal conditions. These are further restricted by design restrictions and operational incidents, both on the spacecraft and on the ground. The considerations in this chapter are based on the initial link design for data communication experiments, and can be somewhat relaxed for the beacon mode case, as it will be shown later.

5.1.1 General Statistics and Considerations

In a polar orbit and a period of 100'51", FedSat passes over every point on the earth's surface several times per day, but at different maximum elevation angles. Theoretically, this would mean a large number of possible observations (4 per *day*), but in practice, this number is significantly diminished by conditions imposed by the payload and earth station design. Fig. 5.1 shows the distribution of maximum elevations observed at the UTS earth station over a period of 200 days. Due to the particular radiation pattern of the spacecraft Ka band antenna (Section 3.5.2), the link budget requires a minimum elevation angle of approximately 30°. As the chart shows, 77% of all passes already fall below this limit, and less than 5% reach a maximum elevation of 70° or higher. The statistic includes both descending (day) passes and ascending (night) passes.
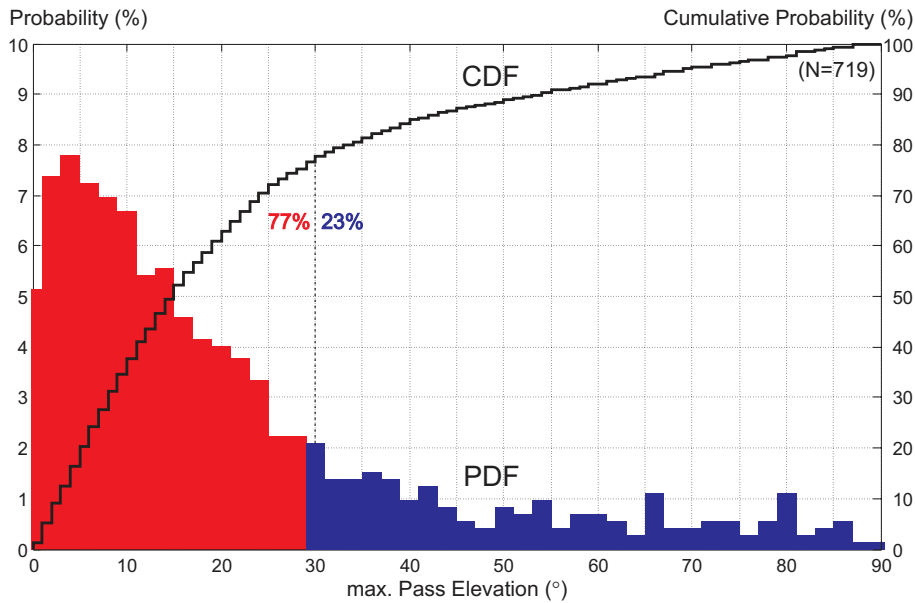
Figure 5.1: PDF and CDF of maximum pass elevations over a 200-day period. The red area indicates maximum elevations below the design limit of 30°, which make up 77% of all possible passes.

Besides, in order to maximise the time for data collection over a wide range of different elevation angles, one would aim to select passes with the longest duration. The interesting relationship between maximum observed elevation angle and the duration of the pass (for 2 cases) is depicted in Fig. 5.2, based on the same set of 200-day data. The upper curve shows the relationship of the pass duration with the maximum elevation of that particular pass. All visible passes (max. elevation $\geq 0°$) are taken into account, and as intuitively expected, low-elevation passes have a fairly short duration. However, above

approximately 20°, a further increase in pass duration is not that significant any more (800 s at a 20° pass versus 915 s at a 90° pass). A similar effect can be observed when masking all visible passes by the minimum 30° requirement (lower curve), which not only decreases the total pass duration to 338 s, but shortens the tracking time of passes of less than $35 - 40°$ so significantly that the experiment time can be considered too short to be of interest. This further limits the percentage of practically "usable" passes to less than 16% of the total, or 4 passes per *week* on average. Taking into account the operational restrictions, no site access at night due to safety regulations, leaves only *two* practical passes per week and a potential data collection window of less than 10 minutes each.
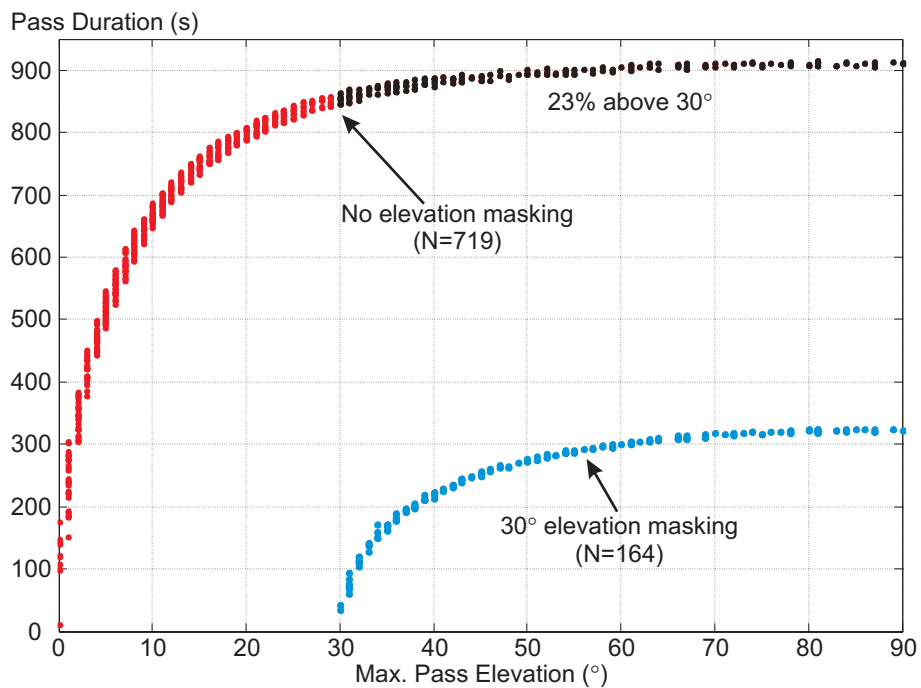
Figure 5.2: Pass duration vs. maximum elevation for visible passes and for passes with a 30° elevation mask

It can therefore be concluded that successful propagation data collection from a low-power LEO satellite like FedSat is a very challenging venture, simply because of the small number of suitable passes. On the positive side, a wide range of elevation angles can be observed in a single pass, and it is worthwhile to look into the occurrence of certain elevation angles for that purpose. Fig. 5.3 shows the statistical analysis of the momentary elevation angles occurring per 1-second interval on all visible passes during a 100-day period. In this case, elevation angles above the design limit (blue) make up only 12% of all elevations encountered, and angles over 70° account for less than 0.7% of the total time.
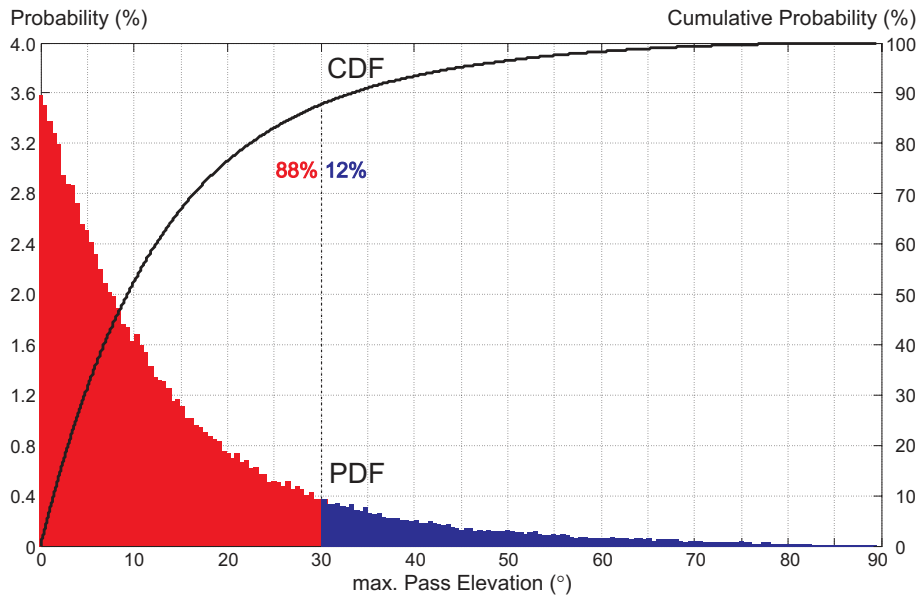
Figure 5.3: Statistics of elevation angles encountered in 1-second intervals over a 100-day period

It will be shown in Chapter 6 that these considerations could be somewhat relaxed for the case of beacon reception, since successful signal tracking was in fact possible well below the 30° design limit.

5.1.2 Selection of Suitable Passes

Ka band experiments via FedSat were usually scheduled in two stages, long-term an short-term. Due to the fact that the communications experiment had to share the resources with the other payloads, the mission operations officer always had the authority to limit experiments to certain days or times in order to ensure the health and stability of the spacecraft. Typically, the UTS team would generate a long-term ephemeris for about 4-6 weeks and select a number of suitable passes, based on the following considerations:

- Day of the week,

- Maximum elevation and pass duration, and

- Possible blockage by surrounding structures along the calculated trajectory.

The resulting preference list, usually containing 2 passes per week, would have been sent to the operations officer for pre-approval and to the TT&C ground station at ITR. After tentative confirmation, arrangements would be made to conduct Ka band experiments on those days.

The "day of the week" condition was introduced by the mission operations officer for practical reasons. As explained in 3, it is vital for the Ka band experiment that accurate pointing is maintained throughout the pass. However, especially during the early phase, FedSat's attitude control system tended to slightly drift out of pointing mode or even into tumbling within a day or two if not manually adjusted; a behaviour that was corrected only much later. Since the TT&C ground station generally remained unmanned on weekends, the pointing error could not be interactively corrected until *after* the first pass on Monday morning. As a secondary effect to the ACS instability, the available battery power was usually below average due to the suboptimal exposure of the spacecraft's solar panels. Therefore scheduling a very power-demanding Ka band experiment for Saturday, Sunday and Monday could have destabilised the satellite even further. As a result, for most of the experimental phase, passes were only scheduled on four out of seven days, further restricting the available events.

5.1.3 Pass Request and CRCSS Cooperation

After the pre-approval of the long-term pass list, the TT&C ground station would be contacted again about 2 days before an experiment to confirm the spacecraft's condition and possible conflicts with other experiments. In addition, the local weather forecast would only now be reliable enough to make a very broad judgement about the possible weather conditions on the pass morning, and the Ka band operation mode would be chosen accordingly. Having calculated the visibility times, a formal pass request with payload activation/deactivation GPS times, Ka band mode and manual telecommand intervention, if any, is lodged with TT&C for final approval.

In parallel, UTS would request a recent block of raw GPS data from the GPS payload group in order to predict the most accurate orbital information for FedSat. Using a proprietary extraction, extrapolation and conversion program integrated in the UTS Earth Station Utility software (Section 4.6.5), the GPS coordinates would be converted into the required tracking coordinates for the UTS earth station. Alternatively, recent NORAD TLE parameters can be obtained and processed. The selection of the most reliable and practical source of orbital data is discussed in Section 5.2.3.

5.2 Determination of Tracking Coordinates

Once a pass has been requested, the precise tracking time and the pointing angles need to be calculated. For FedSat, two possible sources exist: the on-board GPS receiver and the NORAD orbital parameters provided as two-line elements (TLEs). While there has

been much debate over the *theoretical* accuracy of TLEs for high-precision LEO tracking, for example in [82], the author has endeavoured to verify the tracking suitability of TLEs practically. Before presenting the methodology, the two sources are briefly portrayed.

5.2.1 On-board GPS Receiver Data

Due to the power budget restrictions, the GPS receiver is periodically active for a maximum of 20 minutes of every 100-minute orbit, which means that only part of the orbital coordinates are recorded. In this pattern, it takes several subsequent orbits of data to extract a reliable set of parameters.

The GPS receiver measurements are temporarily stored in the satellite's mass memory before it can be forwarded to the TT&C ground station on the next visible pass (usually within 10-12 hours maximum). The raw data is extracted and forwarded to the GPS research group at QUT, who runs data conditioning software and quality checks to determine its suitability as an orbital parameter source. Often, this step involves manual editing of corrupted files, which is very time consuming. Only then is the data fit for use as an input to the UTS Utility software to extrapolate the pointing angles for future passes with a reasonable lead time.

This brief summary of the procedures involved to obtain GPS-based pointing angles already highlights one major issue: the validity of the data due to delay. Depending on the amount of manual intervention required, the time frame between the acquisition of coordinates by the GPS receiver and the supply to UTS can be two to four days, and then it will usually be another 12-16 hours between the processing of the coordinates and the morning pass. The interested reader is referred to [120] for an assessment of the GPS coordinate accuracy.

5.2.2 NORAD Two-Line Elements

The "North American Aerospace Defense Command" (NORAD) was originally established in 1958 as an organisation providing aerospace warnings and control by tracking man-made objects which could pose a threat to North America [121]. Since then, NORAD's capability has expanded to tracking any object, such as small satellites and even pieces of space debris as small as 10cm [122]. For most non-military objects, the orbital parameters are provided to certain civilian interest groups in the form of two-line elements, a NASA standard, which supply the entire information required to accurately and unambiguously determine any kind of earth orbit. While an example of FedSat's two-line elements is shown in Fig. 5.4, a detailed explanation of the TLE structure and relation of the data elements to a satellite's

orbital dynamics is beyond the scope of this work, and is extensively documented in the literature, for instance [2], pp. 463-465.

```
1 27598U 02056B   05307.25344481 -.00000041  00000-0  85626-6 0  7739
2 27598 098.5547 017.6473 0009543 154.4114 205.7538 14.27908769150582
```

Figure 5.4: Example of NORAD two-line elements for FedSat, valid at epoch year 2005, fractional day 307.25344481 (3 Nov 2005, 06:04:57.6 UTC)

While it is relatively easy to track large and slow objects by radar, such as aircraft, the detection of an object of FedSat's size in a 800 km orbit requires sophisticated sensors. The quality of TLE data can be quite variable from set to set, as quoted in [123]. Hence, it is justified to question the suitability of TLEs for the successful tracking of FedSat under the very stringent pointing accuracy requirements. A thorough analysis of the relationship between the TLE epoch and their reliability has been provided in [82]. The conclusion of this source is that unprocessed TLEs are *not* suitable for tracking LEO satellites like FedSat at the required accuracy, since the tolerance exceeds 0.3° at high elevation angles even for the most recent data set.

It has therefore been one of the objectives to experimentally compare the observation of FedSat with GPS and TLE data. In order to obtain the TLE data sets more frequently than publicly available, the UTS CRCSS subscribed to Space-Track [124] (access to this source requires a registration process and U.S. Government approval due to national security restrictions). The TLE data available from this source is often updated several times daily, so in most cases, the TLEs to be used for tracking FedSat are only hours old, not days. This fact has led to the hypothesis that very recent TLEs may be accurate enough.

5.2.3 Pointing Accuracy Assessment

In order to confirm that the overall pointing accuracy of the earth station lies within the specifications, a methodology based on FedSat's trajectory has been devised. At the same time, any discrepancies between the GPS and TLE data sources for tracking can be assessed. While great care has been taken during the design to minimise tolerances, the worst-case addition of the maximum errors just exceed the crucially required pointing accuracy (0.3°), and also the desired one (0.1°), Table 5.1. However, it must be noted that the largest contributing item, the gearbox backlash, will only be significant at *one* particular angle (in balance) and will be immediately compensated for by the MINT algorithm. The precise values of other errors, for example the north declination or the

feed offset angle, are unknown but constant, therefore these possible errors still allow a consistent calibration of the earth station for the duration of the experiment.

Component	Max. Error (°)
North declination	0.040
Levelling	0.010
Gearbox backlash	0.120
Position encoder resolution	0.018
Position error	0.010
Timing (equiv.)	<0.010
SGP4 coordinate conversion [125]	0.075
Feed offset angle	0.071
Two-line elements	unknown
Total	0.354

Table 5.1: Sources contributing to the overall pointing error

This only leaves the original source of the pointing coordinates, the TLEs, as the main, unknown contributor. As stated in [82], the main source of TLE inaccuracy are not the coordinates as such, but the timing. In order to assess how GPS and TLE generated pointing angles compare, a timing comparison method has been devised, illustrated in Fig. 5.5. The prerequisites for this method to be meaningful are the availability of good quality GPS data no older than one day and TLE data no older than several hours, both valid for a *high-elevation* pass (>75°). A higher maximum elevation results in a higher relative velocity of the spacecraft and therefore in a more accurate measurement. It is also important that the experiment takes place under clear sky conditions to avoid major measurement perturbation by atmospheric effects. Using either the TLE or GPS coordinate source, the following procedure has been implemented in MINT™ as a "Time-Referenced Positional Move", and runs automatically:

Just prior to AOS, position the antenna at a certain X/Y coordinate along the trajectory of the pass, point (1) in the graph. The elevation should be high enough so that the signal is likely to be observed in the noise, for example 30°. As the satellite passes through this point, the signal will appear, quickly rise to a maximum value and then fade again as it passes through the antenna aperture. All signal levels should be recorded with precise time-stamps. When the satellite has moved on (several seconds after the calculated time), drive the antenna to another point along the trajectory (2) at a higher velocity so it is positioned there well before the calculated time that the satellite passes through. Repeat the measurement procedure from above, and subsequently move to all remaining points
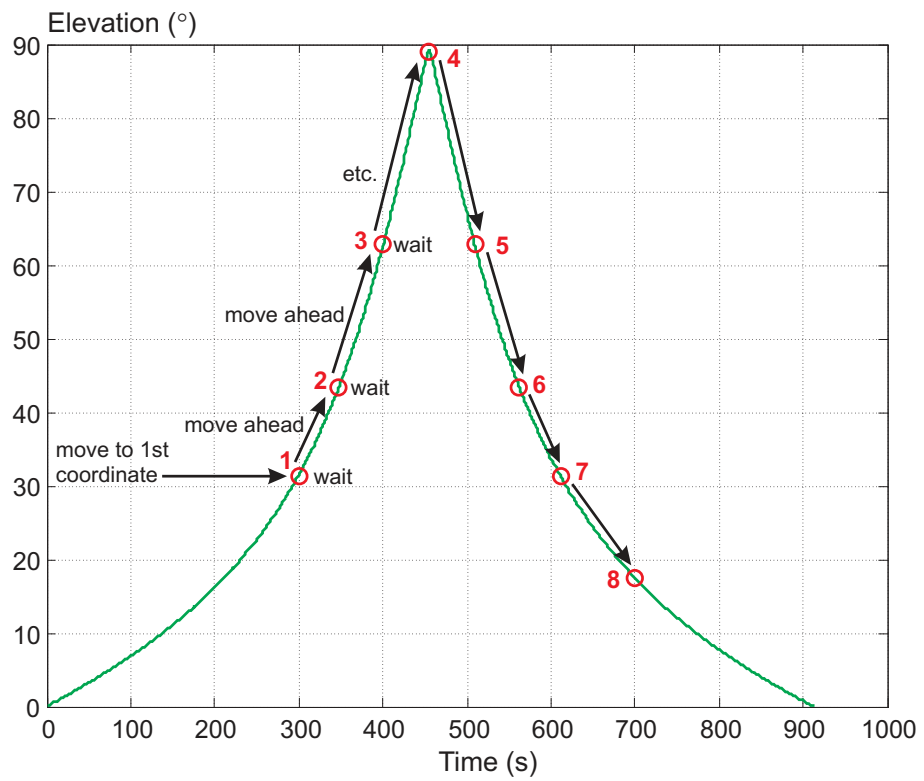
Figure 5.5: Conceptual illustration of the "time-referenced positional move" strategy to determine timing offsets

along the path (3)-(8). The signal observation time on each point will be shortest around the maximum elevation, and longest closer to the horizon due to the relative spacecraft velocity perceived at the earth station. The evaluation of the measurements is conceptually illustrated in Fig. 5.6.
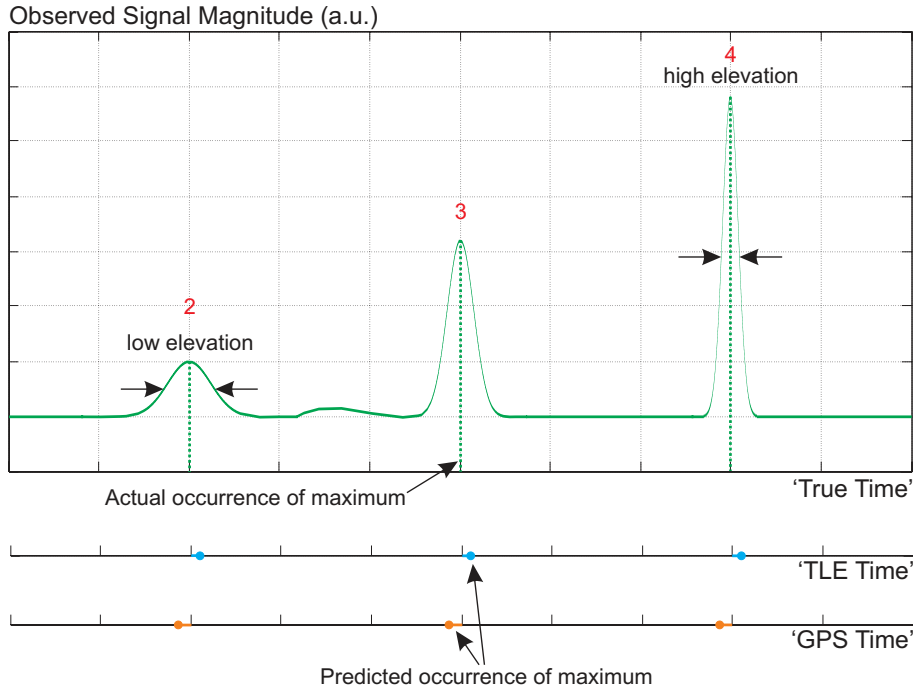
Figure 5.6: Illustration of the timing offset evaluation of GPS and TLE data in relation to the observed signal maximum at positions 2, 3 and 4

Since all recorded power levels are precisely time-stamped every 4 ms, it is possible to determine the occurrence of each maximum fairly accurately at a given look angle (some low-pass filtering may be necessary at low C/N ratios). Especially the measurement near the maximum elevation (4) is of interest, since the peak is very well defined and allows a most accurate estimate on the time instance. Having identified the 'true' position of the spacecraft at a certain time, direct comparisons with the 'predicted' times can be made. As previously stated, most TLE inaccuracies are expected to be of timing offset nature, but this method will also work for a small amount of timing *and* cross-track error. The predominant type of GPS coordinate error is unknown, however quality-controlled GPS coordinates have generally been considered more accurate than the TLE coordinates. Comparing the timing between the true time and the GPS/TLE coordinates at the given instance (some interpolation may be required), it is possible to quantify the amount of timing error for both methods. At near-overhead passes, a timing offset of 1 second

translates to an angular offset of approximately 0.5°, which is considerable. Conversely, a timing offset of 200 ms would just meet the desired specifications.

Based on several such measurements during high-elevation passes and clear weather conditions (June-August 2003), the following conclusions can be drawn:

- The accuracy of the coordinates produced from the GPS source varied with both the GPS data age and with the quality (assessment provided by the QUT GPS research group).

- For very recent source data of good quality (GPS: 1 day, TLE: 12-24 hours), the difference between the resulting offsets is negligible.

- For very recent source data of good quality (GPS: 1 day, TLE: 12-24 hours), the offsets are <300 ms ($\equiv 0.15°$), and predominantly <200 ms ($\equiv 0.1°$) for both sources.

- TLE data more than 5 days old shows significant deviations from more recent TLE and GPS data and should be considered unsuitable for tracking (this has not been verified through experiments though).

These encouraging results led to the judgement that *TLE* data instead of GPS data should be considered as the primary source for orbital elements, especially due to the awkward and complicated procedure of obtaining the GPS data within the required time frame. The "Space-Track" database would provide reliable access to the most recent TLE data sets, and would result in a similar tracking accuracy compared to GPS data.

Conclusion: For data no older than 24 hours, two-line elements can be considered a valid source for the successful spatial tracking of FedSat (and possibly for similar LEO satellites), achieving a pointing accuracy of better than 0.15°.

During the subsequent 2.5 years of operation, *not a single* experiment was deemed unsuccessful due to pointing angle inaccuracies (Section 5.6), but could always be attributed to other earth station or spacecraft malfunctions. This fact validates the above claim that very recent TLEs are suitable for fast-tracking LEO satellites. In addition, this section has demonstrated that the spatial tracking tolerances and other sources of error listed in Table 5.1 are small enough (<0.5° worst case, <0.25° realistically) as a basis for reliable power measurement results.

5.3 Power Measurement Calibration and Accuracy

Since the power level measurement at the analog interface card input is relative to the gains and losses along the RF downconversion circuit, the recorded values do not immediately allow the deduction of the path loss from spacecraft to earth station. Hence, a calibration of the equivalent received power level is required, i.e. what power level measured corresponds to what input level at the antenna. Also, the accuracy of these measurements depends on several internal and external influences.

5.3.1 Ka Band Payload Transmit Power

Firstly, a possible external source of error must be investigated, which could be the degradation of the spacecraft's Ka band transmit power over time. Since the beginning of operations, the Ka band payload has been frequently activated independently of propagation experiments to monitor the performance of the receiver and the transmitter through telemetry. A very detailed report by the Ka band payload research group at CSIRO has established that "The transmitter output power and the input power both in beacon mode and bent pipe mode show no reduction over time indicating that the gain of the transmit module is almost constant with respect to time" [126]. As a result, the spacecraft transmit power can be eliminated as a source of error. Examples of Ka band transmit power telemetry during beacon and bent pipe mode passes, processed by the CRCSS-developed Telemon package [78], is provided in Fig. 5.7 (it should be noted that the Telemon display time is in local time = GPS+10h-13").

5.3.2 Satellite Attitude

Further consideration must be given to the variability of the spacecraft's attitude in orbit. While deviations from pointing mode and incidents of tumbling have occurred, especially during the first year of operation, this is usually evident from the telemetry provided by the ACS. This is an important factor for the validity of the spacecraft's antenna radiation pattern, since any significant error on the pitch and roll axes will cause asymmetries in the footprint and therefore result in wrong power measurements.

After every Ka band experiment, the corresponding telemetry file was obtained from the TT&C ground station at ITR, archived and evaluated for the relevant attitude parameters. A review of the telemetry for *all* Ka band passes by the author has led to the conclusion that only two scenarios are prevalent: either the satellite was accurately in "pointing mode" with deviations usually better than than 0.5° (mostly <0.2°), or the satellite's attitude was so much perturbed that the experiment could not take place, hence
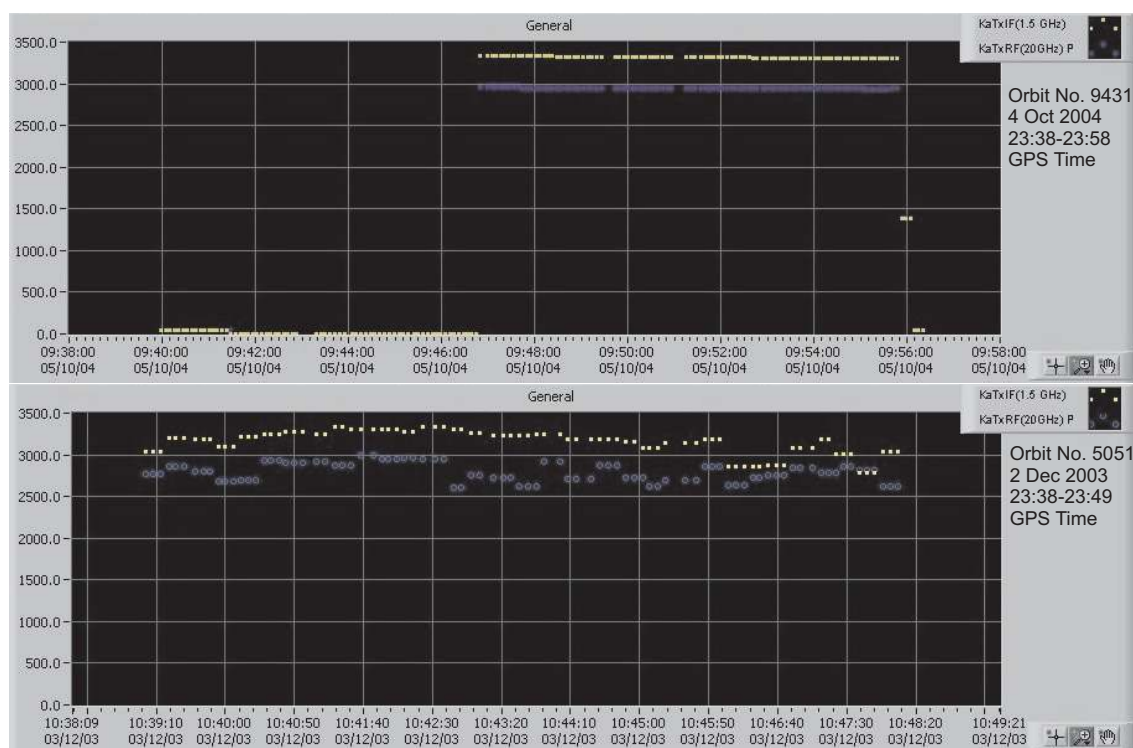
Figure 5.7: Raw telemetry of the Ka band payload transmit power (blue) during a beacon pass (top) and a bent pipe mode pass (bottom)

no signal was received in the first place. As a result, all recorded power measurements can be regarded as sufficiently accurate in terms of satellite attitude influence. Two examples of typical angular fluctuations during actual Ka band experiments are shown in Fig. 5.8. Please note that the magnitude of the fluctuations is similar between both cases, but on different scales.
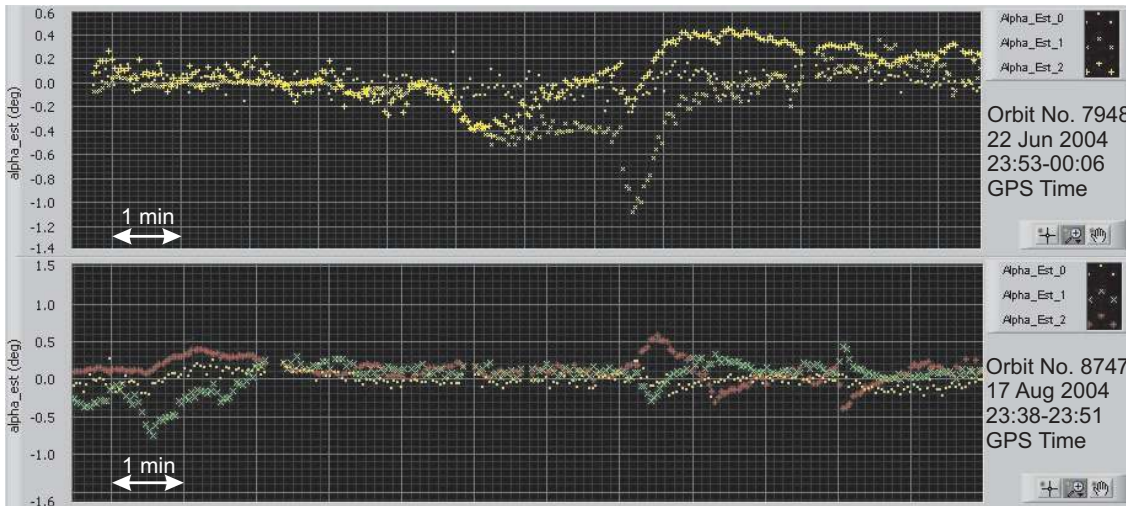
Figure 5.8: Examples of attitude telemetry recorded during two separate Ka band experiments. The Alpha_Est_0,1,2 variables correspond to the spacecraft's X, Y and Z axes.

5.3.3 Squint Angle Calculation

In pointing mode, the 20 GHz transmit antenna project a rotationally symmetric gain footprint onto the earth's surface. During a pass, the slant path to the satellite approaches the horizon and the earth station moves out of the footprint, according to the antenna's gain pattern. The effect is strongly noticeable if the off-angle between spacecraft antenna and earth station (squint angle, Fig. 5.9) exceeds $\pm 50°$, as previously shown in Fig. 3.21. This loss of antenna gain results in the perception of additional attenuation if it remains unaccounted for, hence the influence of the radiation pattern must be modelled and taken into account when post-processing the received power measurements. This is a very important difference to GEO signal strength measurements, where the radiation pattern does not need to be taken into account once the receiver has been calibrated.

The squint angle between the antenna boresight (nadir) axis and the earth station pointing angles can be derived from the orbital parameters. However, while Nova™ does not provide an output in intermediate frames of reference other than SEZ, the look angles can still be relatively easily used to 'reverse' calculate the desired coordinates in other
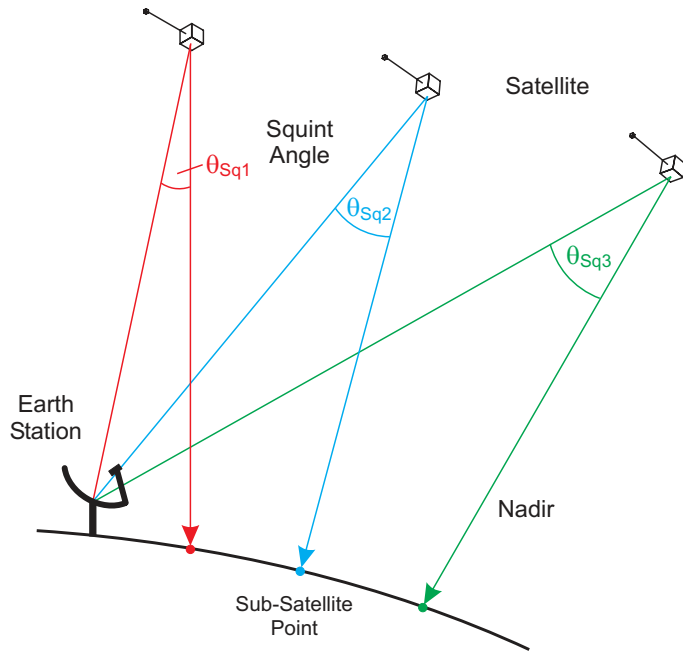
Figure 5.9: Illustration of the squint angle as a function of the satellite position relative to the earth station (not to scale)

frames of reference. In addition to the look angles (in 1-second increments), the range ρ between earth station and the spacecraft, the satellite height h_S and the subsatellite point SSP coordinates are additionally calculated by Nova™ with sufficient accuracy. Also, the earth station's geographic coordinates Lat_{ES}, Lon_{ES} and height H_{ES} are precisely known:

$$
\begin{aligned}
Lon_{ES} &= 151.160550° \text{ E} \\
Lat_{ES} &= 33.790320° \text{ S} \\
H_{ES} &= 78.5 \ m
\end{aligned}
$$

It is now possible to relate the earth station and the satellite in the geocentric-equatorial (IJK) coordinate system, which is the most suitable frame of reference in this case (see [2], pp. 47-54), Fig. 5.10.

First, the earth radius vector R_{ES} from the centre of the earth to the earth station needs to be determined, considering the earth's oblateness and the actual radius at the earth station's latitude:

$$
\mathbf{R}_{ES} = \begin{pmatrix} \left(\dfrac{a_E}{\sqrt{1-e_E^2 \sin^2 Lat_{ES}}} + H_{ES} \right) \cos Lat_{ES} \cos Lon_{ES} \\[2ex] \left(\dfrac{a_E}{\sqrt{1-e_E^2 \sin^2 Lat_{ES}}} + H_{ES} \right) \cos Lat_{ES} \sin Lon_{ES} \\[2ex] \left[\dfrac{a_E}{\sqrt{1-e_E^2 \sin^2 Lat_{ES}}} \left(1 - e_E^2 \right) + H_{ES} \right] \sin Lat_{ES} \end{pmatrix} \tag{5.1}
$$
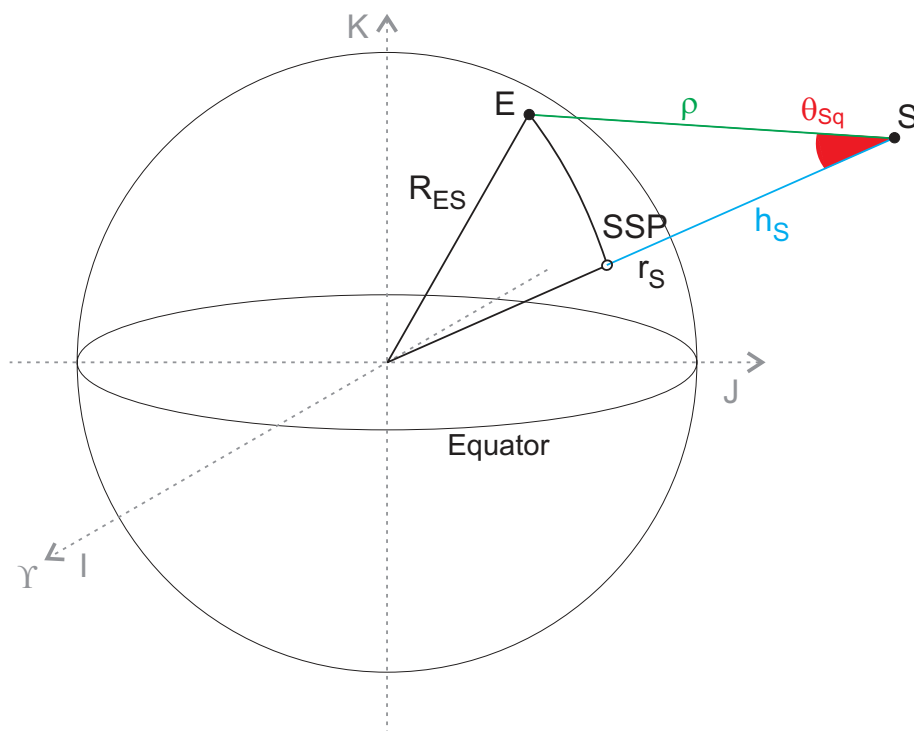
Figure 5.10: Earth station and satellite position vectors for squint angle calculation in the IJK frame (not to scale)

with the earth's semimajor axis $a_E = 6378.1414$ km and the eccentricity $e_E = 0.08182$. For the UTS earth station, the values are:

$$\mathbf{R}_{ES} = \begin{pmatrix} -4648.1849 \\ 2559.5295 \\ -3527.1868 \end{pmatrix} \text{ km} \tag{5.2}$$

Hence the magnitude of the earth station IJK vector is $|\mathbf{R}_{ES}| = 6371.6450$ km. With the knowledge of the satellite's SSP coordinates and its height above the SSP, the same procedure can applied to the satellite IJK vector $\mathbf{r}_S$ at any given time of the pass.

$$\mathbf{r}_S = \begin{pmatrix} \left(\frac{a_E}{\sqrt{1-e_E^2 \sin^2 Lat_{SSP}}} + H_S \right) \cos Lat_{SSP} \cos Lon_{SSP} \\ \left(\frac{a_E}{\sqrt{1-e_E^2 \sin^2 Lat_{SSP}}} + H_S \right) \cos Lat_{SSP} \sin Lon_{SSP} \\ \left[\frac{a_E}{\sqrt{1-e_E^2 \sin^2 Lat_{SSP}}} \left(1 - e_E^2 \right) + H_S \right] \sin Lat_{SSP} \end{pmatrix} \tag{5.3}$$

The difference between these two vectors is the range vector ρ from the earth station to the satellite.

$$\rho = \mathbf{r}_S - \mathbf{R}_{ES} \tag{5.4}$$

$|\rho|$ must be calculated next. For verification purposes, $|\rho|$ must be identical to the range value calculated by the SGP4 algorithm in Nova™. Now that all vectors and magnitudes of this 3-dimensional triangle are known, the cosine of the squint angle θ_{Sq} can simply be obtained by the dot product of the two enclosing vectors divided by the product of their magnitude ([127], p. 62):

$$\cos \theta_{Sq} = \left(\frac{\rho \cdot \mathbf{r}_S}{|\rho||\mathbf{r}_S|} \right) \tag{5.5}$$

Since some of the input parameters are provided in different time increments (1 s Nova™ output versus 4 ms measurements), these numerical calculations have also required several intermediate steps of spline interpolation and curve smoothing (filtering). Great care has been taken to maintain accuracy while processing the data. As a result, the squint angle is accurately known for all time instances and look angles during a pass. Fig. 5.11 shows an example of the squint angle calculated for a particular pass, both as a function of pass time and elevation. It is interesting to observe that the squint angle is not completely symmetrical about the maximum elevation in its ascending and descending sections due to the inclined orbit. The squint angle can now be used in place of the 'off-boresight angle' in conjunction with the antenna radiation pattern, which is handled in the following section.
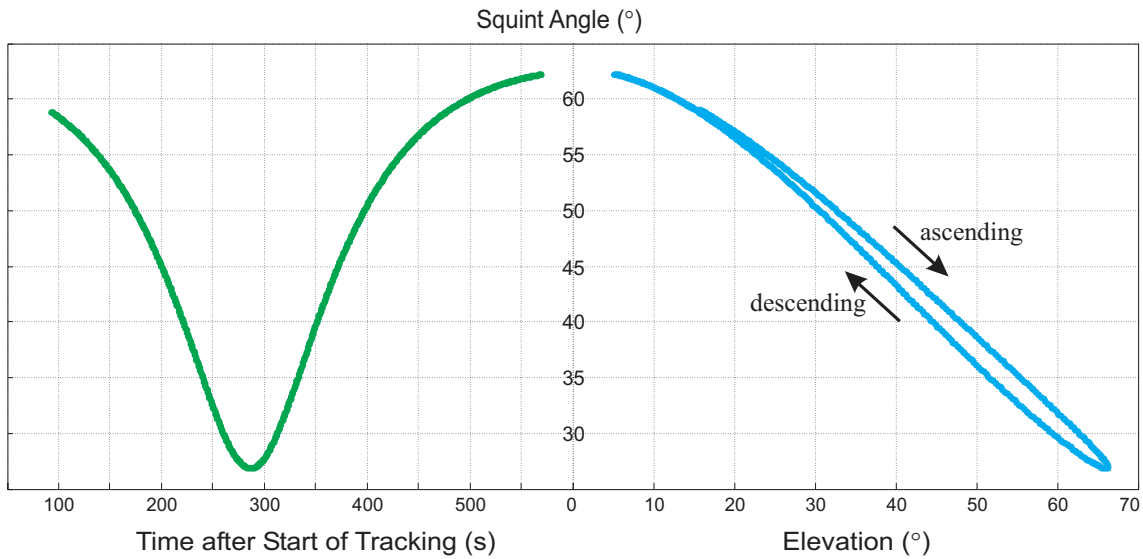
Figure 5.11: The squint angle calculated for a particular pass as a function of time (left) and elevation angle (right)

5.3.4 Antenna Radiation Pattern Modelling

Due to the rotational symmetry of the spacecraft antennas' radiation pattern, it would stand to reason that an analytical *model* for the uplink and the downlink is most convenient, based on the existing *measurements* of the actual spacecraft antenna (see Section 3.5.2). A polynomial approach of the form

$$p(x) = p_1 x^n + p_2 x^{n-1} + \ldots + p_n x + p_{n+1} \tag{5.6}$$

appears to be the obvious solution, and numerical regression based on the least squares algorithm using Matlab™ results in a best fit for a polynomial of 14th order, with the coefficients as in Table 5.2. A graphical output for both antennas verifies the suitability of the model (Fig. 5.12).

For beacon mode measurements, which constitute the majority of the experiments by far, only the transmit antenna pattern is important. Due to the rotational symmetry, the radiation pattern can easily be transformed into a 3-dimensional model, which is then used to correct the received signal strength at the earth station (Fig. 5.13).

By modelling the antenna pattern *analytically* and using this model in conjunction with the prevailing squint angle, the processing time of up to 150,000 power measurement data points per pass was greatly shortened.

n	p_{nRx}	p_{nTx}
14	$-4.4734 \cdot 10^{-24}$	$-5.9695 \cdot 10^{-24}$
13	$-4.1188 \cdot 10^{-23}$	$3.4529 \cdot 10^{-23}$
12	$1.0605 \cdot 10^{-19}$	$1.3815 \cdot 10^{-19}$
11	$1.1223 \cdot 10^{-18}$	$-5.4071 \cdot 10^{-19}$
10	$-1.0342 \cdot 10^{-15}$	$-1.3116 \cdot 10^{-15}$
9	$-1.0950 \cdot 10^{-14}$	$2.9736 \cdot 10^{-15}$
8	$5.3179 \cdot 10^{-12}$	$6.5454 \cdot 10^{-12}$
7	$4.9258 \cdot 10^{-11}$	$-6.7889 \cdot 10^{-12}$
6	$-1.5099 \cdot 10^{-8}$	$-1.8020 \cdot 10^{-08}$
5	$-1.0616 \cdot 10^{-7}$	$5.7409 \cdot 10^{-09}$
4	$2.1307 \cdot 10^{-5}$	$2.4855 \cdot 10^{-05}$
3	$9.9918 \cdot 10^{-5}$	$1.3619 \cdot 10^{-07}$
2	$-1.0781 \cdot 10^{-2}$	$-1.2666 \cdot 10^{-02}$
1	$-2.9629 \cdot 10^{-2}$	$-2.5439 \cdot 10^{-03}$
0	6.0000	5.7685

Table 5.2: Coefficients for the polynomial spacecraft receive and transmit antenna models
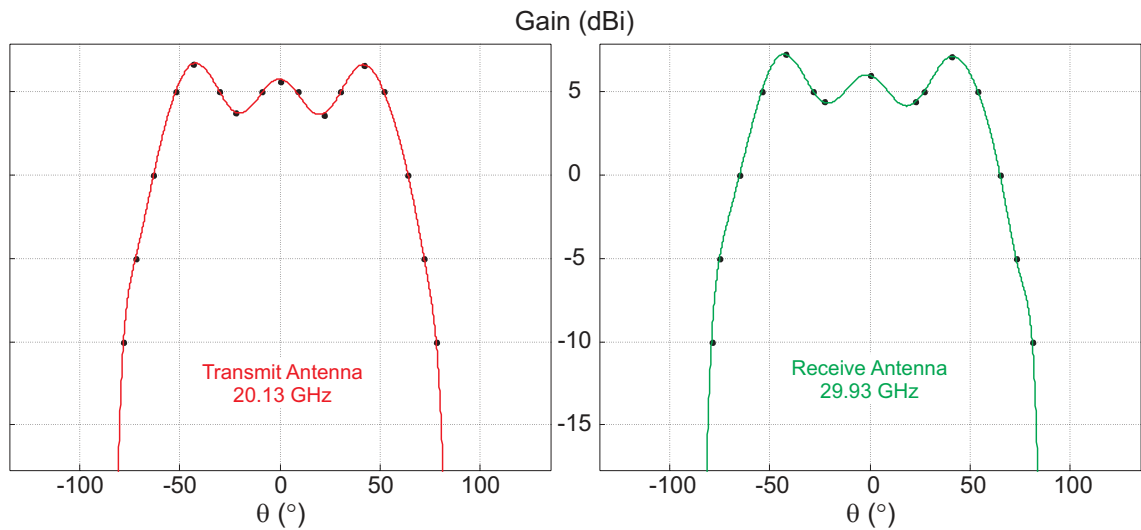
Figure 5.12: Approximation of the Ka band antenna radiation patterns by polynomial models. The black dots represent the original gain measurements on the spacecraft antennas.
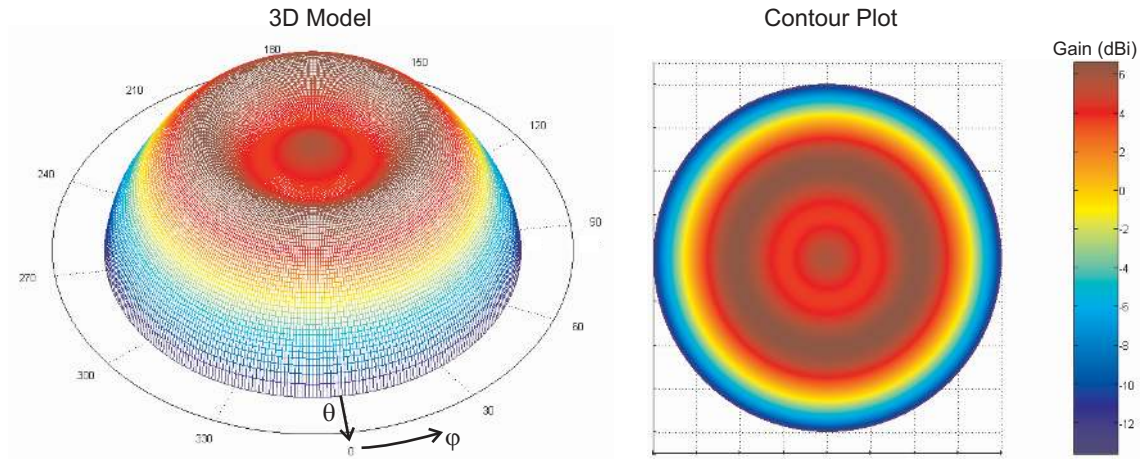
Figure 5.13: 3-dimensional visualisation of the spacecraft transmit antenna model (left) and the associated contour plot, indicating the variable off-boresight gain values.

5.3.5 Pointing Angle Accuracy to Power Measurement Uncertainty Conversion

It has previously been established in Section 5.2.3 that the maximum pointing accuracy is better than $\pm 0.5°$, with a typical value of probably not more than $\pm 0.25°$. Referring to the receive antenna 3 dB beamwidth measurements in Section 4.3 and applying the formula derived in [82], the off-boresight loss $L_{off-boresight}$ for very small angles on parabolic reflector antennas can be expressed as

$$L_{off-boresight} = 12 \cdot \left(\frac{\theta}{\theta_{3dB}} \right)^2 \text{ dB} \tag{5.7}$$

where θ is the estimated pointing angle uncertainty established in this section, and θ_{3dB} is the half-power beamwidth measured and provided by the manufacturer (0.92° at 20 GHz). This model, specifically derived for the particular type of reflector used at the UTS earth station, is valid for $\theta < 0.8°$. The curve in Fig. 5.14 quantifies the possible error with 0.89 dB for 0.25° uncertainty, and 3.5 dB for 0.5° uncertainty.

It can be concluded that the power measurement uncertainty due to pointing errors, in addition to the clear sky calibration uncertainty, should realistically be better than 1 dB (for an assumed 0.25° pointing error) most of the time. The (unlikely) higher pointing error margin of 0.5° would lead to a significant disturbance of the measurements.

Given the successful tracking history and especially the successful bent pipe mode experiments where pointing errors are even more critical, an error $\ll 1$ dB is probable. This assumption is supported by the telemetry in Fig. 5.7, where the bent pipe transmit
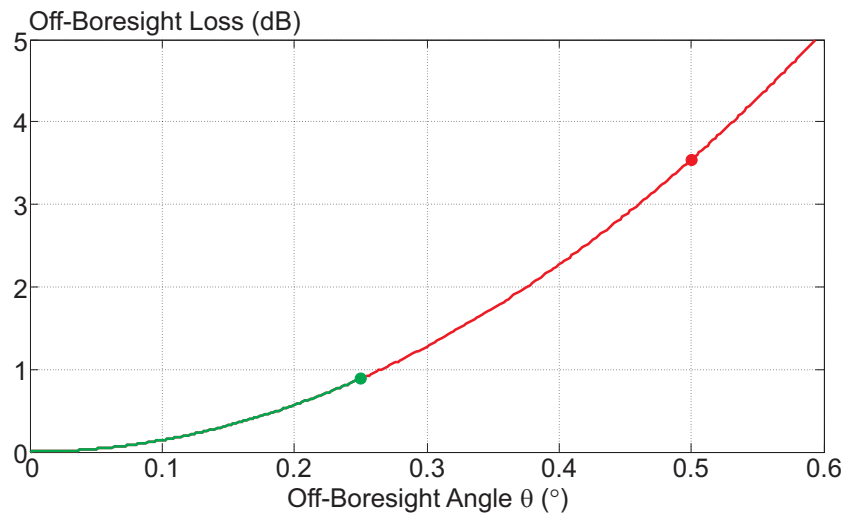
Figure 5.14: Relationship between the pointing angle accuracy, or off-boresight angle, θ and the corresponding off-boresight loss $L_{off-boresight}$ (adapted from [82])

mode power levels are as high as in beacon mode (without automatic gain control). While most other propagation experiments over GEO satellites with *fixed* or only slowly varying azimuth and elevation angles would probably have even better pointing accuracies, it must be remembered that the rapid, *dynamic* tracking of the spacecraft with a largely custom-designed earth station is one of the most challenging aspect of this project.

5.3.6 Multipathing Effects

Multipathing effects occur because the signal arrives at the antenna via two or more separate propagation paths, caused by reflection on objects in the direct path. Due to the presence of obstructions in some of the trajectories, several interesting observations of multipathing effects could be made. However, it must be stressed that these measurements are of no value to the propagation experiment since the true power levels have been significantly distorted, and that the sections affected by multipathing have been removed from the analysed data set.

The most severe multipathing effects are observed when tracking easterly passes at lower elevation ($<60°$), because the metallic mast in close proximity obstructs the line-of-sight between the antenna and the satellite. On some occasions, this complete blockage and the expected resulting loss of signal has not occurred; instead, a strong attenuation with several fluctuations has been observed without a complete loss of lock. Fig. 5.15 shows the received IF signal power of two similar passes where, in *both* cases, part of the

pass was completely blocked by the mast, but with slightly different trajectories. In the left example, multipathing caused the signal to be attenuated, but enough energy still reached the antenna to avoid signal loss. In the right case, the multipathing effects were not strong enough and the signal was lost for about 30 s, then reacquired. If the blockage had not occurred, the curve would be almost symmetrical.
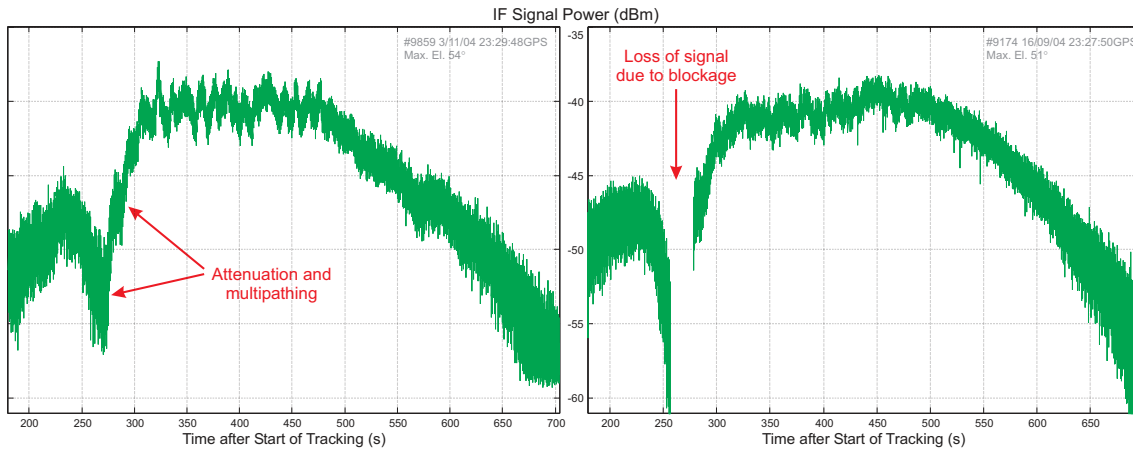
Figure 5.15: Received IF power during a pass with physical path blockage. Multipathing effects sustain signal lock (left), and loss of reception occurs during another, similar pass (right).

A further interesting example of a different type of multipathing, caused by effects *other* than close proximity obstruction, is presented and discussed in the context of attenuation results in Section 6.2.3.

5.3.7 Other Noise and Interference Sources

Previous experiments on GEO satellites have reported the observation of severe receiver noise due to sun transit, which occurs when the sun passes nearby or behind the satellite. The sun is a very hot noise source, and all other received signals are completely eliminated by the steep rise in antenna temperature. Accurately, this should only affect reception for a few minutes twice a year, but depending on the VSAT beamwidth, even marginal transits can cause additional outage. For LEO satellites, the same effect can also be observed, but it is strongly dependent on the type of orbit.

FedSat is in a sun-synchronous orbit, which means that the angle between the sun and the orbital plane is always *constant*. With a sufficiently large angle, spacecraft and sun can be separated enough so that a sun transit (which would only last seconds, not minutes) will *never* occur, as in FedSat's case. Sun noise can therefore be eliminated as a major

additional source, apart from the known thermal effects on the antenna and the physical effects in the ionosphere, which are included in the measurements, but not quantified.

Other objects in the sky also emit energy on certain frequencies, and complex maps of the background sky noise temperature have been developed for various frequencies, including Ka band and much higher [128]. While the author is aware of the possible noise temperature increases of several 10s to up to 200 Kelvins, depending on elevation [129], the dynamic nature of the LEO propagation experiment on one side and the high level of complexity that would be added to the data analysis on the other side do not justify the inclusion of this quantity in the measurements within the scope of this work.

In terms of terrestrial and man-made sources, despite the exposed location, the noise floor on the frequencies of interest proved to be very low. As previously stated, none of the high-power mobile phone and terrestrial microwave links operated in a similar frequency range as the earth station's IFs. The only incident that interference caused a problem was a spurious emission within the earth station's RF module. Other than the 70 MHz IF, no other frequencies are identical on uplink and downlink. While testing the carrier bent pipe mode during the calibration phase, it was discovered that a small amount of carrier power from the 70 MHz VSAT output leaked into one of the 70 MHz receive circuits, which caused the receiver to lock onto the transmitted signal. The origin was quickly discovered, and additional shielding of the final 1 MHz-wide receive bandpass filter, which is located in close proximity to the transmitter circuits, resolved the problem promptly.

5.3.8 Dish and Feed Horn Wetting

The effect of a wet antenna surface on propagation data statistics has been very controversially discussed in the literature, even years after the actual experiments [88–90], as mentioned in Section 4.3.2. Especially on Ka band frequencies, a wet surface has the potential to add up to 3 dB of attenuation (20 GHz) in a rain storm scenario [36] (p. 175), and it will therefore perturb the actual attenuation attributed to propagation. In addition, previous experiments have stated that it is difficult to model this effect accurately [38]. In this experiment, and especially due to the dynamic nature of spatial LEO tracking and the hydrophobic properties of the reflector surface, it is very difficult to quantify the amount of antenna wetting at any given time. Unless the reflector is temporarily in a near-horizontal position, most droplets would run off immediately. However, unlike in fixed-angle GEO experiments, it is practically difficult to shield the entire tracking pedestal or even just the feed horn from exposure to rain. It has been observed that during a pass, there were droplets present on the outside of the clear membrane that protects the feed horn aperture. The possible influence of these droplets during rain passes has not been quantified

within the scope of this work, and all measurements during rain passes (at low rain rates) *may* include a small contribution to the measured attenuation from feed horn and antenna wetting. It should be mentioned that condensation, if any, has always been removed from the reflector surface before an experiment.

5.3.9 Power Measurement Calibration

In previous sections, the contribution of *mechanical* errors to the overall power measurement uncertainty has been explored. For accurate results, the earth station must also be calibrated in terms of its receiver gain (internal calibration) and in terms of the gaseous absorption under clear sky conditions (external calibration). The calibration factors are then used in the analysis software set propagation reference levels and to account for variations over time, if any, in order to obtain the attenuation predominantly caused by atmospheric effects (Fig. 5.16).

For the **receiver calibration**, the receiver's total system gain (amplifiers) and loss (mixers, filters, splitters, couplers etc.) have periodically been measured under typical conditions (see Appendix A). Even before deployment, all RF and data acquisition components had been subject to a meticulous integrated systems test in conjunction with the spacecraft, where system gains and dynamic processes were recorded. After the installation of the earth station on-site, several other techniques were employed to ensure consistency of the measurements. By inserting a 1530 MHz source in place of the LNB output and measuring the received power level at the data acquisition point, the entire receiver chain was calibrated. The variable attenuator allows to compensate for slight design deviations due to static component tolerances, and to set the power level within the dynamic range of the analog interface card. The relative LNB gain was quantified in a repeatable setup by placing a 20.13 GHz source at a defined far-field distance d from the feed horn and measuring the signal power level at the LNB output. The two results were then combined to obtain the overall system gain, which was incorporated into the data analysis software.

With the earth station at operating temperature, no short-term drifts were detected over the usually short duration of a LEO satellite pass (10-15 minutes). Long-term drifts due to component ageing was assessed by repeating the initial calibration procedures for both LNB and remaining RF chain periodically on-site. Within the calibration precision of the signal generators and spectrum analysers used, no significant long-term drift was detected over the course of the project.

Clear sky calibration is based on the measurement of gaseous absorption, which means quantifying the attenuation solely introduced by gases (other than water vapour)
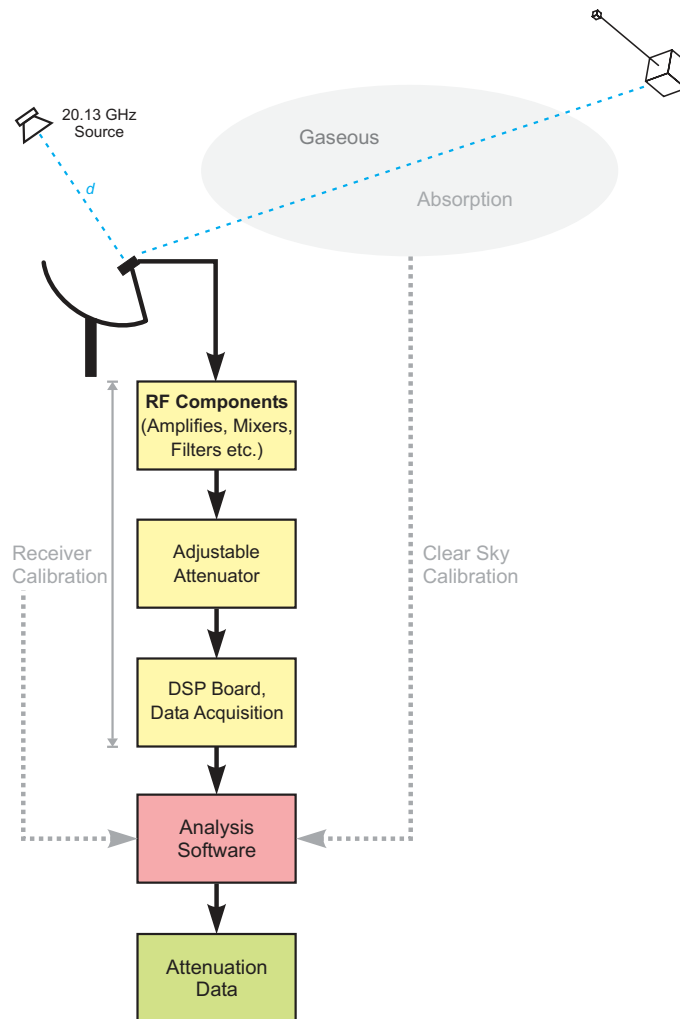
Figure 5.16: Power calibration procedure, consisting of receiver gain calibration and obtaining a clear sky reference level (gaseous absorption calibration)

permanently present in the atmosphere (also see Section 2.3.1). In absence of a radiometer, the results proposed by Chakraborty, Davarian and Stutzman [33], who quantified the clear sky attenuation within approximately 1 dB at 20 GHz at a *fixed* elevation angle, were considered as a reference. Alternatively, many members of the research community have published attenuation measurements relative to clear sky conditions. The calibration relative to clear sky involves the collection of data *initially* without a known calibration reference, which is later scaled by a gaseous absorption offset in the analysis software, resulting in the pure attenuation due to atmospheric effects. The offset was approximated by observing a suitably large number of clear sky, high elevation passes, ideally at a similar ground humidity, and by comparing the received power levels at similar elevations. After filtering the scintillations, the received clear sky power levels were regarded as the "relative to free spacer" zero reference level, hence any additional signal attenuation introduced was consequently due to atmospheric effects (not considering other sources of error). The described evaluation took place during 2003 and 2004 on a number of clear sky passes, and is validated in the discussion of the results in Chapter 6.

It should be noted that both the receiver gain and the clear sky calibration bear the risk of being affected by small, systematic measurement errors due to possible equipment calibration issues and inconsistent conditions during the clear sky experiments. Unlike those errors introduced by mechanical tracking inaccuracies, the offsets used in the analysis software are *fixed*, and relative observations, such as the magnitude of scintillations and depth of fades, are therefore unlikely to be affected in their accuracy.

5.4 Pass Preparation and Operation

The section briefly describes the extensive preparations required for each single experiment, both off-site and on-site, regardless of whether it eventually led to the successful collection of data or not. The general scheduling routine and the exchange of information between CRCSS research groups weeks to days before the experiment has already been portrayed in Section 5.1.3.

5.4.1 Required Instrumentation

During the deployment and the calibration phases, it has proven very convenient to observe the received signal on the L band IF via a spectrum analyser during the pass. It has also been vital during the investigation of suspected malfunctions, both of the earth station and the satellite. For this reason, a spectrum analyser has been carried from the CRCSS laboratory to the experimental site for every single pass. (Due to the fact that

the instrument was required in the laboratory for other purposes, it could not be left on-site permanently). Examples of the signals monitored on the spectrum analyser will be presented in Chapters 6 and 7.

5.4.2 Pass Preparation Routine

Due to the sun-synchronous orbit, all practical morning passes usually take place between 9:30am and 10:30am Australian Eastern Standard Time (AEST = UTC+10 hrs). Preparations at the UTS laboratory begin at 7am with the preparation of the latest tracking coordinates from TLE data as described above, and the two staff required to operate the earth station arrive at the site at around 9am.

For equipment safety reasons, all RF and power cables between the indoor and outdoor units are disconnected between experiments, which has proven essential due to static charge or lightning, which actually did damage to some outdoor equipment, see Section 7.1. After reconnecting those cables, a functional test of the PCs and the indoor electronics follows. The outdoor unit is powered up and checked for any physical damage due to wind or water intrusion. Next, communication between the servo drives and the tracking software is confirmed, after which the manual levelling procedure is conducted via a two-way radio link. Observing any displacement of the reflector on the spirit level, the person at the antenna would specify a corrective angle (for example -0.02°) to the other person operating the indoor terminal, initiating a compensating move with the respective motor. After the iterative levelling procedure is complete, the position and motor encoder values of the entire system would be reset to zero (home position). The antenna system is now calibrated.

Finally, the previously generated pass file, containing the timing reference, the X/Y pointing angles in 1-second increments and the pre-calculated, normalised Doppler offset frequency (for uplink compensation), is placed in the earth station software's watch directory. When a future pass is detected, count-down timers for motion and signal processing are activated, and the pass trajectory is graphically displayed. The relatively simple pass file contains all the information required for tracking (Fig. 5.17).

In 'live pass' mode, the software will automatically calculate the time it takes to position the antenna at the first X/Y coordinate, and activate the motors accordingly to arrive there at least 10 seconds prior to the start of tracking. Precisely at the given time, spatial tracking and signal processing would commence. Any received signal on the first L band IF can simultaneously be observed on the spectrum analyser. For verification and

```
730,UTS,12,10,2004,23,24,54.0000,1.000

X (deg),Y (deg),ND (Hz/Hz)

-76.573911,81.375450,0.000021681666
-76.525797,81.265694,0.000021665999
-76.487470,81.154076,0.000021649059
-76.439169,81.044785,0.000021635218
-76.390775,80.935738,0.000021617866
...
```

Figure 5.17: Example of a pass information file. The first line provides the number of tracking elements in this pass, the earth station ID, timing reference for the first element (GPS date/time) and the increment of subsequent entries in seconds. In the body, each line indicates the X angle, Y angle and the normalised Doppler frequency.

fault-finding procedures, the spectrum analyser's display is recorded with a video camera and later archived.

5.4.3   Visual Observation and Recording of Received Signals

The earth station tracking software provides several real-time displays during a pass by which the status of spatial and frequency tracking can be observed. Fig. 5.18 was recorded during a live beacon mode pass on 29 April 2005. The countdown timers for antenna positioning, AOS and LOS are located at the top, showing that 284 seconds of tracking are remaining in that pass. Further below are message windows for spatial and frequency tracking, which are logged for future reference. The following screen section provides very detailed information about the motion control subsystem, most importantly a frequently updated record of the true position error during the pass. In this figure, the position error is as low as $0.003°$, which is at the resolution limit of the encoder. This confirms that the improved algorithm presented in Section 4.9.2 is very effective.

During signal lock, the graph in the lower left shows the ± 500 kHz spectrum around the estimated beacon frequency, normalised to the maximum received signal power and updated every 100 ms. On the right, the green curve represents the trajectory of the current pass that has already been completed, and the yellow part the remaining pass coordinates. The display can be switched between X/Y and the classical Az/El coordinate systems; numerical values for the current coordinate (circle) are given as well. The pass in this example has started near the northern horizon and stays completely on the western side, with a maximum elevation of $62°$. All displayed values are automatically time-stamped, logged and saved to the hard disk, either during or after the pass.

In bent pipe mode, the software essentially functions the same way, except for additionally generating the pre-compensated uplink Doppler signal through the uplink DDS.
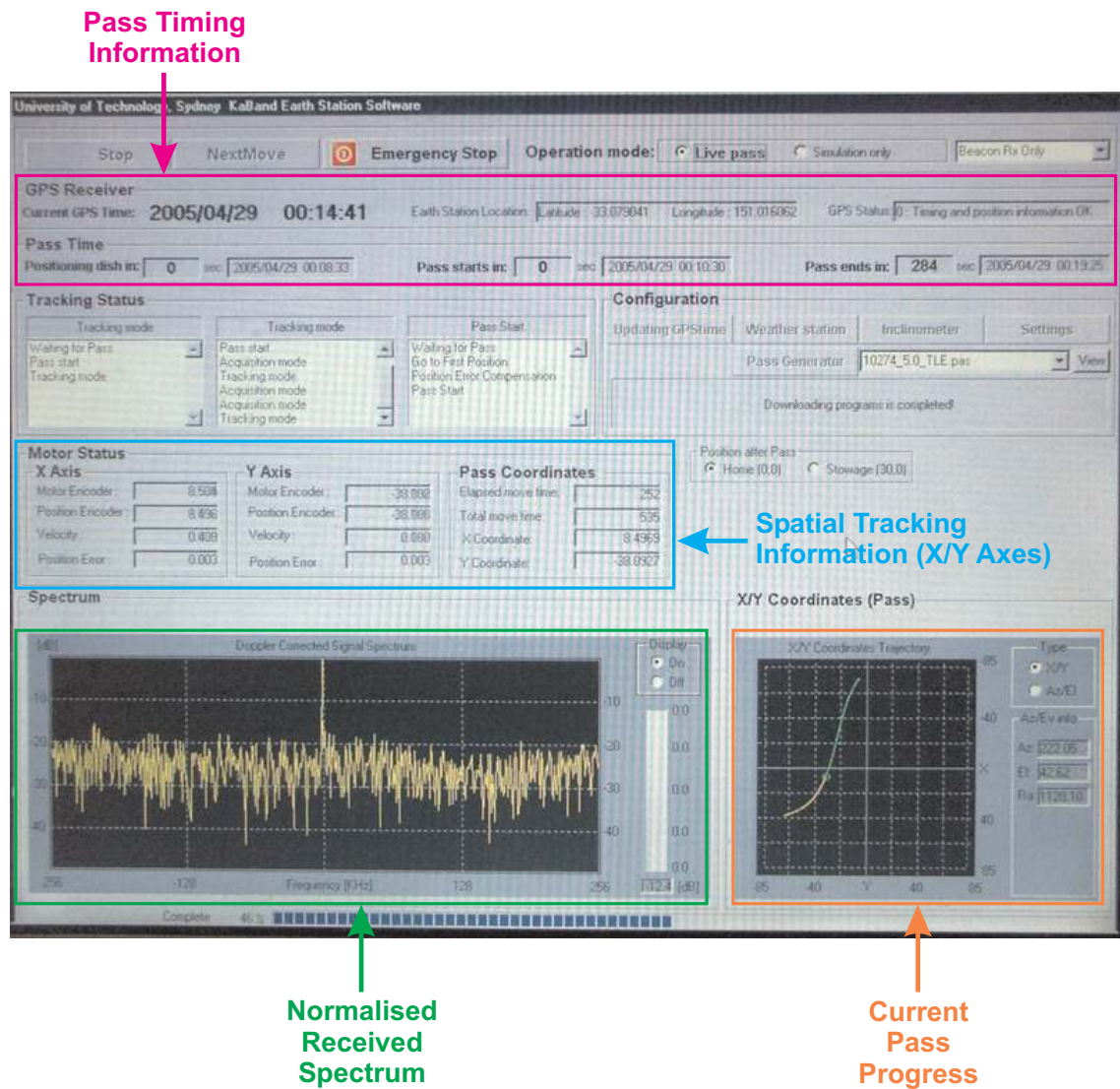
Figure 5.18: Screen photo of the tracking software user interface during a live pass, providing timing and spatial tracking data, received spectrum display and pass progress information

The re-transmitted signal is then tracked and recorded as above.

5.4.4 Archival and Post-Processing of Measurements

The diligent *time-referenced* archival of all parameters and measurements recorded for this pass is very important, since the spatial coordinates need to be directly linked to the observed signal. The earth station software saves most of the generated data in convenient 'comma separated value' files, which can be easily imported for post-processing with Matlab™. For information purposes, an example of the recorded files and their approximate size is given in Table 5.3.

File Content	Typical size
FedSat Two-Line Elements	1 kB
Nova™ output file (UTC)	120 kB
X/Y pass coordinates (GPS)	25 kB
Az/El, range, height, SSP (UTC)	50 kB
Pre-computed uplink Doppler shift (4 ms)	4,500 kB
DSP acquisition and tracking logfile	10 kB
Spatial tracking and position data logfile	500 kB
Power estimates and Doppler shift (4 ms, GPS)	2,500 kB
Spectrum (100 ms, GPS)	130,000 kB

Table 5.3: Example of the archive files generated by the tracking software after a successful pass

However, due to constant improvements to the software in terms of efficiency and functionality, different file structure versions have existed over the duration of the project, which has in turn led to a complication of the Matlab™ analysis software. Also, as indicated in the table, the data originating from Nova™ is given in UTC, not GPS, and for different AOS/LOS times than actually tracked by the earth station. Since some of the information is crucially required, for example the SSP coordinates, rather complicated UTC/GPS time-stamp search and correction routines had to be developed. This complication is further dealt with in Section 7.1. In addition, the previously described squint angle correction and antenna modelling were implemented, as well as statistical analysis and complex graphical plotting routines. The number of Matlab™ code lines that have been implemented by the author for the analysis and display of the power estimates and the spectrum for each data set version well is over 1,200.

5.4.5 Collection of Meteorological Data

For propagation experiments, it is desirable to record the prevailing meteorological conditions during a particular pass in order to relate them to the measurements as closely as possible. The archival of precipitation is particularly important, since it has the greatest influence on the signal. For experiments via GEO satellites, it has therefore been common to place a rain gauge at the earth station location, and optimally several more along the *fixed* slant path projection. [130], p. 215, has shown that rainfall at the receiver site is not directly related to observed signal attenuation, and suggests to position rain gauges along the path. With a fairly good knowledge of the different approximate rain rates along the path, the observations can be matched to a model derived from the rain data.

Unfortunately, the situation is significantly different for LEO experiments. Pass trajectories are highly variable from experiment to experiment, and in addition, the weather conditions that are experienced along the slant path to the satellite can change rapidly. For example, as illustrated in Fig. 5.19, clear sky, clouds, stratiform rain and convective rain can all affect propagation during the same pass as the signal passes through these tropospheric regions.
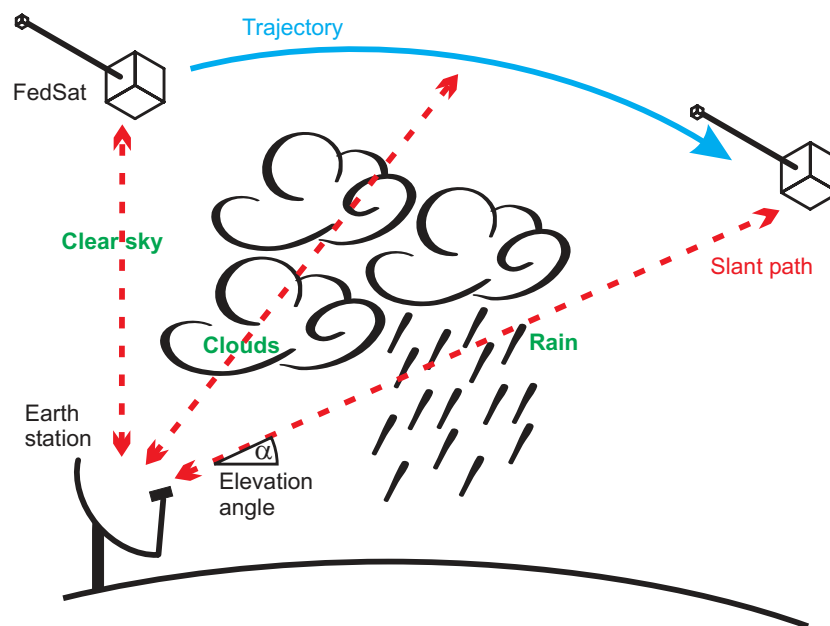
Figure 5.19: The variable slant path of a LEO satellite pass allows measurements during different weather conditions

In order to gather precipitation data as accurately as in the GEO case, a very dense network of rain gauges within a radius of 100 km and beyond would be necessary, which

is practically not feasible. Alternatively, cloud and rain attenuation levels (up to a certain level) can be detected by radiometers, and some GEO experiments have chosen to complement their earth station with such a device to improve their models. In some rare cases, a full rain radar was employed to estimate the rain rate along the slant path through microwave reflectivity. Both of these solutions are very expensive and regrettably beyond the financial capabilities of this project. Instead, the following resources have been used to approximately gather local precipitation data and estimates of rain rates along the path.

5.4.5.1 Photography of Local Weather Conditions

In many cases when no precipitation was present, some clouds could be observed along the trajectory of the satellite. After early observations of influences on the received signal, it was decided to take photographic or video records of the sky along the path, so they could later be matched with the temporary occurrence of higher attenuation. Fig. 5.20 shows one example of scattered altocumulus clouds with an overlay of the approximate slant path trajectory. The signal in this particular case was lost at an elevation of 8°. The corresponding results will be presented in Chapter 6. However, it should be noted that variations in the air humidity are not always as clearly visible as in clouds, as evident in some clear sky cases.

Figure 5.20: Photo of sky conditions during a pass, indicating the approximate satellite trajectory and LOS point at 8° elevation

5.4.5.2 Weather Radar

Weather radars are commonly installed in the vicinity of populated areas for the early detection of severe storms, heavy precipitation and other significant meteorological events.

An omnidirectional microwave pulse is periodically transmitted from the radar site. When the radio waves encounter an object in their path, such as rain droplets or ice crystals, part of the energy is scattered back to the same radar site, where it can be detected by a receiver at distinct elevation scan angles. The wavelength of the transmitted frequency, typically 1-10 cm, is chosen at approximately 10 times the physical size of the target hydrometeors so that Rayleigh scattering effects are dominant [131]. Shorter wavelength radars (for example Ka band) are able to detect even small particles, such as mist and fog. Incidentally, this is the frequency of interest in the presented propagation experiment. However, the Ka band radar range is much more limited due to signal absorption, thus most weather radars operate at S or C band frequencies. The magnitude of the received echoes is measured in a reflectivity scale (dBZ) and is, ideally, approximately proportional to the density of hydrometeors in the scanned section of the sky, relative to $1\mu m^3$, and is therefore representative of a certain rain rate. The actual calibration depends on the type of radar used. With omnidirectional scans, the results can be displayed graphically and combined with topographic maps, creating an easy to interpret tool for prediction and analysis (Fig. 5.21), especially when the images are available in near real-time. Like many similar government organisations worldwide, the Australian Bureau of Meteorology (BOM) also provides this complimentary service online at [132].

Level	Colour		Approx. Rainfall Intensity (mm/hr)	Reflectivity (dBZ)
0	clear	Not visible	Under 0.2	
1		Off-white	0.5	11.8
2		Sky-blue	1.5	23.0
3		Light Blue	2.5	28.0
4		Blue	4	31.0
5		Light Cyan	6	34.0
6		Cyan	10	37.0
7		Dark Cyan	15	40.0
8		Yellow	20	43.0
9		Yellow-orange	35	46.0
10		Orange	50	49.0
11		Orange-red	80	52.0
12		Red	120	55.0
13		Dark Red	200	58.0
14		Maroon	300	61.0
15		Dark Brown	over 360	64.0
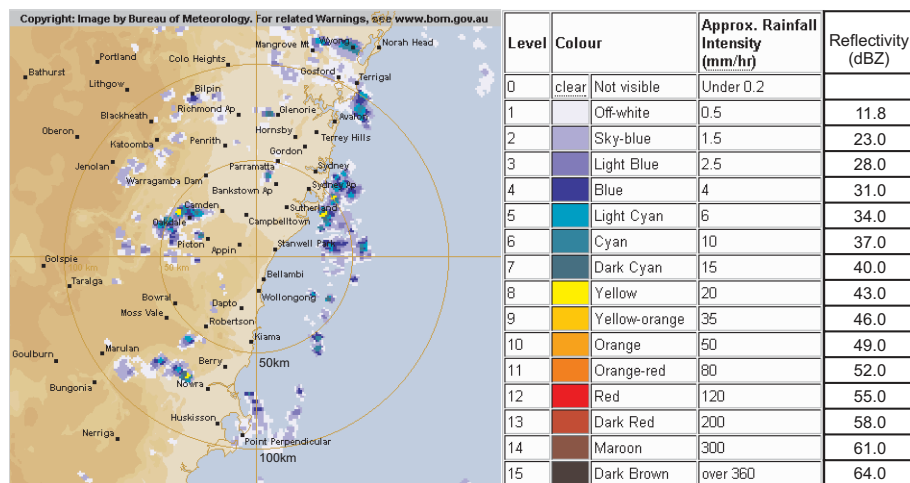
Figure 5.21: Example of a weather radar map for the Sydney region, including a reflectivity and rain rate scale [132]

The advantage of a weather radar, compared to the ground-based observation of precipitation, is that it is virtually instantaneous, and especially that it can provide a 3-dimensional view of the scanned volume, allowing a fairly good estimate of the rain height

and the horizontal spread of precipitation [133]. The latter can otherwise be very difficult for large convective clouds, such as a thunderstorm cloud (cumulonimbus). On the negative side, the reflectivity scale calibration relies on many assumptions, such as the droplet size and shape, on which the quantification of the rain rate is based. It also suffers from the fact that the curvature of the earth does not allow the detection of low-level precipitation at an increased distance from the site [132], as well as the occurrence of artifacts, for example false echoes ('clutter') from terrain, the sea surface and even insect swarms. In some cases, the emitted signal it attenuated so severely by a first front of precipitation (for instance a thunderstorm band) that the echoes in a subsequent region will be obscured ('shading'). A second weather radar, located at a certain distance from the first, can provide a different perspective of the approaching storm bands and therefore solve this problem.

Despite the fact that the rain rate measurements conducted with weather radars have some limitations, especially considering their accuracy under some atypical conditions, their use for this project still appears reasonable for inclusion in the planning and evaluation of Ka band propagation experiments. With respect to the earth station site in Sydney, two separate S band radar sites are operated in the region by the Australian Bureau of Meteorology, located approximately 26 and 60 km south. An exemplary weather radar sequence, recorded during a severe thunderstorm event in Sydney (but unfortunately not during a pass), is shown in Fig. 5.22. The maps are provided by a secondary weather agency [134], but originate from the same BOM source data. A different colour scale is used, however the threshold values are identical.

A further improvement would be the use of vertical cross-sections, which allow the precise determination of the melting layer, rain height and equivalent path length, as shown in Fig. 5.23. With this data, a reasonably precise calculations should be possible for the ITU model.

By projecting the ground track and the slant path onto the map, it would be possible to approximate the cumulative rain rate of each point along the trajectory.

For this research, the BOM polar weather radar sources were extensively used in order to predict possible precipitation in the short term, but only to a limited extent for the analysis of rain passes due to the very limited number of rain events. However, rain rate information provided by other sources was correlated with the weather radar results for verification purposes. Despite this fact, it is important to include the availability of these sources in this work, since it would have assisted considerably in the analysis of more rain propagation data. Although this type of 2-dimensional weather radar image may not be suitable for the precise quantification of rain rates along the slant path, it can
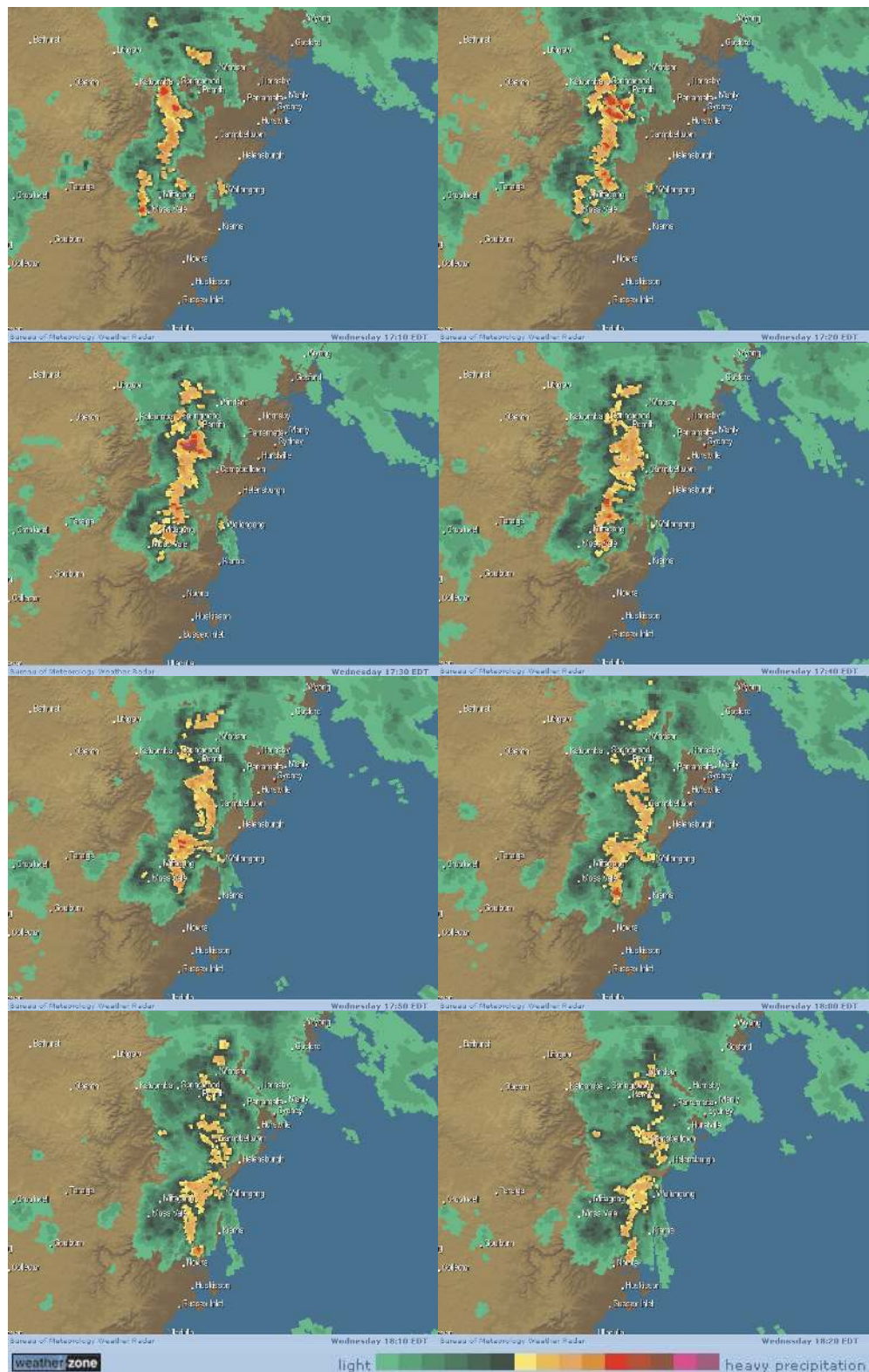
Figure 5.22: Sydney weather radar sequence of an approaching thunderstorm band, recorded over 70 minutes in 10 minute intervals
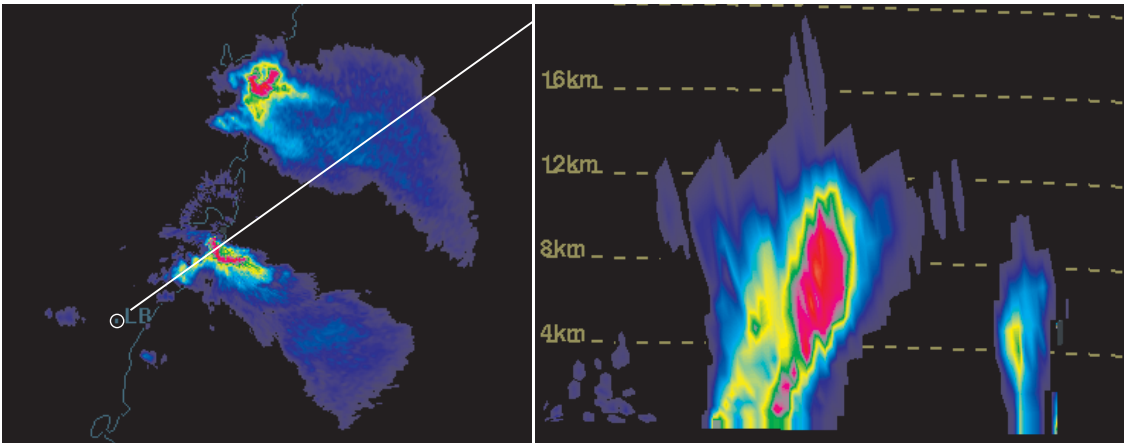
Figure 5.23: Example of horizontal (polar) and vertical radar during a severe storm event in Sydney [135]. This example also highlights the 'shading' effect evident at the right storm cell.

certainly assist in the correct interpretation of attenuation in the received signal strength. One concrete event where the local precipitation was observed before, during and after a scheduled Ka band experiment in 10 min intervals is illustrated in Fig. 5.24.

The first two frames in this sequence of six show a large rain cell developing about 20 km south-west of the earth station location, with several smaller cells scattered in the vicinity. The radar map in graphic 3 illustrates the exact conditions *during* the satellite pass. The ground track of this descending, near-overhead pass is marked by the green line, with the slant path from satellite to the earth station actually extending out of the 2D plane. Several points along the ground track are marked with their time stamp, converted to UTC to match the radar map reference, and their respective elevation angles. By following the dashed, red lines, it is now possible to infer certain precipitation intensities along the path. However, it is important to take the elevation angles into account, since a rain cell further away from the earth station may sometimes *appear* to be in the projected path when it is, in fact, entirely bypassed above the rain height. For example, the signal received from the satellite along the 83° elevation slant path would appear to be passing through the large rain cell with moderate rainfall (ca. 10 mm/h) first, before arriving at the earth station, where light precipitation prevails in a small, local cell. Due to the high elevation angle, only very little (if any) rain attenuation of the large cell would be noticeable in the resulting received signal strength, while most of it is likely to be introduced by the light rain at the earth station location only. In contrast, several rain cells along the path at *low* elevation can be much better interpreted using the weather radar, since the distinct cells may not all be visually observable from the ground.
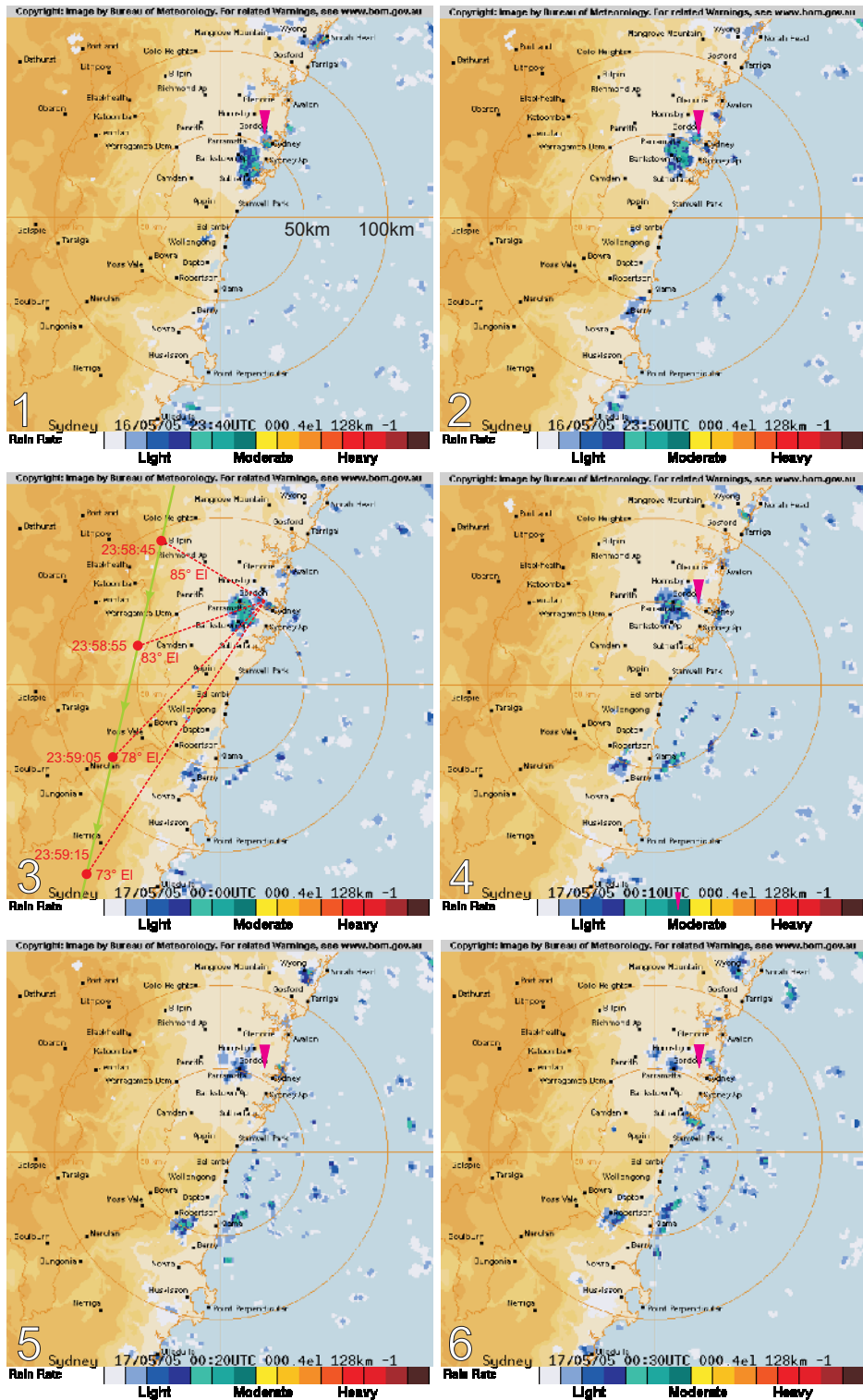
Figure 5.24: Weather radar sequence before, during and after pass #12642 in 10 minute intervals [132]. The earth station is located at the pink triangle. Frame 3 illustrates how the satellite slant path can be matched to prevailing local precipitation.

The example in Fig. 5.24 concludes with the rapid disintegration of the large cell and the formation of numerous new, smaller cells within the subsequent 30 minutes, emphasizing the challenging dynamics involved in precipitation prediction and monitoring during a short LEO satellite pass. Unfortunately, no data was recorded on this occasion due to a malfunction.

5.4.5.3   Official Weather Station and Pluviometer Records

Although it would have been beneficial to have a professional weather station installed on-site, the high density of automatic, official BOM weather stations in the Sydney region was believed to be sufficient for the collection of humidity and wind speed data, and rain data to a lesser extent. Given the variability of the look angles for different passes, it should be considered to also obtain the rain records of weather stations further away from the site. Cumulative data and long-term statistics (monthly, yearly, historic) is readily available from various sources [118], [134], which all rely on the official data provided by the BOM. An example of general observations during a rain pass on 8 November 2005 AEDST (7 Nov 2005 GPS) is given in Fig. 5.25. It can be verified that at the actual pass time (10:41-10:52), there was an increment in the recorded rainfall. Corresponding numerical data has also been obtained and correlated.

The local weather observations are complemented by data from rain gauges (pluviometers), recording the rainfall and rain rate at 1 minute intervals. The local water authority, Sydney Water, operates a very dense network of pluviometers across the Sydney metropolitan and the catchment areas [119]. 30 minute interval rainfall data is publicly available, and ITU-conforming 1 minute data is accessible on request. Fig. 5.26 depicts the locations of pluviometers in the Sydney region, with either cumulative or daily rainfall indicated for each site [118]. It can be seen that the Ka band earth station location is in close proximity to several pluviometers within only a few kilometres. It is also noticeable that the network of gauges has significantly grown between 2004 and 2007. "Since-9 am" rainfall statistics are also available in hourly intervals.

Especially for the monthly statistics, a clear west-east rainfall gradient with a ratio of well over 10:1 can be observed within a distance of only 50 km, indicating that the local weather between the mountain ranges and the ocean shore is highly variable.

In summary, with access to 3-D radar images, 1 minute rain data and a model of the variable slant path geometry, it would be possible to correlate ground rain rates and the attenuation experienced by the satellite link during a pass. However, this very elaborate
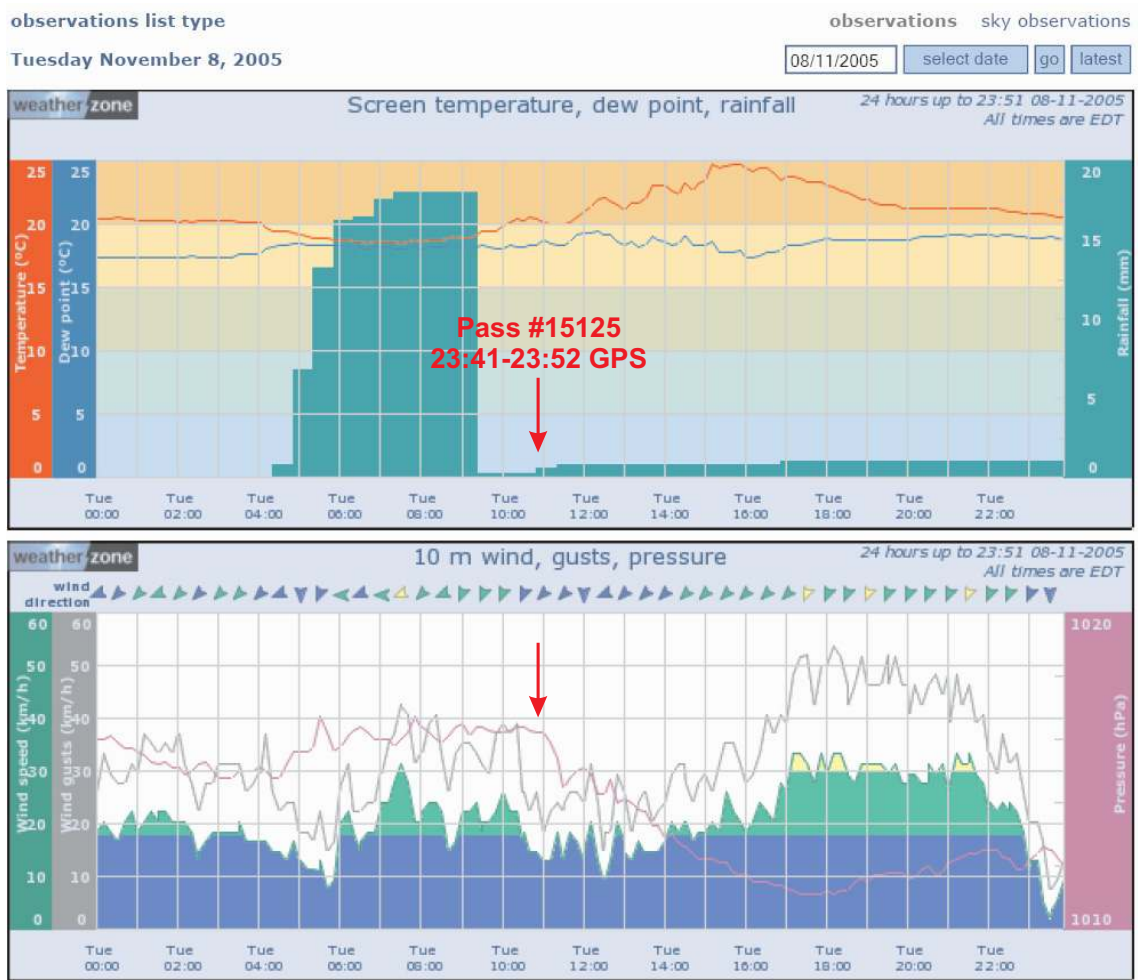
Figure 5.25: 24-hour weather data recorded in the vicinity of the earth station location during a rain pass [134]
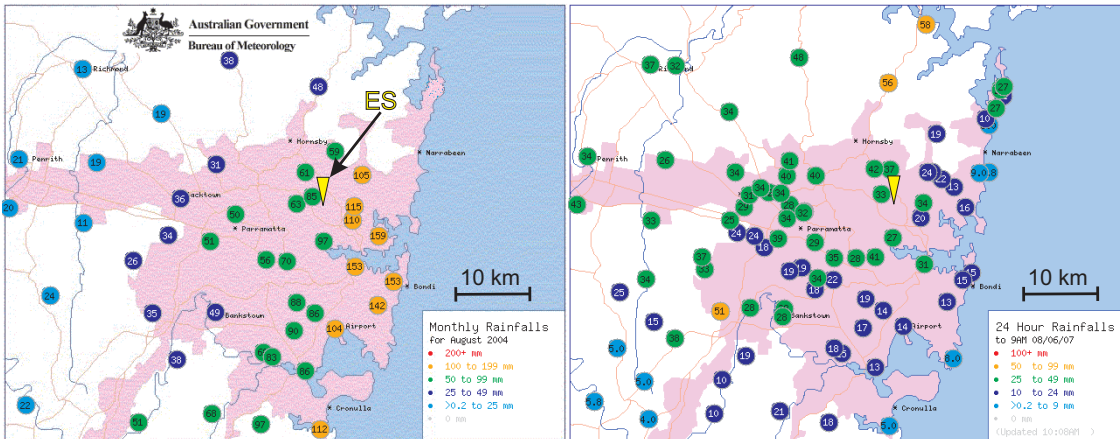
Figure 5.26: Pluviometer locations in the Sydney metropolitan area. The graphic on the left shows *monthly* rainfall records, while the map on the right indicates *daily* cumulative rainfall [118].

analysis approach, correlating physical weather conditions along the trajectory and the attenuation measurements, has been deemed beyond the scope of this thesis, and is believed to provide great potential for future research.

5.5 Doppler Frequency Tracking Performance

As previously explained in Section 4.1.1.3, the large Doppler shifts that result from a low-earth orbit and the use of Ka band require frequency compensation on the uplink and downlink. Due to the additional uncertainty of LO offsets, carrier frequency acquisition and tracking is advisable on the downlink, as opposed to relying on pre-calculated compensation values only. This section will present some examples of successful Doppler tracking using the developed algorithm [14] and discuss certain aspects. During the calibration phase and the first tracking experiments, any fixed bias of the detected Doppler shift at maximum elevation was removed to provide a zero frequency offset reference for future measurements.

5.5.1 Examples of Doppler Frequency Tracking

As part of the signal power measurement, the detected Doppler shifts have been recorded together with the other pass data for later analysis. Fig 5.27 shows the Doppler tracking performance during a beacon mode experiment with a direct overhead trajectory which maximises the Doppler rate at zenith and provides the most demanding practical verification of the algorithm. The point values of the Doppler shift curve are unfiltered, raw

values; only the Doppler rate curve, which has been numerically obtained as the first derivative of the Doppler shift, is low-pass filtered for better illustration purposes.
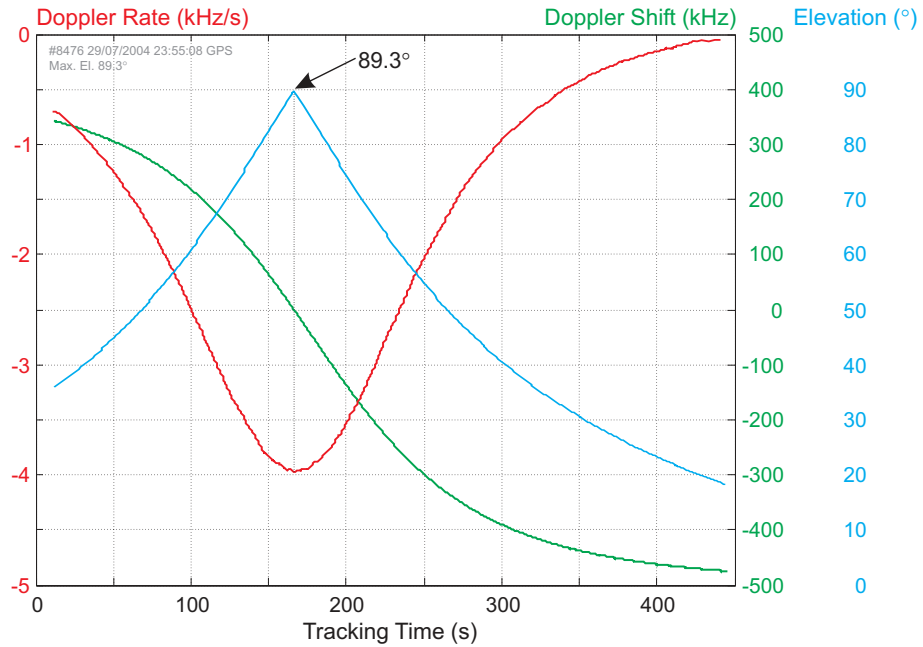
Figure 5.27: Measured Doppler shift and Doppler rate tracking performance during an overhead pass. The elevation curve is also shown for reference.

Fig. 5.28 was measured during a *bent pipe mode* pass with 62° maximum elevation, which means that the signal was Doppler pre-compensated on the uplink and then re-transmitted by the onboard transponder on the 20 GHz downlink, which will be further discussed in Chapter 6. For comparison purposes, the theoretical Doppler shift curve is also indicated.

5.5.2 Discussion

For the beacon mode example, the following observations can be made:

- The highest elevation coincides with the zero-crossing on the Doppler shift and with the minimum of the Doppler rate, therefore confirming theory.

- The Doppler Shift curve is completely smooth and does not show any discontinuities, indicating that the signal was continuously tracked without loss of lock from AOS to LOS. In fact, it is in complete agreement with the theoretical curve (not shown here).
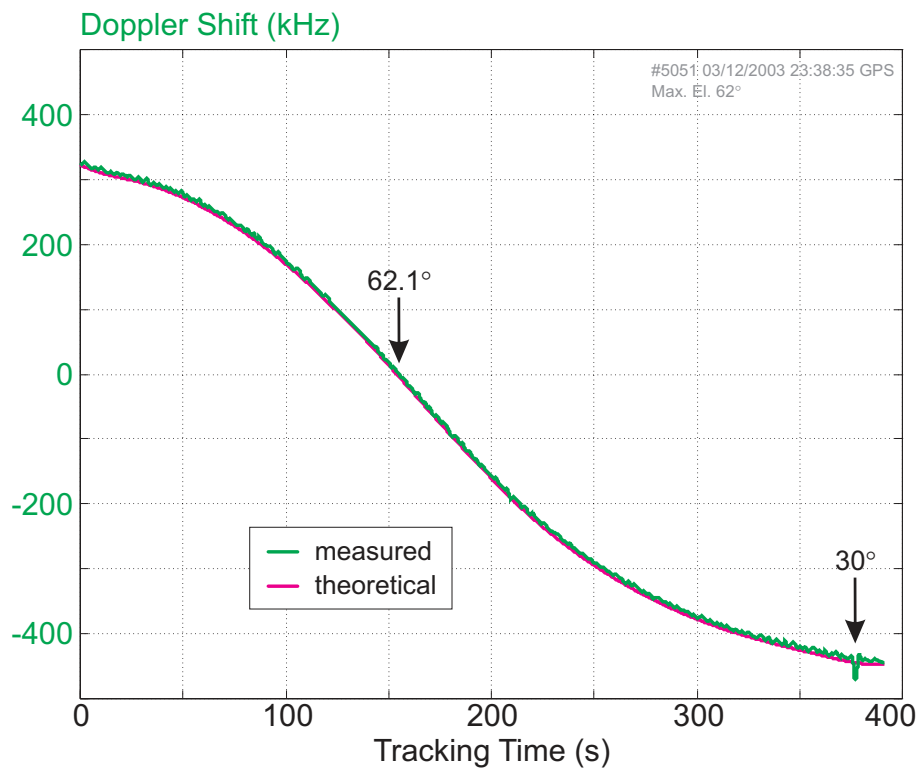
Figure 5.28: Comparison between the measured and the calculated Doppler shifts during a bent pipe mode pass.

- The Doppler rate curve, as the first derivative of the Doppler shift, has been averaged and also approximates a smooth curve. At no time does the curve reveal any major steps, which would be an indication for false or lost lock.

- Only at the highest absolute Doppler rate, there are very minor deviations from a theoretical shape due to the rapidly occurring frequency shift. The Doppler shift curve itself still appears very smooth, and the effect can be neglected for all practical purposes.

- The signal is successfully tracked to an elevation of about 18°, at which point the tracking algorithm permanently loses lock.

It can be concluded that the tracking algorithm is very stable and accurate in beacon mode. The evaluation of other passes confirms this statement.

In bent pipe mode, the uplink noise is added to the transmitted signal, therefore decreasing the SNR at the receiver and making tracking significantly more challenging. (For an appreciation of the total downlink noise, Fig. 6.15 may already be referred to.) The following observations can be made for bent pipe mode Doppler shift tracking:

- Again, the highest elevation coincides well with the zero-crossing on the Doppler shift, confirming accuracy.

- The curve shows minor ripples throughout the pass, which increase with lower elevation. This is related to the lower SNR at decreasing elevation angles. The curve is relatively smooth around the maximum elevation mark.

- There is a very good correspondence between the theoretical (downlink) Doppler shift curve and the measurement. Only a very minor *fixed* difference can be observed which is likely to originate from uplink LO offsets (in the order of several kHz).

- The signal is successfully tracked to an elevation of about 20°, when a temporary loss of lock occurs due to the decreased signal-to-noise ratio. The signal is re-acquired virtually instantaneously and tracked for another 15 seconds, before it is eventually lost at approximately 18° elevation. It should be noted that this elevation is well outside the design specifications. The additional attenuation introduced by the squint angle is particularly significant on the 30 GHz uplink (higher antenna off-angle loss).

The Doppler tracking of a bent pipe mode pass is similarly reliable, despite the increased noise. However, an earlier loss of lock can be expected. As a conclusion, the power estimates recorded after the removal of the detected Doppler shift can be deemed reliable in both operation modes.

5.6   Pass Statistics and Summary

During the 30 months of operation between May 2003 and November 2005, the UTS CRCSS team has performed 84 separate experiments with the UTS Ka band earth station for various purposes: power calibration, timing verification, payload status verification, payload fault-finding, beacon signal strength measurements and bent pipe mode tests. The most important milestone of the earth station's operation, proof of concept, has therefore been achieved. One of the secondary goals, the collection of propagation data, was conducted only on a subset of those passes.

The chart in Fig. 5.29 shows a statistic of all passes tracked during the operational period. With respect to the propagation experiment, passes were only counted "successful" when usable power estimates were recorded for at least the majority of the pass duration. The remaining "successful" experiments can be attributed to timing tests, as described in Section 5.2.3, or fault finding, where data collection was not possible due to the nature of the test. It may seem surprising that the total share of successful experiments is less than half, with only a third of all passes resulting in data collection.
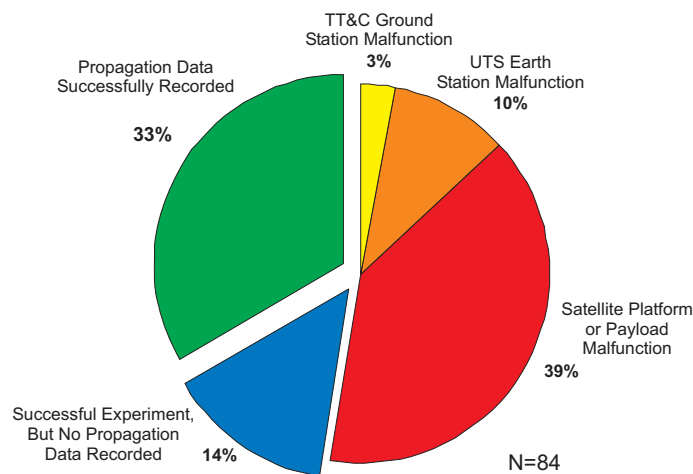
Figure 5.29: Percentages of successful and unsuccessful experiments, also indicating the origins of malfunctions

One of the major reasons for this relatively low success rate lies in the spacecraft data

handling and attitude control systems (DHS, ACS), which caused numerous platform resets and unreliable spacecraft attitudes, especially in the first half of the experimental phase. While all preparations had gone according to plan, i.e. the time-tagging and upload of telecommands from the TT&C ground station during good satellite stability, during pass time, no signal was received. Telemetry often later confirmed attitude problems or a platform reset, which caused the time-tagged commands for the Ka band payload to be lost. Only on a few occasions was the ground station able to intervene and to turn on the payload by manual telecommands during the pass. As a result, a large number of otherwise promising passes were lost, despite successful preparations and spatial tracking of the Ka band earth station. Another persistent spacecraft malfunction in bent pipe mode has been undesired interference from the UHF payload, which was only discovered and resolved after extensive fault-finding procedures and therefore lost passes.

11% of all experiments were unsuccessful due to malfunctions of the earth station for a wide variety of reasons. This topic is further discussed in Chapter 7.

Finally, on a few occasions, the upload of the telecommand stack from the TT&C ground station had failed, or the data was corrupted, therefore the payload did not turn on. The notification of this fact usually came too late to cancel the preparations immediately before the pass, which was of course unsuccessful.

Only looking at the 28 passes where actual propagation data was recorded, this can be further broken down into beacon and bent pipe modes, and into the prevailing weather conditions at the time of the pass. Fig. 5.30 illustrates that the majority of all data was, in fact, collected under clear sky conditions or with few clouds present. On only three occasions was beacon mode data recorded with some precipitation present somewhere along the trajectory. The estimated rain rates in all of these three cases was between 5 and 15 mm/h, as derived from weather radar and pluviometer statistics. No data was recorded during rain storms or other significant events with high rainfall rates.

5.7 Summary of Operation and Data Collection

This chapter has given an overview of several topics related to the tracking of FedSat and the data collection. It has been argued that the selection of suitable passes is very limited due to elevation and duration constraints, and even further due to site limitations (access, obstructions). It has also been shown that, despite other opinions in the current literature, TLE data has been sufficient for the tracking of FedSat with sufficient accuracy, in conjunction with diligent spatial and temporal calibrations. Besides, the usual procedure of conducting tracking experiments has been describes, as well as supporting
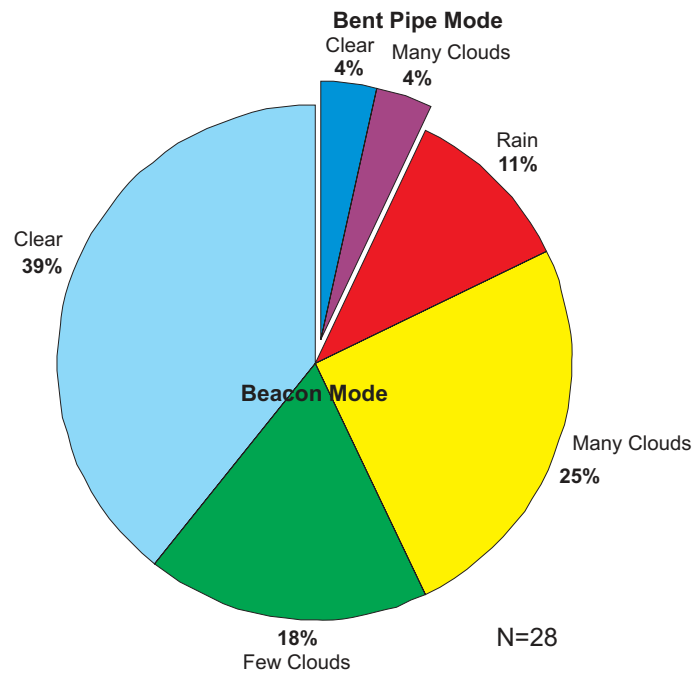
Figure 5.30: Percentage of prevailing weather conditions during beacon and bent pipe mode experiments with data collection

weather data sources complementing the analysis of the measurements. Finally, the operational statistics of the prototype earth station in conjunction with the space segment have been presented, revealing a limited success rate in data collection and especially under the desired rain conditions. Consequently, it must be admitted that the experiment was not successful in recording statistically relevant amounts of data in order to develop new or suggest modifications of existing propagation models under rain conditions. Possible explanations for this unsatisfactory outcome are discussed in Section 7.1.9. However, other significant tropospheric effects were also observed and are presented in the following chapter.

Chapter 6

Attenuation Data Analysis and Discussion

Previous chapters have offered a detailed insight into the design and operation of FedSat and the UTS Ka band earth station as a research platform, the methodology of propagation data collection as well as technical challenges and project limitations. In this chapter, actual results of attenuation measurements under various conditions and for both beacon and bent pipe mode will be presented and discussed. Due to the limitations imposed by the small number of rain passes, a comparison to existing attenuation models is not representative, but attempted on an exemplary basis. The author's previous publications [15], [16] and this chapter represent the first published data of Ka band propagation measurements over a LEO *micro*satellite.

6.1 Analysis Software Development and Data Processing

Chapter 5 has already introduced some of the systems-related aspects that need to be taken into account in data processing, such as GPS versus UTC timing, antenna pattern modelling and squint angle compensation. Since the pre-computed Nova™ coordinates, actual spatial tracking, power measurements and the recorded spectrum all initially operate on different time lines and in varying intervals, they must be precisely related to each other and interpolated, if required. In order to automate the processing of the large amount of data for each pass, the author has developed an analysis package under Matlab™, which also includes plotting routines for visualisation purposes. With reference to the files generated before and during a pass, Table 5.3, Fig. 6.1 illustrates how the various data is imported, synchronised with respect to UTC/GPS time, validated and saved as processed data files.
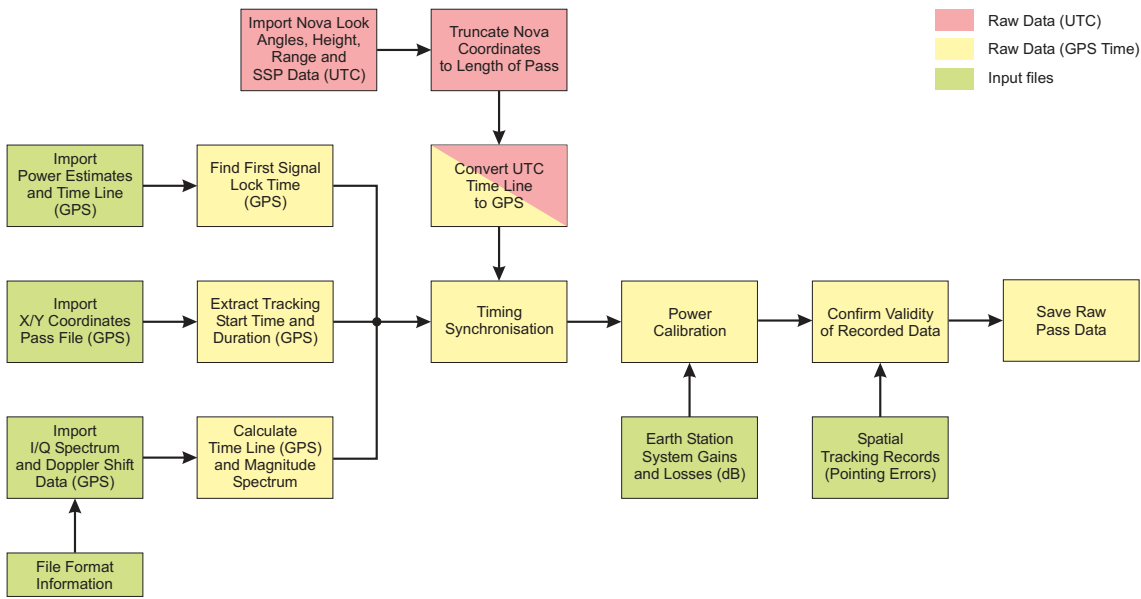
Figure 6.1: Block diagram of the developed Matlab™ data import program, also indicating the different timing references

After the raw data import, the power measurements have to be translated to path attenuation by subtracting the free-space path loss and by taking the squint angle and the antenna radiation pattern into account (Fig 6.2). The result is then expressed in terms of elevation rather than time and plotted. A statistical analysis of the attenuation allows the generation of the familiar '% Attenuation > Ordinate' graph. Due to the very large amount of spectral data (approximately 130 MB of source data per pass), it needs to be downsampled (interpolated) first for plotting purposes only. An exemplary run of the Matlab™software is shown in Fig. 6.3.

6.2   Attenuation - Beacon Mode Examples

In this section, several examples of the measured atmospheric attenuation on the downlink (20.13 GHz) will be presented, all of which were conducted by receiving the satellite's beacon signal and measuring the power at the earth station. An example of the beacon observed on the spectrum analyser at several instances during the pass is depicted in Fig 6.4, clearly showing the Doppler shift occurring over time.

While not all experimental results can be examined within the scope of this work, those selected do highlight very typical features observed on most passes during the operational
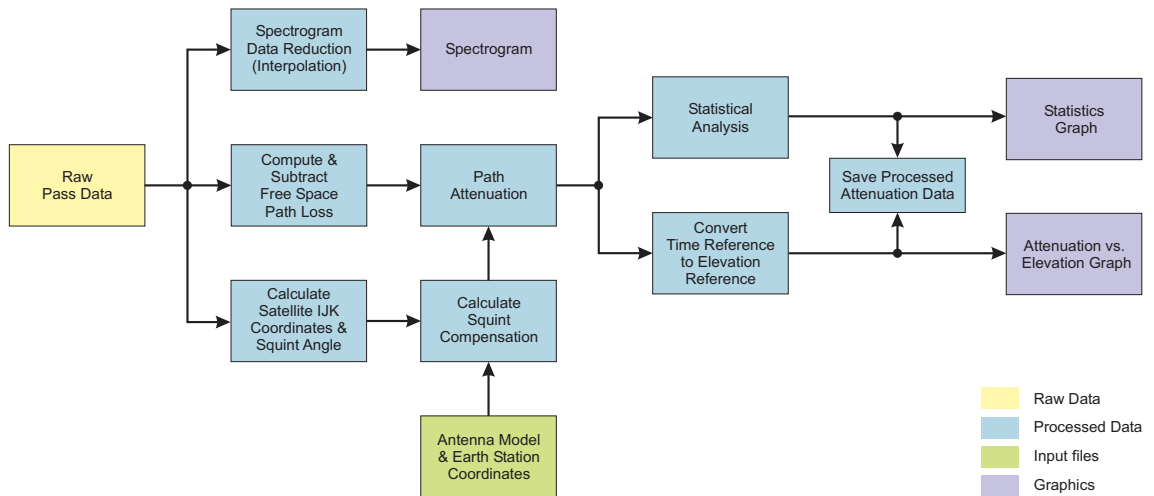
Figure 6.2: Block diagram of the Matlab™ data processing program for free space path loss and squint angle compensation, plus plotting routines

phase, which will be further discussed and validated. Each graph represents a time series on an elevation-scale abscissa for better comparison between passes. According to the above procedure, all *known* contributors to attenuation have been subtracted, such as free space path loss and the antenna gain according to the squint angle. It is also important to note that due to the physical restrictions of the X angle to the north (feed offset), observations do not generally commence below 25° to 30° elevation. On the descending path, the signal is tracked much longer until the SNR drops below the tracking threshold into the noise floor (typically around 10° to 15° elevation, even below 10° in exceptional cases). Consequently, most recorded graphs will not be symmetrical about the maximum elevation.

6.2.1 Clear Sky Conditions

Under 'ideal' clear sky conditions, i.e. no clouds, haze and a low ground humidity, very little attenuation would normally be expected on 20 GHz and at high elevation angles [33]. As the elevation decreases, the slant path length that lies within the atmosphere increases, and additional effects would be expected to become evident in the graph. Fig. 6.5 shows the received signal recorded over a duration of 8'55" and at a maximum elevation of 64°.

It can be observed that the shape of the curve is mostly symmetrical about the max-

```
=================================================================
  UTS Earth Station Data Import, Processing and Plotting Procedure
                   (c) T. Kostulski 2003-2008
=================================================================

Please select Mode:
-------------------
Import and re-process ALL data [N]? Y

The following tasks will be performed:
=============================================
   Importing spectrogram, power estimates and ancillary data from disk
   Processing spectrogram and power estimates
   Computing and interpolating spatial angles
   Computing antenna squint compensation
   Plotting both spectrogram & power estimates
=============================================

Checking data files...
----------------------
   Spectrogram Data file found.
   Power Estimates Data file found.
   X/Y Pass Data file found.
   Az/El Data file found.
   Nova Data file found.

Importing Spectrogram
---------------------
   Importing raw spectrogram data from disk (1-2 min)...
   Clipping 7 frames from start and 2 frames from end of spectrogram, 4747 frames remaining.
   File format: Type 3. Extracting data fields...
   Calculating spectrogram frequency range and time line...
   Start of recorded spectrogram data is 7-11-2005 23:43:30.987 GPS.
   Converting complex data to magnitude values, scaling by 65.2 dB...
   Spectrogram variables saved in 15125_Spectrogram.mat

Importing Power Estimates and Coordinates
-----------------------------------------
   Importing power estimates data file...
   Importing look angle data file...
   Importing X/Y data file...
   Importing Nova data file...
   ==> Pass start entry found (23:41:47, GPS index = 136).
   Power estimates, look angles, SSP coordinates and timing variables saved.

Processing Spectrogram
----------------------------------------
   Interpolating spectrogram data...
   Interpolated spectrogram data saved to 15125_Spectrogram_plot.mat

Processing Power estimates and look angles...
---------------------------------------------
   Power estimates MAT file loaded.
   Antenna model MAT file loaded.
   Interpolating sub-satellite point coordinates...
   Calculating spatial vectors...
   Interpolating coordinates and path attenuation...
   Processed power estimates...
   Spatial coordinates saved to 15125_PwrCoords_plot.mat.

Plotting 3D Spectrogram...
----------------------------------------
   Power estimates & coordinates MAT file loaded.
   3D Spectrogram plot created.

END
```

Figure 6.3: Run time example of the propagation data analysis software, performing various import and processing tasks.
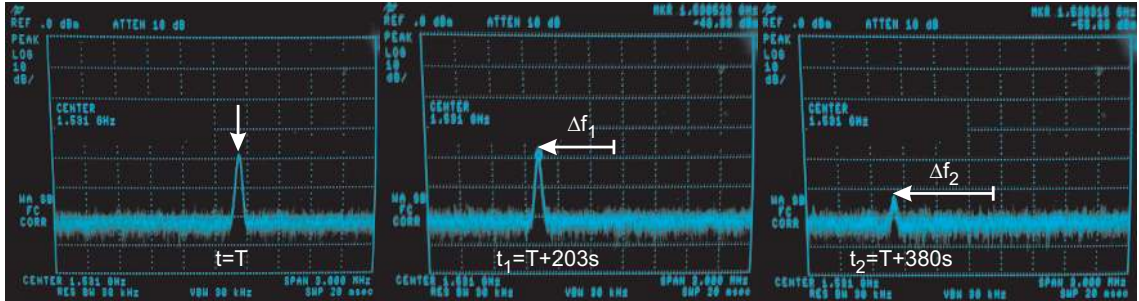
Figure 6.4: Spectrum analyser beacon observation (L band IF), indicating the decreasing Doppler shift and the signal magnitude variations (23, 20 and 7 dB C/N)
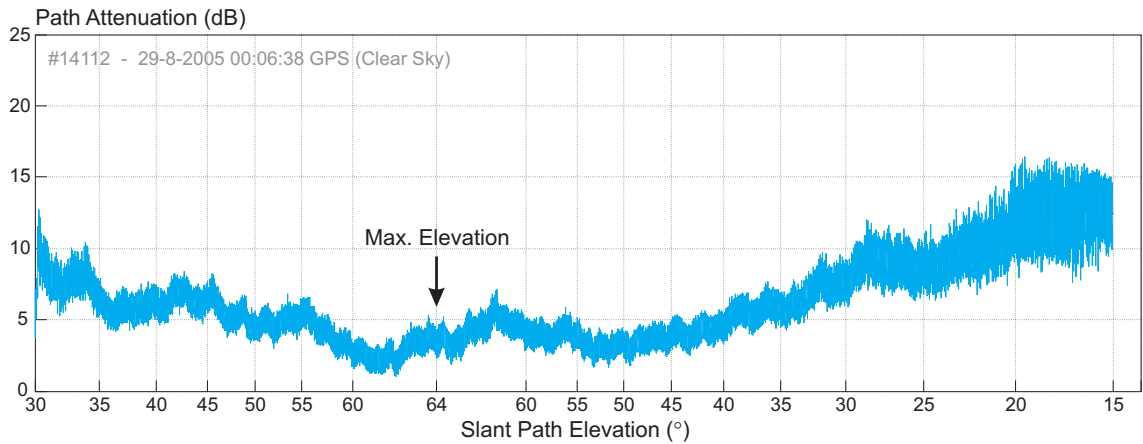
Figure 6.5: Beacon reception in clear sky conditions and 55% ground humidity on a 64° maximum elevation pass

imum elevation point, with a few 1 to 2 dB low-frequency fluctuations on the ascending path. On the descending side, the underlying variations are small, and the attenuation slope ascends linearly. The difference between low and high elevation angles is in the order of 10 dB. The high-frequency component superimposed onto those variations extends to about 1.5 to 2 dB in magnitude around the highest elevation and rises significantly to approximately 5 to 6 dB at 20° elevation and below.

For comparison, Fig. 6.6 was recorded during a high-elevation pass (83°). In this case, the variability of attenuation over the duration is somewhat greater and shows several abnormalities. While the low-angle attenuation on the descending path corresponds very well with the previous example, the values at from start to maximum elevation are higher. The minimum attenuation does not occur at closest proximity of the spacecraft. The amount of high-frequency fluctuations is very similar at corresponding elevations, and slightly lower at near-zenith angles (1 to 1.5 dB).
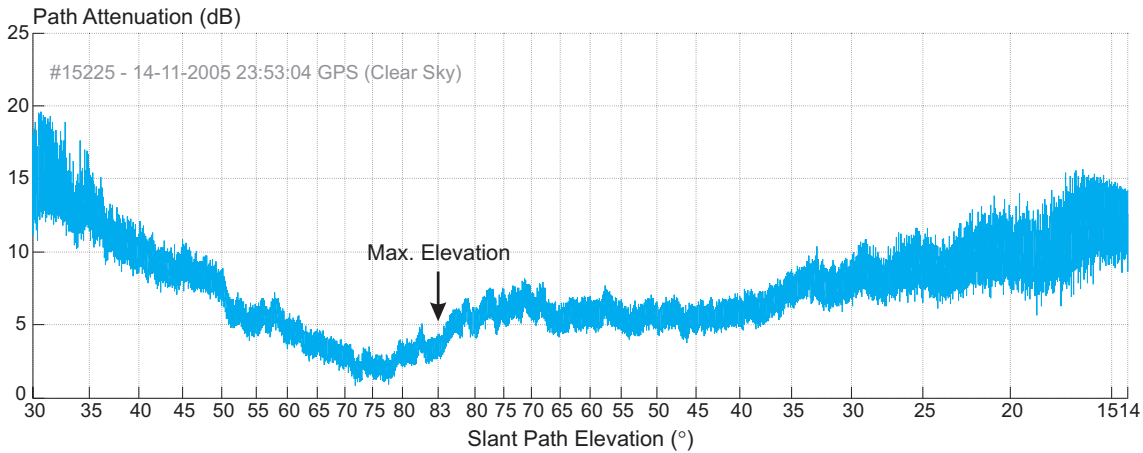
Figure 6.6: Beacon reception in clear sky conditions and 43% ground humidity on a 83° maximum elevation pass

When observing the right side of the previous graphs, one may observe a slight 'tapering' of the scintillation. This effect is caused by the receiver on the analog interface card, which has reached its lower limit of the dynamic range. The slight slope is introduced by the free space path loss subtraction and the squint angle compensation. At the receiver input, the weak signal is virtually disappearing in the noise floor at the elevation decreases,

yet it is still being reliably detected by the frequency tracking algorithm. It must be noted that signal tracking at this low elevation is well below the design specifications, hence the magnitude of the scintillations is likely to be slightly under-represented at elevations below approximately 16° in these graphs.

For experimental purposes, the dynamic range was adjusted by means of the variable attenuators. Fig. 6.7 shows a low-elevation clear sky pass that was unfortunately affected by multipathing of the mast. Disregarding the area marked in red, this clear sky pass shows the familiar features of relatively little disturbance by low-frequency variations, with the exception of a short increase in attenuation around 43° on the descending path. The signal was continuously tracked to an elevation of only 7° above horizon before lock was lost.
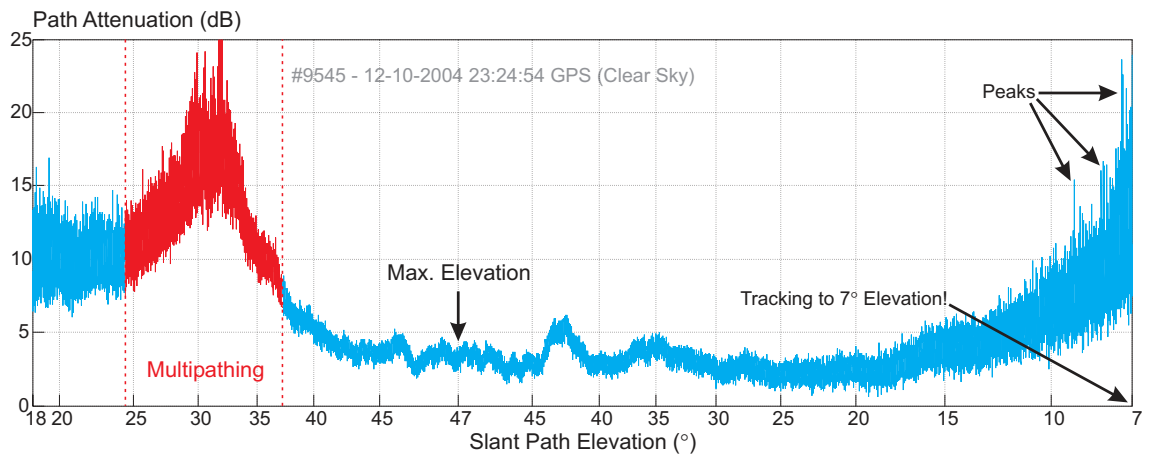
Figure 6.7: Beacon reception in clear sky conditions down to 7° elevation, but with multipathing effects due to obstructions. Severe scintillation is evident at low elevation angles.

Interpretation: The general shape of the recorded data essentially validates existing models that path attenuation is particularly prominent at low elevation angles. In absolute numbers, the clear sky attenuation around the highest elevation of each pass is also within the expected range of 1 to 2 dB when superimposed fluctuations are removed. However, it is evident that low-frequency disturbances in the order of 2 to 3 dB occur even in perfect clear sky conditions, possibly due to localised humidity and temperature convection of the air close to the ground.

Tropospheric scintillation is clearly the cause of the high-frequency fluctuations (fading), and the fact that it reaches magnitudes of more than 10 dB at very low elevation angles ($<10°$ in the last graph) has serious implications for the choice of suitable modulation schemes in satellite communications (see Section 6.2.3). Especially in last example, the long path through the atmosphere causes very severe scintillation and possibly some multipathing (peaks!), as terrestrial propagation models start to become valid [3].

6.2.2 Cloudy Conditions

Previous experiments on GEO satellites have established that clouds are a minor, yet non-negligible factor at Ka band frequencies, and their presence can be very well observed in the propagation measurements during corresponding passes. Since clouds can form very complex structures in multiple layers, each one can introduce different effects which are cumulatively observed. The following examples have been recorded under a variety of cloudy weather conditions.

Fig. 6.8 shows a $79°$ elevation pass, for which visual observations (photography/video) have recorded a full altostratus cloud cover to the north (AOS) and overhead. Descending from about $45°$ elevation, the cloud cover suddenly ends, and clear sky appears for the rest of the pass until LOS. Comparing these records to the attenuation, most of the undulations can be noticed in the cloudy section, where variations of 2-3 dB occur on one occasion, and minor ones to a lesser extent. In contrast, the descending path (below approximately $55°$) is virtually free of such fluctuations. The magnitude of tropospheric scintillation is again fairly symmetrical about the maximum elevation point.

The pass shown in Fig. 6.9 could possibly be mistaken for a clear sky pass due to the apparent absence of any fluctuations larger than 1 to 2 dB. However, small, scattered altocumulus clouds covered about half of the sky, but do not seem to have any major impact on the signal. The tropospheric scintillation appears as previously discussed and is most probably unreliable below $15°$ (clipping).

The data displayed in Fig. 6.10 was recorded during sky observations of a uniform, full stratus could cover. Status clouds have the potential to produce light to moderate
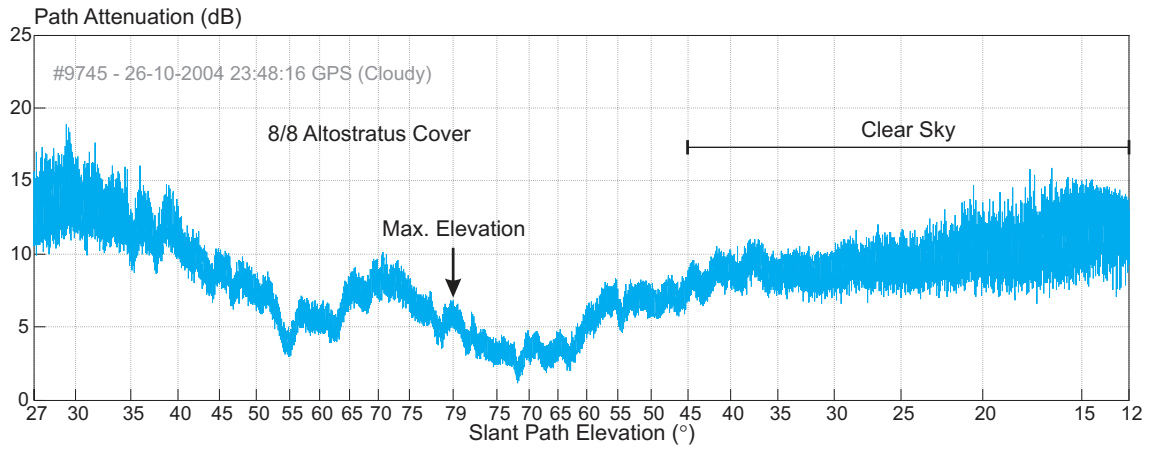
Figure 6.8: High-elevation beacon mode pass recorded with a full cloud cover at AOS and overhead, and clear sky on the descending path.
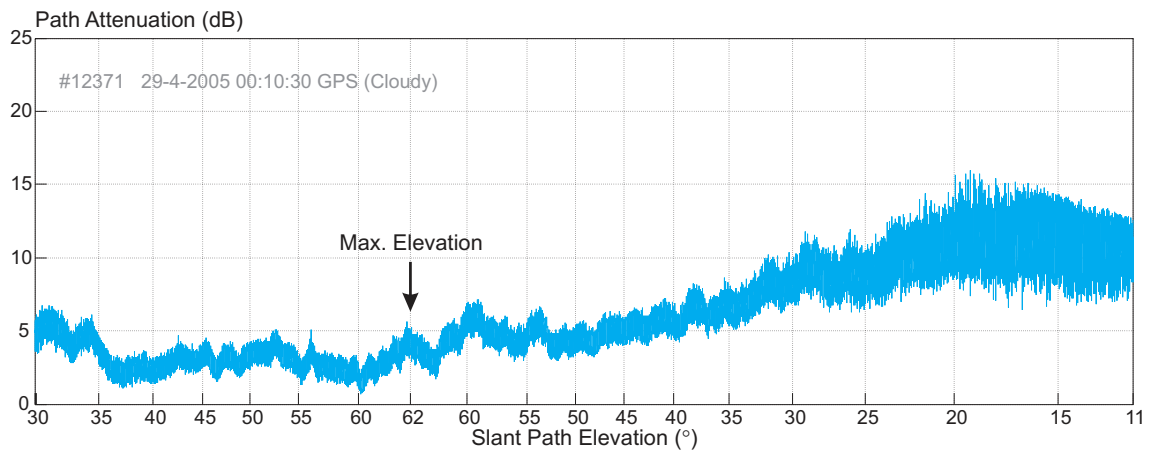
Figure 6.9: Beacon mode experiment during a 62° elevation pass with 4/8 scattered stratocumulus cloud cover.

precipitation, which is usually widespread. In this case, no precipitation was recorded neither at the earth station site nor at surrounding pluviometers. The generally elevated and less defined attenuation level around the maximum elevation (of only 61°) suggests that the clouds hold an amount of hydrometeors that is significant enough to cause some cloud attenuation and fluctuations of only short duration. Scintillation levels do not appear to be affected.
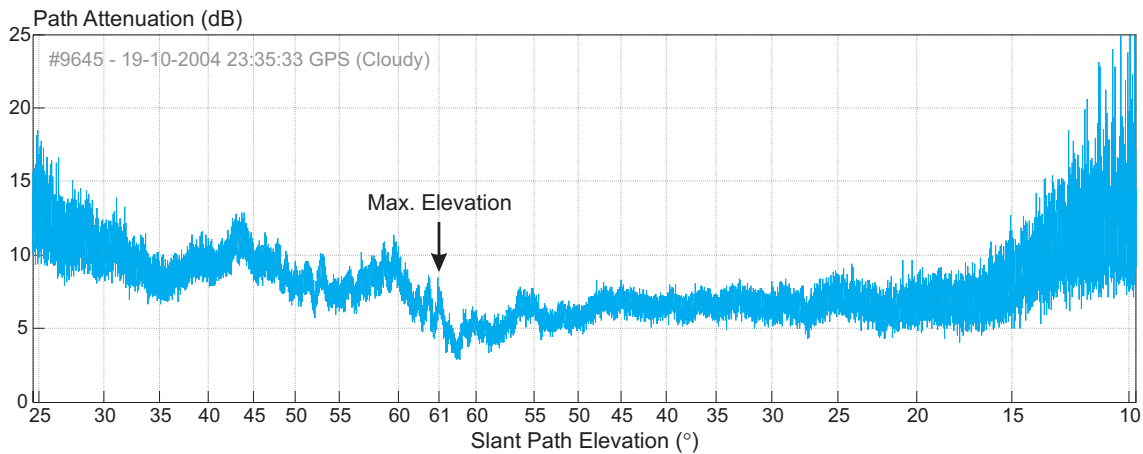
Figure 6.10: Beacon mode experiment (61° maximum elevation) with a complete 8/8 stratus cloud cover

Interpretation: Although some attenuation effects can be related to the presence of cloud cover during the pass, observations differ from the presented clear sky case only to a minor extent. Generally, any undulations tend to be of shorter duration, which would be related to the rapid movement of the satellite across the sky. This analysis is limited, since no large convective clouds (for example cumulonimbus) have been observed during the course of the project.

6.2.3 Rain Cells

It has previously been shown that this project has suffered from a lack of rain events coinciding with satellite passes, and only three passes with full or partial precipitation have been recorded in total. Since rain attenuation is the main contributor to propagation effects in Ka band satellite communications, it would have been very desirable to record

more significant rain events than those presented in this section. The possible causes for this deficiency are discussed in Section 7.1.9. However, some interesting observations can still be made.

The pass in Fig. 6.11 presents the signal power received during a partial rain pass with isolated cells. The elevated attenuation at AOS, 18 dB (average), suggests the presence of a significant rain cell, possibly nimbostratus, which was estimated at a rain rate of 10-15 mm/h according to weather data. The signal recovers quickly to 'normal' levels, as evident by the steep slope, before the slant path passes through another rain cell and experiences an attenuation of roughly 8 dB. No further rain attenuation is evident for the remaining descending path.
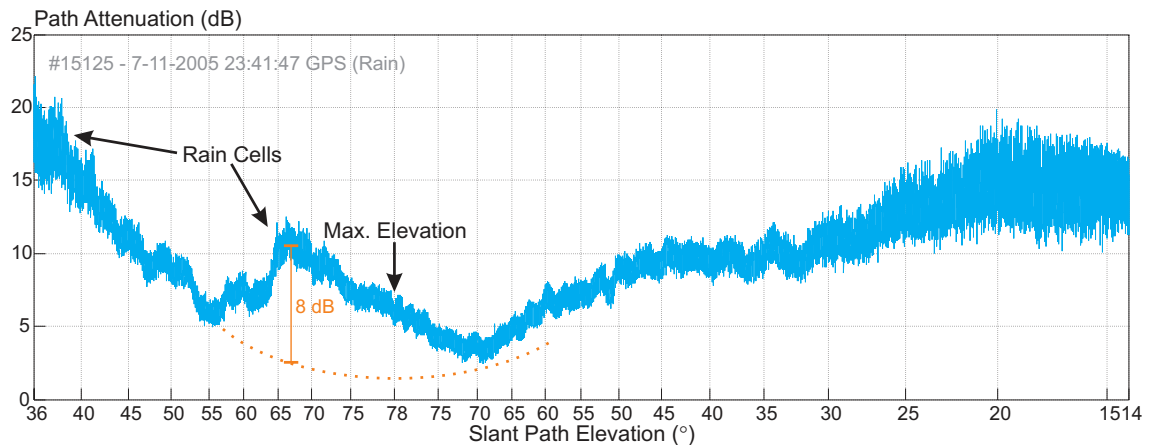
Figure 6.11: Beacon mode rain pass with two separate rain cells

Fig. 6.12 was recorded during a partial rain pass, with stratus clouds between the AOS point and maximum elevation. The rain rate recorded near the earth station was between 3-5 mm/h for the duration of the pass due to a medium-size rain cell. The trajectory continued into a widespread, stratiform rain band to the south (LOS).

Comparing the visual observations with the attenuation data, the effect of the single rain cell is immediately obvious, with an estimated total attenuation of approximately 5-6 dB due to rain and clouds; dish wetting may have also been a factor, but this cannot be quantified sufficiently. The stratiform rain band (approximately 5 mm/h) at the descending path allows very interesting observations. At elevation angles below 40°, the
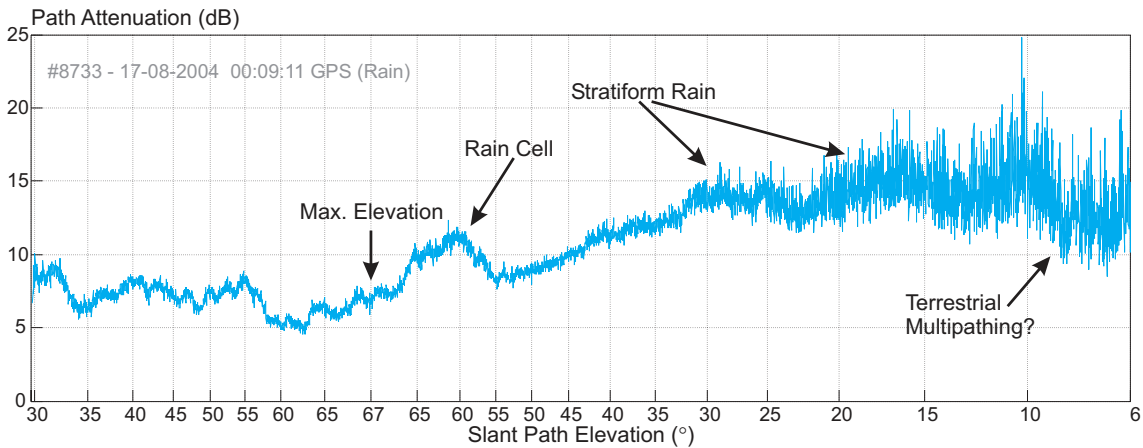
Figure 6.12: Beacon mode power affected by scattered rain cells and a stratiform rain band

slant path length through the rain is considerable, and a large amount of attenuation, compared to a clear sky, is introduced (estimated at 7-8 dB). As expected, scintillation also increases significantly at lower elevation angles, and it would be reasonable to expect that path attenuation would also increase further as the slant path drops below 10° elevation. Quite in contrast, the attenuation *decreases* by several dB (with some fluctuations), providing evidence that *terrestrial* multipathing effects are indeed very significant at these low angles and can even lead to signal amplifications through reflection in combination with the rain.

The final example comprises a pass conducted under localised, light rain (5-10 mm/h) on the following day (Fig. 6.13). The pass commences in a northerly direction that is not immediately affected by precipitation, but soon moves into an extensive rain cell that introduces approximately 8-10 dB attenuation. The maximum elevation point is affected by 3-4 dB attenuation above the normal clear sky value for 66°, and a second rain cell appears and weakens the signal by similar amounts as the first one. Below 45° elevation, no further rain attenuation can be observed.

Fig. 6.13 also contains a comparison of the measurements without (grey) and with (blue) squint angle compensation. The two graphs correspond in only two points, at ±50° elevation, and any measurements without the antenna pattern and squint angle compensation would introduce very significant errors in their measurement in excess of
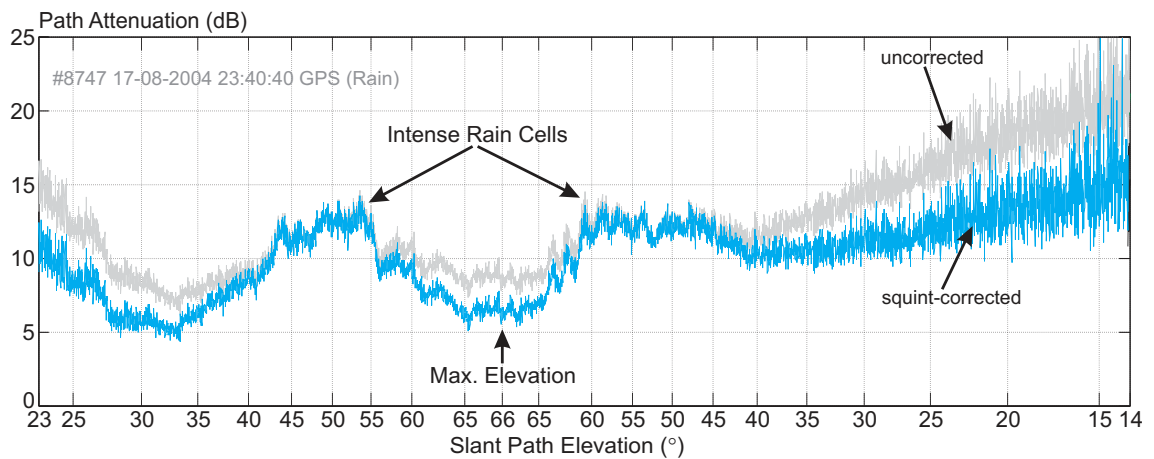
Figure 6.13: Beacon mode pass under light rain conditions, also illustrating the significance of the squint angle correction

5 dB at low elevations.

Interpretation: It is evident that even relatively light rain events can severely affect Ka band signals, as it is well understood from previous experiments. In this project, the limited amount of rain data has produced observations of up to 10 dB attenuation. In addition, interesting low-angle observations under rain conditions have been made, which can be attributes to terrestrial multipathing effects, leading to an unexpected amplification of the signal at elevations below 10°. Even more than in the previous cases, the very strong fades at low elevations pose serious challenges for higher-order modulation schemes in digital communications. More efficient schemes than PSK, but without constant envelopes, such as 16-QAM, are more vulnerable to the perturbation of decision boundaries during the deep fades.

The magnitude of scintillation does not appear to change significantly with rain present and stays within the same range as observed under the previous conditions. However, this statement is limited to the observation of Fig. 6.11 only and excludes very low elevations due to clipping. The attentive reader would have noticed that the magnitude of scintillation in the other two rain pass records is *significantly* lower than all other examples presented so far. The reason for this lies in the fact that the passes with seemingly smaller

scintillation have been recorded at the lower sampling interval of 100 ms instead of the improved 4 ms interval, as explained in detail in Section 4.9.4. Apparently, the original sampling rate is clearly insufficient to record the rapid fading precisely enough to detect the larger magnitude fluctuations. This is a very important realisation and a clear endorsement of the proposed design modification. Although the scintillation magnitude is likely to be inaccurately in Figs. 6.12 and 6.13, they are still considered worthy of publication due to the documented rain events.

6.3 Attenuation - Bent Pipe Mode Examples

In bent pipe mode, a Doppler pre-corrected carrier signal is transmitted by the UTS earth station to the spacecraft on 29.93 GHz. The Ka band transponder downconverts the received signal, plus uplink noise, via several IF stages to the 20.13 GHz downlink frequency and re-transmits it. At the earth station side, the originally transmitted signal is received again, with both uplink and downlink noise added. In this 'single earth station' configuration for research purposes, the same prevailing weather conditions will affect both the uplink *and* the downlink, but to a different extent (Fig. 6.14). The example presented in this section was recorded under cloudy conditions (8/8 stratus), which has precipitation potential. However, no rain was recorded at the time of the pass around the site.

Similar to the previous beacon mode experiments, the signal power is recorded and compensated for free space path loss, antenna squint angle and earth station system gains and losses. It is important to note that path attenuation indicated in Fig. 6.15 is with respect to the *downlink only*. The power level has been calibrated to the nominal spacecraft beacon mode Ka band RF transmit power, which has previously been illustrated in Fig. 5.7 for *this particular pass* (#5051, bottom graph). Comparing the beacon mode power level and the maximum bent pipe mode power levels, this choice of reference appears very appropriate. The same graph (in 1-second intervals) also confirms that the transmit power varies over the duration of the pass according to the signal strength received on the uplink. The maximum (around 10:42:30 local time) roughly corresponds to the calculated maximum elevation of the pass at the UTS earth station in GPS time.
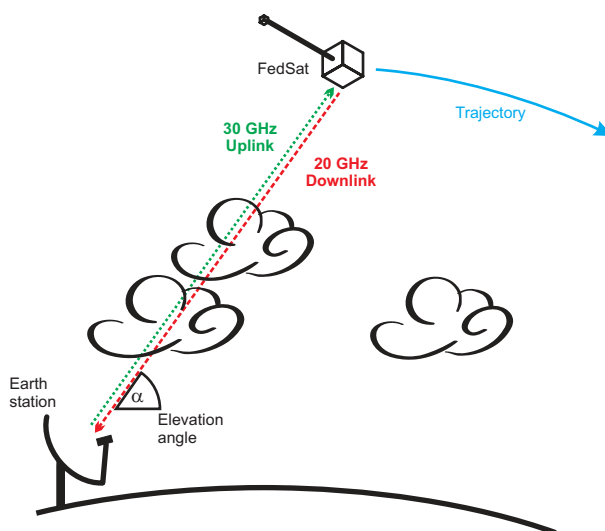
Figure 6.14: Illustration of bent pipe mode signal transmission and reception by the same earth station
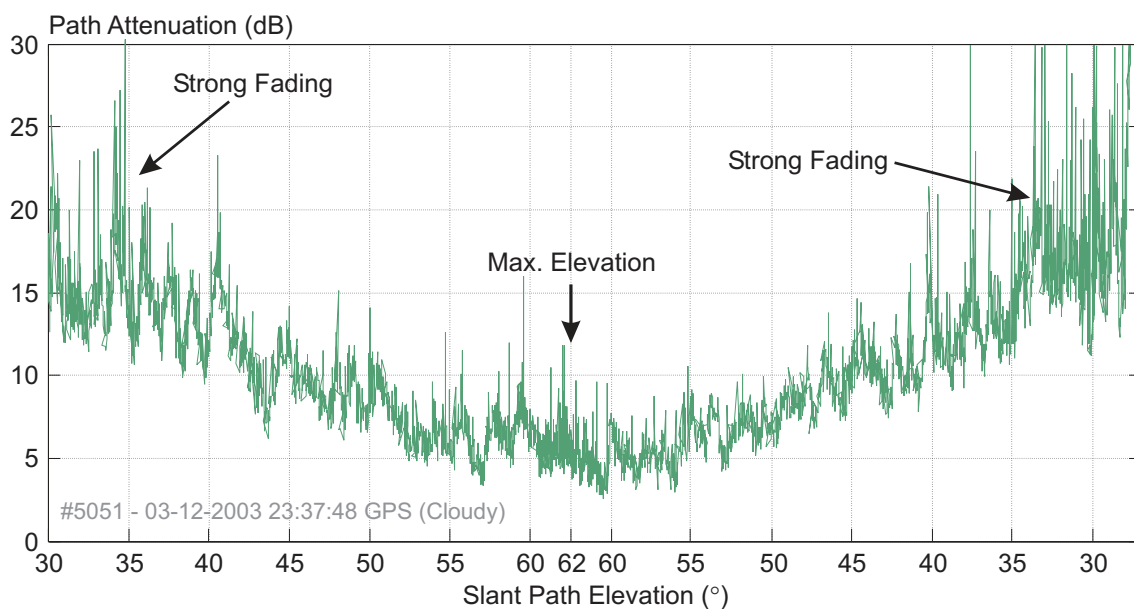
Figure 6.15: The signal received in bent pipe mode is subject to downlink attenuation, as well as re-transmitted uplink fading

When comparing the bent pipe mode with the beacon mode examples, it should be observed that the attenuation scale has increased to 30 dB in order to accommodate the large fades. Also, this pass was recorded with a 100 ms sampling interval only. Essentially, the curve follows the familiar convex shape at higher elevations, and the attenuation slopes descending from the highest elevation are slightly more inclined than in the beacon mode case. The superimposed scintillation shows very significant fluctuations between 3 to 5 dB even around 60°. Very deep fades in the order of 10 dB become a prominent feature below 40° elevation, even more so below 35° (10-15 dB).

When relating the measurements to the sky observations, one must realise that the signal had to penetrate a full cover of low stratus clouds *twice*, experiencing different rates of attenuation on 30 GHz and 20GHz due to the size and distribution of hydrometeors contained in the clouds. It is reasonable to assume that since the signal has to travel a *long* path particularly through low-level stratus clouds, it does experience quite significant attenuation (more prominent on the uplink than on the downlink). Unfortunately, due to the insufficiently low sampling rate of the spacecraft telemetry system, the effects of uplink and downlink attenuation cannot separated in this experiment.

Since the uplink noise received at the spacecraft is amplified and re-transmitted, the carrier-to-noise ratio $(C/N)_{tot}$ is combined from the uplink ratio $(C/N)_u$ and the downlink ratio $(C/N)_d$ as follows [2]:

$$\left(\frac{C}{N}\right)_{tot} = \frac{1}{\left(\frac{C}{N}\right)_u + \left(\frac{C}{N}\right)_d} \qquad (6.1)$$

A 3-dimensional view of the spectrogram recorded for this bent pipe mode pass is shown in Fig. 6.16. It will be shown in Chapter 7 how a different perspective of this graph helped resolving a very persistent onboard problem with bent pipe mode operation and discovering the reason for a large number (9) of unsuccessful bent pipe mode experiments.

The Doppler tracking performance for this bent pipe mode pass has previously been presented in section 5.5.1. With the new knowledge of very severe fades below 40°, it is quite remarkable that lock was maintained below 30° elevation with great accuracy.

Fig. 6.17 depicts the received signal during the same bent pipe mode pass, viewed on a
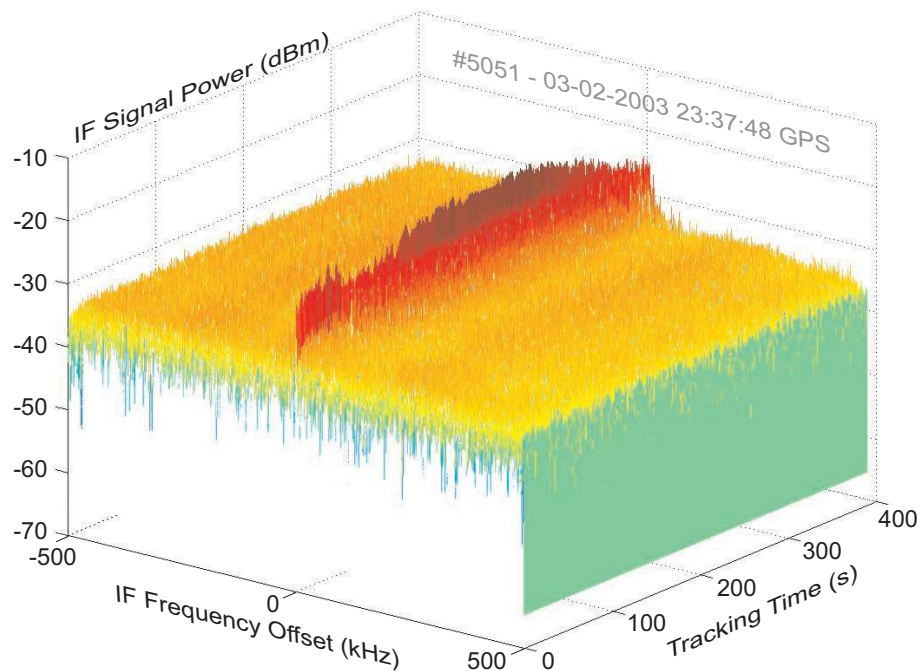
Figure 6.16: Spectrogram of the bent pipe mode pass, with the detected carrier signal perfectly in the centre (Doppler compensated)

spectrum analyser on L band. With a span of 3 MHz, the raised, "bell-shaped" noise floor around the carrier signal can be observed. This additional feature, compared to a beacon mode pass, is the re-transmitted *uplink* noise, filtered by the 1 MHz wide bandpass filter in the Ka band bypass in the UHF payload (see Fig. 3.11). It can also be observed that the carrier signal lies right in the centre of the filter in both photos, confirming that the uplink Doppler pre-compensation is very accurate and that the Ka band LO drifts are indeed small. This observation justifies the previous remark that the measured Doppler curve is very close to the theoretical one, including uplink frequency offsets.

6.4 Validation and Discussion of Results

Chapter 2 has already shown that previously published and verified data for LEO Ka band propagation experiments is not readily available for comparison due to commercial-in-confidence or military restrictions. The results published from the only other LEO Ka band research satellite, ROCSAT-1 [12], are of very limited scope and quantity, and do
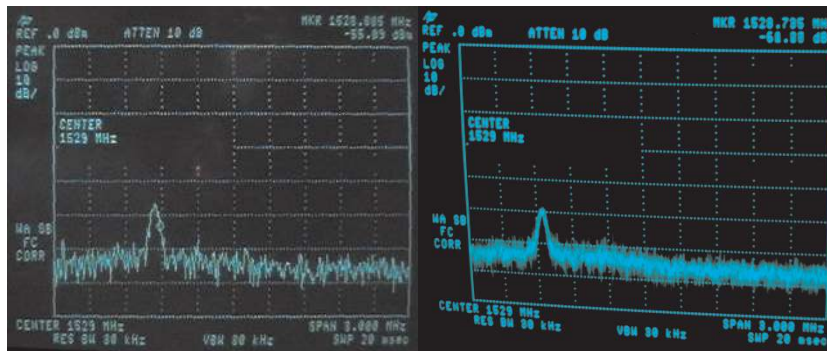
Figure 6.17: The bent pipe mode signal as viewed on the L band spectrum analyser

not allow a direct validation. Consequently, results from the many GEO experiments over ACTS, Olympus and similar satellites serve as sources to validate the observations made in this chapter. In addition, Ippolito [136] has extended the understanding from GEO Ka band propagation experiments to predictions about LEO behaviour under similar conditions.

Fig. 6.18, obtained from [137], was recorded from the 20/27.5 GHz beacons of ACTS at Vancouver, a location with a maritime climate similar to Sydney, although at at higher latitude. The GEO satellite was observed at 29.3° elevation, which is a frequently observed elevation in the FedSat experiments.
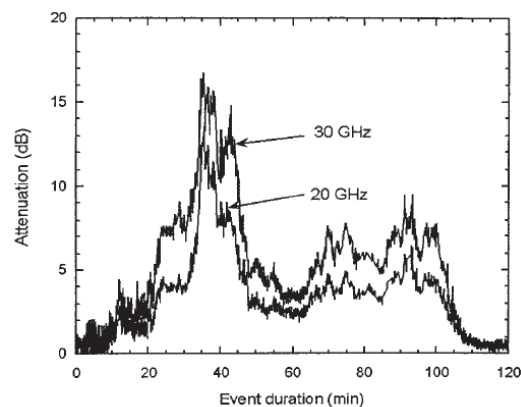
Figure 6.18: Rain event recorded from the ACTS 20/27.5 GHz beacons at Vancouver in 1997 [137]

The range of attenuation observed during the **rain** event is similar to the rain pass

observations presented in this chapter. Although no rain rates are given, the phrase "widespread rain typical of maritime climates" used in this source is likely to refer to precipitation originating predominantly from low-level stratiform clouds, such as stratus. Similar precipitation has been observed in the FedSat experiment, with very comparable results at similar elevation angles (5-10 dB attenuation).

A multitude of events has also been recorded in [138] via the OLYMPUS 20 GHz beacon, with the observing earth station being located in Bradford, England. Most results for rain events lie within the range observed here, 5-15 dB attenuation. JPL [33] has also been involved in the OLYMPUS Ka band propagation measurements. The OLYMPUS beacon was observed at a relatively low 14° elevation angle from Blacksburg, VA, in preparation for the ACTS experiments, yielding comparable results and attenuation *ranges* as observed at low elevation angles in the UTS experiment (Fig. 6.19). However, the peak attenuation of up to 40 dB in the right graph was certainly due to an extreme event and was not observed at UTS due to the lack of high rain rates.

The time series for the signals received at 20 and 30 GHz on January 7, 1991.

20 GHz beacon attenuation (∘) and fade slope (+) from 10-second block-averaged data, May 6, 1991.
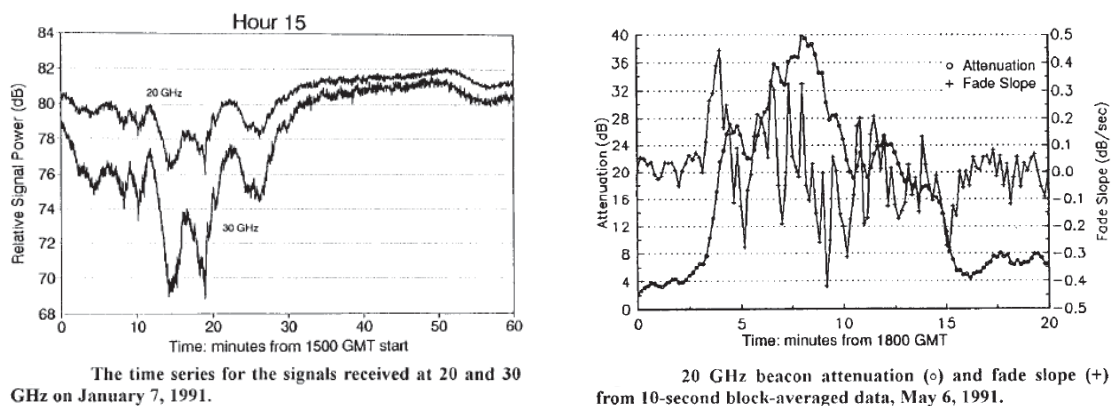
Figure 6.19: Attenuation events recorded by JPL in Blacksburg, VA, at 14° elevation from the OLYMPUS satellite in 1991 [33]

Fig. 6.20 presents a second OLYMPUS result from Blacksburg, depicting a recorded rain event with rates up to 80 mm/h. The *onset* of this event allows a comparison with FedSat data, because at an estimated rate of 10-15 mm/h, both the OLYMPUS and the FedSat example (Fig. 6.11 show an approximate attenuation of 7-8 dB at 20 GHz.

An interesting graph quantifying **cloud attenuation** on 15/35 GHz and up to 20° ele-
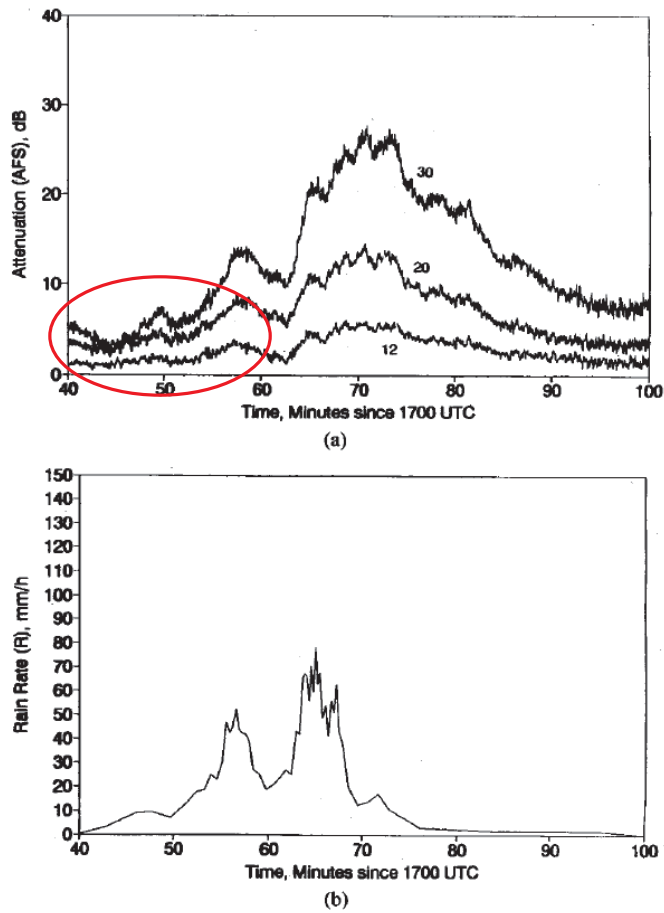
Figure 6.20: Rain event (bottom) recorded from the Olympus 12, 20 and 30 GHz beacon signals (top) in Blacksburg, VA, in 1991 at 14 °elevation (relative to free space). The rain rate region of interest is indicated. [139]

vation can be found in [21]. Although not specifically containing results for 20 and 30 GHz frequencies, values for the Ka band can be inferred. In addition to the graphs for slightly non-unform clouds already reproduced in Fig. 2.4, the curves in Fig. 6.21 represent the attenuation introduced by highly irregular (left) and heavy clouds (right) as functions of the slant path distance and the elevation angle, respectively. The effect of gaseous attenuation is included in the graphs. These measurements are of interest, because Boston, where the data was obtained, has a temperate, coastal location not very dissimilar from Sydney (although somewhat cooler), hence some parallels can be drawn. The fact that several decibels of cloud attenuation were observed even at moderate elevation angles in both studies for highly irregular and heavy clouds appears to qualitatively validate the results from UTS. Whether a LEO satellite moving rapidly across the sky, and therefore rapidly through clouds, can cause effects very similar to highly irregular *static* clouds is open to further discussion.

Angle/slant path distance dependence of attenuation for highly irregular cloud conditions.

Maximum observed attenuations for conditions of heavy cloud.
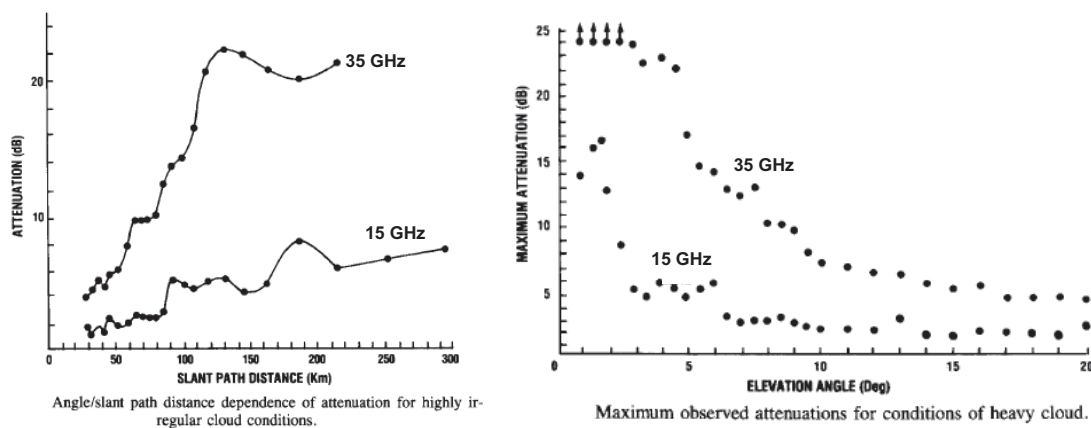
Figure 6.21: Attenuation introduced by irregular cloud formations as a function of path length (left) and elevation (right) on 15 and 25 GHz [21]

In addition, a more recent study in [140] presents highly averaged *long-term* measurements in New York and Germany with an attenuation of up to 1.5-2 dB, depending on the type of cloud. While extensive theoretical models are derived and compared in this work, they are mostly geared towards the assessment of GEO availability and do not focus on *short-term* observations on LEO satellites, as in the UTS case. It therefore appears that the cloud attenuation levels observed in the UTS experiment are slightly higher than

in [140].

The frequency and magnitude of **tropospheric scintillation** observed in the UTS experiment can be best compared to the beacon measurements by Mayer et al. [141]. In clear sky conditions and 8° elevation, scintillations with a magnitude standard deviations of over 1 dB commonly occur on 20 GHz, according to Fig. 6.22.
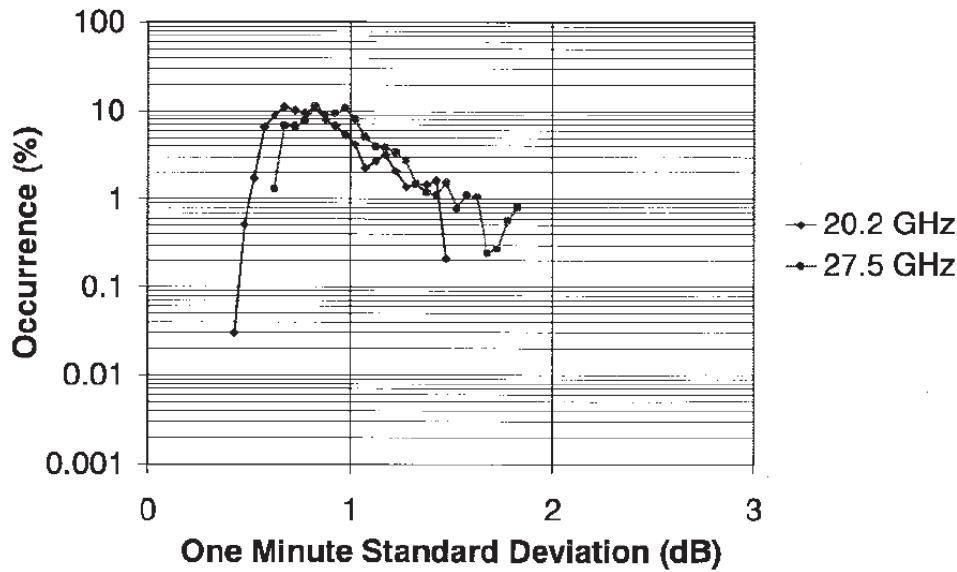
Figure 6.22: One-minute standard deviation of the scintillation on 20 and 27.5 GHz, measured over the ACTS satellite [141]

Data was sampled at up to 5 ms per second, which is similar to the 4 ms interval in the UTS experiment. A most recent publication about GEO Ka band beacon observations states that at least 2 samples per second are required to record tropospheric scintillation accurately, which "*dots*occur[s] at rates up to 0.5 Hz" [60]. A thorough frequency analysis of the scintillation recorded in the UTS LEO experiment (25 Hz sampling rate) has not yet been conducted, however it is apparent that neither the magnitude nor the frequency is in accordance with results in those two sources. Assuming that the statement in [60] and the graphs in Fig. 6.23 are correct for *GEO* observations, this gives rise to the hypothesis that the characteristics of the *perceived* scintillations may have been altered by the rapid movement of the LEO satellite across the sky. There is much room for further research

here, and the author is determined to pursue the investigation of this phenomenon.
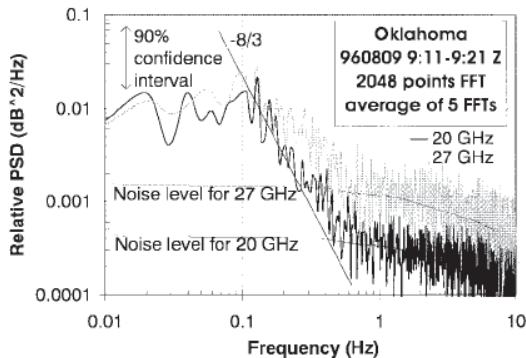
Fig. 17.   Power spectral density, Oklahoma.
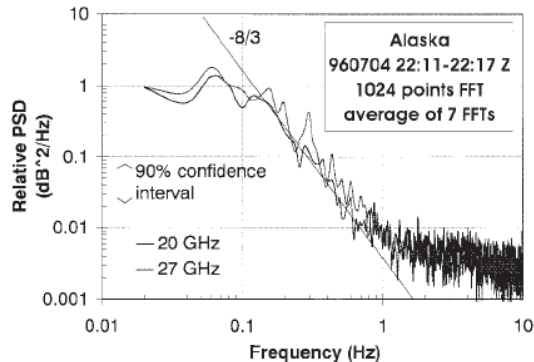
Fig. 18.   Power spectral density, Alaska.

Figure 6.23: Power spectral density of the ACTS Ka band beacon signals, observed in Oklahoma and Alaska [141]

Ippolito [136] theoretically assesses how the knowledge from GEO Ka band experiments, such as ACTS, can be transferred to emerging LEO communication systems. For a Ka band LEO satellite in polar orbit similar to FedSat, the graph in Fig. 6.24 suggests link margins (or conversely, attenuation) similar to the order of attenuation that has been previously presented. The sharp increase of the gaseous absorption at low elevation angles (beginning and end of the pass) are also accurately observed through low-angle fading.

Finally, it would be possible to compare the results by adapting the corresponding ITU model (or any of the other applicable models, for that matter) to varying elevation angles. ITU-R P.618-7 [23] and ITU-R P.839-3 [32] provide very extensive models for rain and cloud attenuation, as well as scintillation and low-angle fading/multipathing. Although these lengthly computations are elevation angle dependent and must therefore be processed in elevation increments, it would be very worthwhile to compare the validity of the model with actual measurements on Ka band, of which not many exist. However, it must be stressed that all models are based on long-term effects and not short-term observations of several minutes, as presented in this study, therefore discrepancies will most likely occur. Unfortunately, the implementation of the ITU recommendation and the modelling of the
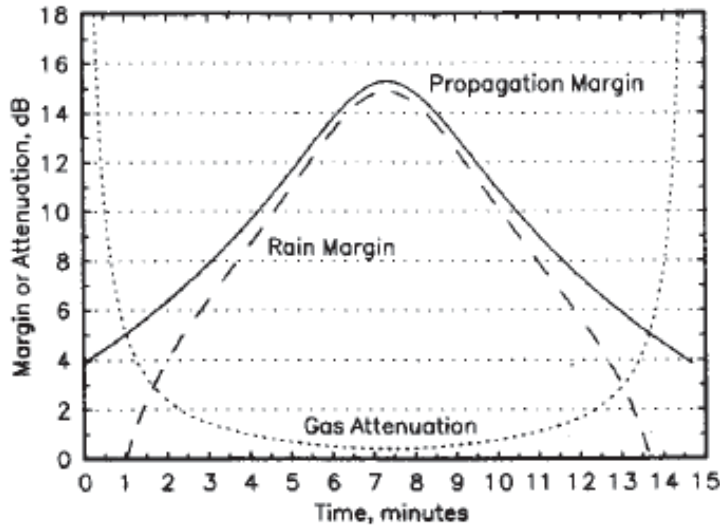
Figure 6.24: Proposed link margin for Ka band polar LEO satellite, including gaseous absorption and free space path loss [136]

propagation for all elevation angles is beyond the scope of this experimental dissertation and must be left for future work.

Conclusion: The measurements have confirmed that the earth station and the spacecraft are capable of operating in bent pipe mode. The even tighter constraints in terms of earth station antenna beamwidth and therefore pointing/tracking accuracy have been successfully met, and the Doppler tracking algorithm has also performed unexpectedly well. The additional, more severe attenuation introduced by the uplink contributed significantly to a much degraded downlink attenuation, resulting in deep fades in excess of 10 dB on medium to low elevation angles, but the effects of uplink and downlink cannot be separated due to telemetry limitations. Measurements over GEO satellites, especially for rain events, have yielded similar attenuation ranges under comparable conditions, and earlier theoretical considerations have been qualitatively verified through this experiment. Some interesting points for discussion have been raised regarding possible differences between LEO and GEO observations, which may be related to the *rapidly* varying slant path. Further study and the comparison with established models is needed.

Chapter 7

Project Review and Suggestions

It has already been mentioned in previous chapters that the design of both the satellite and the earth station had to compromise between desired technical capability, available time and most importantly budget. While the decision to develop space and earth station hardware within the CRCSS, along with most of the supporting software, has led to important knowledge about their successful performance on one side and shortcomings on the other. This chapter covers a brief review of the operation of the earth station and offers suggestions for improvements for future research groups who wish to look into this design.

7.1 Difficulties Encountered

Even before the operational period, several risk factor for the successful collection of propagation data were identified. However, in some respect the initially gravest concerns, such as pointing accuracy and timing, have *not* occurred at all, while the (temporary) failure of mechanical hardware and relatively simple software flaws have compromised the reliability significantly. A few examples are given in the following sections, including the record of an extensive, remote fault-finding procedure for a spacecraft malfunction.

7.1.1 Satellite Reliability

Referring to Fig. 5.29, it is striking that satellite malfunction has played a major role in unsuccessfully conducted experiments. Unlike other experiments (GPS, NewMag, FPGA,

star camera), the Ka band propagation experiments were required to take place under very controlled spatial and timing constraints. Both factors rely on the proper functioning of the DHS and the ACS, which have proven to cause frequent resets and therefore a loss of pointing mode, payload schedule other data.

A second unfortunate factor is related to FedSat's retrograde orbit and the location of the TT&C ground station. Because FedSat was visible much earlier from the Ka band earth station for any daylight (morning) pass than from the TT&C ground station, it was not possible to assess the satellite's health *before* engaging in the extensive, manual pass preparations, as described in Section 5.4. Although a confirmation was sought after the ascending pass the night before by accessing the telemetry remotely, often the disturbances happened during the next few orbits, and the experiment the next day failed due to satellite problems.

It should be mentioned that the Ka band payload itself has never been the cause of a problem during all experiments. While most difficulties can be related to the DHS and ACS, there has been a challenging interference problem, which is described below.

7.1.2 Payload Interference

In Chapter 3, it was regarded necessary to explain the FedSat communication payload in great detail, since a thorough understanding of its internal structure is crucially required when difficulties arise. Almost one year after the first successful bent pipe mode transmission and reception, the earth station developed difficulties in locking onto the bent pipe mode carrier, which was clearly visible on the spectrum analyser. Tracking was only possible for one or two seconds, before lock was lost again, despite a sufficient signal strength and flawless performance in beacon mode.

A thorough re-testing of the earth station for both transmit and receive, as described in Section 4.8.4, did not reveal any malfunctioning, but subsequent bent pipe mode passes resulted in the same effect. A first indication that the problem may not be with the earth station was given by the fact that the observed signal did *not* disappear from the spectrum analyser when the transmitter was turned off. A close analysis of the spectrograms recorded during the first, successful passes allowed a very interesting observation,

as displayed in Fig. 7.1.
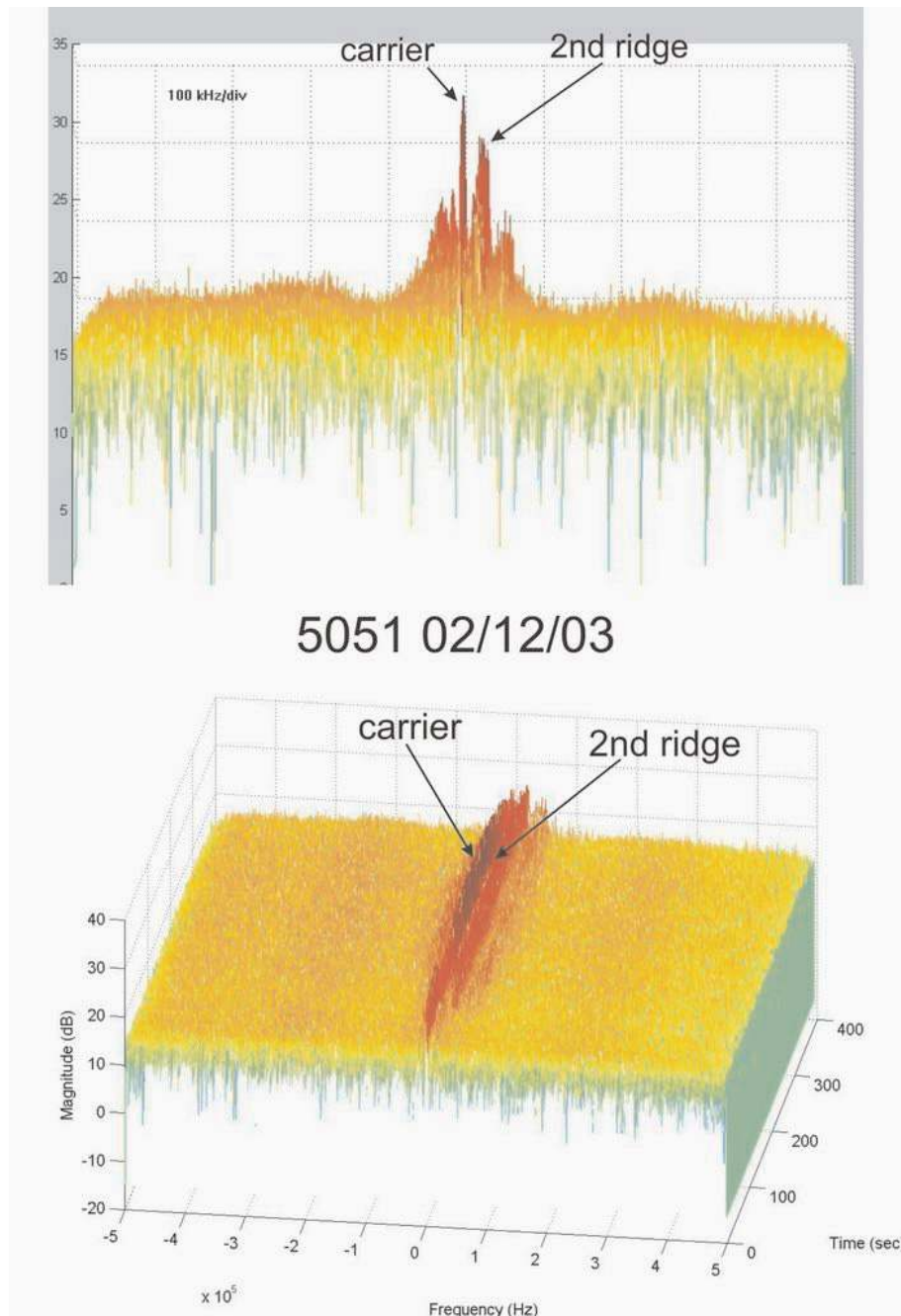
Figure 7.1: Investigation of the bent pipe mode problem: a look at the spectrogram of previous passes, revealing a spurious signal close to the bent pipe mode carrier

Although the frequency tracking algorithm managed to track and record the real signal correctly, the origin of the spurious emission had to be investigated. The fact that a signal

was transmitted from the spacecraft *without* an uplink carrier present caused a look at the telemetry for one such passes run in bent pipe mode, shown in Fig. 7.2. It turned out that the transmit signal power was as high than during a beacon mode pass, leading to the conclusion that a signal other than amplified uplink noise must be present.
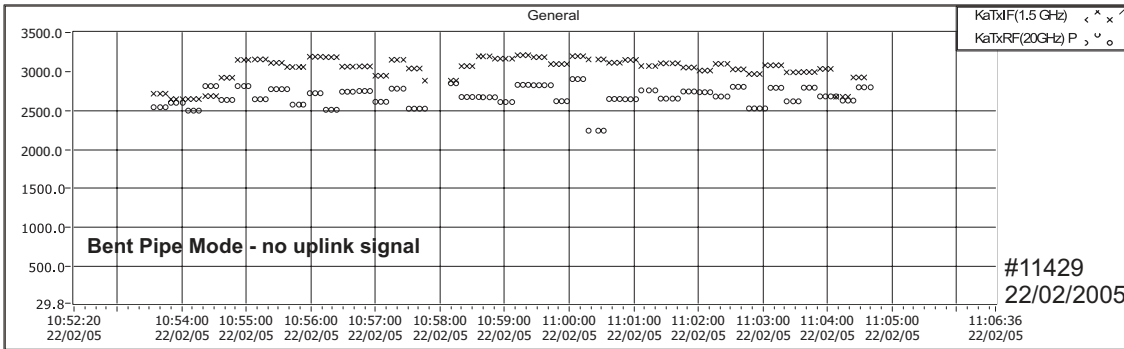
Figure 7.2: Ka band transmit power telemetry for a bent pipe mode pass *without* uplink signal (arbitrary units)

In cooperation with the TT&C ground station staff, the circuit diagrams of the signal paths were examined for the accidental insertion of a signal, together with the possible attenuation of the true uplink signal. The following components were identified (Fig. 7.3, also cf. Fig. 3.10):
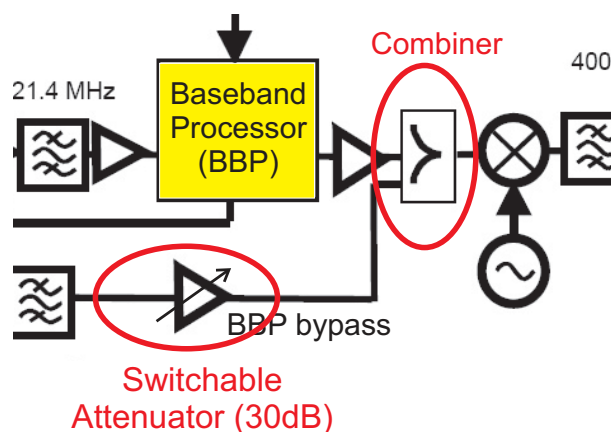
Figure 7.3: Detail view of the FedSat communications payload, 21.4 MHz IF, and possible causes of the fault

- *Combiner* - It is a possibility that a signal is accidentally inserted from the BBP through the combiner (not an RF switch)

- *Attenuator* - The switchable attenuator may have malfunctioned or failed, resulting in the complete removal of the uplink signal (nominal value: 0 dB).

There was now strong evidence that the spurious emission, which had probably always been present, but at a lower level, originated from the BBP. It must be recalled that the BBP needs to be powered up even during Ka band bent pipe mode, since it contains the local oscillators for the UHF circuit. The investigation was referred to the BBP research team, who looked at certain mode switches and software changes over the past months, including enabling and disabling the attenuator. Over the course of several experiments, different telecommands and BBP/Ka band modes were experimentally run before the cause was finally established.

The cause for this accidental signal emission was a BBP software flaw that transmitted a modulated carrier ("store&forward signal") not only in UHF bent pipe mode, but also in Ka band bent pipe mode. Due to in-orbit changes of the BBP software and the modification of the output level for the modulated signal, the following scenario seems likely: The BBP inserted the modulated carrier into the combiner at a much higher power level than the bent pipe mode signal travelling through the bypass. In the subsequent limiter (see Fig. 3.15) the small signal suppression effect attenuated the bent pipe mode signal, and only the modulated carrier could be observed on the downlink. Since the frequency tracking algorithm had not been adapted to modulated carriers, it could not acquire and track the signal. The attenuator in the BBP bypass was found to function as intended.

Fig. 7.4 shows the telemetry of a pass without any uplink signal, but with the BBP signal eliminated from the combiner. Compared with Fig. 7.2 (different scale), the lower power level indicates that the signal is indeed absent, and that only uplink noise is amplified. An experimental pass, combined with beacon mode for verification purposes, later confirmed that the fault had been eliminated (Fig. 7.5).

The author was instrumental in investigating, identifying and rectifying this spacecraft malfunction, with the support of the BBP and TT&C teams. Unfortunately, valuable pass
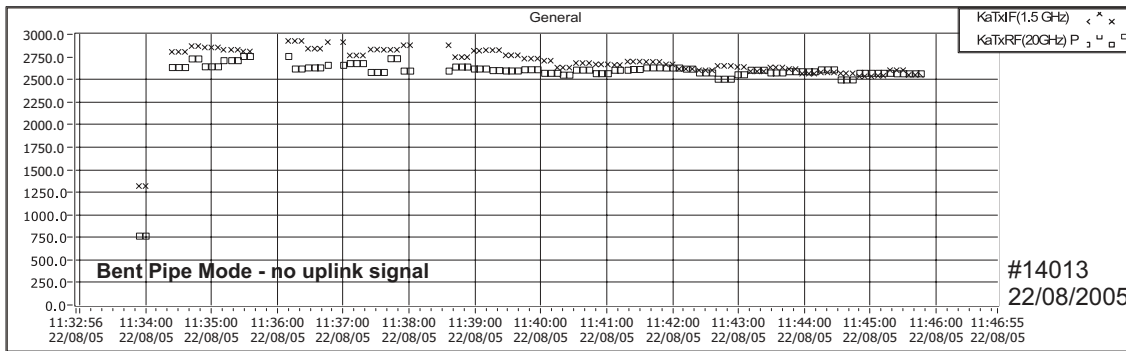
Figure 7.4: Ka band transmit power telemetry for a bent pipe mode pass without uplink signal and without BBP signal (arbitrary units)

time was lost not only through the non-availability of the bent pipe mode over long periods of time, but also through the numerous passes that had to be dedicated to the investigation and correction not available for propagation measurements.

7.1.3   Earth Station Reliability

It must be conceded that, despite its generally excellent performance, the earth station has also suffered from several malfunctions and damages by external influences. Many areas were affected to some extent, but especially the recurrence of some electro-mechanical problems will certainly lead to a design review of the components involved. The author hopes that the documentation of these defects will help in the design of subsequent prototypes.

7.1.4   Mechanical Failure

As explained in Chapter 4, the X/Y pedestal had been specifically designed for high-velocity LEO satellite tracking. In the current pedestal configuration, the available angular tracking range on both axes is maximised, which causes mechanical challenges of clearing the entire structure on large tilt angles. This is the main reason why counterweights on both axes of an X/Y pedestal are difficult to install, and the resulting design *without* counterweights requires several hundred Nm of torque especially on the lower Y axis to hold and accelerate the upper X axis, frame, reflector and feed assembly at low elevation angles. This puts enormous strain on the gearbox, which is rated for this torque, but not
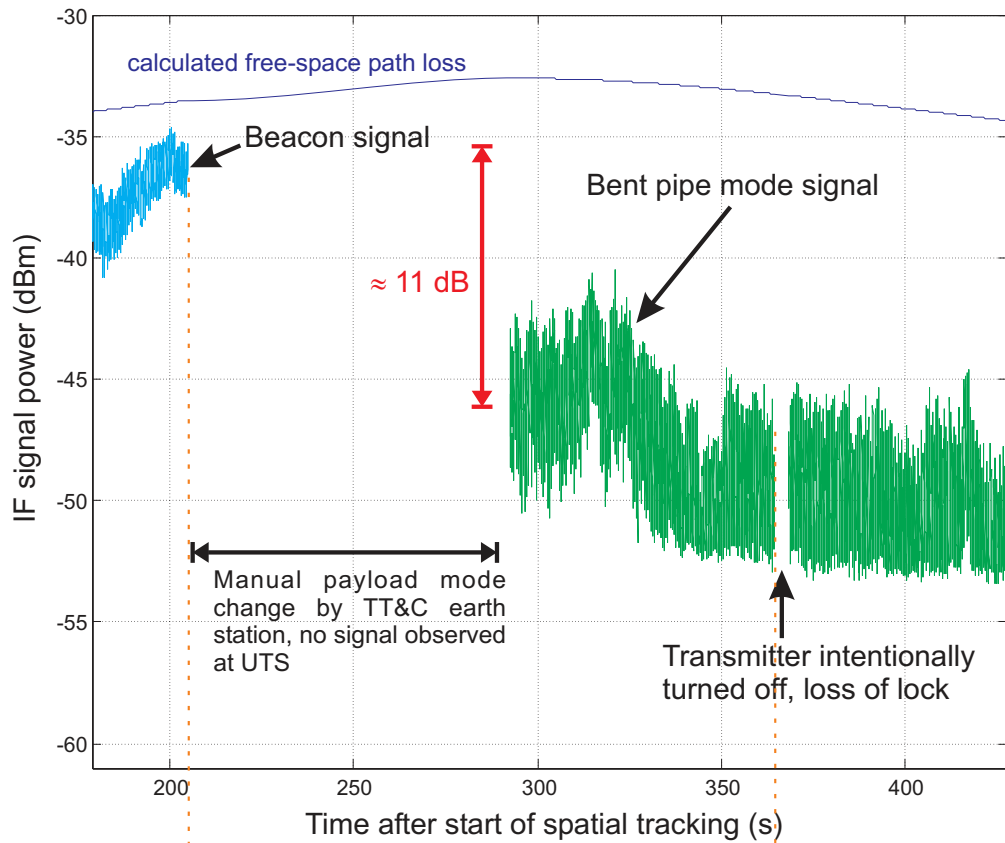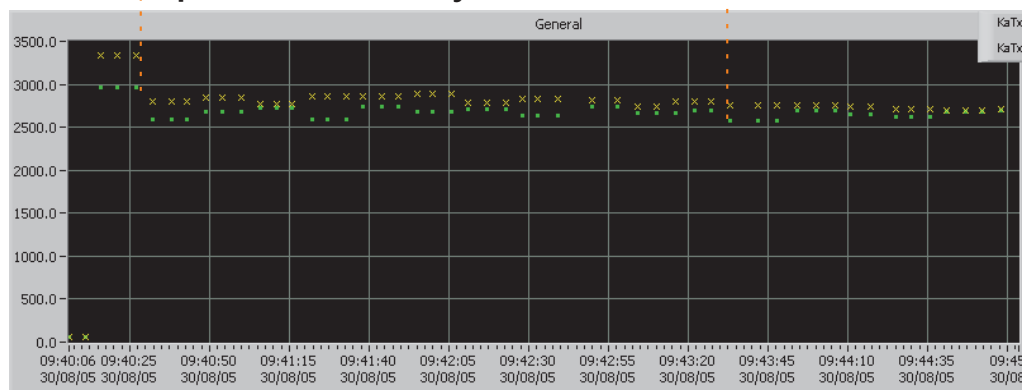
Figure 7.5: Re-verification of proper bent pipe mode operation. Note the loss of lock when the transmitter was turned off.

for possible jolts arising out of accidental higher velocities or malfunctions.

During the very early stages of deployment, a required motor tuning procedure resulted in a higher velocity response than expected, and the antenna moved at several degrees per second. In order to avoid a crash into the mechanical limits, the drives were immediately turned off and the brake engaged. Recalling from Fig. 4.16 that the brake is located on the motor side of the gearbox, this caused a large torque difference between the brake end (input) and the load end (output). As a result, the pinion inside the planetary gearbox sustained shearing damage, and the entire precision gear plate had to be replaced at great cost and manufacturer back-order time, during which the earth station was inoperative (10 weeks), Fig. 7.6. After the repair, the electro-mechanical system had to be re-tuned and re-calibrated.
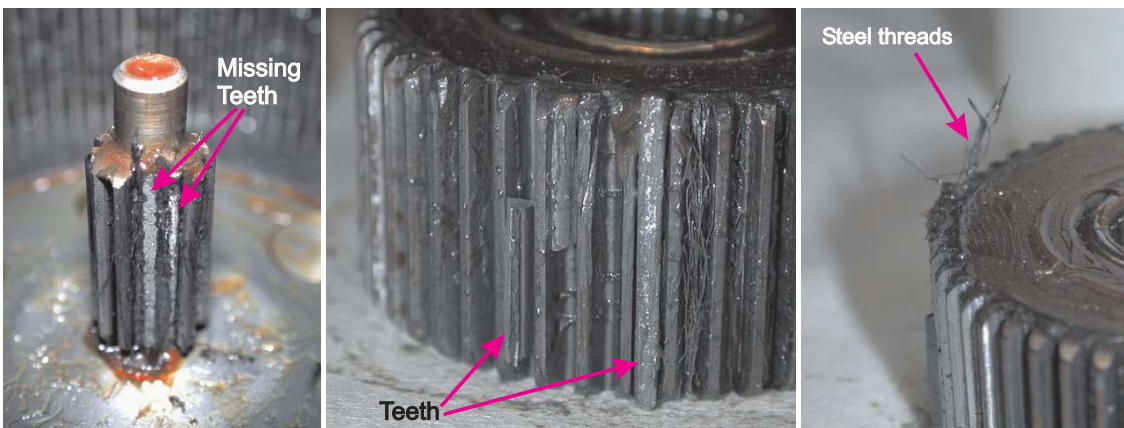
Figure 7.6: Gearbox damage after a high-velocity stop, causing the shearing of several pinion teeth

The previously described design improvement of replacing the feed assembly arm by a lighter structure and relocating the HPA also assisted in alleviating the gearbox strain and reducing wear.

A similar accident re-occurred under very different circumstances. In preparation of a pass under heavy, continuing rain (>40 mm/h), the manual levelling procedure was initiated when the antenna suddenly accelerated uncontrolled and drove into the rubber stop on one axis, causing the same gearbox damage as above. Since a software fault

could be excluded due to manyfold, successful operation before, hardware problems were investigated. An inspection on the servo drives, located in the outdoor unit enclosure, revealed that, due to the very heave rain and high winds, tiny amounts of water had blown under a shield and intruded the enclosure. One drop had leaked onto the circuit board of the drive near the feedback encoder inputs, perturbing the position measurement and initiating large reactions by the internal control loop. The repair of both the drive and the gearbox resulted in an unscheduled downtime of 8 weeks, since the drive model had been updated by the manufacturer, and a compatible model was only available from overseas.

7.1.5 Ka band RF Electronics Failure

On another occasion, it was observed that the Ka band LNA had suddenly become insensitive, and the noise figure had increased dramatically. Laboratory measurements confirmed that it must have been damaged by external influences, such as static electricity by lightning. The manufacturer, located in Belgium, confirmed the damage and was able to repair the unit. Downtime: 4 weeks.

7.1.6 Ka Band Hardware Damage

This damage occurred before the feed arm replacement by a lighter structure. On a routine check of the antenna system before a pass after several extremely stormy days with gale-force winds, it was realised that the feed assembly was resting on the reflector. One of the supporting stays, keeping the arm in position, had failed at its fixture point to the rim of the dish, causing the collapse. As a result, the sensitive feed horn had sustained a deformation, changing is highly accurate geometry and therefore the coherence of both the receive and the transmit signal, compromising the power calibration. The reflector received a negligible surface scratch. Additionally, the feed membrane was destroyed, and surface corrosion of the horn due to moisture was observed within a few days. The damage is illustrated in Fig. 7.7. A replacement feed was ordered from the manufacturer, resulting in a period of limited operability of 5 weeks.

Figure 7.7: Feed horn deformation after a mechanical failure of one of the supporting structures due to gale-force winds

7.1.7 Reflector Replacement

A highly unusual incident, according to the manufacturer, gradually occurred during the first 18 months of operation to the reflector. The precision reflective layer and and the hydrophobic paint started to show small 'bubbles', which eventually burst and destroyed the surface at that particular spot, Fig. 7.8. When the effect, which could not be repaired, was first discovered, immediate arrangements were made to have the reflector replaced as soon as possible, since surface area and accuracy was constantly being lost. It can only be suspected that this unseen damage must have been caused by chemically very aggressive droppings from birds, which had been perching on the feed assembly structure directly above the damaged surface.
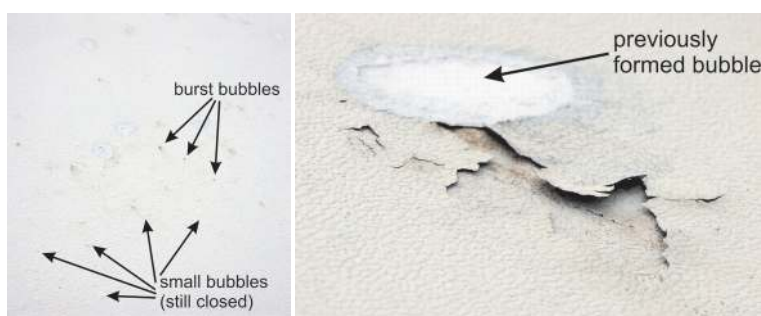
Figure 7.8: Damage to the reflector surface through small 'bubbles', possibly resulting from bird droppings

7.1.8 Software Deficiencies

As previously stated, the UTS Earth station software fulfils a multitude of tasks simultaneously and is optimised for performance. Being a full in-house development, it has been constantly improved and re-designed, and occasionally (but rarely) resulting in malfunctions during a pass and lost propagation data.

While timing accuracy was handled extremely well, as demonstrated above, the conversion and real-time comparison of different time formats (GPS and UTC) was an unnecessary complication for preparation, operation and data post-processing that should definitely be avoided in future designs.

7.1.9 Local Weather Pattern

Despite all the malfunctions and impediments outlined in this chapter, the greatest obstacle for the successful collection of rain propagation data has certainly been the weather itself. Between 2001 and 2007, and therefore exactly during the time of this experiment, the vast majority of south-eastern Australia has suffered from drastically reduced rainfall and drought [142], even east of the Great Dividing Range, Fig. 7.9.

Apart from the strong year-to-year rather than seasonal variations in south-eastern Australia, the *daily* weather patten also had a large impact on the research. Since FedSat is in a sun-synchronous orbit, passes with similar trajectory will always occur at the same local time, therefore not allowing for any averaging over daily weather patterns. With a few rare exceptions, convective rain events, such as thunderstorms, are much more likely to happen in the late afternoon than in the morning. In fact, over the almost three years of operation, not a single storm event was observed during a possible pass time (around 9:30-10:30am AEST). Only stratiform rain was present during stable, easterly on-shore winds, but even that was a rare opportunity to coincide with a possible pass time. For the merit of averaging, a sun-synchronous orbit is not desirable, or at best the insertion of the spacecraft should be times so that it coincides with the daily weather events of interest.

Another way of looking at the rarity of significant rain events during the campaign is statistically. The Australian Bureau of Meteorology has recently released rainfall charts for
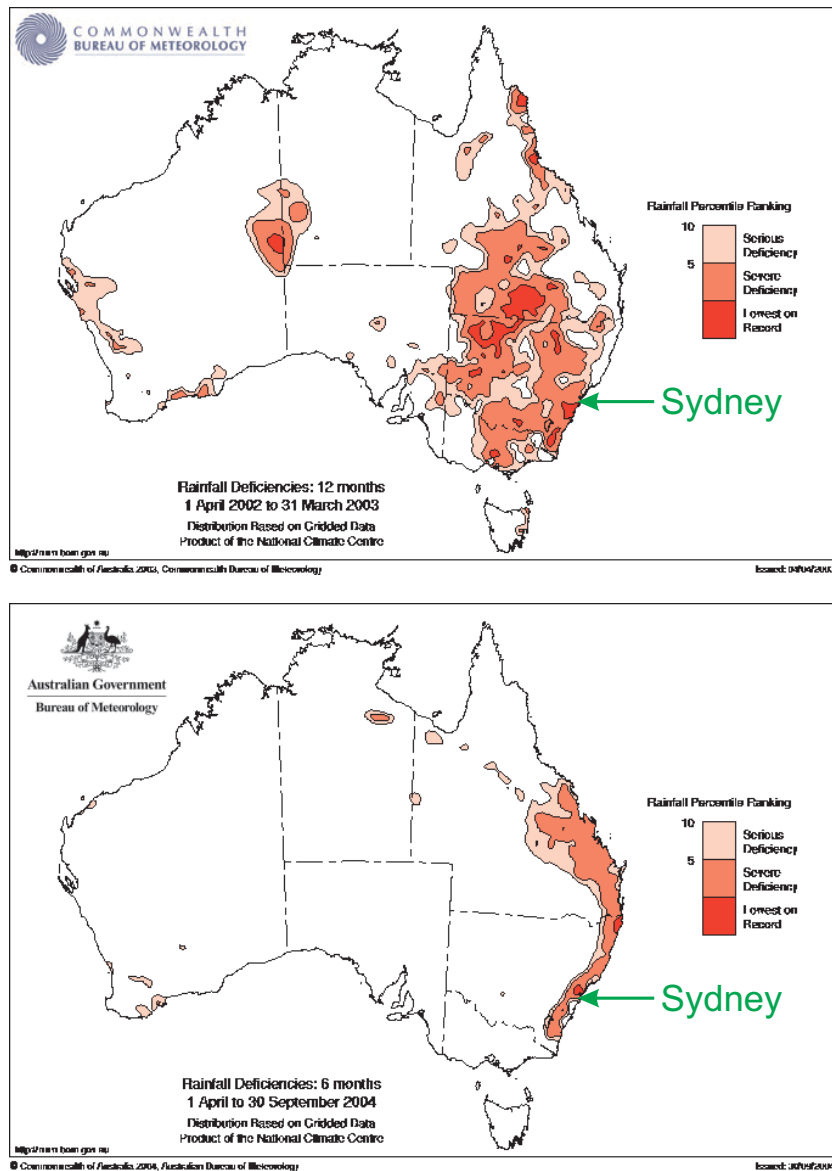
Figure 7.9: Map of drought-affected areas in Australia in 2003 and 2004, indicating serious drought, severe drought and lowest rainfall on record [142]

intensity, frequency and duration for a large number of locations [143]. Based on the same long term statistics as the ITU data, it allows the calculation of the recurrence interval of a particular rainfall rate of a given duration. The chart in Fig. 7.10 has been created for the UTS earth station location, and it shows that the chance of encountering a rainstorm with a rain rate of >70 mm/h within the usual duration of a LEO pass (10 minutes) is less than *one per year* (blue dot). This figure would be the correct statistical likelihood for 10 minutes of heavy rain when observing a GEO satellite, which is always present, however this small likelihood must be combined with the chance of a suitable satellite pass, as outlined in Section 5.1. It is obvious that heavy rainfall coinciding with a LEO pass is a very fortunate event.
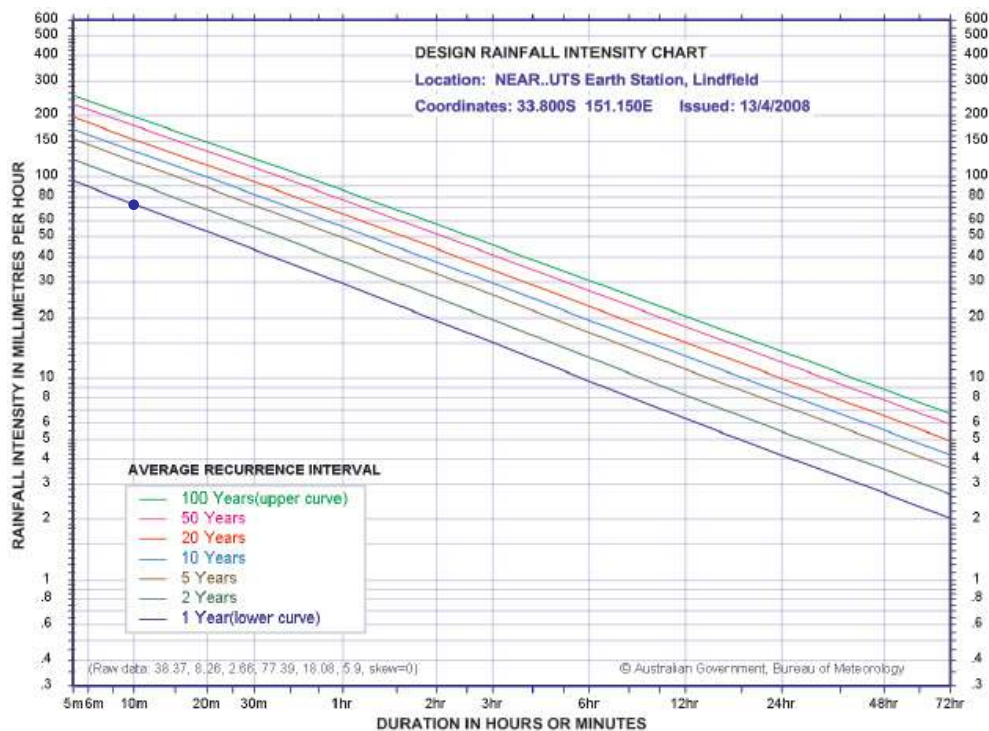
Figure 7.10: Intensity-Frequency-Duration chart for statistical rainfall rate re-occurrence predictions [143]

7.1.10   Impact on the Research Outcome

The topics covered in this section have demonstrated that the success of an experimental project like this depends on many factors: good technical design, cooperation and

even chance. With respect to propagation data collection, the long outage periods and the unfavourable drought conditions in the region have unfortunately not resulted in the expected amount and significance of data under rain conditions.

7.2 Suggestions for Future Earth Station Designs

The earth station design review, the suggested and implemented design improvements and the difficulties encountered lead the way to several suggestions for further design improvements that may be helpful for future research teams in this field.

7.2.1 Location and Siting

Despite the restrictions of an urban environment in this case, the author regards it as absolutely essential to select a site with as few horizon obstructions as possible. Although multipathing and loss-of-signal effects can be removed from the data manually, it does hinder the coherent analysis and interpretation significantly. It has also been identified that low angles are of particular interest, hence it is even more important to maximise the visibility of the sky.

7.2.2 Counterweighted Pedestal

Most of the difficulties encountered in tuning the servo motors were due to the changing load over the duration of a pass. A decrease of the maximum required torque and subsequent tuning has resulted in significant reduction of vibrations and better accuracy. In addition, the lop-sided weight of the antenna when fully tilted over causes increased wear and risk of damage to the gearbox, not just under uncontrolled conditions. It should therefore be endeavoured to fit a counterweight at least to the lower (Y) axis in order to reduce the total torque. This solution is more difficult for the upper (X) axis due to the required physical clearance. However, from a dynamic point of view, any additional weights will lower the mechanical resonant frequency of the entire structure, which is undesired and must be carefully considered. In summary, a counterweighted X/Y pedestal would lighten the demand on the electromechanical system to a large extent, making it less costly, greatly more reliable and less prone to accidental damage.

7.2.3   Robustness of the Electro-Mechanical Subsystem

In combination with counterbalancing the antenna, a re-design of the electro-mechanical drive train is also recommended. As previously stated, the servo motor operated within less than 1% of its revolution-per-minute range in order to deliver the very low angular velocities required. The 100:1, 2-stage gearboxes assist with this objective, but it has proven too fragile under accidental conditions. On the positive side, the servo motors with two control loops, consisting of multiple feedback encoders, have ensured flawless accuracy during tracking. The author would therefore recommend the selection of a similar servo motor system, but with a much lower nominal 'rpm range' and a more robust gearbox.

7.2.4   Levelling and Fully Automated Operation

It has been one of the more significant strategic decisions in this project to abandon automatic levelling and therefore the automatic operation of the earth station. Due to the selection of - for this purpose unsuitable - relative position encoders and the insufficient accuracy of the inclinometer, which were both *early* design decisions, the desired pass-to-pass pointing accuracy could not be achieved automatically. For future designs with high accuracy requirements, it is recommended to research the availability of more suitable sensors, for example transducers, which are less prone to drifting and deliver reproducible results. The UTS earth station software is already configured for remote control over the internet, and with automatic levelling and a more reliable mechanical system in place, the fully automated collection of Ka band LEO propagation data should be feasible.

7.2.5   Feed Blower

Although it is unknown whether the moisture and rain drops on the feed cover had any significant effect on the measurements, a small feed blower (as standard in many large commercial earth stations) would most likely improve the situation. However, it will be very challenging to protect the reflector surface from wetting, other than by a radome, due to the required movement of the antenna during a pass.

7.3 Suggestions for Operational Strategies

Apart from technical improvements, there are also several suggestions for operational improvements in relation to external cooperation and routine scheduling of passes.

7.3.1 Integrated Collection of Precipitation Data

For projects entirely focussed of propagation data collection, it is suggested to integrate a weather station into the earth station itself, as well as contacting organisations operating rain gauges and pluviometers in a large geographic area. As previously explained, the estimation of rain rates along the slant path can be unreliable using weather radar or radiometers (at very high rainfall rates), and the addition of optimally 1-minute, real-time pluviometer data may add some more confidence in the correlation of observed weather conditions with the data measured.

7.3.2 Automatic Recording of Visual Weather Observations

Although initiated at the UTS earth station as an undergraduate student project, this idea has not been further pursued with the end of the CRCSS. The addition of a small, high-quality, auto-iris camera to the reflector, pointing in the antenna's boresight direction, would have given additional, visual records of the weather conditions in the path direction. Recording software on a separate computer would have timed the recording to coincide with the tracking schedule and added a time stamp. A second camera would statically observe the entire pedestal from a short distance for confirmation of its activity and status, which could be accessed from a remote location over the internet.

7.4 Summary

Despite the obstacles of equipment damage and long, forced outage periods, the author is very content with the successful verification of a low-cost Ka band earth station for LEO tracking, which has, in addition, collected some hopefully helpful samples of propagation data. The design improvements that *were* implemented and the reflection on recommendations for future designs have resulted in a very good insight into the topic.

Chapter 8

Conclusion and Suggestions for Further Work

The work contained in this thesis has aimed to demonstrate the variety of aspects that were required to be covered in a strongly experimental context, and especially under low-budget restrictions. Dealing with the design of a highly complex system, its principal merit lie in the communication *systems engineering* field, with contributions also made to propagation studies through initial results. This chapter summarises the outcomes of the research project and provides suggestions for the manifold opportunities for future work.

8.1 Project Outcomes

In Chapter 1, the following *primary objectives* were stated:

- "Creation of a highly complex, low-cost, fast-tracking *operational* Ka band earth station.

- Prototype verification of the earth station's system design and implementing significant design improvements."

- Development of an earth station with the purpose of enabling the collection of LEO satellite Ka band propagation data and presentation of preliminary attenuation results.

8. CONCLUSION AND SUGGESTIONS FOR FURTHER WORK

Following the introduction of the microsatellite 'FedSat' as the space research plat-
form in Chapter 3, the fundamental design of the earth station has been reviewed. With
a thorough knowledge about the systematic interaction between the earth station compo-
nents, Chapter 4 also identified several crucial design modifications that were considered
essential for the success of the project. The author has been able to demonstrate both
the necessity and the positive results of those improvements in the following Chapter 5,
together with the analysis of operational considerations, including the assessment of LEO
ephemeris data and of the tracking accuracy using two-line elements.

Chapter 6 presented proof that the earth station has been operating regularly and
successfully for a number of both beacon and bent pipe mode experiments, therefore val-
idating the fundamental design, the implemented design improvements and the accuracy
assessment, fulfilling the objectives stated above.

The *secondary objective* of this work was stated as follows:

- Demonstration of the author's knowledge and practical skills in experimental re-
  search, especially in the fields of high-accuracy LEO satellite tracking operations
  and Ka band propagation data collection.

Chapter 2 has laid a very brief foundation of the propagation effects dominating Ka
band satellite communication, followed by an overview of past research activities mainly
over GEO satellites. Chapter 6 focussed on the preliminary analysis of power measure-
ments collected by the UTS earth station during the experimental phase under various
weather conditions, which are amongst the first comprehensive Ka band LEO propaga-
tion results published in the literature. The data obtained is compared to existing GEO
propagation measurements for validation purposes, and several interesting phenomena,
commonalities and differences are pointed out.

Due to the limitations in budget and staffing of this project, especially during the op-
erational phase, the author was required to fulfil a multitude of theoretical and practical
tasks without external assistance in order to achieve the goals stated above, well exceed-

ing the scope of the research alone. This necessity has resulted in a profound insight into the design of complex systems, which consist of elements from several cross-disciplinary fields, like surveying, electro-mechanical systems, RF engineering, electronics, software engineering and meteorology. By making and implementing numerous design improvement suggestions and by providing logical links between certain topics of this work, the author has aimed to demonstrate both theoretical and practical competence in systems engineering, to the extent possible within the scope of this thesis.

Nevertheless, there are numerous, promising aspects where the research could have been taken much further, but had to be limited to meet completion requirements. The following section lists selected topics with great research potential based on the work presented above, which the author will endeavour to pursue.

8.2 Suggestions for Future Work

Although the further design improvement of the earth station in term of cost and performance appears to be a rewarding extension of this project, the closure of the CRCSS and the inoperability of FedSat is limiting these efforts. With currently no other accessible Ka band LEO in orbit, the launch of only the second LEO satellite with a 20/30 GHz Ka band payload (after FedSat), 'ILSE', being built by the German University of Stuttgart, will hopefully continue the potential of Ka band LEO propagation research. With respect to the data collected in this project, the following future directions look very promising.

8.2.1 Low Elevation Analysis

The Teledesic Ka band system design included very severe restrictions in terms of low elevation angle masking due to the increased effects of atmospheric attenuation. Within the scope of this project, several interesting observations at low angles have already been made, including the onset of low-angle fading and an increased scintillation magnitude. Particularly the latter point is a potentially **important finding** of this work and warrants further investigation, since this effect does not appear to be well documented for LEO satellites in published literature. It would be interesting to pursue this path further and

to quantify the effects observed, and to make direct comparisons with GEO data and with existing models. A possible outcome would be concrete recommendations for the design of digital communication systems being able to operate at low elevation angles through the adaptive selection of modulation scheme and data rate.

8.2.2 Fade Slope Analysis

Fade slope analysis has been a very active field in the wake of the OLYMPUS and ACTS experiments. The fade slope describes how rapidly the attenuation changes (in dB/sec), for example through scintillation. This is an extremely important topic for the design of very fast automatic gain controls in digital receivers, and also for the performance of higher-order modulation schemes with non-constant envelopes, such as quadrature amplitude modulation (QAM). Deep fades disturb the decision boundaries, resulting in symbol errors and degraded performance. While there have been extensive publications in this area, it was beyond the scope of this work.

However, the author is in contact with other international research groups, for example [52], about *simulation models* for Ka band propagation via LEO satellites. A comparison of the currently mostly theoretical models with the measurements from FedSat appears to be a very suitable extension of this project.

8.2.3 Correlation with Local Precipitation Data

Within the scope of this thesis, the comparison of the observed attenuation with meteorological data has been limited to visual observations and rather qualitative rain assessments. Given the existence of a high-density rain gauge network in the Sydney region and three-dimensional weather radar imaging, it would be more than worthwhile to *quantitatively* link the archived weather data recorded during passes to the measurements. By matching the geometry of the variable slant path to the weather conditions on the ground and in the sky, it should be possible to draw more precise conclusions from the FedSat data, especially with respect of the influence of the rapid spacecraft movement on scintillation magnitude and frequency.
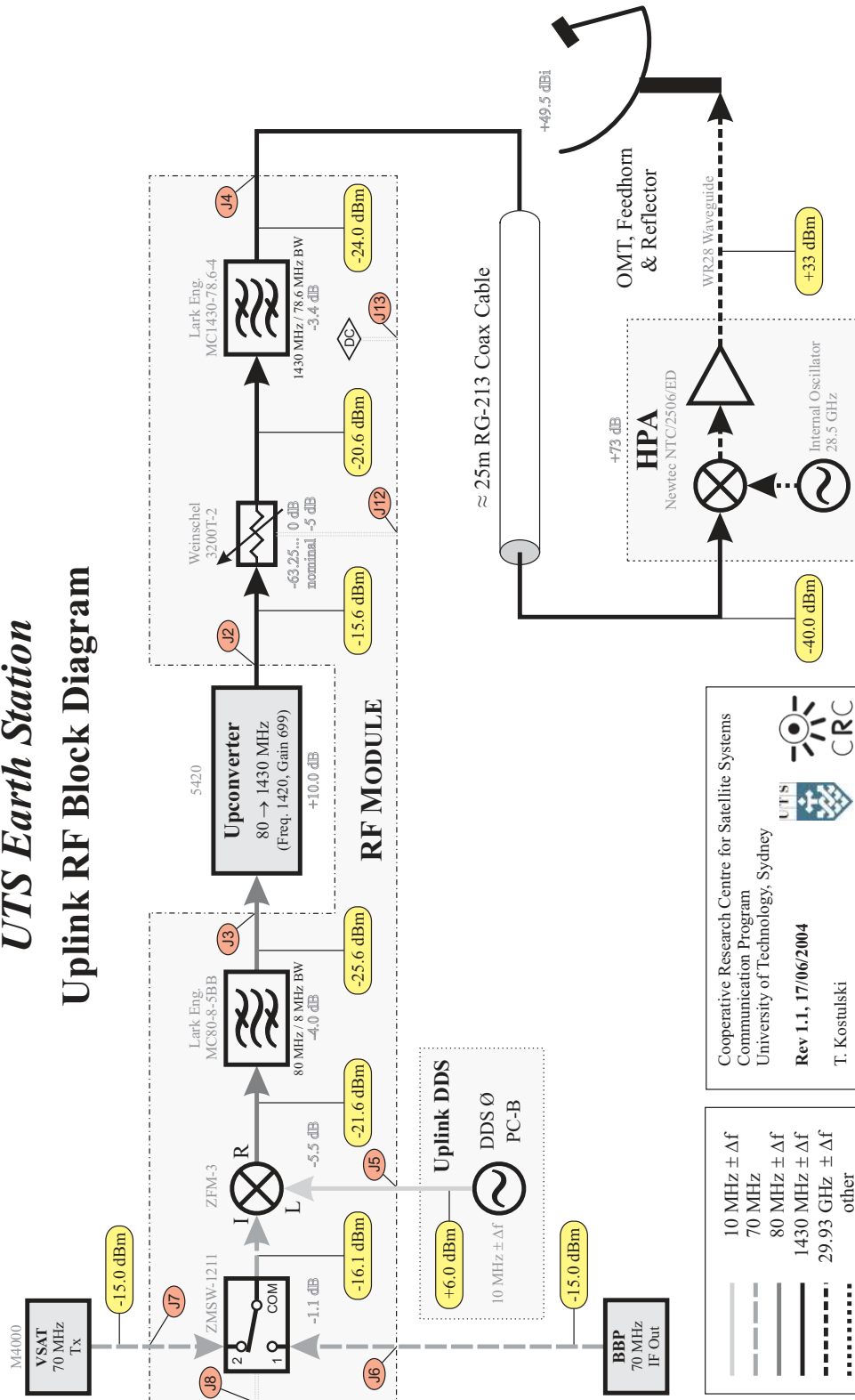
Appendix A

UTS Ka Band Earth Station RF Block Diagrams

Figure A.1: Detailed block diagram of the uplink RF circuits, including manufacturer part numbers and reference power levels
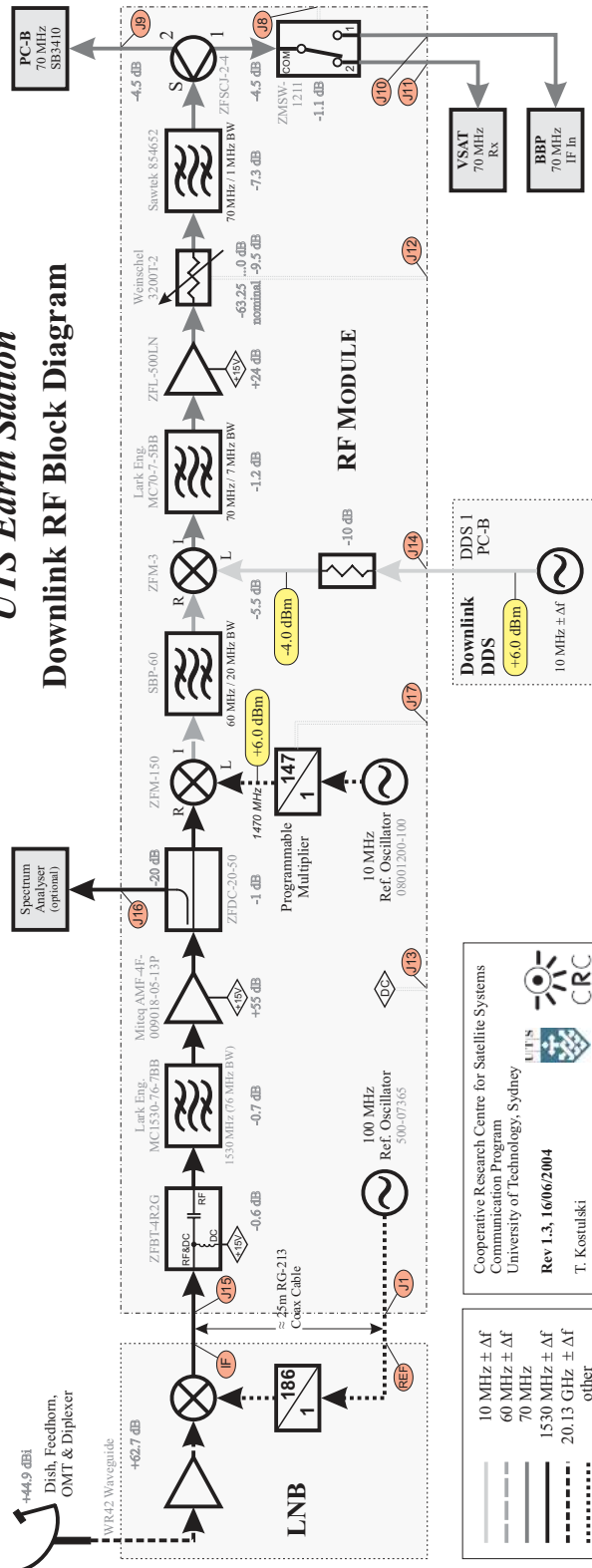
Figure A.2: Detailed block diagram of the downlink RF circuits, including manufacturer part numbers

Bibliography

[1] NASA – National Space Science Data Center, "NSSDC Master Catalog", $http://nssdc.gsfc.nasa.gov/nmc/$, Version 4.0.5, Last accessed: 28 Feb 2008.

[2] D. Roddy, *Satellite Communications*, McGraw Hill, New York, NY, second edition, 1996.

[3] T. Pratt, C. Bostian, and J. Allnutt, *Satellite Communications*, John Wiley & Sons, Hoboken, NJ, second edition, 2003.

[4] J.V. Evans and A. Dissanayake, "The prospects for commercial satellite services at Q- and V-band", *Space Communications*, vol. 15, no. 1, pp. 1–19, Jan 1998.

[5] P.W. Fortescue, J. Stark, J.P.W. Stark, and G. Swinerd, *Spacecraft Systems Engineering*, John Wiley & Sons, Hoboken, NJ, 2003.

[6] A.G. Uyttendaele, "Evolution of Antenna Sidelobe Regulation", *IEEE Transactions on Broadcasting*, vol. BC-32, no. 4, pp. 85–88, 1986.

[7] I. Burton, J. Edelson, and N. Pelton, *Satellite Communications Systems and Technology - Europe, Japan, Russia*, William Andrew Inc., Norwich, NY, 1995.

[8] J. Farserotu and R. Prasad, "A Survey of Future Broadband Multimedia Satellite Systems, Issues and Trends", *IEEE Communications Magazine*, vol. 38, no. 6, 2000.

[9] T. Iida F. Gargione, "Services, Technologies, and Systems at Ka Band and Beyond - A Survey", *IEEE Journal on Selected Areas in Communications*, vol. 17, no. 2, pp. 133–144, Feb 1999.

[10] A. Dissanayake, "Ka-Band Propagation Modeling for Fixed Satellite Applications", *Online Journal of Space Communication*, 2002.

[11] L. Wood, "Big LEO Tables", $http://info.ee.surrey.ac.uk/Personal/L.Wood/constellations/tables/tables.html$, 1999, Last accessed: 10 Apr 2008.

[12] Y.H. Chu, S.P. Shih, and G.S. Liu, "First Measurement of Scintillation and Attenuation of 19.5 GHz Beacon Signal for Experimental Communication Payload of ROCSAT-1", in *Space Weather Study Using Multipoint Techniques, Proceedings of the COSPAR Colloquium*, Wanli, Taipei, Taiwan, 27-29 Sep 2000, pp. 301–306.

[13] J. Kingwell, "CRC for Satellite Systems - Grant Schedule", Personal communication, UTS Research Office, 1997.

[14] S. Reisenfeld, "A highly accurate algorithm for the estimation of the frequency of a complex exponential in additive Gaussian noise", in *5th Australian Communications Theory Workshop*, Canberra, ACT, 4 Feb 2004, pp. 154–158.

[15] T. Kostulski and S. Reisenfeld, "Ka Band Propagation Experiments on the Australian Low-Earth Orbit Microsatellite 'FedSat'", in *6th Australian Communications Theory Workshop*, Brisbane, Queensland, 2-4 Feb 2005, pp. 95–99.

[16] T. Kostulski and S. Reisenfeld, "Variable Slant-Path Ka Band Propagation Measurements on the Australian LEO Microsatellite 'FedSat'", in *11th Ka and Broadband Communications Conference*, Rome, Italy, 25-28 Sep 2005, pp. 365–372.

[17] Bhamer, "Atmosphere with Ionosphere", *http : //en.wikipedia.org/wiki/Image : Atmosphere_with_Ionosphere.svg*, 30 May 2007, Last accessed: 11 Apr 2008.

[18] R.K. Crane, "Ionospheric Scintillation", *Proceedings of the IEEE*, vol. 65, pp. 180–199, 1977.

[19] Cooperative Research Centre for Satellite Systems, ", *http : //www.crcss.csiro.au/*, 1998-2005, Last accessed: 28 Feb 2008.

[20] ITU-R P.676-3, *Attenuation by Atmospheric Gases*, ITU Radiocommunication Bureau, Geneva, 1997.

[21] E.E. Altshuler and R.A. Marr, "Cloud Attenuation at Millimeter Wavelengths", *IEEE Transactions on Antenna and Propagation*, vol. 37, pp. 1473–1479, 1989.

[22] A. Dissanayake, J. Allnutt, and F. Haidara, "Cloud Attenuation at Millimeter Wavelengths", *International Journal of Satellite Communications*, vol. 19, pp. 335–345, 2001.

[23] ITU-R P.618-8, *Propagation Data and Prediction Methods Required for the Design of Earth-Space Telecommunication Systems*, ITU Radiocommunication Bureau, Geneva, 2003.

[24] R.K. Crane, "Propagation Phenomena Affecting Satellite Communication Systems Operating in the Centimeter and Millimeter Wavelength Bands", *Proceedings of the IEEE*, vol. 59, no. 2, pp. 173–188, Feb 1971.

[25] ITU-R P.837-1, *Characteristics of Precipitation for Propagation Modelling*, ITU Radiocommunication Bureau, Geneva, 1994.

[26] ITU-R P.837-5, *Characteristics of Precipitation for Propagation Modelling*, ITU Radiocommunication Bureau, Geneva, 2007.

[27] ITU-R P.837-4, *Characteristics of Precipitation for Propagation Modelling*, ITU Radiocommunication Bureau, Geneva, 2003.

[28] W. Li, C.L. Law, J.T. Ong, and V. Dubey, "Ka-band land mobile satellite channel model: with rain attenuation and other weather impairments in equatorial zone", in *Vehicular Technology Conference Proceedings*, Tokyo, Japan, 15-18 May 2000, pp. 2468–2472.

[29] R. Acosta, S Johnson, W. Feliciano, R. Pollard, and L.A. Gonzales, "NASA's New Radio Wave Propagation Experiment", in 8th *Ka Band Utilization Conference*, Baveno, Italy, 25-27 Sep 2002.

[30] H.E. Green, "Propagation Impairment on Ka-Band SATCOM Links in Tropical and Equatorial Regions", *IEEE Antenna and Propagation Magazine*, vol. 46, no. 2, pp. 31–45, 2004.

[31] ITU-R P.838-3, *Specific attenuation model for rain for use in prediction methods*, ITU Radiocommunication Bureau, Geneva, 2005.

[32] ITU-R P.839-3, *Rain Height Model for Prediction Methods*, ITU Radiocommunication Bureau, Geneva, 2001.

[33] D. Chakraborty, F. Davarian, and W.L. Stutzman, "The Ka-Band Propagation Measurement Campaign at JPL", *IEEE Antennas and Propagation Magazine*, vol. 35, no. 1, pp. 7–12, Feb 1993.

[34] J.D. Laster and W.L. Stutzman, "Frequency scaling of rain attenuation for satellite communication links", *IEEE Transactions on Antennas and Propagation*, vol. 43, no. 11, pp. 1207–1216, Nov 1995.

[35] E. Kubista, F.P. Fontan, and M.A. Vazquez Castro et al., "Ka-Band Propagation Measurements and Statistics for Land Mobile Satellite Applications", *IEEE Transactions on Vehicular Technology*, vol. 49, no. 3, pp. 973–983, May 2000.

[36] R.T. Gedney, R. Schertler, and F. Gargione, *The Advanced Communication Technology Satellite*, SciTech Publishing, Mendham, NJ, 2000.

[37] R. Bauer, "Ka-Band Propagation Measurements: An Opportunity with the Advanced Communications Technology Satellite (ACTS)", *Proceedings of the IEEE*, vol. 85, no. 6, pp. 853–862, Jun 1997.

[38] R.K. Crane and A.W. Dissanayake, "ACTS Propagation Experiment: Attenuation Distribution Observations and Prediction Model Comparison", *Proceedings of the IEEE*, vol. 85, no. 6, pp. 879–892, Jun 1997.

[39] D.V. Rogers, L.J. Ippolito, and F. Davarian, "System Requirements for Ka-Band Earth-Satellite Propagation Data", *Proceedings of the IEEE*, vol. 85, no. 6, pp. 810–820, Jun 1997.

[40] F. Davarian, "An Update on NASA Ka-Band Propagation Measurements", *IEEE Antennas and Propagation Magazine*, vol. 36, no. 3, pp. 14–18, Jun 1994.

[41] L.J. Ippolito, "Propagation Effects Handbook for Satellite System Design", in 6th *Ka Band Utilization Conference*, Cleveland, OH, 31 May - 2 Jun 2000.

[42] D. Kohn, Teledesic Corporation, USA, "The Teledesic Network: Using Low-Earth-Orbit Satellites to Provide Broadband, Wireless, Real-Time Internet Access Worldwide", $http : //www.isoc.org/inet96/proceedings/g1/g1\_3.htm$, 1996, Last accessed: 12 Apr 2008.

[43] L. Wood, "Big LEO Overview", *http : //info.ee.surrey.ac.uk/ Personal/L.Wood/constellations/tables/overview.html*, 14 Jan 2000, Last accessed: 12 Apr 2008.

[44] L. Wood, "Lloyd's satellite constellations", *http : //personal.ee.surrey.ac.uk/ Personal/L.Wood/constellations/teledesic.html*, 19 Dec 2004, Last accessed: 12 Apr 2008.

[45] D. Barboza, New York Times, "The Teledesic Network: Using Low-Earth-Orbit Satellites to Provide Broadband, Wireless, Real-Time Internet Access Worldwide", *http : //partners.nytimes.com/library/tech/00/04/biztech/articles/11iridium.html*, 11 April 2000, Last accessed: 13 Apr 2008.

[46] S.P. Shih and Y.H. Chu, "Ka Band Propagation Experiments of Experimental Communication Payload (ECP) on ROCSAT-1 - Preliminary results", *Terrestrial, Atmospheric and Oceanic Sciences Journal*, vol. Supplementary Issue, pp. 145–164, Nov 1998.

[47] C.K. Chen and K. Tseng, "ROCSAT-1 Ka Band Experimental Communication Payload Operations", in *SpaceOps Conference Proceedings*, Houston, TX, 9-12 Oct 2002.

[48] Y.H. Chu and S.P. Shih, "An Investigation of 19.5GHz Sky Noise Temperature over Taiwan Area", *Terrestrial, Atmospheric and Oceanic Sciences Journal*, vol. 10, no. 4, pp. 821–834, Dec 1999.

[49] K.K. Reddy, S.P. Shih, and Y.H. Chu, "Study of a precipitationg cloud system using Ching-Li VHF radar", *Radio Science*, vol. 37, no. 4, pp. 1067, Aug 2002.

[50] Wave Propagation Laboratory, "TGT 2000", *http : //wpl.ss.ncu.edu.tw/research/tgt/tgt2000.html*, 2000, Last accessed: 12 Apr 2008.

[51] J.H. Yeh, "Research of Low-Earth Orbit Satellite Ka Band Beacon Signal Characteristics", Master's thesis, Institute of Space Science, National Central University, Chung-Li, Taiwan, 2002, Language: Chinese.

[52] W. Liu, B. Diallo, and D.G. Michelson, "Fade Slope Analysis of Ka-band LEO Satellite Links", in *IEEE VTC 2007 Fall*, Baltimore, Maryland, Sep 2007.

[53] D.G. Michelson, University of British Columbia, "Discussions regarding the FedSat campaign", Personal communication, 2007, 2008.

[54] R.K. Flavin, *Earth-Space Path Rain Margins Above 10 GHz in Australia (Report #7358)*, Australian Telecommunication Commission, Melbourne, VIC, 1980.

[55] R.K. Flavin, *Rain Attenuation Considerations for Satellite Paths (Report #7505)*, Australian Telecommunication Commission, Melbourne, VIC, 1981.

[56] R.K. Flavin, *Proposed Amendment to Recommendation ITU-R P.841-2*, ITU Radiocommunication Study Group, Geneva, 2001.

[57] Australian Bureau of Meteorology, "Pluviometer Statistics", $http$: $//www.bom.gov.au/hydro/has/rainservices\_provided.shtml$, undated, Last accessed: 12 Apr 2008.

[58] C.J. Kikkert, *JCU-STRAP - Digital Beacon Receiver and Radiometer*, James Cook University, Townsville, QLD, Australia, undated.

[59] C.J. Kikkert, B. Bowthorpe, and Ong Jin Teong, "A DSP based Satellite Beacon Receiver and Radiometer", in *Asia Pacific Microwave Conference*, Yokohama, Japan, 8-11 Dec 1998.

[60] C.J. Kikkert, "The Design of a Ka band Satellite Beacon Receiver", in 6th *International Conference on Information, Communication and Signal Processing*, Singapore, Dec 2007.

[61] The Radio Amateur Satellite Corporation (AMSAT), "A Brief History of Amateur Satellites", $http$: $//www.amsat.org/amsat/sats/n7hpr/history.html$, 2003, Last accessed: 25 Feb 2008.

[62] A.J. Barrington-Brown, A.N. Wicks, L. Boland, and S.J. Gardner, "FedSat - An Advanced Micro-Satellite Based on a MicroSIL Bus", in *Proc. 12th Annual AIAA/USU Conf. on Small Satellites*, Utah State Univ. Logan, USA, Aug-Sep 1998.

[63] Department of Innovation, Industry, Science and Research, "Cooperative Research Centres", $https$: $//www.crc.gov.au/Information/default.aspx$, undated, v8.0.1, Last accessed: 28 Feb 2008.

[64] The Satellite Encyclopedia, "Satellite Fact Sheet - FedSat", $http$: $//www.tbs-satellite.com/tse/online/sat\_fedsat.html$, 2007, Last accessed: 28 Feb 2008.

[65] A. Parfitt, *CRCSS Press Release*, CRC for Satellite Systems, Canberra, ACT, 13 Dec 2004.

[66] Australian Department of Defence, "Defence to Manage FedSat Satellite", $http$: $//www.defence.gov.au/minister/Hilltpl.cfm?CurrentId = 5341$, 23 Dec 2005, Last accessed: 1 Mar 2008.

[67] Northern Lights Software Associates, "Nova for Windows", $http$: $//www.nlsa.com$, 12 Jan 2008, Last accessed: 1 Mar 2008.

[68] E.S. Seumahu, C. Graham, M. Petkovic, S. Sussell, and M. Vesely, "The FedSat Microsatellite", in *Proc. 2nd Intl. Conf. on Information, Communications & Signal Processing*, Singapore, Dec 1999.

[69] The Australian Space Weather Agency, "FEDSAT Information", $http$: $//www.ips.gov.au/World\_Data\_Centre/1/5/2$, 2007, Last accessed: 27 Feb 2008.

[70] C. Wang and R. Walker, "Single Antenna Attitude Determination for FedSat with Improved Antenna Gain Patterns", in *The 6th Intl. Symposium on Satellite Navigation Technology*, Melbourne, Victoria, 2003.

[71] NASA, Goddard Space Flight Centre, "Magnetic Field missions for solid-earth and near-Earth Space Geophysics", *http* : *//denali.gsfc.nasa.gov/research/mag_field/purucker/mag_missions.html*, 2006, Last accessed: 27 Feb 2008.

[72] E.S. Seumahu, T.S. Bird, W.G. Cowley, and A.J. Parfitt, "The FedSat Communications Payload", in *Proc. 2nd Intl. Conf. on Information, Communications & Signal Processing*, Singapore, Dec 1999.

[73] P. Roberts, B. Cowley, J. Dahlenburg, and W. Farrell, *FedSat Communications Payload Interface Document*, CRCSS/ITR Internal Document, Adelaide, South Australia, Oct 2002.

[74] W.G. Cowley, W.N. Farrell, and D.A. Powel, "Baseband Processor for FedSat", in *Intl. Mobile Satellite Conference*, Ottawa, Canada, Jun 1999.

[75] J. Kingwell and W. Deeker (Ed.), *Annual Report 2002/2003*, Cooperative Research Centre for Satellite Systems, Canberra, ACT, 2003.

[76] N. Rao, A. Parfitt, A. Dadello, D. Ward, and T. Bird, "A Low Noise Ka-Band Down Converter for Space Applications", in *30th European Microwave Conference*, Paris, France, Oct 2000.

[77] S.G. Hay, S.J. Barker, and S.H.H. Lim, *Radiation-Pattern Measurements of FedSat Antennas on TinSat*, CRCSS/CSIRO Internal Document TIPP 965, Epping, New South Wales, Jan 2000, (Commercial-in-confidence).

[78] W.G. Cowley, M. Tykesson, A. Burge, T. Kemp, H. Soetiyono, and A. Bish, "An S-band Ground Station for FedSat and CHIPSat Operations", in *10th Aust. Intl. Aerospace Congress (AIAC 2003), incorp. in the 14th National Space Engineering Symposium*, Brisbane, Queensland, Jul-Aug 2003.

[79] S. Reisenfeld, E. Aboutanios, K. Willey, M. Eckert, R. Clout, and A. Thoms, "The Design of the FedSat Ka Fast Tracking Earth Stations", in *8th Intl. Aerospace Congress*, Adelaide, SA, 13 Sep 1999.

[80] Orbital Systems, "Model 2.4 XLSA System", *http* : *//www.orbitalsystems.com*, Jun 2005, Last accessed: 15 Mar 2008.

[81] K. Ostmo, "Keyhole problem", *http* : *//en.wikipedia.org/wiki/Image* : *Keyhole_problem.png*, 19 Jul 2006, Last accessed: 15 Mar 2008.

[82] K. Willey, *Pointing Error Reduction when Tracking LEO Satellites with a Low-Cost, Rapidly Deployed, Transportable Earth Station*, PhD thesis, University of Technology, Sydney, Faculty of Engineering, 2002.

[83] S. Reisenfeld, "Quote for a commercial Ka band tracking station", Personal communication, UTS CRCSS, 2008.

[84] S. Reisenfeld, *Revised Link Budget*, CRC for Satellite Systems, Internal Document, Sydney, NSW, 23 March 2000.

[85] P. Wade, "Offset-Fed Parabolic Dish Antennas", *The ARRL UHF/Microwave Projects Manual*, vol. 2, 1998.

[86] J. Robinson and J. Vezmar, "Comparison of Metal and Fiberglass (SMC) Satellite Antennas For Tx/Rx Ku and Ka band Applications", White Paper, unknown.

[87] General Dynamics, "Products/Antennas, Series 3120 Specification Sheet", *http : //www.gdsatcom.com/antennas.html*, 2007, Last accessed: 16 Mar 2008.

[88] R.J. Acosta, "Special Effects: Antenna Wetting, Short Distance Diversity and Depolarization", in *Online Journal of Space Communication*, http://www.spacejournal.org, Fall 2002, 2.

[89] M.M.Z. Kharadly and R. Ross, "Effect of Wet Antenna Attenuation on Propagation Data Statistics", *IEEE Trans. on Antennas and Propagation*, vol. 49, no. 8, 2001.

[90] R.K. Crane and D.V. Rogers, "Comments on 'Effect of Wet Antenna Attenuation on Propagation Data Statistics'", *IEEE Trans. on Antennas and Propagation*, vol. 50, no. 9, 2002.

[91] C. Chapman, *Mechanical Design of a Fast-Tracking Pedestal for the UTS Ka Band Earth Station*, UTS (Internal Design Document), Sydney, NSW, Nov 2002.

[92] Baldor, *Brushless AC Servo Motor Specifications*, Australian Baldor Pty Ltd, North Ryde, NSW, Oct 2004.

[93] Advanced Orientation Systems Inc., *EZ-Compass-3 Application Manual*, AOSI, Linden, NJ, Oct 2004.

[94] Stabila GmbH, "Stabila Precision Spirit Levels", *http : //www.stabila.de*, undated, Last accessed: 23 Mar 2008.

[95] User Manual, *20 GHz Phase Locked LNB*, NewTec Cy, Sint-Niklaas, Belgium, Feb 1999.

[96] User Manual, *Ka Band Transmit Module for Satellite Interactive Terminals*, NewTec Cy, Sint-Niklaas, Belgium, Jun 1999.

[97] Miteq, "Microwave Components & Assemblies", *http : //www.miteq.com/*, undated, Last accessed: 23 Mar 2008.

[98] Mini-Circuits, "RF/IF & Microwave Components", *http : //www.minicircuits.com*, 2008, Last accessed: 23 Mar 2008.

[99] T. Bird, *FedSat Ka band local oscillator specifications*, CSIRO-TIP, Marsfield, NSW, Mar 2008, Personal Communication.

[100] S. Reisenfeld and E. Aboutanios, "A new algorithm for the estimation of the frequency of a complex exponential in additive Gaussian noise", *IEEE Communication Letters*, vol. 7, no. 11, pp. 549–551, Nov 2003.

[101] D.J. Cooper, "Practical Process Control - Proven Methods and Best Practices for Automatic PID Control", *http : //www.controlguru.com/pages/table.html*, 2006-2008, Last accessed: 21 Sep 2008.

[102] R. Muszynski, "Tests and Criteria for Tuning and Evaluation of Servo-Drive Control System", in *Intl. Symposium on Industrial Electronics*, Dubrovnik, Croatia, 20-23 June 2005.

[103] Zeli Systems, "SATPAK PCI", $http://www.zeli.com/SATPAK-PCI.htm$, undated, Last accessed: 23 Mar 2008.

[104] R. Stehle, "Magnetometer 1-PPS Synchronization", $http://transport.sri.com/projects/maccs/wiki/Timing$, Apr 2005, Last accessed: 23 Mar 2008.

[105] Federal Aviation Administration (US), "Navigation Services", $http://gps.faa.gov$, Mar 2008, Last accessed: 23 Mar 2008.

[106] Navstar GPS Joint Program Office, *Navstar GPS Space Segment/Navigation User Interfaces, IS-GPS-200, Revision D*, Space and Missile Systems Center (SMC), El Segundo, CA, USA, 7 Dec 2004.

[107] Texas Instruments, "TMS320C6711D Floating-Point Digital Signal Processor (Rev. B)", $http://focus.ti.com/docs/prod/folders/print/tms320c6711d.html$, Jun 2006, Last accessed: 23 Mar 2008.

[108] BlueWave Systems, *SB3410 Digital Transceiver User Manual*, BlueWave Systems Inc., Carrolton, TX, 1999.

[109] Analog Devices, *AD9835 50 MHz CMOS Complete DDS Specifications*, Analog Devices, Norwood, MA, 1998.

[110] Analog Devices, Inc., "A Technical Tutorial on Digital Signal Synthesis", $http://www.ieee.li/pdf/essay\_dds.pdf$, 1999, Last accessed: 16 Sep 2008.

[111] Thoms, A., *UTS Earth Station DSP Implementation*, UTS (Internal Design Document), Sydney, NSW, 2002.

[112] Y.S. Kim, *UTS Ka Band Earth Station Software Design Documentation*, UTS (Internal Design Document), Sydney, NSW, 2004.

[113] unknown, "AD9835 Direct Digital Synthesis", $http://hem.passagen.se/communication/dds.html$, 16 Nov 2001, Last accessed: 16 Sep 2008.

[114] Analytical Graphics, Inc., "Satellite Tool Kit", $http://www.stk.com$, 2008, Last accessed: 26 Mar 2008.

[115] Aboutanios E., *UTS Earth Station Utility Software Documentation*, UTS (Internal Design Document), Sydney, NSW, 2003.

[116] T. Aubrey, *Test Results for FedSat Ka Band Link*, CRCSS/UTS Poster, Sydney, NSW, 2000.

[117] A. Brady, *UTS Earth Station Survey Results*, CRCSS/UTS Internal Communication, Sydney, NSW, Jan 2003.

[118] Australian Bureau of Meteorology, "Sydney Basin Rainfall", *http* : *//www.bom.gov.au/hydro/flood/nsw/sydney_metro.shtml*, 2003-2008, Last accessed: 29 Mar 2008.

[119] Sydney Water, "Hydstra Precomputed Reports", http://www.sydneywater.com.au/monitoringservices/rainfall/, 2003-2008, Last accessed: 29 Mar 2008.

[120] R. Walker, "Preliminary In-Orbit Performance Analysis of the FedSat GPS Receiver", in *The 6th Intl. Symposium on Satellite Navigation Technology & Applications*, Melbourne, Vic, 22-25 July 2003.

[121] NORAD, "North American Aerospace Defense Command", *http* : *//www.norad.mil/about/index.html*, 2008, Last accessed: 31 Mar 2008.

[122] T.S. Kelso, "Space Surveillance", *Satellite Times*, vol. 4, no. 1, pp. 68–69, 1997.

[123] T.S. Kelso, "More Frequently Asked Questions", *Satellite Times*, vol. 4, no. 5, pp. 76–77, 1998.

[124] United States Government, "SpaceTrack - The Source for Space Surveillance Data", *http* : *//www.space-track.org*, 2004-2008, Last accessed: 31 Mar 2008.

[125] T.S. Kelso, "Real-World Benchmarking", *Satellite Times*, vol. 3, no. 2, pp. 80–82, 1996.

[126] N. Rao, *FedSat Comms Payload Ka band Transponder In-orbit Performance Report*, CRCSS/CSIRO Internal Document, Epping, New South Wales, Mar 2004.

[127] R.R. Bate, D.D. Mueller, and J.E. White, *Fundamentals of Astrodynamics*, Dover Publications, Mineola, NY, first edition, 1971.

[128] P. de Bernardis, P.A.R. Ade, J.J. Bock, J.R. Bond, and J. Borrill et al., "A flat Universe from high-resolution maps of the cosmic microwave background radiation", *Nature*, vol. 40, no. 4, pp. 955–959, Apr 2000.

[129] Y.S Chu and S.P. Shih, "An Investigation of 19.5 GHz Sky Noise Temperature over Taiwan Area", *Terrestrial, Atmospheric and Oceanic Sciences Journal*, vol. 10, no. 4, pp. 821–834, Dec 1999.

[130] R.E. Henning, R.A. Bauer, F. Davarian, and H. Helmken, "ACTS Propagation Research - A Key to Increased Satellite Communication Capacity", in *IEEE National Telesystems Conference*, San Diego, CA, 26-28 May 1994, pp. 211–216.

[131] R.J. Doviak and D.S. Zrnic, *Doppler Radar and Weather Observations*, Academic Press, San Diego, CA, second edition, 1993.

[132] Australian Bureau of Meteorology, "The Australian Weather Watch Radar", *http* : *//www.bom.gov.au/reguser/by_prod/radar/about/index.shtml*, 2008, Last accessed: 4 Apr 2008.

[133] N.H.H. Kliamis, O.A.R Sharif, Z. Hanzaz, and A. Baharom, "Determination of the Melting Layer from Meteorological Radar Data in Malaysia", in *Intl. Symp. on Microwave, Antenna, Propagation and EMC Technologies for Wireless Communications*, Hangzhou, China, 16-17 Aug 2007, pp. 1467–1470.

[134] WeatherZone, "Sydney Weather Radar - Radar and Lightning", *http : //www.weatherzone.com.au*, 2008, Last accessed: 6 Apr 2008.

[135] Australian Bureau of Meteorology, "Radar Archive - Polar Format Datasets & Display Images", *http : //www.bom.gov.au/nmoc/archives/Radar/samples/*, 2008, Last accessed: 5 Apr 2008.

[136] L.J. Ippolito and T.A. Russell, "Propagation Considerations for Emerging Satellite Communications Applications", *IEEE Proceedings*, vol. 81, no. 6, pp. 923–929, Jun 1993.

[137] C. Amaya and D.V. Rogers, "Characteristics of Rain Fading on Ka-Band Satellite-Earth Links in a Pacific Maritime Climate", *IEEE Transactions on Microwave Theory and Techniques*, vol. 50, no. 1, pp. 41–45, Jan 2002.

[138] N.J. McEwan, Z.A. Abdul Rashid, and S.M.R. Jones, "Calibration Techniques for Olympus 20GHz Switched Polarization Satellite Beacon Measurements", *IEEE Trans. on Antennas and Propagation*, vol. 44, no. 9, pp. 1266–1276, Sep 1996.

[139] W.L. Stutzman, T. Pratt, and A. Safaai-Jazi et. al., "Results from the Virginia Tech Propagation Experiment Using the Olympus Satellite 12, 20 and 30 GHz Beacons", *IEEE Trans. Antennas and Propagation*, vol. 43, no. 1, pp. 62, Jan 1995.

[140] A. Dissanayake, J. Allnutt, and F. Haidara, "A prediction model that combines rain attenuation and other propagation impairments along Earth-satellite paths", *IEEE Trans. on Antennas and Propagation*, vol. 45, no. 10, pp. 1546–1558, Oct 1997.

[141] C.E. Mayer, B.E. Jaeger, R.K. Crane, and X. Wang, "Ka-Band Scintillations: Measurements and Model Predictions", *IEEE Proc.*, vol. 85, no. 6, pp. 936–945, Jun 1997.

[142] Australian Bureau of Meteorology, Statement on Draught, "Long-term rainfall deficiencies persist, mainly in the east", *http : //www.bom.gov.au/announcements/media_releases/climate/drought/*, 5 May 2004, Last accessed: 12 Apr 2008.

[143] Australian Bureau of Meteorology, "Rainfall IFD Data System", *http : //www.bom.gov.au/hydro/has/cdirswebx/cdirswebx.shtml*, 2008, Last accessed: 12 Apr 2008.

This thesis was written in LaTeX